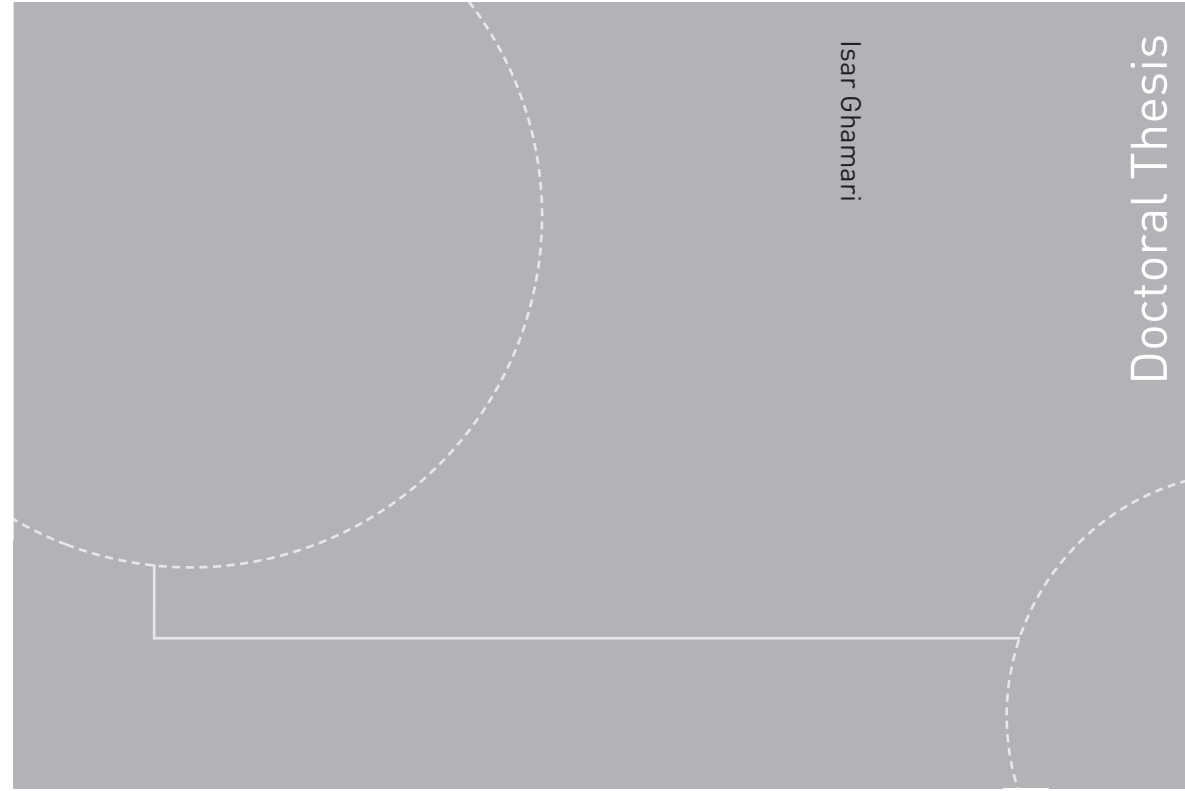


Doctoral theses at NTNU, 2019:21

Isar Ghamari

Numerical and Experimental Study on the Ship Parametric Roll Resonance and the Effect of Anti-Roll Tank



ISBN 978-82-326-3654-9 (printed version)
ISBN 978-82-326-3655-6 (electronic version)
ISSN 1503-8181

Doctoral theses at NTNU, 2019:21

NTNU
Norwegian University of
Science and Technology
Faculty of Engineering Science and Technology
Department of Marine Technology

 **NTNU**
Norwegian University of
Science and Technology

 **NTNU**

 **NTNU**
Norwegian University of
Science and Technology

Isar Ghamari

Numerical and Experimental Study on the Ship Parametric Roll Resonance and the Effect of Anti- Roll Tank

Thesis for the degree of Philosophiae Doctor

Trondheim, January 2019

Norwegian University of Science and Technology
Faculty of Engineering Science and Technology
Department of Marine Technology



Norwegian University of
Science and Technology

NTNU

Norwegian University of Science and Technology

Thesis for the degree of Philosophiae Doctor

Faculty of Engineering Science and Technology
Department of Marine Technology

© Isar Ghamari

ISBN 978-82-326-3654-9 (printed version)

ISBN 978-82-326-3655-6 (electronic version)

ISSN 1503-8181

Doctoral theses at NTNU, 2019:21



Printed by Skipnes Kommunikasjon as

to my wife
to my parents

Abstract

The parametric resonance in roll motion (known shortly as parametric rolling) is studied for a fishing vessel and container ship in regular waves. This is an instability and resonance phenomenon can lead the roll motion to reach very high oscillations amplitudes at its natural frequency, depending on the damping level involved. In the worst cases, it is responsible for vessel capsizing. Here, the problem is investigated numerically and experimentally, performing dedicated physical tests on a typical Norwegian fishing vessel with blunt hull and small length-to-beam ratio.

Different numerical solvers with different level of sophistication were developed and used to study the parametric rolling (PR) phenomenon, its occurrence and features. A 5-DOF numerical simulator was developed based on the Salvesen-Tuck-Faltinsen (STF) strip theory (Salvesen et al. [1]) formulation first and was validated for a post-Panamax C11 class container ship in regular waves. To study the PR for the fishing vessel, with beam-to-length ratio twice the ratio of studied container ship, 3D effects must be considered more adequately. Therefore, another simulator was developed based on a 6-DOF 3D hybrid method where the radiation and diffraction potentials were computed for zero forward speed by WAMIT and used in the STF strip theory to obtain speed dependent loads. The convolution integrals were used to account for the effect of radiation free-surface memory effect (Cummins [2]). The non-linear Froude-Krylov and restoring loads were calculated in each time step of the simulations, by integrating the undisturbed incident wave dynamic pressure and the hydrostatic pressure over the instantaneous wetted hull surface up to the undisturbed incident free surface and accounting for the body motions. It was observed that using weak-scatterer hypothesis in radiation and diffraction loads provides better results in long and steeper waves ([3], [4]). The coupling with horizontal motions also showed to be important in capturing the PR phenomenon. A dedicated experimental campaign was also carried out in the CNR-INSEAN test basin for the SFH112 fishing vessel. The tests were performed for the cases without forward speed and with forward speed, with corresponding Froude number $Fn = 0.09$ and $Fn = 0.18$. The tests were carried out with different wave frequencies and wave steepnesses. The numerical simulations showed good agreement with the experimental results. For the cases near the instability border, the physical and numerical predictions were different in terms of PR occurrence.

The effect of free-surface anti-roll tank on the PR was also studied experimentally and numerically. In the numerical simulation, a CFD sloshing

solver, based on the “Open source Field Operation And Manipulation”, known in short as Open-FOAM, and assuming 2D laminar flow conditions, was coupled to the main seakeeping simulator to account for the sloshing loads from the tank. From present studies, the tank-ship interaction cannot be modeled as a weak coupling. Here an iterative strategy was proposed, which proved to be successful when compared against established 2D experiments [5] and against our dedicated tests on the fishing vessel. In the experimental side, different tank sizes have been tested to study the tank effects in the PR region. The coupled simulator is validated based on the mentioned experimental data. The performed analysis suggests that a well-designed anti-roll free surface tank could easily avoid the parametric rolling phenomena.

Acknowledgement

Carrying out the requisite work and then writing this thesis was, undoubtedly, the most demanding task I have ever undertaken. However, one of the joys of having completed the thesis is looking back at everyone who has helped me over the past six years.

I would like to begin by thanking my supervisor, Prof. Odd Faltinsen and my co-supervisor, Prof. Marilena Greco. It is an often used cliché, but in this case it is no overstatement to say that without the consistent guidance, support, unparalleled knowledge, and encouragement of my two supervisors, this thesis would never have existed. I would like to thank Prof. Faltinsen for giving me the privilege to be his last PhD student. I learned a lot from him during these years. I would also like to thank Prof. Marilena Greco who has always been there for me. I have been extremely lucky to have a co-supervisor who cared so much about my work, and who responded to my questions and queries so promptly.

The experiments for the fishing vessel model in this thesis, were done in CNR-INSEAN, Italy, under the supervision of Prof. Claudio Lugni. The contribution from him and CNR-INSEAN staff are highly appreciated. I would like to thank Dr. Renato Skejic for providing me with the 2D strip theory code. Prof. Nicholas Newman is thanked for his help with the use of WAMIT. Dr. Reza Firoozkoohi helped me with the sloshing part and OpenFOAM. Bureau Veritas helped me with free use of HydroStar. I also want to express my appreciation for the valuable suggestions from and discussions with Dr. Babak Ommani, Dr. Maxime Thys, Dr. Madjid Karimirad, Dr. Yugao Shen, Finn Christian W. Hanssen, Dr. Mohsen Bardestani and Dr. Peng Li.

I would also like to thank all my classmates and colleagues and administrative staff at the Marine Technology Department at NTNU. These years became easier by socializing, chitchats, coffee breaks and having lunch together with them. Dr. Mahdi Ghane, Dr. Amir Rasekhi Nejad, Mostafa Jalali, Dr. Mehdi Zadeh, Dr. Mahmoud Etemaddar, Daniele Borri, Dr. Mauro Candeloro, Dr. Mohammad Saud Afzal, Sabah Alwan, Dr. Afshin Abbasi Hosseini, Dr. Vahid Hassani, Reza Mohseni and Ramin Dehbashi are thanked.

My deepest gratitude goes to my parents (Moosareza and Fatemeh) and brothers (Meysam, Misagh and Mostafa) for their support, encouragement and unflagging love through all these years. I also thank my in-laws for their support during these years.

At last but not least, I thank my beautiful wife, Hoda, who was always

there, and always supported me unconditionally. I do not forget the dark long nights when nothing seemed to work in my project but she patiently and passionately tried to show me the light at the end of the tunnel. Thank you my love for always believing in me. Our old plan is now complete, and the next adventure has begun. I am blessed to be able to share it with such a magnificent lady.

I dedicate this thesis to my wife and my parents.

Isar Ghamari

Trondheim, January 2019

Nomenclature

Abbreviations

2D	Two-dimensional
3D	Three-dimensional
BEM	Boundary Element Method
BVP	Boundary Value Problem
CFD	Computational Fluid Dynamics
COG	Centre of Gravity
DOF	Degrees of Freedom
FFT	Fast-Fourier Transformation
ITTC	International Towing Tank Conference
LCB	Longitudinal Center of Buoyancy
LCG	Longitudinal Center of Gravity
PR	Parametric Rolling
RAO	Response Amplitude Operator
RK	Runge-Kutta method
STF	Salvesen-Tuck-Faltinsen
VCG	Vertical Center of Gravity

Greek Letters

η_j	Displacement in the j th mode
----------	---------------------------------

λ	Wave length
μ	waters dynamic viscosity
∇	Ship displacement
ν	waters kinematic viscosity
ω_0	Wave circular frequency
ω_e	Wave frequency of encounter
$\phi(x, y, z, t)$	Total velocity potential
ϕ_D	Diffraction velocity potential
ϕ_I	Velocity potential due to incident waves
ϕ_j	Radiation velocity potential due to motion in j th mode
$\phi_S(x, y, z)$	Steady-state velocity potential
$\phi_T(x, y, z, t)$	Unsteady velocity potential
ρ	Waters mass density
ξ_j	Complex amplitude of the j th mode of motion
ζ_a	Wave amplitude
ζ	Free-surface elevation

Mathematical Operators

\cdot	Dot-product
$\nabla \cdot$	Divergence
$\nabla \times$	Curl
∇^2	Laplacian
∇	Gradient
\times	Cross-product

Roman Letters

A_{jk}	Added mass coefficient in j th mode due to the motion in k th direction
B	Ship beam
B_{jk}	Damping coefficient in j th mode due to the motion in k th direction
C_B	Vessels block coefficient
C_{jk}	Restoring coefficient in j th mode due to the motion in k th direction
D	Ship draft
Fn	Froude number
g	Gravitational acceleration
GM_L	Logitudinal metacentric height
GM_T	Transverse metacentric height
H	Wave height
I_{jk}	Product of inertia
I_{xx}, I_{yy}, I_{zz}	Moment of inertia
k	Wave number
$K_{jk}(t)$	Response impulse function
K_{xx}	Radius of gyration in roll
K_{yy}	Radius of gyration in pitch
K_{zz}	Radius of gyration in yaw
L_{pp}	Ship length between perpendiculars
L_{wl}	Ship length at the waterline
M	Ship mass
M_{jk}	Generalized mass matrix
p	Pressure

p_a	Atmospheric pressure
S_0	Mean wetted body surface
S_B	Wetted body surface
U	Ship mean forward speed
x', y', z'	Body-fixed coordinate system
X, Y, Z	Earth-fixed coordinate system
x, y, z	Seakeeping coordinate system
Z_B	Vertical position of the center of buoyancy
Z_G	Vertical position of the center of gravity

Contents

1	Introduction	1
1.1	Overview	1
1.1.1	The M/V APL China incident	1
1.1.2	The Maersk Carolina incident	2
1.1.3	Parametric Roll Resonance	4
1.2	Previous Studies	9
1.3	Classification Societies and other Organization's Guidelines	14
1.4	Literature about use of the anti-roll tanks	15
1.5	Current study	17
1.5.1	Thesis Outline	17
1.5.2	Main Contributions	18
2	Seakeeping formulation in regular waves	21
2.1	General assumptions	21
2.2	Wave body interaction problem	22
2.2.1	Radiation Loads	25
2.2.1.1	Radiation Loads in frequency and time domain	33
2.2.2	Non-linear Froude-Krylov and restoring loads	40
2.2.3	The undisturbed regular incoming waves	41
2.2.4	Diffraction Loads	42
2.3	Final Formulation of the Governing Equations of Motion	46
2.3.1	Linear frequency domain equations of motion	46
2.3.2	Time domain equations of motion	52
2.4	Conclusion	55
3	Modules in the numerical simulation model	57
3.1	2D numerical sloshing solver	57
3.1.1	Validation of the numerical 2D sloshing solver	59
3.1.1.1	Free surface flow in a 2D tank forced to sway motion	59

3.1.1.2	Validation of the roll moment and phasing in forced 2D sloshing	61
3.1.1.3	Validation of the roll moment and horizontal forces for a 2D tank forced to roll	64
3.2	Coupled seakeeping-sloshing solver	68
3.3	Module of mooring cables calculations	74
3.4	Weak-scatterer hypothesis formulation	78
4	SFH112 fishing vessel model and experimental set-up	81
4.1	Introduction	81
4.2	SFH112 fishing vessel model	81
4.3	Mooring system	86
4.4	Anti-roll tank set-up	87
5	Experiments and numerical simulations (using strip theory) of parametric rolling in post-Panamax C11 class container- ship	89
5.1	Experimental set-up and numerical solver	89
5.1.1	Experimental set-up	89
5.1.2	Numerical solver	92
5.2	Results	92
5.3	Conclusion	103
6	Experiments and numerical simulations on a fishing vessel in cases without anti-roll tank	105
6.1	Cases at $F_n=0$	106
6.1.1	Cable identification and wave characteristics	106
6.1.2	Numerical and experimental results	115
6.2	Cases at $F_n=0.09$	126
6.2.1	Cable identification and wave characteristics	127
6.2.2	Numerical and experimental results	131
6.3	Cases at $F_n=0.18$	143
6.3.1	Cable identification and wave characteristics	143
6.3.2	Numerical and experimental results	146
6.4	Conclusion	160
7	Experiments and numerical simulations for a fishing vessel with anti-roll tank at $F_n=0$	167
7.1	Free surface anti-roll tank mechanism	168
7.2	Roll decay tests and cable identifications	170
7.3	Tank width=3.0 cm, tank water depth=3.9 cm	175

7.4	Tank width=4.0 cm, tank water depth=3.9 cm	184
7.5	Tank width=5.1 cm, tank water depth=3.9 cm	193
7.6	Tank width=8.1 cm, tank water depth=3.9 cm	207
7.7	Conclusion	216
8	Summary and further work	221
8.1	Numerical solvers	221
8.2	Different ships studied	222
8.2.1	Cases without tank and $Fn = 0$	225
8.2.2	Cases without tank and $Fn=0.09$	229
8.2.3	Cases without tank and $Fn=0.18$	230
8.2.4	Cases with tank at $Fn=0$	230
8.3	Conclusion	233
8.4	Recommendation for further work	234
	References	237
A	Retardation function formulation	245
A.1	Integrals in the retardation formulation	245
A.2	Retardation functions for the fishing vessel SFH112	246
B	Experimental uncertainties	249
B.1	Instrument precision	249
B.2	Error analysis: Repeatability error	250
C	Further experiments and numerical simulations	261

Chapter 1

Introduction

1.1 Overview

Parametric roll resonance was not considered as a serious technical issue for naval architects and maritime researchers until several incidents occurred during the past two decades. Two of them will be explained in detail here.

1.1.1 The M/V APL China incident

In October 1998, the *M/V APL China* (a C11 class post-Panamax container ship with 260 m length and 40 m breadth) was travelling from Kaohsiung, Taiwan, to Seattle, USA, carrying around 4000 containers most of which, full of cargo for the Christmas season. Off Alaska's Aleutian Islands, she was overtaken by a severe storm lasting more than 12 hours. At the harshest points, green water at bridge level was observed by the crew (reported by officers). The ship master attempted to turn her towards the high waves and reduced the speed.

Besides the violent storm, very large motions during the worst part of the storm made the situation even more critical. Significant heave and pitch amplitudes in addition to a roll angle reached around 35-40 degrees made this incident one of the biggest in its type in the history. The following day, the damage was quantified: One fourth of the 1300 on-deck containers were lost overboard and almost similar amount were severely damaged [6] and the ship itself suffered structural damage [7]. This is said to be the biggest cargo disaster in history, in which the total lost cargo worth over USD 100 millions [8] (even more than the total value of the ship (USD 50 millions)[7]). Some pictures of the ship when she arrived in USA is shown in figure1.1.



Figure 1.1: The APL China Incident [Images from www.cargolaw.com].

1.1.2 The Maersk Carolina incident

Another incident occurred for the *Maersk Carolina* ship (a container ship 292m long and 32m wide) in January 2001, which was travelling from Algeciras, Spain, to Halifax, Nova Scotia, Canada carrying more than 2100 containers. In a bad weather at east of Nova Scotia, she confronted a high sea-state, then the ship master reduced the speed and turned her towards the waves according to the standard procedures. Very high heave and pitch motions were experienced by the ship and at one point, very large roll motion built up in a few cycles and reached to 47 degrees or even more (the ship inclinometer saturated at that value). Around 133 containers were lost and around 50 were damaged. The cargo loss cost around USD 4 millions besides the damage that occurred for the ship structure ([8], [7], [9]). Some pictures of the ship and the containers after this incident are shown in Fig. 1.2.



Figure 1.2: The MAERSK Carolina Incident [Images from www.cargolaw.com].

1.1.3 Parametric Roll Resonance

In many fields, the dynamic behaviour of a system due to periodic excitation (input) is of great interest. Two types of oscillatory responses are forced oscillation and parametric oscillation. The first one appears when the system is excited by a periodic input. If the excitation frequency is close to a natural frequency of the system, then resonance (oscillation with large amplitudes, depending on the damping level of the system) will be experienced. Parametric oscillation in the system occurs when there is a periodic time-varying parameter in the system. At certain tunings, the system can experience parametric resonance, which makes large amplitudes as the output in the system responses.

A very classical example of the latter case is a person alternatively standing or crouching on an oscillating swing. To increase the swing motion, the person must crouch in the null and extreme positions of the swing and sits down and stands up in the points between them to minimize and maximize the pendulum length, i.e. the distance between the center of gravity of the person's body to the swing hanging point. This system is equivalent to a pendulum with varying length in which, the center of gravity oscillates in time with a frequency twice the pendulum natural frequency [10]. A schematic explanation for this simple system can be seen in Fig. 1.3.

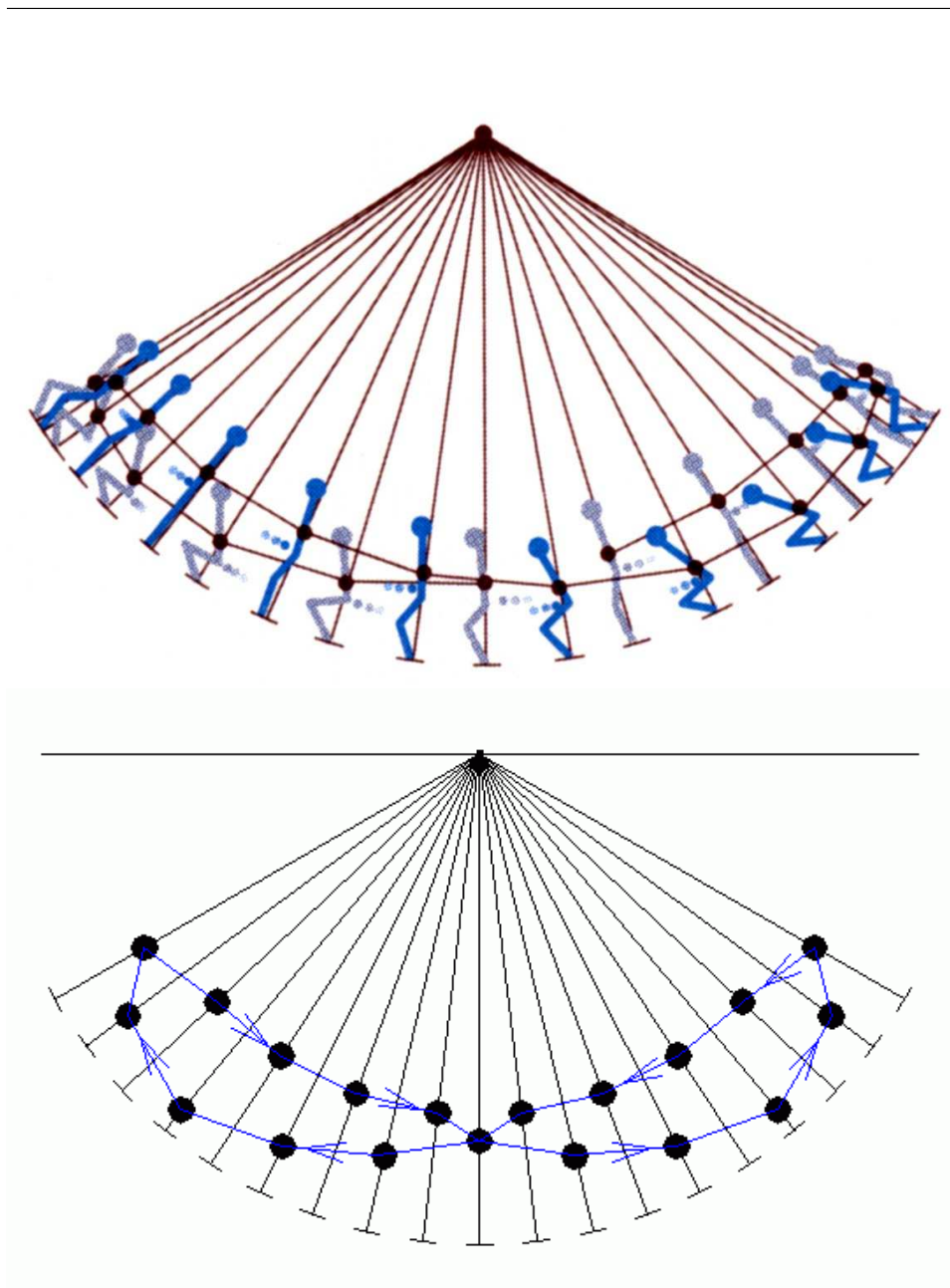


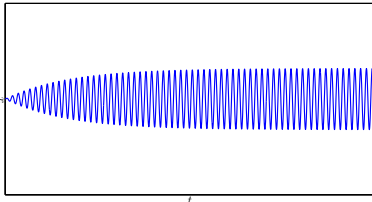
Figure 1.3: Parametric resonance in a swing with center of gravity oscillating with a frequency twice the swing natural frequency. Top: A person on the swing. Bottom: The center of gravity of the person on the swing [Images from www.hcrs.at].

As it can be seen from this figure, the pendulum stiffness is varying harmonically with a frequency twice the natural frequency of the swing. This makes the system unstable and increases the swing motion.

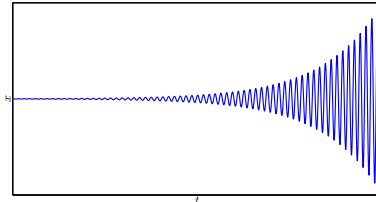
The differences of the forced and parametric resonances could be explained by a simple differential equation for a one degree-of-freedom (1-DOF) system:

$$m\ddot{x} + d\dot{x} + k(t)x = f(t) \quad (1.1)$$

where x is the system state and $d > 0$ is a constant corresponding to a linear damping coefficient of the system. $k(t) = k_0 + k_t \cos(\omega_k t)$ is the stiffness coefficient of the system, with $k_0 > k_t \geq 0$ and oscillating with (circular) frequency $\omega_k > 0$. $f(t) = f_0 \cos(\omega_f t)$ is an external forcing oscillating with (circular) frequency ω_f . If $k_t = 0$ and $f_0 \neq 0$ then the system will experience the ordinary resonance if $\omega_f \approx \omega_n = \sqrt{\frac{k_0}{m}}$, where ω_n is the system undamped natural frequency. In ordinary resonance cases, the response x can reach high values if d is limited. If $f_0 = 0$, $k_t \neq 0$, $\omega_k \approx 2\omega_n$, d is limited and either x or \dot{x} is non zero at the initial time, then the system will be parametrically resonant. Fig. 1.4 shows qualitatively the x behavior in time when the ordinary and the parametric resonances are excited.



(a) Ordinary resonance ($f_0 \neq 0, k_t = 0$)



(b) Parametric resonance ($f_0 = 0, k_t \neq 0$)

Figure 1.4: Two types of resonance.

All the parameters are the same in the two types of resonance except for k_t and f_0 . Despite the different excitation frequencies ($\omega_f = \omega_n$ and $\omega_k = 2\omega_n$), in both resonance cases the response x oscillates with system natural frequency, ω_n . In ordinary resonance, x grows more slowly than in the case of parametric resonance until the system reaches a steady-state condition. At this stage the oscillation amplitude is finite and depends on the damping coefficient d . The parametric resonance is more dangerous as the response of the linear system in Eq. 1.1 grows exponentially. Luckily,

for a real system, at sufficient large amplitude the non-linearities matter. They modify the system equation and keep finite the response.

In marine and offshore engineering, spar buoys and ships also exhibit parametric resonance. In ships, parametric resonance is known to occur in roll motion in certain conditions [10]. The huge roll motion, along with heavy pitch and heave motions, could endanger the vessel structure, the cargo and the crew on-board. The research has shown that the aforementioned incident cases in the beginning of this chapter were caused by parametric roll resonance [11]. The main reason of parametric roll resonance in the ships is the time-varying water-plane area of the hull, which produces a time-varying roll restoring coefficient, corresponding to the spring stiffness in the simple 1-DOF system in Eq. 1.1.

Normally huge roll amplitudes might occur in ordinary resonance condition excited by beam sea waves or in parametric resonance in roll (parametric rolling). Since the ship masters try to avoid severe beam seas by turning the ship into the waves, most of the time, the huge roll motions are more often connected to parametric rolling.

In parametric resonance condition, the system is unstable and any small disturbance could be amplified in a few cycles if the damping of the system is less than a threshold value. Parametric rolling mostly occurs in longitudinal seas which means there is no direct excitation moment in roll. For the parametric rolling to be triggered in regular waves, the following conditions should be met [12]:

- The natural period of roll is equal to approximately twice the wave encounter period.
- The wave length is of the order of the ship length (between 0.8 and 2 times).
- The wave height exceeds a threshold level (this threshold value is the minimum level that could trigger the parametric rolling).
- The roll damping is low.

The ships without full form body and with a very pronounced change of geometry around the mean water line in the bow and stern regions are more vulnerable to parametric roll resonance. The change of geometry around the mean water level makes a big change of water-plane area between wave crest and wave trough at midship section. These ships normally may be container ships, cruise ships and fishing vessels.

A schematic view of variation of the water-plane area and a simple graphic explanation of parametric rolling mechanism in one wave period is shown in the Fig. 1.5.

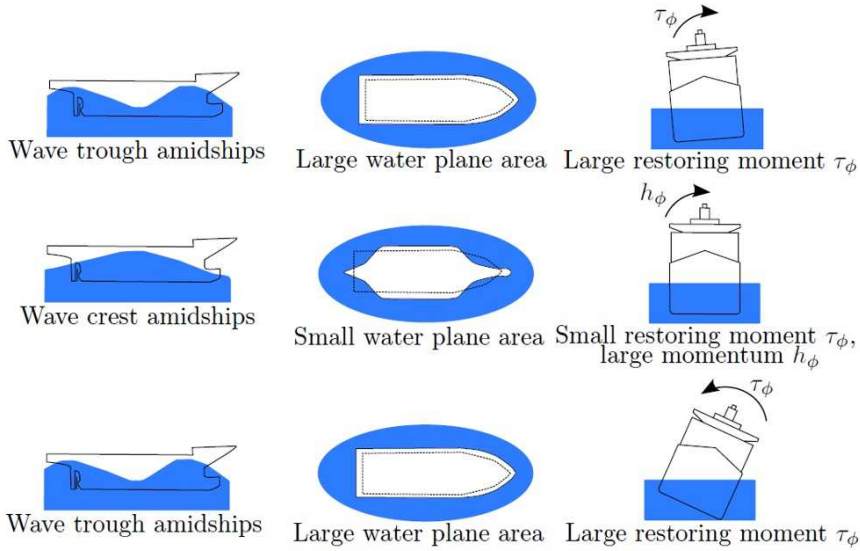


Figure 1.5: Parametric rolling mechanism in one wave period [7].

This change of water-plane area makes the transverse metacentric height (GM) and roll restoring vary consequently. Fig. 1.6 shows a sample GM variation versus time for a container ship in head sea waves.

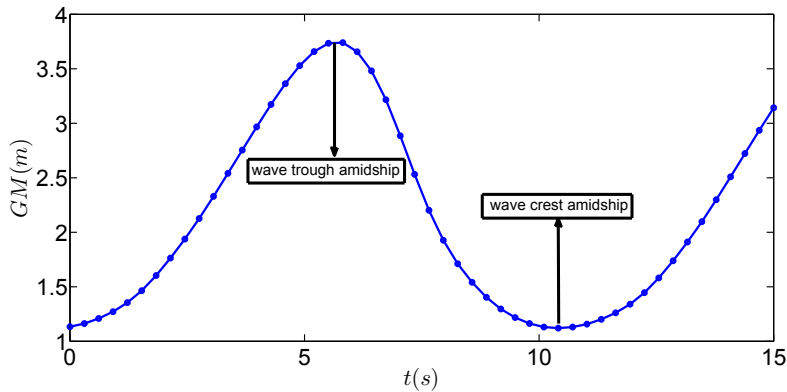


Figure 1.6: GM variation of a C11 class containership in head sea waves [12].

The GM varies with encounter frequency which corresponds to ω_k in Eq. 1.1 for a 1-DOF model.

The mentioned incidents among other ones, made a thorough analysis of this phenomenon, necessary. Many researchers worked on this problem and also some classification societies and maritime regulatory organizations like IMO, tried to issue guidelines and conventions in this regard. In the next sections a literature study on this phenomenon is presented.

1.2 Previous Studies

For the first time, the parametric rolling resonance in ships was observed by William Froude, who in 1861 reported that a ship shows undesirable sea-keeping characteristics, dangerous and even leading to capsizing, especially in roll. This is seen when the natural frequency in heave and pitch is almost twice the natural frequency in roll [13].

Grim [14] and Kerwin [15] have studied the instability in roll motion by a simple Mathieu equation which implies a roll restoring moment oscillating with the encounter-wave frequency. They investigated the roll stability by assuming that roll restoring oscillates as a function of wave passage.

Paulling [16], investigated ship forced motions in calm water with three degrees of freedom. They analyzed the non-linear coupling between heave, roll and pitch motions and they concluded that unstable motion may occur if any of the degree of freedom gets excited by one of the other two and the instability will occur when the unstable mode natural frequency is nearly half of the modes which are excited. This statement is confirmed by some experiments for a roll-heave system of a ship with forced heave in calm water.

Dunwoody [17],[18] showed a relation between the astern incident wave spectra and the metacentric height spectra and then found that the variation of metacentric height has the same effect as reducing the roll damping and then he tried to find the roll stability limits in this process.

Parametric rolling might build up very fast to high roll angles and might even lead to capsizing of the ship. As a try to understand and explain the basic mechanisms of ship capsizing, some researches tried to study the problem with simplified theoretical and numerical model, (Umeda et al.[19], Sanchez et al. [20], Oh et al.[21]). Hamamoto and Panjaitan [22], did an analytical study of the ship capsize phenomenon due to parametric rolling to identify the limits of critical conditions in this regard. Munif and Umeda [23], used a 6-DOF non-linear mathematical model to study the parametric roll and capsizing limits for a ship in astern sea and verified the results

with experiments which, showed a good agreement. They found that the effect of heave and pitch might be negligible in low steepness waves while is important in steep waves.

Initially most of the researches thought that parametric rolling occurred in the following-sea waves but gradually some works started to analyse the occurrence of parametric rolling in head-sea waves as well. Perez and Sanguinetti [24] did some experiments regarding the parametric rolling in longitudinal seas for small fishing vessels with different stern sections. They showed that a transom stern can amplify the roll motions stronger than round stern. They also concluded that since this phenomenon can make the ship reach a very high roll angle in a very short time, the crew of the ship also should be aware of this latent threat.

Neves et al. [25] studied, numerically and experimentally, the dynamic stability of two small fishing vessels in head sea. They compared the vulnerability of two types of stern to parametric excitation and concluded that a transom and wide stern is more prone to go into the unstable zone than a round stern.

Neves [26] studied the motions of a fishing vessel using a 3-DOF (heave, roll and pitch) model and using the Taylor series expansion of up to second order for restoring loads. This model showed a tendency to overestimate the roll motion in the unstable zones. Neves and Rodriguez [27] continued the previous work but using the Taylor series expansion for coupled restoring loads up to the third order, which showed a better agreement with experimental data.

Hua [28] analyzed a RoRo ship subjected to parametrically excited roll motion in longitudinal waves and the effect on parametric roll of many variables, such as ship speed, ship loading, wave amplitude, is investigated. The RoRo and the cruise ships normally have large flare near the waterline at bow and stern to allow for larger cargo space and higher operational speed. Hua [29] investigated the non-linear characteristics of the GM variation of a RoRo ship in irregular waves by means of available non-linear probability theories.

After the APL China incident in 1998, several incidents involving parametric roll in head-sea waves were reported such as: destroyers incidents (Franchescutto [30]), Maersk Carolina ship incident in January 2001, RoPax ships (Franchescutto et al., [31]) and PCTC vessels (Palmquist and Nygren, [32]). So an increasing attention was given to head-sea parametric rolling and many researchers started more research on stability issues in head sea. Francescutto et al. [31], investigated, numerically and experimentally, the conditions for parametric rolling with discussion on the threshold value for

the roll damping to avoid parametric rolling and on the threshold value of wave excitation to trigger parametric rolling. He also examined the parametric-roll amplitude once the instability is excited. Spyrou [33] reviews the state-of-the-art regarding the parametric rolling for a deterministic and probabilistic environment and presented some new ideas about the development of practical design criteria. The work by Francescutto (2004) and Spyrou (2005) made the foundation for the ITTC recommended procedure and guidelines for predicting the occurrence and magnitude of parametric rolling, published in 2006 [34].

France et al., [11] investigated numerically the head-sea parametric rolling for a container ship and its effect on the securing and lashing system of the onboard containers. They also checked three types of bow flare and three types of stern against parametric rolling and concluded that the vessels with flat transom stern and significant bow flare are most prone to parametric rolling due to the large variation of the water-plane area that these vessels undergo in head seas. Levadou et al. [35], studied the parametric rolling problem in different loadings and wave heading (head and bow seas) conditions and as a function of ship speed. They documented several polar diagrams with the steady-state roll amplitude against varying speed and headings for a given wave period. Many graphs are presented for different wave periods and these diagrams can be used as operational guidance for helping the ship masters in order to avoid extreme roll motions. Shin et al. [36] discusses the technical background of the American Bureau of Shipping (ABS) Guide for the assessment of parametric roll resonance in the design of container ships. They verified the susceptibility and severity criteria in the mentioned report using a series of numerical simulations and finally concluded that both susceptibility and severity criteria were verified and showed to be reasonable and reliable. They did some calculations for nine ships and the criteria predicted correctly the presence or absence of the parametric roll in all ships. The paper also showed that in order to obtain reliable results in irregular seas, one realization is not enough and the distribution of parametric roll resonance might not be Gaussian.

From full scale observation, at high values of metacentric height, the occurrence of parametric rolling is associated to head sea conditions (Lovstادت and Bloch Helmers [37]). However, the problem can happen in following and quartering seas for lower values of intact stabilities [38]. Kruger [39] addressed the problem of ship intact safety parameters. He provided some dynamic stability criteria that will account for a minimum stability margin to ensure sufficient ship safety. He used many simulations for different types of ship for the assessment of the mentioned criteria. The problem of cargo

loss of a post-Panamax container ship was analyzed by Kruger [40]. He used the strip theory for the calculation of the ship motions. He concluded that the ship suffered a 1:1 parametric resonance in roll in stern quartering seas. Here 1:1 means encounter frequency equals the natural roll frequency.

Silva et al. [41], studied the parametric rolling of a container ship in regular and irregular waves using a partly non-linear strip theory formulation. They used a frequency domain 5-DOF (all motions except surge) system and a roll damping coefficient from the decay tests. The results and comparison with experiments show that this method gives reasonable results for parametric resonance. They also suggested that there should be some revision to the IMO's "Guidance to the Master for Avoiding Dangerous Situations in Following and Quartering Seas". They mentioned also that, in bow-sea scenario and in parametric resonance, the first action could be increasing the speed rather than reducing it to quit unstable zone. Levadou et al. [42], studied the main dimension, hull form and appendages configuration effects on parametric roll while keeping the draft, GM and natural roll period constant. They used a relatively simple one degree of freedom non-linear model along with some model tests and concluded that, for the C11 container ship, the aft body shape is more important than the bow flare in parametric rolling. They also mentioned that a V-shape aft body is preferable to a U-shape aft body for avoiding parametric roll. Mccue et al. [43], also studied the effect of topside shape on parametric rolling for a destroyer in longitudinal seas. Spyrou et al. [44], systematically investigated a post-Panamax container ship rolling, on the basis of several analytical formulas that exist in the industrial guidelines and that are evaluated by a step-by-step process against various numerical predictions. Identification of the instability boundary and the prediction of steady amplitude of roll oscillations were also assessed in their work. Belenkey et al. [45], presented a background for parametric roll risk analysis of a ship operating in head seas. The ship motions are studied numerically in irregular waves with the conclusion that despite large amplitude motions, pitch and heave retain their ergodic qualities and normal character of distribution while the roll motion clearly is not ergodic and is not necessarily a Gaussian stochastic process. If the statistical properties of a random process could be deduced from a single and sufficiently long random sample, it is ergodic process, otherwise it is not.

Bulian et al. [46], presented the preliminary results regarding the problem of non-ergodicity of parametric roll in longitudinal irregular long-crested waves. Some numerical simulations using an analytical 1.5-DOF were performed and showed the effect of ship speed and sea spectrum shape on

parametric roll. The alternative to a 6-DOF system for studying parametric rolling, is to consider fewer-DOF systems like 3-DOF or 1.5-DOF, where some coupling terms and some degrees of freedom are assumed to be zero in order to simplify the problem while maintaining, hopefully, the relevant terms. In a 1.5-DOF model, for instance, the roll restoring moment is a function of time and roll angle, and should be calculated a priori. Bulian et al. [47], proposed a 1.5-DOF analytical and numerical system for parametric rolling analysis in regular and irregular head seas where heave and pitch motions were considered quasi-static. They used this model as a tool to find the instability threshold and the roll amplitude above threshold. They validated their model against experimental results of a RoRo ship in both regular and irregular waves.

According to Turk [38], it is quite accepted that the wave effect on roll restoring moment can be qualitatively estimated with the Froude-Krylov assumption. However, some of the authors reported that the Froude-Krylov prediction could overestimate for a fishing vessel known as the ITTC ship A-2 as a result of captive model experiments [48]. Umeda et al. [49] mentioned that the captive model experiments for a container ship known as the ITTC Ship A-1, showed that the Froude-Krylov prediction could overestimate the values of roll restoring moment at low speed cases and therefore could overestimate the danger of capsizing associated with parametric rolling. They used a single-DOF model with roll damping from decay tests and restoring moment from Froude-Krylov assumption and captive model tests to investigate parametric rolling in a container ship. Munif and Umeda [50] continued the work numerically investigating the parametric rolling for an Icelandic trawler. This ship shows no significant variation in hydrostatically-obtained metacentric height but it shows parametric rolling at some conditions in experiments. They also used a 1-DOF model with balanced heave and pitch motions and a 6-DOF coupled model showing that the 6-DOF model was able to reproduce the parametric rolling while the 1-DOF could not. They concluded that the coupling effect from heave and pitch motions to roll restoring are essential for parametric rolling [50].

Greco et al. [51] examined numerically and experimentally the parametric rolling of a fishing vessel in head sea with possibility of bottom slamming and water on deck by using a 3D domain decomposition strategy. Ghamari et al. [12] investigated the parametric rolling of a C11 class post-Panamax container carrier ship with and without forward speed using strip theory. They validated the results with some experimental data from literature and showed that, for this ship, the used strip theory method could capture most of the experimental cases.

1.3 Classification Societies and other Organization's Guidelines

After the big incidents of parametric rolling in some container ships, some authority organizations in maritime industry, tried to prepare suitable guidelines regarding parametric rolling prediction and analysis in different ships.

The American Bureau of Shipping (ABS) published one of the very first quite comprehensive guidelines for prediction of parametric rolling for container ships in September 2004 and updated it in June 2008 [52]. It contains the rules and the other design and analysis criteria that ABS issues for the classification of container carriers in relation to parametric roll resonance phenomenon. It first provides a brief description of the physical phenomenon of parametric roll resonance, which may cause an excessive roll of a container ship in longitudinal (head and following sea) waves. Afterwards it provides a description of criteria used to determine if a particular vessel is vulnerable to parametric roll (susceptibility criteria) and how large these roll motions might be (severity criteria). Recommendations are given for further actions if a ship is found to be endangered by the possibility of parametric roll, including numerical simulations and a model test. Means of mitigation of the parametric roll consequences are briefly considered. In case of satisfaction of all these criteria and requirements, ABS may assign an optional class notation as recognition of safety performance in relation to parametric roll resonance. In March 2008, three container ships from Hyundai Merchant Marine fleet got the first optional class notation specific to parametric rolling [38]. The "PARRC1" notation was granted to 4700 TEU "Hyundai Forward" and 8600 TEU "Hyundai Faith" and "Hyundai Force" container ships.

Lloyd's Register of shipping (LR) investigated the container securing requirements and parametric rolling of container ships with a simple 1-DOF method. LR suggests some simplified actions for taking the ship out of the parametric instability zone based on the vessel stability variation waves plus the relationship between ship speed, roll natural frequency and wave encounter frequency [53].

Bureau Veritas (BV) presented a two stage solution for checking of parametric roll. At the first stage, the mathematical model is based on a simple Mathieu-type of equation where a 1-DOF model is used and the roll restoring coefficient is considered like a simple sinusoidal function. Based on this method it can be easily checked if the vessel is in the instability zone or not. However, in the next stage and for more critical cases, it uses a fully non-linear model to check the phenomenon more accurately [54].

DNVGL issued a container ship update and provided owners and operators with some new services, like Active Operator Guidance, advice on extreme roll motions (parametric rolling) and how to survive and avoid parametric rolling for a given sea-state, ship speed and heading. This Active operator Guidance uses a computer program for simulation of ship motions and also the real time sea-state from some wave radars technology onboard ships. This active system relates the ship motions and wave characteristics and implements the available guidance and criteria to limit different critical phenomena like water on deck, excessive impact pressure, large roll motions and so on [38].

IMO also addressed parametric rolling through several revised technical notes and documents ([55] [56] [57] [58] [59]). IMO, for instance, has published revised guidance for the ship master for avoiding dangerous situations in adverse weather and sea conditions in resolution MSC.1/Circ.1228 and the physical phenomena connected with parametric roll motions are explained. Operational guidance on how to avoid dangerous conditions with risk of successive high waves in following and head seas is given. The possibility of inception of parametric roll in head-sea waves is explained. Parametric rolling is considered dangerous not only in terms of possible capsize but also as a threat for cargo handling, due to the potentially significant accelerations involved.

As it was mentioned before, ITTC published a recommended procedures and guidelines for predicting the occurrence and magnitude of parametric rolling in 24th ITTC [60], [34]. They explain the parametric rolling basic concepts, prediction of occurrence of this phenomenon and the amplitude of the roll motion in case of its occurrence based on a 1-DOF model. They also discussed the effect of motions coupling on the parametric-roll occurrence.

1.4 Literature about use of the anti-roll tanks

The effectiveness of a passive free surface anti-roll tank (ART) in avoiding parametric rolling for a fishing vessel is investigated in this thesis by numerical simulations and experiments. The numerical simulations are validated with experiments and will be shown in chapter 7 of this thesis. For this reason, a literature survey is performed for the anti-roll tanks.

Many studies investigated the effect of anti-roll tanks on the roll motions and parametric rolling. Van den Bosch et al. [61] examined experimentally the concept of free-surface tanks as source of roll damping. They did many experiments for many cases of a passive anti-roll tank which could be a good benchmark for free-surface tank analysis in terms of provided roll moment.

When the sloshing natural frequency is equal (or a bit lower) than the ship natural roll frequency, then the tank roll moment is in phase with minus roll velocity at resonance and acts as an extra damping to the system. The general procedure for designing of the passive tanks is also provided. The authors pointed out that this device could provide enough damping to control self-excited oscillations and roll motion increase. More explanations about the mechanism of this type of anti-roll tanks can be found in section 7.1.

A complete theoretical study on passive U-tube tank, as well as discussion on the tank damping, tank mass, location relative to ship CG (Center of Gravity) and tuning is covered in detail by Gawad et al. [62]. They showed that an optimum tank position is at or above the ship CG for highest damping and lowest ship roll amplitude. They stated that a light stabilizer might not be strong enough and a very heavy one is dangerous in lowering the metacentric height too much besides occupying too much space. They suggested that the tank mass-to-ship mass ratio of 3.5% will lead to the optimal tank mass.

Shin et al. [63] investigated the influence of U-tube anti-roll tanks on roll motion in container ships. They used a computer program and calculated the maximum roll angle in different wave frequencies in regular waves. They showed that the passive U-tube tank might be a very effective device to avoid mitigation of parametric rolling in many scenarios.

The use of sponsons and anti-roll tanks has been investigated by Umeda et al. [64]. Sponsons are some extra parts attached to the ship body around the water line, to reduce the time variation of roll restoring and consequently the reduction of roll amplitude. Their model experiments on a 6600TEU container ship showed that the sponsons with width of 11.7% percent of the ship breadth could reduce the maximum roll amplitude from 20 degrees to 15 degrees with a wavelength-to-ship length ratio equal of 1.6. They also showed experimentally that installing an anti-roll tank would avoid completely parametric rolling for a wavelength-to-ship length ratio equal of 1.3. They also concluded that an anti-roll tank with a size of 1.65 percent of the ship displacement is an economic option for risk control of parametric rolling during the 20 years trans-Pacific services.

Marzouk et al. [65] examined numerically the effectiveness of active and passive anti-roll U-tube tanks for a Series 60-cargo ship in rough sea-states. They found out that the roll motion is more severe in following, quartering and head seas, so they focus their anti-roll tank analysis on these three conditions. The studies demonstrated that active anti-roll tanks outperforms the passive ones. They stated that the active ones are more

effective in reducing the roll motion, they require much less working liquid and their performance is insensitive to their natural frequencies and so to their geometric design. But the active system costs for installation and maintenance are of course higher than those for the passive one.

Neves et al. [66] investigated the effect of anti-roll U-tube tanks on parametric rolling for a small vessel with transom stern. The numerical simulations were done for four tanks with different designs to study the effect of the tank mass, tank natural frequency and tank internal damping and vertical position of the tank on the control of parametric rolling. They concluded that the use of an anti-roll tank may eliminate parametric rolling amplification at some conditions, but they emphasized that some experimental studies are required for more analysis.

In spite of all research done, the literature lacks in some areas. Parametric rolling is reported for many fishing vessels, but the lack of experimental data as a research benchmark and the need for more numerical studies of this phenomenon for this kind of ships are clearly felt. Numerical and experimental investigations on the effect of anti-roll tanks are also limited in the current literature.

1.5 Current study

1.5.1 Thesis Outline

After the introduction in this chapter, the seakeeping formulation in regular waves is introduced in the next chapter and some validation of such approach is also presented for different parts. In chapter 3, the tank sloshing model and its coupling with main seakeeping solver is introduced and the sloshing solver and the coupled seakeeping-sloshing tank solver are validated by comparing the numerical results against different experimental results. In chapter 4, the SFH112 fishing vessel and the experimental set-up used in CNR-INSEAN (Rome, Italy) are discussed in detail. The results of a 5-DOF numerical solver based on the frequency domain STF strip theory for a C11 class post-Panamax container ship are described in chapter 5. The results of the experiments and the final 3D numerical simulations for the cases of the fishing vessel without anti-roll tank, with and without forward speed are presented in chapter 6. The study on the effect of anti-roll tank and the experimental and numerical simulation results for these cases are presented in chapter 7. The final conclusions, summary and suggestions for further work are given in chapter 8.

1.5.2 Main Contributions

A new time domain numerical seakeeping solver is developed for studying the parametric rolling instability, its occurrence and features. This tool has also the capability of accounting of the tanks on-board the vessel with CFD calculations. Some dedicated experiments are performed to study the parametric roll resonance and the effectiveness of a free surface anti-roll tank. The numerical model and the experiments have some new aspects which are listed below:

1- Different numerical solvers with different level of sophistication were developed and used in the numerical study of the parametric rolling in this thesis. First, a linear seakeeping formulation based on the STF strip theory (Salvesen et al. [1]) with some non-linear modifications (as explained in chapter 2), which are necessary for capturing the parametric rolling phenomenon was used. This solver showed good capability in capturing PR in ships with certain slender hulls. For cases with more bluff bodies with higher beam-to-length ratio, where the 3D effects are more important, we developed further another simulator. We used the so-called hybrid method to solve the radiation and diffraction problems in cases with forward speed based on the solutions of cases without forward speed from a 3D code. This method is quite new and practical. For instance, one can use the existing codes for the wave-body interaction at zero forward speed (like WAMIT) to obtain the results in cases with forward speed. The Froude-Krylov and restoring forces are calculated in time with integrating the incident wave dynamic pressure and hydrostatic pressure on the wetted surface of the ship up to the incident wave elevation and accounting for the body motions. The effect of using the weak-scatterer assumption in modifying the radiation and diffraction loads is also modelled and studied. This solver is a 3D 6-DOF time-domain code with weak-scatterer assumption. The complete code was developed in this project and only the weak-scatterer assumption part, water on deck and bottom slamming loads are implemented from another solver [67]. The water on deck and bottom slamming loads did not show any effect on the parametric rolling in this study.

2- A computational fluid dynamic (CFD) sloshing solver was also customized in OpenFOAM platform and was validated against several experimental data in literature. This solver was coupled to our seakeeping solver in an iterative fashion. It was shown that non-iterative coupling does not give acceptable results. The new coupled solver which was quite fast (comparing to CFD codes), shows good agreement with experimental results.

This coupled solver was validated against the experimental results in [5] for a system of 1-DOF motion with tank onboard. The agreement with experimental results is good. Besides, it shows that our solver is capable of predicting the ship motions in the sloshing resonance frequency better than non-linear sloshing results presented in [5]. The coupled solver was also validated against the experiments for the 6-DOF motions of SFH112 fishing vessel with anti-roll tank. It could predict most of the cases with and without parametric rolling instability. This coupled solver benefits from both low computational time of the potential-flow method (in the seakeeping part of the solver) and the accuracy of the CFD method (in the sloshing part of the solver).

3-New sets of experiments for the parametric resonance investigation in a fishing vessel with and without forward speed are performed together with professor Claudio Lugni as the principle investigator. The experimental data is analyzed as part of this PhD project afterwards. These experiments are performed for cases with Froude number $Fn = 0$, $Fn = 0.09$ and $Fn = 0.18$ in the wave frequencies near the parametric-roll resonance. All cases of these experiments are simulated using the numerical solver and the results are compared against each other and show good agreement. These experimental data could be a valuable benchmark for validating different numerical simulations.

4-New experiments are also performed (under the leadership of Prof. Claudio Lugni) to study the effect of free surface anti-roll tank in avoiding parametric resonance in roll. The experiments are performed for different tank widths. All of these cases are simulated numerically also and the results are compared against each other which show good agreement. Besides, the effect of tank width in avoiding the parametric roll is studied.

The results of this thesis have been published and presented in two conferences ([12] and [68]) and two journal papers are also under preparation.

Chapter 2

Seakeeping formulation in regular waves

2.1 General assumptions

A numerical simulator is developed to study the parametric resonance in roll motion of a ship in regular waves. For studying this phenomenon, we used a linear seakeeping formulation with some non-linear modifications, which are necessary for capturing the parametric rolling phenomenon. The linear theory means that the wave-induced motions of the vessel are linearly proportional to the wave amplitude ζ_a of the incident low-steepness regular waves. The combination of non-linear modification with the linear method has proven to be fast in computation and able to deliver interesting results [69]. Since the fishing vessel that is studied (in chapters 6 and 7) has a high beam to length ratio, a 3D hybrid method, which combines the STF strip theory (Salvesen et al. [1]) with a 3D zero-forward speed Green function method has been used to capture some of the 3D effects of the flow around the hull. First, we describe the Boundary Value Problem (BVP) and then the formulation, which solves it.

Three coordinate systems are used to describe the ship position and its motions. The Earth-fixed coordinate system (X, Y, Z) is a fixed, inertial, right-handed coordinate system with positive Z axis pointing upward and XY plane in the undisturbed free surface. The $x'y'z'$ coordinate system is a non-inertial right handed coordinate system, which is fixed to the body and moves (translational and rotationally) with the ship in time. The x' axis points to the ship bow and the y' axis points to the ship port. The origin of the coordinate system lies in the undisturbed free surface when the ship has no oscillatory motions and z' axis points upward and goes through

the center of gravity of the ship. The third coordinate system is xyz and is called the seakeeping coordinate system. This is an inertial right handed coordinate system and only moves with the ship mean forward speed. This coordinate system is identical to the $x'y'z'$ coordinate system in a steady forward equilibrium condition. The equations governing the ship motions could be written in the xyz or $x'y'z'$ coordinate systems and are solved in time but the final motions of the ship are provided in the xyz frame. The schematic view of all the mentioned coordinate systems is shown in the Fig. 2.1.

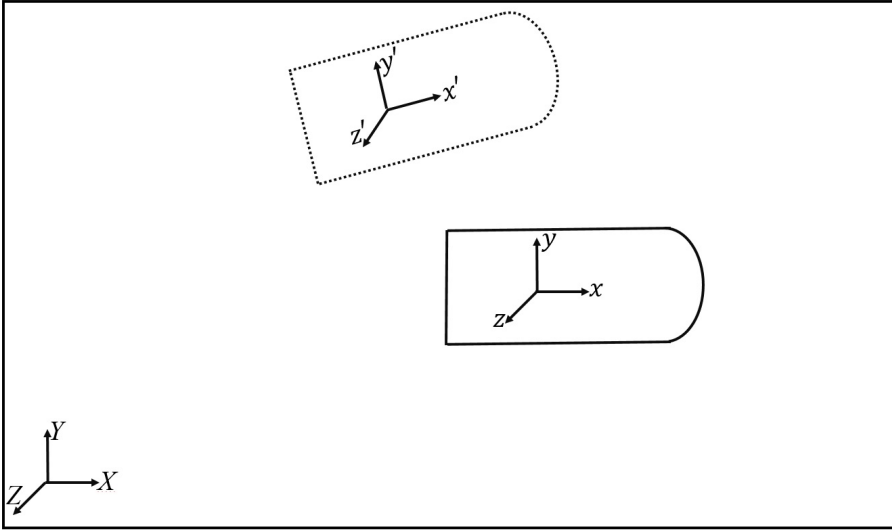


Figure 2.1: Representation of the three coordinate systems.

2.2 Wave body interaction problem

Consider a ship is navigating with mean forward speed U in deep water regular waves, and a mean heading angle Ψ , where the head sea corresponds to $\Psi = 180^\circ$ and the following sea to $\Psi = 0^\circ$. The ship oscillates in a steady state condition with the encounter frequency ω_e which is defined as follows:

$$\omega_e = \omega_0 - kU \cos(\Psi) \quad (2.1)$$

Here ω_0 is the incident-wave circular frequency and k is the wave number which is equal to $\frac{\omega_0^2}{g}$ based on the linear dispersion relation in deep water. We use the potential-flow theory, which means that the fluid is inviscid,

homogenous and incompressible with irrotational flow. The water velocity is described by the velocity potential $\phi = \phi(x, y, z, t)$ in the inertial frame. This velocity potential should satisfy Laplace's equation:

$$\nabla^2 \phi = \frac{\partial^2 \phi}{\partial x^2} + \frac{\partial^2 \phi}{\partial y^2} + \frac{\partial^2 \phi}{\partial z^2} = 0 \quad (2.2)$$

in the water domain where ' ∇^2 ' is the Laplace operator. Following Bernoulli's equation, we will find the water pressure as follows:

$$p - p_a = -\rho \frac{\partial \phi}{\partial t} - \frac{1}{2} \rho (\nabla \phi \cdot \nabla \phi) - \rho g z + C \quad (2.3)$$

where p_a is the atmospheric pressure, ρ is the water density, g is the gravitational acceleration, t is the time variable and '.' means scalar product. C is a constant calculated from the pressure on the free surface. By rewriting the Eq. 2.3 for a point on the free surface and far away from the body (with no disturbances from the body and no incident waves) we obtain,

$$C = \frac{1}{2} \rho U^2 \quad (2.4)$$

Here U is the ship forward speed. Now we should define the boundary conditions to complete the problem for ϕ , governed by the partial differential Eq. 2.2. The first boundary conditions are the free-surface kinematic and dynamic conditions. Based on the kinematic condition, on the free surface $z = \zeta(x, y, t)$, the water particle should remain on free surface which is shown as follows:

$$\frac{D}{Dt} (z - \zeta) = 0 \quad \text{on } z = \zeta \quad (2.5)$$

$\frac{D}{Dt} = \frac{\partial}{\partial t} + \nabla \phi \cdot \nabla$ is the material (Lagrangian) derivative and expresses the rate of change in time if we follow the water particle. Based on the dynamics free-surface condition, the pressure of the particles on the free surface should remain atmospheric:

$$\frac{\partial \phi}{\partial t} + \frac{1}{2} |\nabla \phi|^2 + g \zeta - \frac{1}{2} U^2 = 0 \quad \text{on } z = \zeta \quad (2.6)$$

So we have:

$$\zeta = -\frac{1}{g} \left(\frac{\partial \phi}{\partial t} + \frac{1}{2} |\nabla \phi|^2 - \frac{1}{2} U^2 \right) \quad \text{on } z = \zeta \quad (2.7)$$

By combining the two free-surface boundary conditions (Eqs. 2.5 and 2.7), ζ could be eliminated and we will have the following condition as free surface boundary condition:

$$\frac{\partial^2 \phi}{\partial t^2} + 2\nabla\phi \cdot \nabla \left(\frac{\partial \phi}{\partial t} \right) + \frac{1}{2} \nabla\phi \cdot \nabla (\nabla\phi \cdot \nabla\phi) + g \frac{\partial \phi}{\partial z} = 0 \quad \text{on } z = \zeta \quad (2.8)$$

The body boundary condition simply states that the water cannot penetrate the solid body surface. For satisfying this condition, the fluid velocity normal to the body surface should be equal to the velocity of the body's surface in that direction:

$$\frac{\partial \phi}{\partial n} = \vec{n} \cdot \vec{V} \quad \text{on } S_B \quad (2.9)$$

where $\vec{n} = (n_1, n_2, n_3)$ is the normal vector of the body pointing out (of the body) to the fluid, \vec{V} is the body velocity and S_B is the instantaneous wetted body surface.

The other boundary condition to be considered is bottom boundary condition. By assuming infinite water depth, this condition shows that the disturbances caused by the body fades out far down from the body and reads:

$$\nabla\phi \rightarrow 0 \quad \text{as } z \rightarrow -\infty \quad (2.10)$$

The other condition to be considered is initial or radiation condition. When the time domain solution is considered, the initial condition (definition of the initial elevation and velocity potential on the free surface) must be defined. When the steady-state assumption is used, the radiation condition should be used. The radiation condition is to ensure the uniqueness of the solution. These conditions make a complete 3D boundary value problem.

In case of a ship with the presence of incident waves, by assuming that the unsteady problem is linear in incident wave amplitude, we can use the superposition principle and split the seakeeping problem in radiation and diffraction problems providing the hydrodynamic loads acting on the vessel. In that regard, the radiation and diffraction problems for the case without forward speed are solved separately using the WAMIT code ([70]) which provides us with the velocity potential of radiation and diffraction problems. Then we will use these two solutions and the incident wave potentials for calculating all forces and moments as discussed in the following sections.

2.2.1 Radiation Loads

The radiation problem is defined as the forced-harmonic oscillation of a body with no incident waves. These motions make disturbances in the flow around the body, which leads to hydrodynamic forces and moments on the body, called radiation loads. The linearized problem of a vessel moving with mean constant forward speed U along a straight line and with small oscillations around the mean position is considered. Then the so-called 3D hybrid method in combination with the STF method (Salvesen et al. [1]) and a 3D zero forward speed Green function method is used to calculate added mass and damping coefficients. This approach is used in some literature before like Loken (1989), Papanikolaou and Schellin (1992), McTaggart (2002) and Thys (2013) [69].

Following Salvesen et al. [1], the total velocity potential is decomposed as follows:

$$\phi(x, y, z, t) = [-Ux + \phi_S(x, y, z)] + \phi_T(x, y, z) e^{i\omega_e t} \quad (2.11)$$

Here the velocity potentials are divided in steady component due to forward speed in calm water (ϕ_S) and unsteady component related to the incident wave system and the unsteady body motions (ϕ_T). The effect of the local steady on the unsteady part is neglected. The time dependent part itself is divided into eight parts as follows:

$$\phi_T = \phi_I + \phi_D + \sum_{j=1}^6 \phi_j \xi_j \quad (2.12)$$

where ϕ_I is the velocity potential due to incident wave, ϕ_D is the diffraction velocity potential (which will be explained in the next section) and ϕ_j is the radiation potential due to unit amplitude of motion in j th mode and ξ_j is the complex amplitude of the motion in j th mode in inertial seakeeping frame. As it is stated also in the Eq. 2.12, we have 6 rigid modes, i.e. translational surge, sway and heave motions, respectively, along x , y and z , and rotational roll, pitch and yaw motions, respectively, around x , y and z . For solving the whole problem and finding the values of these potentials, they should satisfy the Laplace's equation in the water domain plus the linearized combined free-surface boundary condition enforced on the mean free surface ($z = 0$) and the body boundary condition on the mean wetted surface S_0 in addition to the bottom and radiation conditions.

We will solve the problem and find all these velocity potentials by combining the 3D hybrid method and the results of a zero forward speed Green function frequency domain code (WAMIT [70]). We explain the radiation problem

in this section, while the diffraction problem will be discussed afterwards. Also the inclusion of non-linear effects in the hydrodynamic loads and in the incident-wave description will be examined later in the text. The linearized free surface condition for the radiation problem is as follows:

$$\left(i\omega_e - U \frac{\partial}{\partial x}\right)^2 \phi_j + g \frac{\partial}{\partial z} \phi_j = 0 \quad \text{on } z = 0 \quad (2.13)$$

and the body boundary condition is:

$$\frac{\partial \phi_j}{\partial n} = i\omega_e n_j + U m_j \quad \text{on } S_0 \quad (2.14)$$

Here n_j is defined as:

$$(n_1, n_2, n_3) = \vec{n} \quad \text{and} \quad (n_4, n_5, n_6) = \vec{r} \times \vec{n} \quad (2.15)$$

where \times means the vector product and $\vec{r} = x\vec{i} + y\vec{j} + z\vec{k}$ is the position vector of any arbitrary point on the body.

The second term in the right hand side of the Eq. 2.14 accounts for interaction between the steady and the oscillatory flow field and, as stated in the Salvesen et al. [1], the generalized vector for m_j could be written as follows:

$$m_j = \begin{cases} 0 & j = 1, 2, 3, 4 \\ n_3 & j = 5 \\ -n_2 & j = 6 \end{cases} \quad (2.16)$$

for low forward speed or a high frequency of encounter, the linearized combined free-surface condition Eq. 2.13 reduces to

$$-\omega_e^2 \phi_j + g \frac{\partial}{\partial z} \phi_j = 0 \quad \text{on } z = 0 \quad (2.17)$$

which is formally the same as for zero-forward speed but involves the encounter frequency. Under these assumptions, the radiation velocity potential can be found as:

$$\phi_k = \begin{cases} \phi_k^0 & k = 1, 2, 3, 4 \\ \phi_5^0 + \frac{U\phi_3^0}{i\omega_e} & k = 5 \\ \phi_6^0 - \frac{U\phi_2^0}{i\omega_e} & k = 6 \end{cases} \quad (2.18)$$

Here ϕ_k^0 is the oscillatory potential component for zero forward speed. One should note that the STF method considers the 2D Laplace equation in the cross sectional planes while the considered hybrid method retains the 3D

Laplace equation. Only the relation between zero forward speed potentials and speed dependent potentials are used from the STF method.

As mentioned earlier, this frequency-domain problem is solved using a zero forward speed Green function method by WAMIT code [70]. Then we can find the hydrodynamics loads (except the restoring loads, which will be explained later) by integrating the pressure over the mean wetted body surface as follows:

$$F_j^{rad} = -\rho \iint_{S_0} n_j \left(i\omega_e - U \frac{\partial}{\partial x} \right) \sum_{k=1}^6 \phi_k \xi_k ds = \sum_{k=1}^6 T_{jk} \xi_k \quad (2.19)$$

Here, $j = 1, \dots, 6$ refers to surge, sway, heave, roll, pitch and yaw modes of motions. The symbol F_j^{rad} indicates the j th component of the generalized radiation force, which is a six-component vector with first 3 components the radiation forces and second 3 components the radiation moments. The term T_{jk} is introduced here and is the load exerted in the body in the j th direction due to unit oscillatory displacement in k th mode and is as follows:

$$T_{jk} = \rho \iint_{S_0} n_j \left(i\omega_e - U \frac{\partial}{\partial x} \right) \phi_k ds \quad (2.20)$$

Due to the definition for velocity potential in WAMIT code, and combining Eq. 2.20 and Eq. 2.18 we can write T_{jk} in the form :

$$T_{jk} = \begin{cases} \rho \iint_{S_0} n_j \left(i\omega_e - U \frac{\partial}{\partial x} \right) (i\omega_e \phi_k) ds & k = 1, 2, 3, 4 \\ \rho \iint_{S_0} n_j \left(i\omega_e - U \frac{\partial}{\partial x} \right) (i\omega_e \phi_5^0 + U \phi_3^0) ds & k = 5 \\ \rho \iint_{S_0} n_j \left(i\omega_e - U \frac{\partial}{\partial x} \right) (i\omega_e \phi_6^0 - U \phi_2^0) ds & k = 6 \end{cases} \quad (2.21)$$

The added mass A_{jk} and damping B_{jk} coefficients are related to T_{jk} as follows:

$$T_{jk} = \omega_e^2 A_{jk} - i\omega_e B_{jk} \quad (2.22)$$

Here we can approximate the hydrodynamic coefficients as given in Eqs. 2.23 and 2.24, i.e. the added mass and dampings for zero forward speed.

$$A_{jk}^0(\omega_e) = -\rho \iint_{S_0} n_j \operatorname{Re}(\phi_k^0) ds \quad (2.23)$$

$$B_{jk}^0(\omega_e) = \rho\omega_e \iint_{S_0} n_j \text{Im}(\phi_k^0) ds \quad (2.24)$$

We also define two extra terms (Eqs. 2.25 and 2.26) to facilitate showing the formulation of added mass and dampings for cases with forward speed.

$$dA_{jk}^0(\omega_e) = -\rho \iint_{S_0} n_j \text{Re} \left(\frac{\partial \phi_k^0}{\partial x} \right) ds \quad (2.25)$$

$$dB_{jk}^0(\omega_e) = \rho\omega_e \iint_{S_0} n_j \text{Im} \left(\frac{\partial \phi_k^0}{\partial x} \right) ds \quad (2.26)$$

Now based on Eq. 2.21 and Eqs. 2.23 to 2.26, we can find the added mass and dampings for cases with forward speed. For $k = 1, 2, 3, 4$ we can write:

$$A_{jk}(U, \omega_e) = A_{jk}^0(\omega_e) + \frac{U}{\omega_e^2} dB_{jk}^0(\omega_e) \quad (2.27)$$

$$B_{jk}(U, \omega_e) = B_{jk}^0(\omega_e) - U dA_{jk}^0(\omega_e) \quad (2.28)$$

with the same procedure for $k = 5$ we can write:

$$A_{j5}(U, \omega_e) = A_{j5}^0(\omega_e) - \frac{U}{\omega_e^2} B_{j3}^0(\omega_e) + \frac{U}{\omega_e^2} dB_{j5}^0(\omega_e) + \frac{U^2}{\omega_e^2} dA_{j3}^0(\omega_e) \quad (2.29)$$

$$B_{j5}(U, \omega_e) = B_{j5}^0(\omega_e) + U A_{j3}^0(\omega_e) - U dA_{j5}^0(\omega_e) + \frac{U^2}{\omega_e^2} dB_{j3}^0(\omega_e) \quad (2.30)$$

and for $k = 6$ we will have:

$$A_{j6}(U, \omega_e) = A_{j6}^0(\omega_e) + \frac{U}{\omega_e^2} B_{j2}^0(\omega_e) + \frac{U}{\omega_e^2} dB_{j6}^0(\omega_e) - \frac{U^2}{\omega_e^2} dA_{j2}^0(\omega_e) \quad (2.31)$$

$$B_{j6}(U, \omega_e) = B_{j6}^0(\omega_e) - U A_{j2}^0(\omega_e) - U dA_{j6}^0(\omega_e) - \frac{U^2}{\omega_e^2} dB_{j2}^0(\omega_e) \quad (2.32)$$

We also need to have the value of these coefficients for zero and infinite frequency. The limiting frequency values for $\omega_e = 0$ could be obtained by the following equations:

$$A_{jk}(U, 0) = A_{jk}^0(0) \quad k = 1, 2, 3, 4 \quad (2.33)$$

$$B_{jk}(U, 0) = -UdA_{jk}^0(0) \quad k = 1, 2, 3, 4 \quad (2.34)$$

$$A_{j5}(U, 0) = A_{j5}^0(0) + \lim_{\omega_e \rightarrow 0} \left(\frac{U^2}{\omega_e^2} dA_{j3}^0(\omega_e) \right) \quad (2.35)$$

$$B_{j5}(U, 0) = UA_{j3}^0(0) - UdA_{j5}^0(0) \quad (2.36)$$

$$A_{j6}(U, 0) = A_{j6}^0(0) - \lim_{\omega_e \rightarrow 0} \left(\frac{U^2}{\omega_e^2} dA_{j2}^0(\omega_e) \right) \quad (2.37)$$

$$B_{j6}(U, 0) = -UA_{j2}^0(0) - UdA_{j6}^0(0) \quad (2.38)$$

And for $\omega_e = \infty$ could be obtained by the following equations:

$$A_{jk}(U, \infty) = A_{jk}^0(\infty) \quad k = 1, 2, 3, 4 \quad (2.39)$$

$$B_{jk}(U, \infty) = -UdA_{jk}^0(\infty) \quad k = 1, 2, 3, 4 \quad (2.40)$$

$$A_{j5}(U, \infty) = A_{j5}^0(\infty) \quad (2.41)$$

$$B_{j5}(U, \infty) = UA_{j3}^0(\infty) - UdA_{j5}^0(\infty) \quad (2.42)$$

$$A_{j6}(U, \infty) = A_{j6}^0(\infty) \quad (2.43)$$

$$B_{j6}(U, \infty) = -UA_{j2}^0(\infty) - UdA_{j6}^0(\infty) \quad (2.44)$$

As suggested by Thys [69], to remove the singularity of the second terms in Eq. 2.35 and 2.37, the lower limit of $L/(0.01g)$ is used for the term $\frac{1}{\omega_e^2}$, where L is the ship length.

Now as an example we consider the C11 post-Panamax container ship. The main particulars of the hull and the bodyplan of this ship are shown in Tab. 2.1 and Fig. 2.2:

Table 2.1: Hull properties of C11 post-Panamax container ship

Length $L \equiv L_{pp}$	262m
Beam B	40m
Draft D	12.34m
Block Coefficient C_B	0.66
Vessel Displacement	76056ton
VCG (Vertical Center of Gravity) above keel	17.51m
Transverse metacentric height GM_T	1.97m
Roll Radius of Gyration k_{xx}	$0.34B$
Pitch and Yaw Radius of Gyration k_{yy}, k_{zz}	$0.24L$

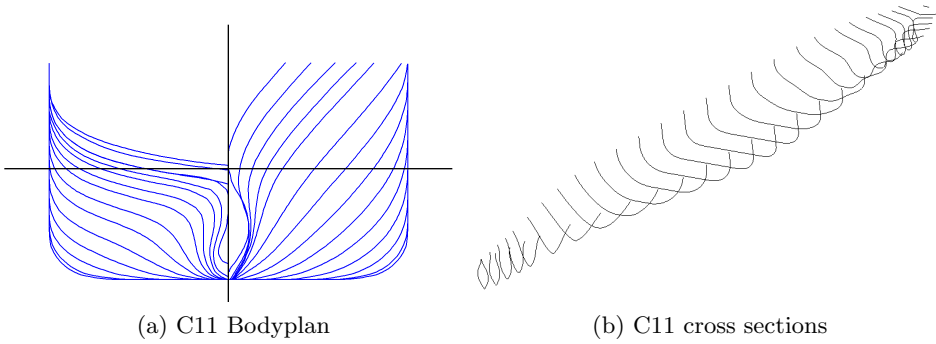


Figure 2.2: C11 container ship body plan and cross sections

The non-dimensional added mass and damping coefficients of this vessel for $Fn = 0$ are shown in Figs. 2.3 and 2.4. The effect of the irregular frequencies, i.e. frequencies where the numerical solution blows up but normally out of the practical frequency range, in the hybrid method coefficients could be seen clearly. A lid is inserted on the free surface inside the ship to minimize the irregular frequencies.

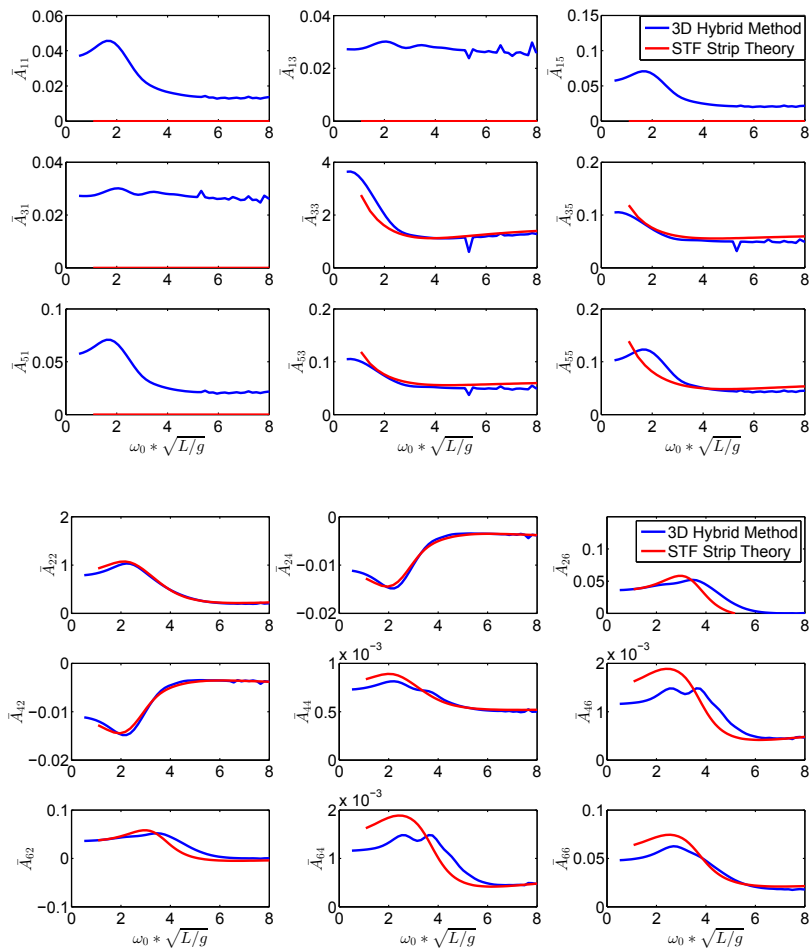


Figure 2.3: Non-dimensional added mass coefficients for C11 post-Panamax container ship with STF strip theory (Salvesen et al. [1]) and 3D method for $Fn = 0$.

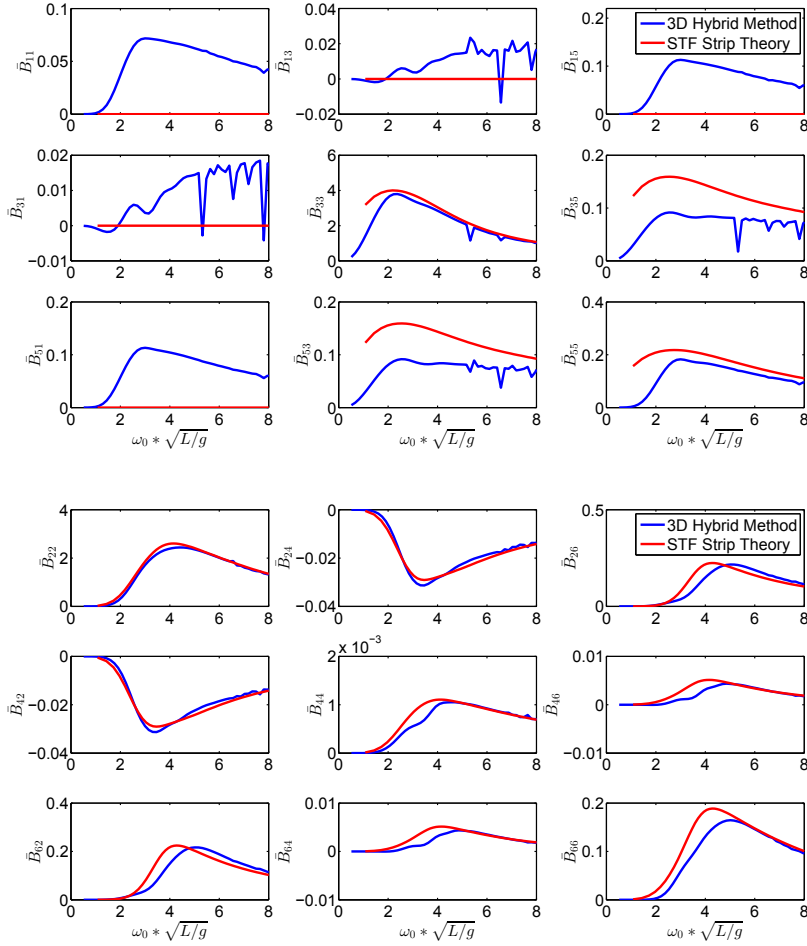


Figure 2.4: Non-dimensional damping coefficients for C11 post-Panamax container ship with STF strip theory (Salvesen et al. [1]) and 3D method for $Fn = 0$.

The values in the Figs. 2.3 and 2.4 are made non-dimensional as follows:

$$\bar{A}_{ij} = \frac{A_{ij}}{\rho \nabla}, \quad \bar{B}_{ij} = \frac{B_{ij}}{\rho \nabla \sqrt{g/L}}, \quad i = 1, 2, 3 \text{ and } j = 1, 2, 3 \quad (2.45)$$

$$\bar{A}_{ij} = \frac{A_{ij}}{\rho \nabla L}, \quad \bar{B}_{ij} = \frac{B_{ij}}{\rho \nabla L \sqrt{g/L}}, \quad i = 1, 2, 3 \text{ and } j = 4, 5, 6 \quad (2.46)$$

$$\bar{A}_{ij} = \frac{A_{ij}}{\rho \nabla L}, \quad \bar{B}_{ij} = \frac{B_{ij}}{\rho \nabla L \sqrt{g/L}}, \quad i = 4, 5, 6 \text{ and } j = 1, 2, 3 \quad (2.47)$$

$$\bar{A}_{ij} = \frac{A_{ij}}{\rho \nabla L^2}, \quad \bar{B}_{ij} = \frac{B_{ij}}{\rho \nabla L^2 \sqrt{g/L}}, \quad i = 4, 5, 6 \text{ and } j = 4, 5, 6 \quad (2.48)$$

where ∇ is the ship displacement.

As it can be seen, there are clear differences in some coefficients which are due to 3D effects of the geometry of the vessel. Please note that since the STF strip theory (Salvesen et al. [1]) does not consider the surge motion, the values related to surge are zero in the graphs.

2.2.1.1 Radiation Loads in frequency and time domain

Once the added mass and damping terms are calculated, we can calculate the steady-state radiation loads as follows:

$$F_j^{rad}(U, \omega_e) = - \sum_{k=1}^6 A_{jk}(U, \omega_e) \delta \dot{u}_k - B_{jk}(U, \omega_e) \delta u_k \quad (2.49)$$

where $\delta \dot{u}_k$ and δu_k are the perturbation acceleration and perturbation velocity vectors, respectively. In interaction of ship and waves, the time domain simulations might be needed where one needs to account for the transient parts of the problem. The radiation forces in frequency and time domain can be related through Fourier transform and as Cummins [2] showed, the time-domain radiation loads could be written as:

$$F_j^{rad}(U, t) = - \sum_{k=1}^6 \left[A_{jk}^* \delta \dot{u}_k(t) + B_{jk}^* \delta u_k(t) + C_{jk}^* \eta_k(t) + \int_0^t K_{jk}(t - \tau, U) \delta u_k(\tau) d\tau \right] \quad (2.50)$$

where η_k is the instantaneous (real) ship displacement from the mean position of the ship at time t . K_{jk} is the retardation function and A_{jk}^* , B_{jk}^* and C_{jk}^* are speed dependent load coefficients. By assuming oscillatory motions with frequency of ω_e and considering the radiation loads terms in time and frequency domain we can write:

$$-A_{jk}^* + \frac{C_{jk}^*}{\omega_e^2} + \frac{1}{\omega_e} \int_0^{\infty} K_{jk}(\tau, U) \sin(\omega_e \tau) d\tau = -A_{jk}(U, \omega_e) \quad (2.51)$$

$$B_{jk}^* + \int_0^{\infty} K_{jk}(\tau, U) \cos(\omega_e \tau) d\tau = B_{jk}(U, \omega_e) \quad (2.52)$$

By evaluating the Eqs. 2.51 and 2.52 for zero and infinite encounter frequency we can obtain the A_{jk}^* , B_{jk}^* and C_{jk}^* coefficients as follows:

$$A_{jk}^* = A_{jk}(U, \infty) \quad (2.53)$$

$$B_{jk}^* = B_{jk}(U, \infty) \quad (2.54)$$

$$C_{jk}^* = C_{jk}^{rad} = -\omega_e^2 A_{jk}(U, \omega_e) \Big|_{\omega_e \rightarrow 0} \quad (2.55)$$

The convolution integral term could be re-written as:

$$\int_0^t K_{jk}(t - \tau, U) \delta u_k(\tau) d\tau = \int_0^t K_{jk}(\tau, U) \delta u_k(t - \tau) d\tau \quad (2.56)$$

In fact by integrating from 0 to t , we have the memory effect of the motions in the past and integrate all their effects. By plotting the retardation function in time, we can see that it tends to zero very quickly in time, so normally for saving the computational time, the researchers do the integration from $t - t^*$ to t . There are many estimates for t^* , but we use the value of $t^* = 12\sqrt{L/g}$ (Maxime Thys [69]). A simple sensitivity study can assess if t^* is enough or not.

The retardation function could be obtained by applying an inverse Fourier transform to Eq. 2.51 or 2.52. The latter is simpler and normally is used in the literature and is as follows:

$$K_{jk}(t, U) = \frac{2}{\pi} \int_0^{\infty} (B_{jk}(U, \omega_e) - B_{jk}(U, \infty)) \cos(\omega_e t) d\omega_e \quad (2.57)$$

The computation of the retardation function needs the values of damping coefficients in all frequencies from 0 to ∞ . In fact the values at limiting values of frequency could be calculated. Normally in the panel method codes, the panel sizes are a function of frequency. The panel size is a fraction of wave length corresponding to the examined oscillation frequency, so for small frequency there is no problem and the damping coefficients can be easily calculated. But there is a numerical challenge, both in terms of memory space and on numerical accuracy, at high frequencies because the panel sizes must reduce for increasing frequencies. On the other hand, for $\omega_e \rightarrow \infty$, the radiation damping must go to zero. So the practical solution for this problem is that the damping coefficients are calculated up to a threshold frequency (let us name it Ω) and we extrapolate the damping-coefficient values from Ω to ∞ , as explained below. It is convenient to express the retardation function in terms of speed independent and speed dependent terms. Now we can write the retardation function as follows:

$$K_{jk}(t, U) = K_{jk}^0 + UK_{jk}^u + U^2 K_{jk}^{u^2} + \chi_{jk} \quad (2.58)$$

where, K_{jk}^0 , K_{jk}^u and $K_{jk}^{u^2}$ are the speed independent terms, terms dependent on U and terms dependent on U^2 , respectively. χ_{jk} is a term added to compensate for the truncation error. This truncation error is based on an expansion of the zero speed damping coefficients for frequencies higher than Ω . Journee [71] proposed $\frac{c_1}{\omega_e^3}$ for extending the zero speed diagonal damping terms. But based on [69], $\frac{c_2}{\omega_e^2}$ is simpler and provides more practical extensions. c_2 is a constant that should be calculated for each damping term from matching the extended and main damping curve at $\omega = \Omega$.

By combining the Eqs. 2.58 and 2.57, we will have:

$$K_{jk}^0 = \frac{2}{\pi} \int_0^{\Omega_e} B_{jk}^0(\omega_e) \cos(\omega_e t) d\omega_e \quad (2.59)$$

$$K_{jk}^u = \frac{2}{\pi} \int_0^{\Omega} (dA_{jk}^0(\omega_e) - dA_{jk}^0(\infty)) \cos(\omega_e t) d\omega_e \quad (2.60)$$

$$K_{jk}^{u^2} = 0 \quad (2.61)$$

for $k = 1, 2, 3, 4$.

For $k = 5$ we will have:

$$K_{j5}^0 = \frac{2}{\pi} \int_0^{\Omega_e} B_{j5}^0(\omega_e) \cos(\omega_e t) d\omega_e \quad (2.62)$$

$$K_{j5}^u = \frac{2}{\pi} \int_0^{\Omega_e} \left[B_{j3}^0(\omega_e) \frac{\sin(\omega_e t)}{\omega_e} - (dA_{j5}^0(\omega_e) - dA_{j5}^0(\infty)) \cos(\omega_e t) \right] d\omega_e \quad (2.63)$$

$$K_{j5}^{u^2} = \frac{2}{\pi} \int_0^{\Omega_e} dB_{j3}^0(\omega_e) \frac{\cos(\omega_e t)}{\omega_e^2} d\omega_e \quad (2.64)$$

Note that we have used the following relation:

$$\int_0^{\Omega_e} (A_{jk}^0(\omega_e) - A_{jk}^0(\infty)) \cos(\omega_e t) d\omega_e = \int_0^{\Omega_e} B_{jk}^0(\omega_e) \frac{\sin(\omega_e t)}{\omega_e} d\omega_e \quad (2.65)$$

When $k = 6$, we will have:

$$K_{j6}^0 = \frac{2}{\pi} \int_0^{\Omega_e} B_{j6}^0(\omega_e) \cos(\omega_e t) d\omega_e \quad (2.66)$$

$$K_{j6}^u = \frac{2}{\pi} \int_0^{\Omega_e} \left[-B_{j2}^0(\omega_e) \frac{\sin \omega_e t}{\omega_e} - (dA_{j6}^0(\omega_e) - dA_{j6}^0(\infty)) \cos(\omega_e t) \right] d\omega_e \quad (2.67)$$

$$K_{j6}^{u^2} = -\frac{2}{\pi} \int_0^{\Omega_e} dB_{j2}^0(\omega_e) \frac{\cos \omega_e t}{\omega_e^2} d\omega_e \quad (2.68)$$

We divide the correction terms in speed dependent and speed independent terms similarly as in Eq. 2.58. For the correction terms, for $k = 1, 2, 3, 4$ we have:

$$\chi_{jk}^0 = \frac{2}{\pi} B_{jk}^0(\Omega_e) \Omega_e^2 \int_{\Omega_e}^{\infty} \frac{\cos \omega_e t}{\omega_e^2} d\omega_e \quad (2.69)$$

$$\chi_{jk}^u = 0 \quad (2.70)$$

$$\chi_{jk}^{u^2} = 0 \quad (2.71)$$

For $k = 5$ we have:

$$\chi_{j5}^0 = \frac{2}{\pi} B_{j5}^0(\Omega_e) \Omega_e^2 \int_{\Omega_e}^{\infty} \frac{\cos \omega_e t}{\omega_e^2} d\omega_e \quad (2.72)$$

$$\chi_{j5}^u = \frac{2}{\pi} B_{j3}^0(\Omega_e) \Omega_e^2 \int_{\Omega_e}^{\infty} \frac{\sin \omega_e t}{\omega_e^3} d\omega_e \quad (2.73)$$

$$\chi_{j5}^{u^2} = 0 \quad (2.74)$$

Similarly for $k = 6$ we can obtain the correction terms as follows:

$$\chi_{j6}^0 = \frac{2}{\pi} B_{j6}^0(\Omega_e) \Omega_e^2 \int_{\Omega_e}^{\infty} \frac{\cos \omega_e t}{\omega_e^2} d\omega_e \quad (2.75)$$

$$\chi_{j6}^u = -\frac{2}{\pi} B_{j2}^0(\Omega_e) \Omega_e^2 \int_{\Omega_e}^{\infty} \frac{\sin \omega_e t}{\omega_e^3} d\omega_e \quad (2.76)$$

$$\chi_{j6}^{u^2} = 0 \quad (2.77)$$

The solution of some of these integrals are given in appendix A.

As an example, we examine the transient heave motion of a 2D semi-circular body with beam-to-draft ratio $B/T = 2$, without excitation forces. We consider a 1-DOF equation of motion with the convolution integral term and without excitation forces. The radiation forces are calculated based on STF strip theory (Salvesen et al.[1]) using a 2D frequency domain BEM (Boundary Element Method) code [72]. The mass is the mass per unit length here. The heave restoring coefficient C_{33} can be calculated using later Eq. 2.91. The heave motion and velocity are shown for two cases. In Fig. 2.5 they are compared in time against the values from Yeung [73], based on a 2D time-domain BEM, and against experiments from Ito et al. [74] with an acceptable agreement.

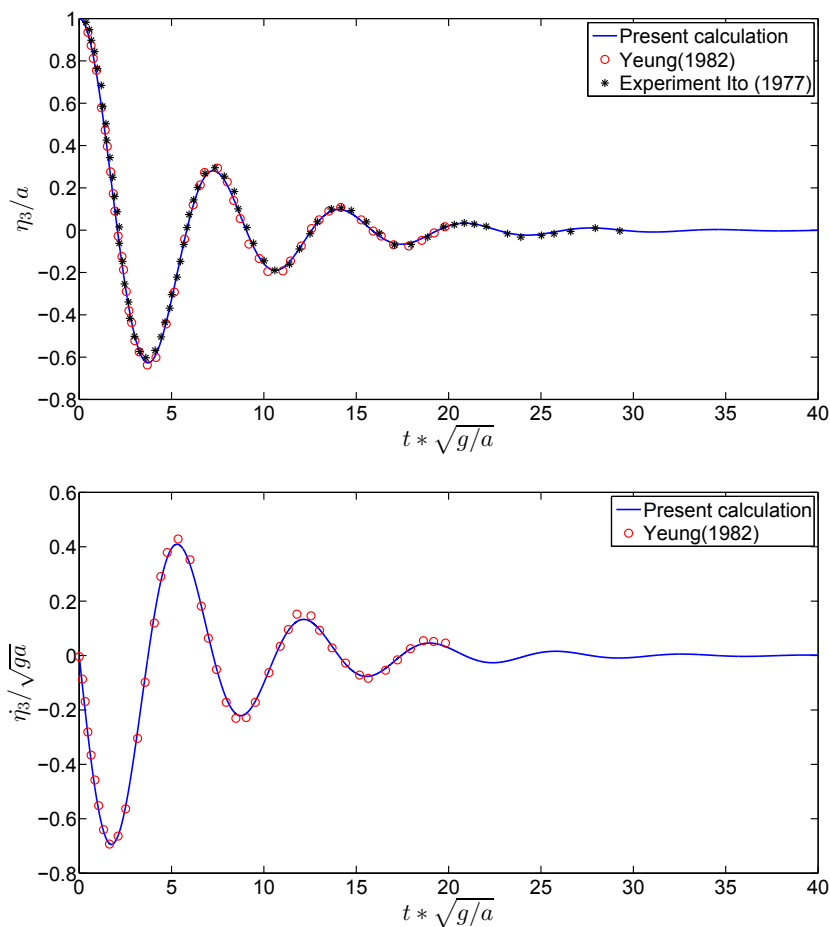


Figure 2.5: Transient heave response of a 2D semi-circular section with beam-to-draft ratio $B/T = 2$ for unit non-dimensional displacement and zero velocity at initial condition. Top: non-dimensional displacement. Bottom: non-dimensional velocity. a is the section radius.

Another example for unit non-dimensional velocity and zero displacement as initial condition is shown and compared with Yeung [73] in Fig. 2.6. The comparison shows a good agreement also for this case.

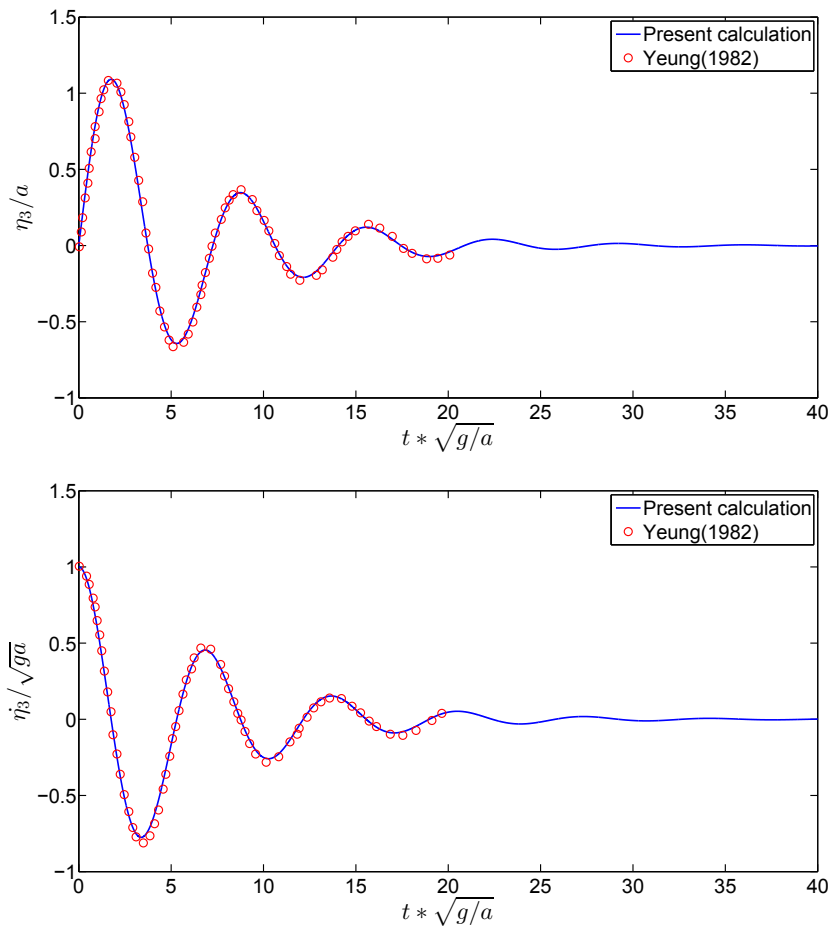


Figure 2.6: Transient heave response of a 2D semi-circular section with beam-to-draft ratio $B/T = 2$ for unit non-dimensional velocity and zero displacement at initial condition. Top: non-dimensional displacement. Bottom: non-dimensional velocity. a is the section radius.

2.2.2 Non-linear Froude-Krylov and restoring loads

In linear theory, the Froude-Krylov loads are obtained integrating the incident-wave linear hydrodynamic pressure along the mean wetted surface of the body up to $z = 0$. The linear restoring coefficients are also calculated based on later Eqs. 2.91 to 2.94. If the integration of the related pressure is done over the instantaneous wetted surface of the body, say S_B^* , the non-linear loads are calculated and could be written as generalized force, i.e.:

$$\vec{\mathbf{F}}^{non-lin} = - \iint_{S_B^*} p \vec{\mathbf{n}} dS \quad (2.78)$$

where p is the pressure (incident-wave linear hydrodynamic pressure for the Froude-Krylov loads and the hydrostatic pressure for the restoring loads), and $\vec{\mathbf{n}}$ is the generalized normal vector with components defined in Eq. 2.15. In the numerical solution of the problem, the ship is discretized in quadrilateral and triangular panels, depending on the local body geometry, and at any time step, the wetted part of the body is identified by the submerged panels considering the ship motions and the incident wave surface. It should be noted that when non-linear restoring loads are calculated, the loads also include the mean buoyancy which balances the ship weight. Therefore, the ship weight should also be considered in the equations of motions.

Checking the triangular elements in terms of being submerged or half submerged or totally out of water is much simpler than checking the quadrilateral elements and the reason is the fewer possible options for triangular elements. Therefore, for simplicity, first we convert all the quadrilateral panels to triangular panels. Then by knowing the incident-wave elevation everywhere and also the rigid body motions at any time step, we can check all the panels for finding the wetted surface of the ship. Four different situations could occur for any panel ([69]):

- 1- The panel is totally submerged. The pressure is calculated at the panel center and then the force is computed by multiplying the pressure with the panel area and normal vector.
- 2- The panel is totally out of water. Then the force is zero on this panel.
- 3- Two corners of the panel are submerged. Then we have to find the submerged part of the panel which is a quadrilateral panel. we divide the new quadrilateral panel in two triangular panels and find the forces as situation 1.
- 4- One corner of the panel is submerged. So we can find the submerged part of this panel as a triangular panel and find the forces as step 1 again.

2.2.3 The undisturbed regular incoming waves

The linear wave theory or non-linear wave theories could be used to describe the undisturbed incoming regular waves. The linear and second order Stokes waves or any other higher-order wave theories could be used in this regard. We used the linear and second-order Stokes waves for describing the incident waves. The results in chapter 5 (parametric rolling investigation of the C11 class containership using frequency domain strip theory) are calculated by linear wave theory and the results in chapters 6 and 7 (parametric rolling investigation on the fishing vessel using time domain 3D theory) are obtained using the second-order Stokes wave theory. The velocity potential and pressure in linear and second-order Stokes waves are given in Tab. 2.2:

Table 2.2: Wave profile, velocity potential and pressure according to the linear and second-order Stokes wave theory for a wave propagating along positive X axis.

	Linear wave theory	Second order Stokes wave theory
free surface elevation	$\zeta_a \cos(\theta)$	$\frac{\zeta_a}{4} \cos(\theta) + \frac{\pi \zeta_a^2}{16\lambda} \cos(2\theta)$
for $-\infty < Z \leq 0$		
velocity potential	$\frac{g\zeta_a}{\omega_0} e^{kZ} \sin(\theta)$	$\frac{g\zeta_a}{4\omega_0} e^{kZ} \sin(\theta)$
dynamic pressure	$\rho g \zeta_a e^{kZ} \cos(\theta)$	$\frac{\rho g \zeta_a}{4} e^{kZ} \cos(\theta) - \frac{\pi \rho g \zeta_a^2}{16\lambda} e^{2kZ}$
hydrostatic pressure	$-\rho g Z$	$-\rho g Z$
for $0 < Z \leq \zeta$		
velocity potential	$\frac{g\zeta_a}{\omega_0} \sin(\theta)$	$\frac{g\zeta_a}{4\omega_0} \sin(\theta) + \frac{Z\omega_0\zeta_a}{4} \sin(\theta)$
dynamic pressure	$\rho g \zeta_a \cos(\theta)$	$\frac{\rho g \zeta_a}{4} \cos(\theta) - \frac{\pi \rho g \zeta_a^2}{16\lambda} + \frac{Z\rho g \zeta_a k}{4} \cos(\theta)$
hydrostatic pressure	$-\rho g Z$	$-\rho g Z$

where ζ_a is the wave amplitude, k is the wave number, λ is the wave length, ω_0 is the wave circular frequency, g is the gravitational acceleration, $\theta = kX - \omega_0 t$, t is time and X and Z are the coordinates in inertial earth-fixed coordinate system.

2.2.4 Diffraction Loads

In the diffraction problem, the presence of the restrained body changes the incident wave flow around the body which imposes loads on the body. The diffraction loads are calculated based on the 3D hybrid method, which is explained in this section. First, we want to define the linearized 3D boundary value problem for the diffraction problem of a ship moving with constant mean forward speed U with a heading angle Ψ . The diffraction velocity potential should satisfy the 3D Laplace's equation:

$$\nabla^2 \phi_D = 0 \quad \text{in the water domain} \quad (2.79)$$

The body boundary condition is:

$$\frac{\partial \phi_D}{\partial n} = -\frac{\partial \phi_I}{\partial n} \quad \text{on } S_0 \quad (2.80)$$

The linearized free-surface condition also could be shown as follows:

$$\left(\frac{\partial}{\partial t} - U \frac{\partial}{\partial x} \right)^2 \phi_D + g \frac{\partial \phi_D}{\partial z} = 0 \quad \text{on } z = 0 \quad (2.81)$$

This free-surface condition could be simplified similarly as done for the radiation problem by use of a low forward speed or a high frequency assumption. Then this condition could be re-written as follows:

$$-\omega_e^2 \phi_D + g \frac{\partial}{\partial z} \phi_D = 0 \quad \text{on } z = 0 \quad (2.82)$$

If we can solve the boundary value problem defined in steady-state conditions by Eqs. 2.79, 2.80 and 2.82 complemented by the sea-bottom boundary condition and the radiation condition, and obtain the complex ϕ_D and $\frac{\partial \phi_D}{\partial x}$ all over S_0 , then we can find the diffraction pressure and forces in the moving inertial frame as follows [69]:

$$p_D = -\rho \left(\frac{\partial}{\partial t} - U \frac{\partial}{\partial x} \right) \phi_D = -\rho i \omega_e \phi_D + \rho U \frac{\partial \phi_D}{\partial x} \quad (2.83)$$

$$F_j^{diff} = - \iint_{S_0} p_D n_j dS = \rho i \omega_e \iint_{S_0} \phi_D n_j dS - U \iint_{S_0} \rho \frac{\partial \phi_D}{\partial x} n_j dS \quad (2.84)$$

$$= F_j^{D0}(\Psi, \omega_0, \omega_e) + U F_j^{DU}(\Psi, \omega_0, \omega_e) \quad (2.85)$$

Where F_j^{D0} is the j th component of the zero-speed generalized diffraction force and F_j^{DU} is the j th component of the speed dependent part of the generalized diffraction force for unit forward speed. This diffraction problem is exactly like the radiation problem except for the body boundary condition. In WAMIT [70], a user can define the diffraction problem as a radiation problem associated with a fictitious extra mode where the encounter frequency is different from wave circular frequency. In this extra modes of motions, one can define the body boundary conditions which could be simplified as follows:

$$\frac{\partial \phi_D}{\partial n} = -\frac{\partial \phi_I}{\partial n} = -n_1 \frac{\partial \phi_I}{\partial x} - n_2 \frac{\partial \phi_I}{\partial y} - n_3 \frac{\partial \phi_I}{\partial z} \quad \text{on } S_0 \quad (2.86)$$

So by having the incident wave frequency, we can easily find the diffraction body boundary condition. By solving the real and imaginary part of the diffraction separately, finally we would obtain complex values for each of these and the final complex diffraction velocity potential would be the combination of these two:

$$\phi_D = \phi_D^{real} + i\phi_D^{imaginary} \quad (2.87)$$

After having the diffraction velocity potential, we can find the diffraction loads easily by using Eq. 2.85.

The diffraction forces for the C11 class post-Panamax container ship and for $Fn = 0$ and $\beta = 135^\circ$ bow waves are shown in Fig. 2.7. The left part of the figure is the amplitude of the forces and the right part is the phase angle in degrees, calculated as:

$$\varepsilon_j = \tan^{-1} \left(\frac{F_j^{Im}}{F_j^{Re}} \right) \quad (2.88)$$

The results are shown based on the STF strip theory (Salvesen et al. [1]) and the 3D code. As it can be seen from the figure, even though the general agreement is not bad, there are some clear differences that probably are related to the 3D effects accounted for in the hybrid method and not in the STF method.

For checking the proposed hybrid method for calculating the diffraction forces in cases with forward speed, we used the mentioned fictitious mode of motion for calculating the diffraction force for zero forward speed and compare the results with the direct loads obtained from WAMIT. They are the same in terms of amplitude and phase which shows that the proposed method works properly.

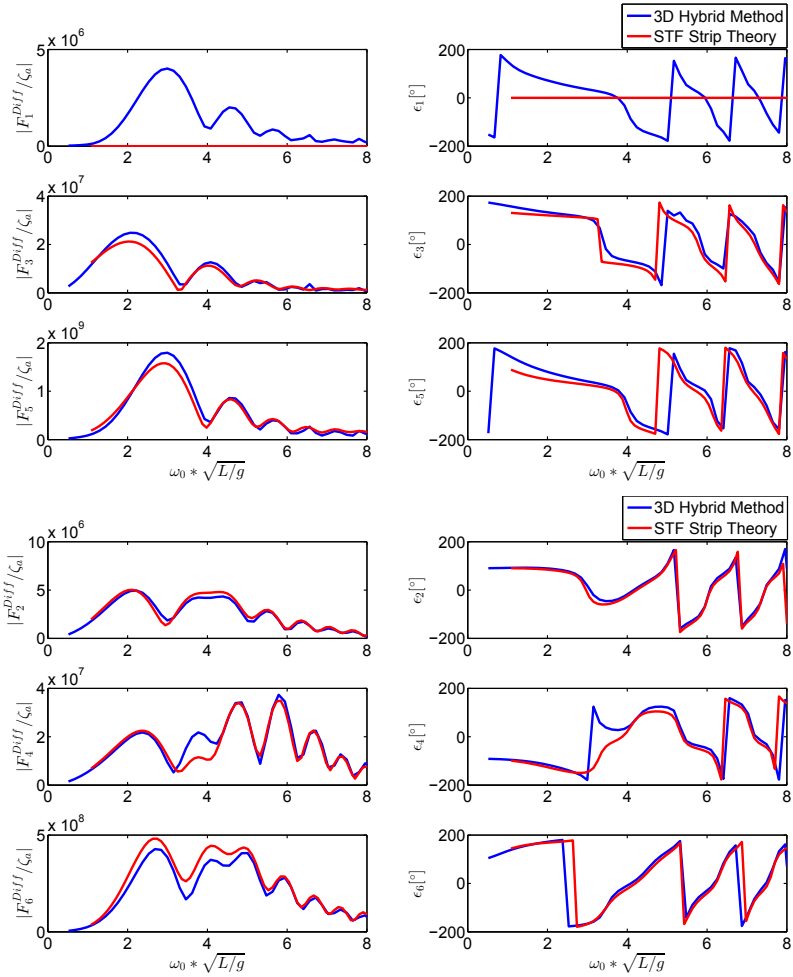


Figure 2.7: Diffraction forces (Left: amplitude, Right: phase angle) for C11 post-Panamax container ship with STF strip theory (Salvesen et al. [1]) and 3D method for $Fn = 0$ and $\beta = 135^\circ$ bow waves.

2.3 Final Formulation of the Governing Equations of Motion

Within the linear theory, the motions of a ship with or without forward speed could be modelled mathematically in frequency or time domain, depending on the assumptions of steady-state or transient conditions. Both of them are explained in this section.

2.3.1 Linear frequency domain equations of motion

Within linear theory, if we assume steady-state conditions, then the hydrodynamic loads and the motions of an advancing ship in regular waves, will oscillate with the frequency of encounter. In this case the body motions can be found in frequency domain. In linear formulation, all forces and moments are linear in terms of incident wave amplitude. We call the complex amplitude of the motions as ξ_k where $k = 1, \dots, 6$ refers to surge, sway, heave, roll, pitch and yaw motions. The complex motions could be written as $\xi_k \exp(i\omega_e t)$. The complex amplitude of the j th component of the generalized exciting force is indicated as F_j . Therefore the complex j th component of the generalized exciting force can be written as $F_j \exp(i\omega_e t)$. The real displacements and exciting forces could be obtained from $\Re(\xi_k \exp(i\omega_e t))$ and $\Re(F_j \exp(i\omega_e t))$, where \Re stands for the real part of the given expression.

Now the system of six coupled equations of motions could be written as:

$$\sum_{k=1}^6 [-\omega_e^2 (M_{jk} + A_{jk}) + i\omega_e B_{jk} + C_{jk}] \xi_k = F_j \quad (\text{for } j = 1, \dots, 6) \quad (2.89)$$

Here M_{jk} is the ship mass matrix. For a ship with lateral symmetry and the center of gravity coordinates as $(0, 0, z_G)$, the M_{jk} is:

$$M = \begin{bmatrix} M & 0 & 0 & 0 & Mz_G & 0 \\ 0 & M & 0 & -Mz_G & 0 & 0 \\ 0 & 0 & M & 0 & 0 & 0 \\ 0 & -Mz_G & 0 & I_x x & 0 & 0 \\ Mz_G & 0 & 0 & 0 & I_y y & 0 \\ 0 & 0 & 0 & 0 & 0 & I_z z \end{bmatrix} \quad (2.90)$$

where M is the ship mass and $I_x x$, $I_y y$ and $I_z z$ are the moments of inertia of the ship with respect to the axes of inertial frame.

A_{jk} and B_{jk} are the matrices of the added mass and damping coefficients, respectively. C_{jk} is the restoring coefficient matrix. It means that, in this

formulation, the restoring loads are assumed linear and connected to the changes in buoyancy due to the body motions. In this way, the non-zero related restoring coefficients C_{jk} can be estimated for a ship with port and starboard symmetry by the following equations:

$$C_{33} = \rho g A_w \quad (2.91)$$

$$C_{35} = C_{53} = -\rho g \int_{A_w} x ds \quad (2.92)$$

$$C_{44} = \rho g \nabla (z_b - z_G) + \rho g \int_{A_w} y^2 ds = \rho g \nabla \overline{GM}_T \quad (2.93)$$

$$C_{55} = \rho g \nabla (z_b - z_G) + \rho g \int_{A_w} x^2 ds = \rho g \nabla \overline{GM}_L \quad (2.94)$$

where z_b is the vertical coordinate of center of buoyancy of the ship. A_w is the water-plane area in calm water, ∇ is the displacement of the ship, \overline{GM}_T and \overline{GM}_L are the transverse and longitudinal metacentric height, respectively. The mean buoyancy force does not appear in Eq. 2.89 as it balances the body weight.

By calling the ship instantaneous motion in k th mode as η_k , we can calculate them at any time t with the following formula:

$$\eta_k = \Re(\xi_k \exp(i\omega_e t)) \quad (\text{for } k = 1, 2, \dots, 6) \quad (2.95)$$

here the \Re stands for the real part of the given expression.

The Eq. 2.89 is in frequency domain and is valid for the steady-state sinusoidal motions and can be rewritten in the time domain as follows:

$$\sum_{k=1}^6 [(M_{jk} + A_{jk}) \ddot{\eta}_k + B_{jk} \dot{\eta}_k + C_{jk} \eta_k] = \Re(F_j e^{i\omega_e t}) \quad (\text{for } j = 1, \dots, 6) \quad (2.96)$$

where $\ddot{\eta}_k$ and $\dot{\eta}_k$ are the ship acceleration and velocity, respectively. One should note that Eq. 2.96 is only the frequency domain equation in time and is not the exact time domain equation of motion. The exact time domain simulation will be explained in the next section and includes the convolution integral in radiation forces.

The motions in the frequency domain for two examples are discussed next. The first one shows the motions of the FRIESLAND frigate. The hull properties and the body plan are shown in Tab. 2.3 and Fig. 2.8

Table 2.3: Hull properties of FRIESLAND ship

Length $L \equiv L_{pp}$	112.4m
Beam B	11.74m
Draft D	3.9m
Block Coefficient C_B	0.554
Vessel Displacement	2959.2ton
VCG above keel KG	3.9m
Pitch Radius of Gyration k_{yy}	$0.259L$

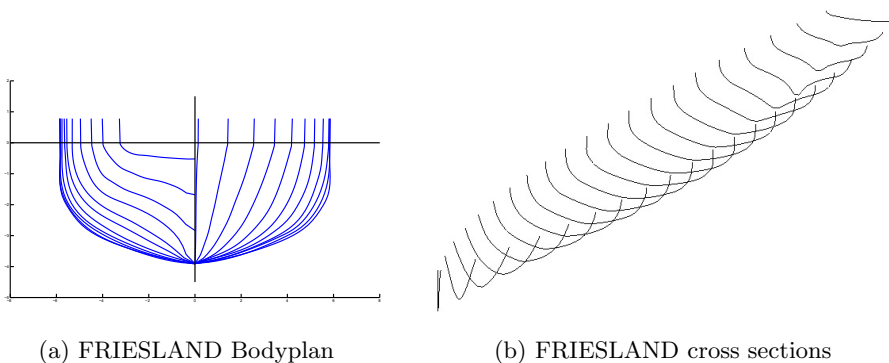


Figure 2.8: FRIESLAND frigate body plan and cross sections

The simulation of heave and pitch motions of this frigate in head sea waves and for $Fn = 0.15$ is computed using the STF method and compared against experimental values by Smith (1966) [75]. The phase angle is calculate using Eq. 2.88. As it can be seen form Fig. 2.9, the results for the linear response amplitude operator (RAO) for heave and pitch for this case are in good agreement with experimental results both in amplitude and phase.

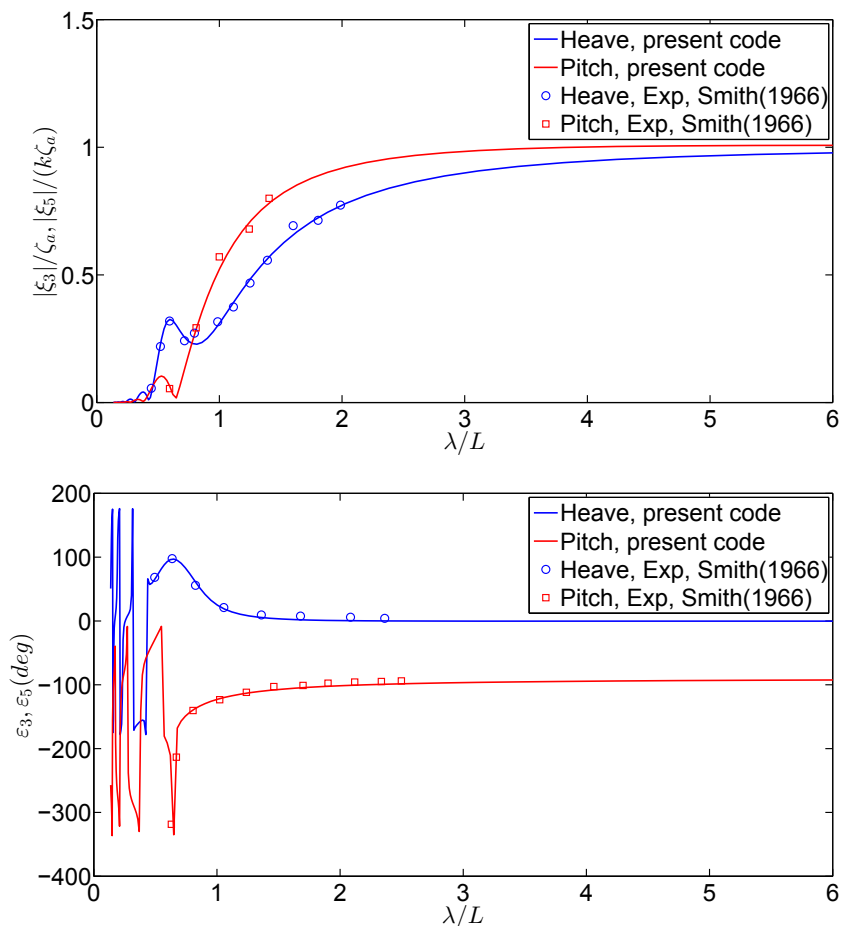


Figure 2.9: The numerical and experimental RAO of heave and pitch motions for FRIESLAND frigate in head sea waves versus wavelength-to-ship length ratio, with $Fn = 0.15$. Top: Non-dimensional amplitude. Bottom: Phase angle.

As second example, the RAO for the mentioned C11 class container ship and for $Fn = 0$ and $\beta = 135^\circ$ bow waves is computed by 3D hybrid method and the STF strip theory method (Salvesen et al. [1]) in Fig. 2.10. The 2D coefficients in strip theory is obtained from the HydroDyn2D code which is written in [72]. In both cases the equations are solved in frequency domain. The comparisons show that even though the general trend and agreement in RAO amplitudes and their phase angles are good, there are clear differences in sway, roll and yaw amplitudes near the roll resonance area. The motions amplitude in the resonance area are highly dependent on the damping. Since the 3D effects of the body are accounted for in the 3D hybrid method and not in the STF method, the radiation damping coefficients might have some differences in these two methods and can be the reason for the RAO differences near resonance.

One should note that the STF strip theory (Salvesen et al. [1]) solves the problem in 5-DOF and that is why there is no surge motion for this method.

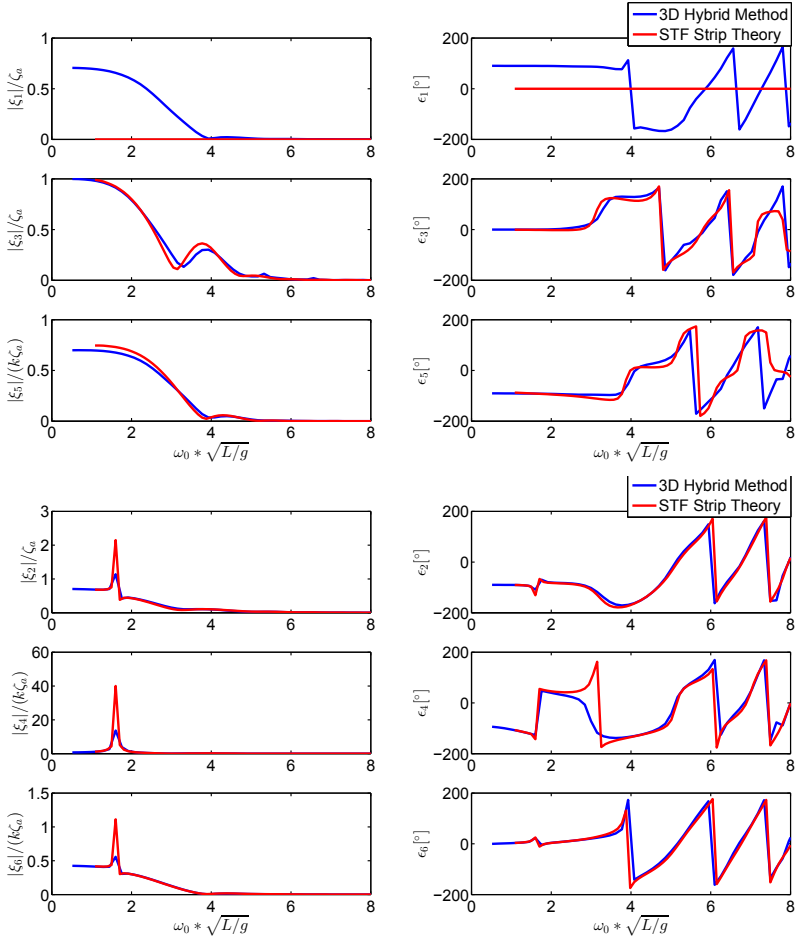


Figure 2.10: Comparison of the ship RAO(Left: amplitude, Right: phase angle) for the C11 class container ship with STF strip theory (Salvesen et al. [1]) and 3D method for $F_n = 0$, $\beta = 135^\circ$ bow waves.

2.3.2 Time domain equations of motion

In transient conditions, even within linear theory, the ship motions must be studied in time domain. This is relevant, for example, when investigating occurrence of parametric roll. The correct formulation for a general ship motion (including the transient part), should include the convolution integral in the radiation forces (as was discussed in the radiation loads part). The radiation loads computed in the frequency domain could be transferred to time domain by Fourier transformation like the formulation in previous sections (Cummins [2]). Then the complete 6-DOF time domain formulation for the body motions can be written as:

$$\sum_{k=1}^6 \left[(M_{jk} + A_{jk}(U, \infty)) \ddot{\eta}_k + B_{jk}(U, \infty) \dot{\eta}_k + C_{jk}^{rad} \eta_k + \int_{t-t^*}^t K_{jk}(\tau, U) \dot{\eta}_k(t - \tau) d\tau \right] \\ = F_j^{Diff} + F_j^{FK} + F_j^{rest} + F_j^{grav} + F_j^{others} \quad (\text{for } j = 1, \dots, 6) \quad (2.97)$$

where the F_j^{Diff} is the diffraction force, F_j^{FK} is the non-linear Froude-Krylov force, F_j^{rest} is the non-linear hydrostatic restoring force, F_j^{grav} is the ship weight and F_j^{others} are the other forces that might be imposed to the ship, like the mooring line forces and so on. All of them are expressed in terms of their j th component. One should note that, strictly speaking Cummin's approach [2], is valid within linear theory, i.e. for linear non steady-state problems. Researchers have stretched this to the limits including on the right-hand-side nonlinear loads and keeping the assumptions of linearity for the radiation and diffraction loads. The same strategy has been used here. The system of the mentioned equations is solved here using a time integration algorithm based on the Rung-Kutta fourth order (RK4) method with constant time steps, 0.005 times of the wave period. As an example, selected results for a fishing vessel using the 3D hybrid method are compared to the STF strip theory (Salvesen et al. [1]) results for a fishing vessel. The hull properties and body plans of this vessel (which will be explained in detail in next chapters) is shown here in brief in Fig. 2.11 and Tab. 2.4.

Table 2.4: Hull properties of SFH112 model scale fishing vessel

Length $L \equiv L_{pp}$	2.95m
Beam B	0.95m
Draft D	0.4m
Block Coefficient C_B	0.58
Vessel Displacement	657.3kg
VCG above keel KG	0.43m
Transverse metacentric height GM_T	0.07m
Roll Radius of Gyration k_{xx}	0.378B
Pitch and Yaw Radius of Gyration k_{yy}, k_{zz}	0.28L

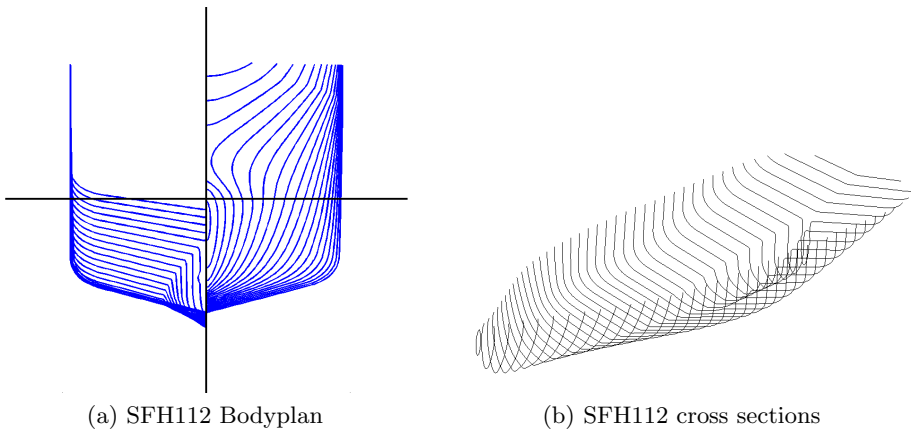


Figure 2.11: SFH112 fishing vessel body plan and cross sections

The diffraction forces for forward speed of $Fn = 0.18$ and head-sea waves using the 3D hybrid method and STF strip theory (Salvesen et al. [1]) are shown in Fig. 2.12.

The beam-to-length ratio is 0.32 and therefore higher than for conventional ships, for instance it is a bit more than twice the value for the C11 class container ship previously examined. As a result, the 3D effects are expected to be more important as it can be observed from Fig. 2.12. The response amplitude operators in surge, heave and pitch for the mentioned scenario are shown in Fig. 2.13. Only these modes are presented because the other modes are zero in this case. In the figure, the results of STF strip theory (Salvesen et al. [1]) in the frequency domain, 3D hybrid method results in the frequency domain and 3D hybrid method results in time domain are compared. In the latter case, the linear excitation force is used

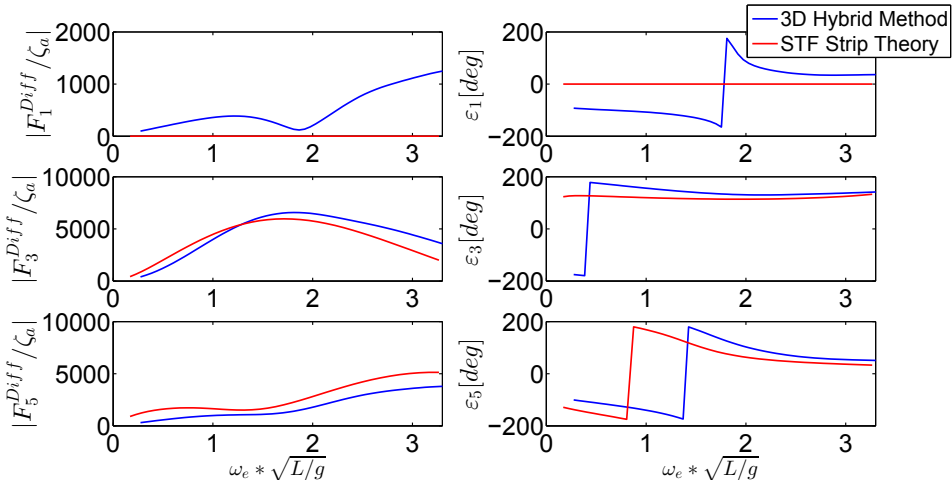


Figure 2.12: Comparison of the diffraction forces (Left: amplitude, Right: phase angle) of the SFH112 fishing vessel in head sea waves with $Fn = 0.18$ using STF strip theory (Salvesen et al. [1]) and 3D hybrid method.

with diffraction forces from 3D hybrid method and linear Froude-Krylov force is computed in time by integrating the incident-wave linear hydrodynamic pressure over the mean wetted surface of the ship.

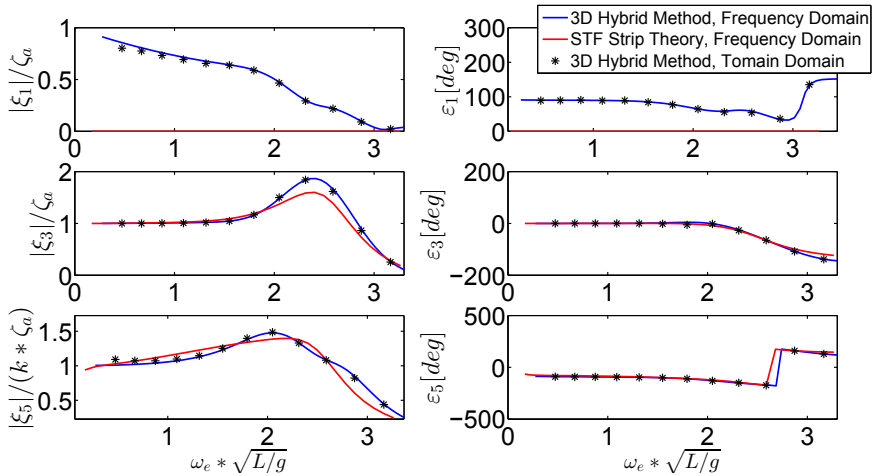


Figure 2.13: Comparison of the response amplitude operator (RAO) (Left: amplitude, Right: phase angle) of the SFH112 fishing vessel in head sea waves with $Fn = 0.18$ using STF strip theory (Salvesen et al. [1]) and 3D hybrid method.

2.4 Conclusion

Different parts needed for developing a seakeeping code including non-linear effects are explained. Since the main objective of this thesis is to investigate the parametric rolling (PR) which is a non-linear phenomenon, some parts are calculated in non-linear form to capture the PR phenomenon. First, the linearized wave-body interaction problem and all needed boundary conditions to make complete the boundary value problem for the velocity potential were explained. WAMIT which is a 3D code was used for solving this problem. The velocity potential was decomposed following Salvesen et al. [1] and then the solution method for different parts were explained in detail. The 3D radiation loads coefficients (added mass and damping) are computed by use of WAMIT [70] and combining it with the STF modified strip theory as it was shown in Salvesen et al. [1] and the added mass and damping coefficients for cases with forward speed were obtained. Then the radiation loads in time domain by use of the convolution integral as it was explained by Cummins [2] were computed. The 3D diffraction loads for zero forward speed could be obtained by use of WAMIT. For the cases with forward speed, we defined some extra motion modes in WAMIT where the diffraction problem was defined and solved in WAMIT as a fictitious radiation problem. The solutions obtained by defining some new modes in

WAMIT were tested for zero forward speed of a ship with results directly obtained from WAMIT and they were the same. The Froude-Krylov and restoring loads are calculated by integrating the dynamic pressure of the incident wave and the hydrostatic pressure along the instantaneous wetted surface of the ship defined by the body motions and the incident-wave elevation. At any time step, the exact submerged part of the body is calculated and the pressure integration were calculated accordingly. These non-linear loads are crucial for catching the parametric rolling in the simulations. Some other loads might be also added to the equation of motions. For example in many experiments, mooring lines are used leading to additional loads on the body. These mooring lines could be added to our model. At the end, the final equations of motions were shown and discussed both in frequency and time domain.

Chapter 3

Modules in the numerical simulation model

In this chapter, the different modules used in the numerical simulator are explained in detail. Since the effect of a free-surface anti-roll tank is studied in dedicated experiments and numerical simulations, the sloshing solver is explained here. The coupling strategy of the sloshing and main seakeeping solver is outlined afterwards. For avoiding the horizontal motions, a special mooring configuration is designed and used in the experiments. The numerical simulation of this mooring part is also explained in this chapter. The weak-scatter hypothesis formulation for adding some weakly non-linearity to the radiation and diffraction forces are explained at the end of this chapter.

3.1 2D numerical sloshing solver

Sloshing is a violent free-surface flow in normally partially filled tanks, which could make big impact loads on the tank walls and the roof. For the tanks installed on ships, very violent sloshing could occur if the ship motions excite the tank sloshing at its lowest natural frequency. The use could be made from this phenomenon to control the roll motion of the ship. The tank shape, filling ratio, amplitude and frequency of the tank motion are the principal parameters that determine the free-surface flow nature. This phenomenon has a complex physics that depends on many parameters. The moment obtained from the sloshing is frequency dependent and if a tank is excited at its lowest natural frequency, the phase lag of the obtained moment is -90 degree compared to the roll motion. Then it can be considered as an extra damping device. But the sloshing natural frequency might vary slightly due to high amplitude motions or shallow water filling-depth of the tank and

consequently, the obtained moment would have a phase angle different than -90 degree, and so it does not act only as a pure damping device.

This phenomenon is studied numerically and experimentally in this thesis. In this chapter, the numerical solver for the sloshing tank and the numerical strategy to couple the sloshing tank with the ship motions are described. Then, the sloshing-tank solver is compared against experiments on the tank, in isolated conditions, which was used for the physical studies on the fishing vessel carried out during this PhD study, as well as against other tank experiments available in literature. The seakeeping-sloshing coupled solver is compared against previous experiments. In the next chapters, the dedicated experiments carried out on a fishing vessel without and with an on-board tank will be described. They will be compared against the proposed numerical solution strategy and the two research tools will be used to perform a physical investigation of parametric roll. Different types of tanks could be used as anti-roll tanks. A simple rectangular tank was used here with a length equal to the ship beam, draft of 3.9 cm and different values of the beam and of the filling ratio. Considering the tank dimensions and also checking the videos of the experiments, numerically we modelled the tank as a two-dimensional (2D) tank in longitudinal sea waves. Computational Fluid Dynamics (CFD) based on the finite volume method is used to perform the numerical simulations of the sloshing phenomenon, in which water and air are assumed as incompressible and the viscous flow to be laminar. The Volume of Fluid (VOF) technique is used to capture the air-water interface. Such a method can provide, for example, the details of the flow inside the sloshing tank and the local and integrated loads acting on the tank walls as a consequence of the internal resonant fluid motion. In particular it is a solver from the ‘‘Open source Field Operation And Manipulation’’, known in short as Open-FOAM, customized here based on our needs. OpenFOAM is an open source package that includes solvers for different problems in fluid mechanics, is used here. A complete formulation could be found in [76].

The Navier-Stokes momentum equation in a tank-fixed coordinate system is as follows [77]:

$$\frac{\partial \vec{u}}{\partial t} + \nabla \cdot (\vec{u}\vec{u}) = -\frac{\nabla p}{\rho} + \vec{g} + \nu \nabla^2 \vec{u} - \vec{a}_0 - (\vec{\omega} \times \vec{v}_0) - \vec{\omega} \times \vec{r} - 2(\vec{\omega} \times \vec{u}) - \vec{\omega} \times (\vec{\omega} \times \vec{r}) \quad (3.1)$$

where \vec{u} is the velocity vector in the tank-fixed coordinate system. \vec{a}_0 and \vec{v}_0 are the acceleration and velocity of the origin of the tank fixed coordinate system relative to Earth-fixed coordinate system. \vec{g} is the gravitational acceleration in the tank-fixed system. $\vec{\omega}$ is the rotational velocity of the co-

ordinate system and the vector \vec{r} is the position vector in the tank reference frame. ρ is the fluid density and ν is the fluid kinematic viscosity. The last two terms in the right hand side of the equation are the Coriolis and centripetal accelerations.

3.1.1 Validation of the numerical 2D sloshing solver

In order to assess the numerical 2D sloshing solver, three different experimental cases are used. In the first case, the free-surface elevation in a 2D tank with forced sway motion is examined. In the next one, the rolling moment of a 2D tank with forced roll motion, is calculated and compared to experiments, for different frequencies. In the last set of validation, the time series of rolling moment and swaying forces due to sloshing of a 2D tank with forced roll motion is compared against experiments.

3.1.1.1 Free surface flow in a 2D tank forced to sway motion

Let us consider a rectangular tank with $1m$ length, $0.1m$ breadth and $0.98m$ height filled with water up to $0.833m$ depth. The tank is in forced harmonic oscillation along its length as follows:

$$\eta_2 = \eta_{2a} (1 - \cos(\omega t)) \quad (3.2)$$

where $\eta_{2a} = 0.00465m$ and $\omega = 6.075rad/s$, which corresponds to 1.1 times the first sloshing frequency (ω_1). A schematic view of the computational domain is shown in Fig. 3.1 [76]:

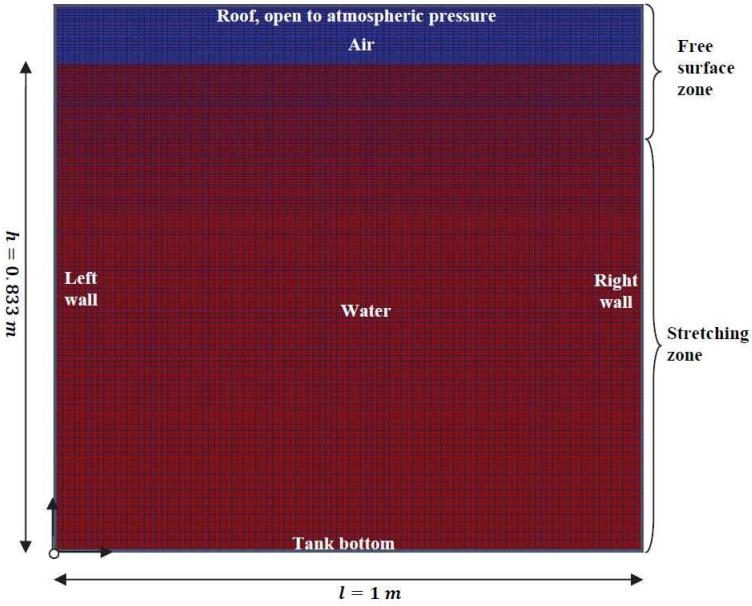


Figure 3.1: Computational domain for the tank with explanation for different parts in the figure

The numerical simulation was done for the shown tank as a 2D tank. The convergence study for the grid size was done and the grid size was selected as is mentioned in [76]. Within the finite-volume field method, along the tank length, the fluid domain is discretized using 100 control volumes (CVs), evenly distributed. It means that the grid size in the tank-length direction is small enough when compared to the wavelength of the lowest natural mode. In the free surface zone, uniform grids were used (60 CVs and each 3 mm thick) while below the free surface, the Cvs are stretched smoothly toward the tank bottom with a growth factor of 1.0164. The comparison between numerical and experimental results ([76]) for the wave elevation at a 5mm distance from the vertical walls are shown in Fig. 3.2.

The time-step size has some effects in the results. The control of the time discretization is through changing Courant number, indicated as CFL in the OpenFOAM platform. This CFL number is calculated using the average fluxes passing the faces of each control volume. By definition for a one-dimensional case, CFL number equals $\frac{u_i \Delta t}{\Delta x_i}$, and provides the number of control volumes a fluid particle passes through in one time step in direction i . u_i , Δx_i and Δt are the fluid velocity, cell edge length in direction i and solution time step, respectively [76]. According to a sensitivity study

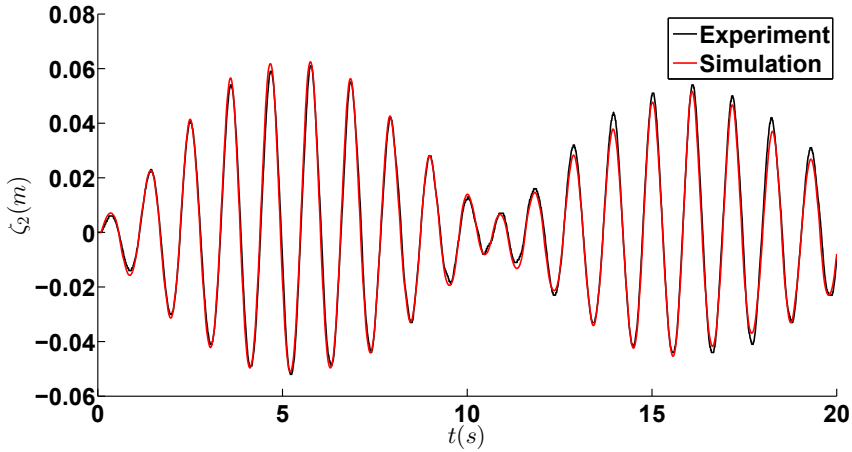


Figure 3.2: Comparison between the numerical and experimental results ([76]) for the wave elevation at 5mm distance from the vertical walls for $h/l = 0.883$, $\eta_{2a} = 0.00465m$, $\omega/\omega_1 = 1.1$.

on the CFL number in [76], $CFL = 0.25$ is small enough considering the results. The source of damping in the numerical simulation is the numerical diffusion, which decreases by decreasing the CFL number, [76]. Therefore, the smaller CFL number might make non decaying waves which is not in agreement with experiments. The numerical result using the mentioned parameters is in a good agreement with the experimental results.

3.1.1.2 Validation of the roll moment and phasing in forced 2D sloshing

As other example for validating the sloshing solver, a study on the roll damping by free-surface tanks by Van den Bosch and Vugts [61], is considered. The experiments were performed in a tank with length of $1m$, height of $0.5m$, width of $0.1m$ and filling depth of h . When the forced sinusoidal rolling motion with amplitude ϕ_a and frequency ω is imposed on the tank, a resulting moment about the axis of rotation is measured with an amplitude M_r and a phase ε_r with respect to the tank rolling motion. The distance from the axis of rotation to the tank bottom is called s and is positive when the axis of rotation is below the tank bottom. The rolling amplitude is varied between 1.9 to 5.7 degrees. Four test cases were selected and the numerical simulations were performed for the corresponding 2D tanks.

Figs. 3.3 to 3.6 show the comparison between non-dimensional ampli-

tude and phase of the measured moments around the axis of rotation for the four cases.

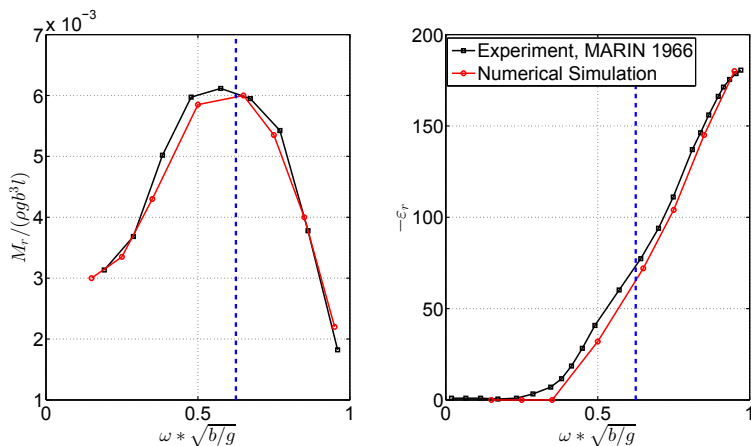


Figure 3.3: Comparison of experimental and numerical results of rolling moment (Left: amplitude, Right: phase angle) around the axis of rotation for $\phi_a = 1.9^\circ$, $h/b = 0.04$, $s = 0$. Blue dashed line shows the theoretical sloshing frequency.

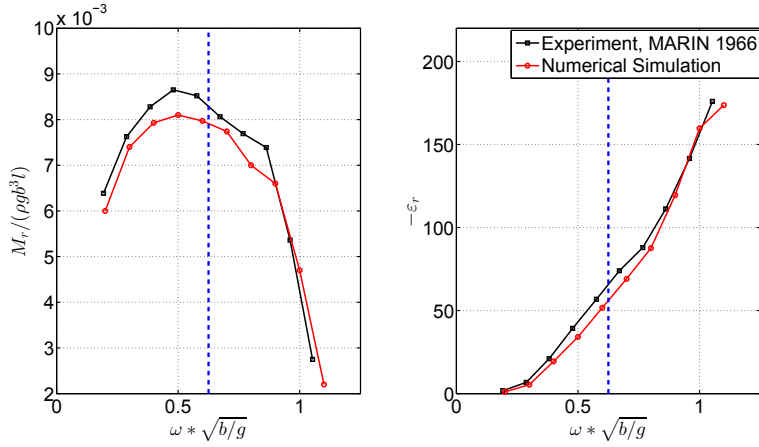


Figure 3.4: Comparison of experimental and numerical results of rolling moment (Left: amplitude, Right: phase angle) around the axis of rotation for $\phi_a = 3.8^\circ$, $h/b = 0.04$, $s = 0$. Blue dashed line shows the theoretical sloshing frequency.

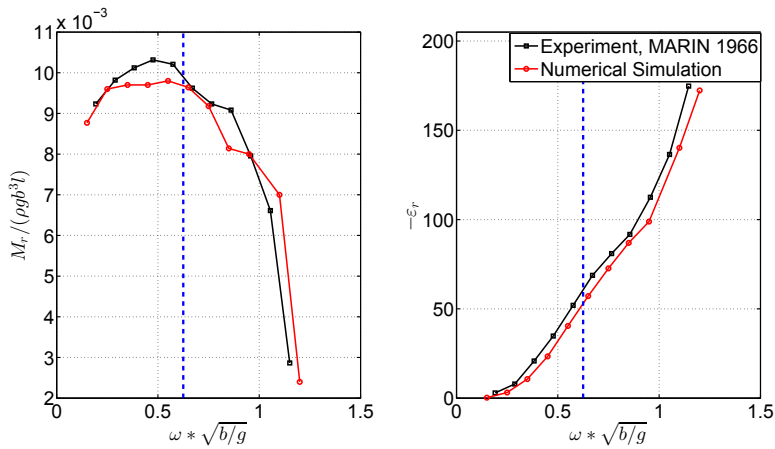


Figure 3.5: Comparison of experimental and numerical results of rolling moment (Left: amplitude, Right: phase angle) around the axis of rotation for $\phi_a = 5.7^\circ$, $h/b = 0.04$, $s = 0$. Blue dashed line shows the theoretical sloshing frequency.

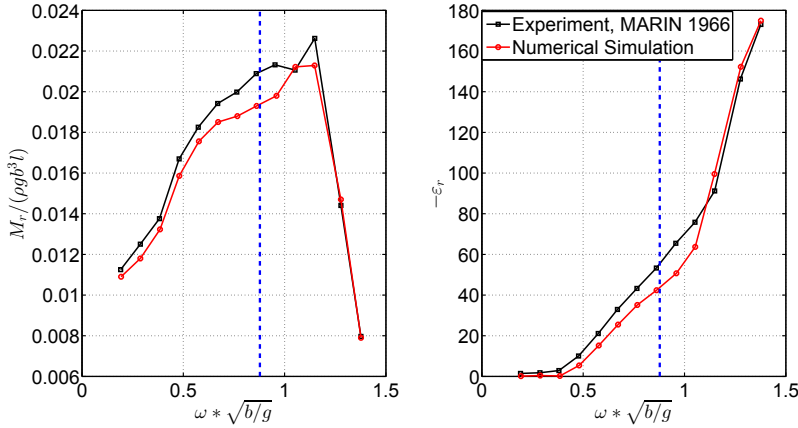


Figure 3.6: Comparison of experimental and numerical results of rolling moment (Left: amplitude, Right: phase angle) around the axis of rotation for $\phi_a = 5.7^\circ$, $h/b = 0.08$, $s = 0.2m$. Blue dashed line shows the theoretical sloshing frequency.

As it can be seen from these cases, the general trend and values in the tank rolling moment and phasing are the same in the numerical results and in the experiments. There are however clear differences between them probably due to the non-linearities in the flow in the experiments not captured by the numerical solver. For the first three cases, the water depth was 4cm and the axis of rotation went through the tank bottom. In Fig. 3.6, the water depth was 8cm and the axis of rotation around which the moments were measured, was 20cm below the tank bottom. As it can be seen from these graphs, the roll moment from the tank does not increase proportionally to the amplitude of the rolling motion. This shows a non-linear behaviour and seems to be proportional to $\sqrt{\phi_a}$ (Van den Bosch et al. [61]). The mechanism of these free-surface anti-roll tank is explained further in section 7.1.

3.1.1.3 Validation of the roll moment and horizontal forces for a 2D tank forced to roll

During this PhD study, an anti-roll tank was designed for installation on a fishing-vessel model in the CNR-INSEAN basin, Rome, Italy. Forced roll oscillation experiments on the isolated tank were performed before the main experiments of the ship with tank. A view of the tank and experimental set-up is shown in Fig. 3.7. The tank has 1m length, 0.5m height and

0.1m width, while the water depth is 4cm. In the isolated tank tests, the centre of roll was 0.4 m below the tank bottom and forces and moments were measured in a body-fixed reference frame centred at the tank bottom. As it can be seen, the tank is mounted on a balance that measures the forces and moments around the tank bottom by using 4 load cells at four point of attachments.

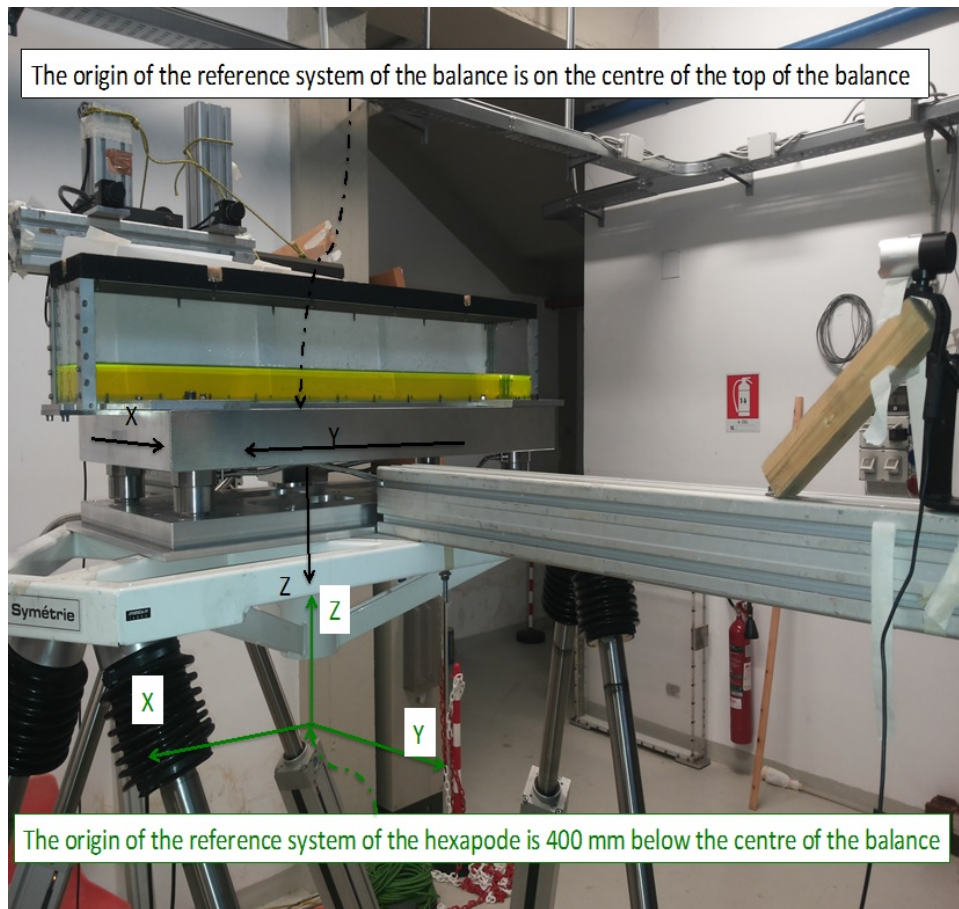


Figure 3.7: Sloshing tank and experiment set-up for isolated sloshing tests in CNR-INSEAN, Rome, Italy.

Several tests for forced roll motion at the tank first sloshing frequency and at different roll amplitudes were performed, listed in the Tab. 3.1.

Table 3.1: Forced roll sloshing tests.

Test No.	$\frac{\omega}{\omega_1}$	ϕ_a (deg)
test06	1.0	6
test20	1.0	4
test30	1.0	2

Here ω_1 is the first natural sloshing frequency of the tank and is 2.0923rad/s . The steady state parts of sway force and roll moment (in ship coordinate system) in the experimental and numerical simulations at $\omega = \omega_1$ and at different roll amplitudes are shown in Figs. 3.8 to 3.10.

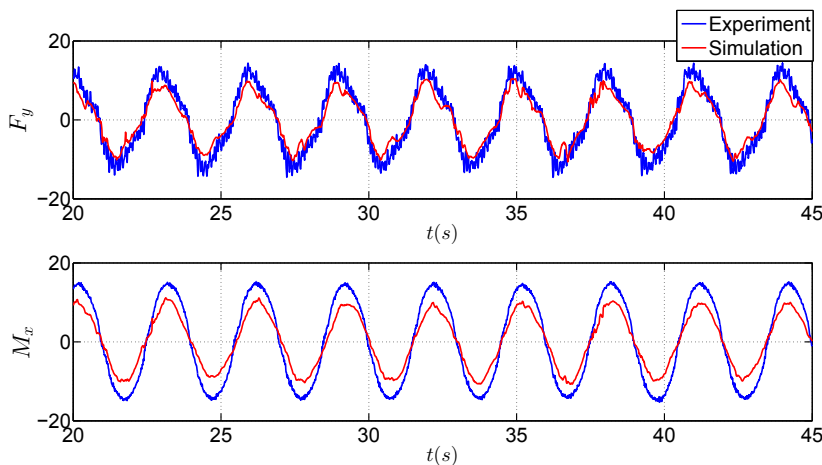


Figure 3.8: Comparison of experimental and numerical results of sway force and roll moment in test06, $\frac{\omega}{\omega_1} = 1.0$, $\phi_a = 6.0^\circ$.

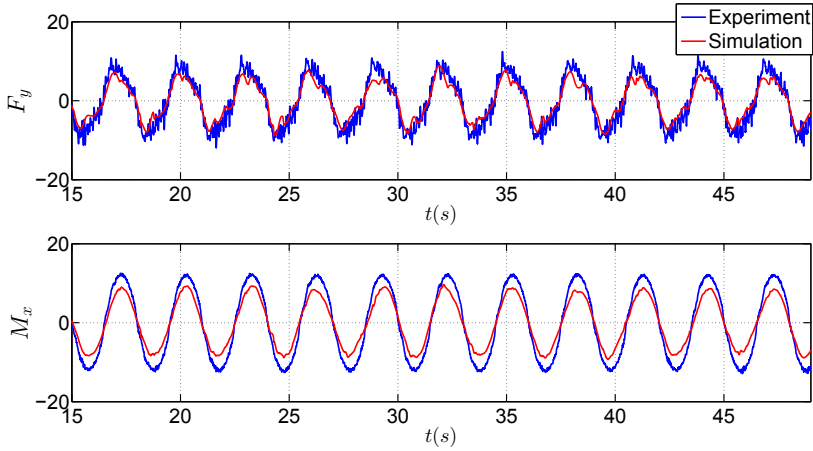


Figure 3.9: Comparison of experimental and numerical results of sway force and roll moment in test20, $\frac{\omega}{\omega_1} = 1.0$, $\phi_a = 4.0^\circ$.

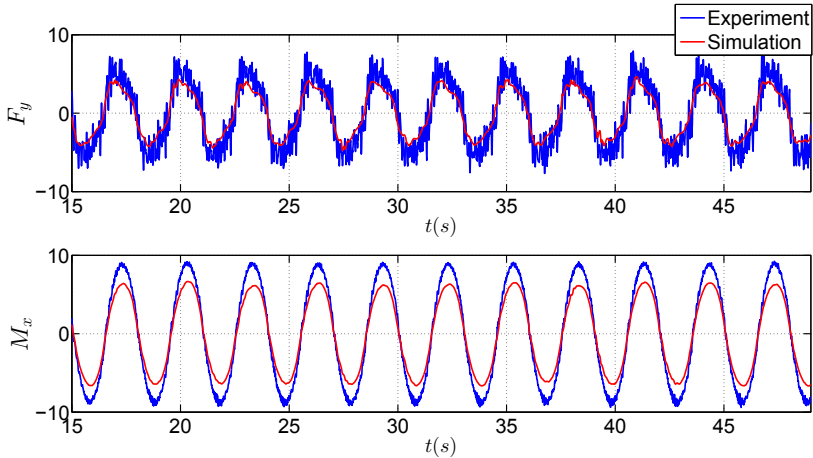


Figure 3.10: Comparison of experimental and numerical results of sway force and roll moment in test30, $\frac{\omega}{\omega_1} = 1.0$, $\phi_a = 2.0^\circ$.

F_y is the force along the tank length (sway force if the tank is mounted on the ship) and M_x is the moment around the tank-width axis. It corresponds to the roll moment if the tank is mounted on the ship. As it can be seen in these figures, the roll moment is under-predicted by around 25% while a clear difference is also seen in the sway force, showing however a better agreement. The differences for the roll moment are probably due to the fact

that these cases are performed at the resonance frequency and as observed in the experiments, there are significant tank roof impacts that make the flow very violent and create pronounced splashes and non-linearities not captured by the sloshing solver. Furthermore, pressures at the tank roof will directly influence roll moments but not directly the sway force. This could explain the better agreement observed for such load. Numerical convergence and conservation of fluid mass were checked in the simulations.

3.2 Coupled seakeeping-sloshing solver

After validating our seakeeping solver in chapter 2 and the sloshing solver in this chapter, we present the coupled solver here. The wave induced motions for ocean-going vessels might excite sloshing. Left side of the Fig. 3.11 shows the spectra of a group of sway acceleration corresponding to several possible sea states. It also shows the spectra of transfer function of sloshing response (lateral force) for different tank dimensions.

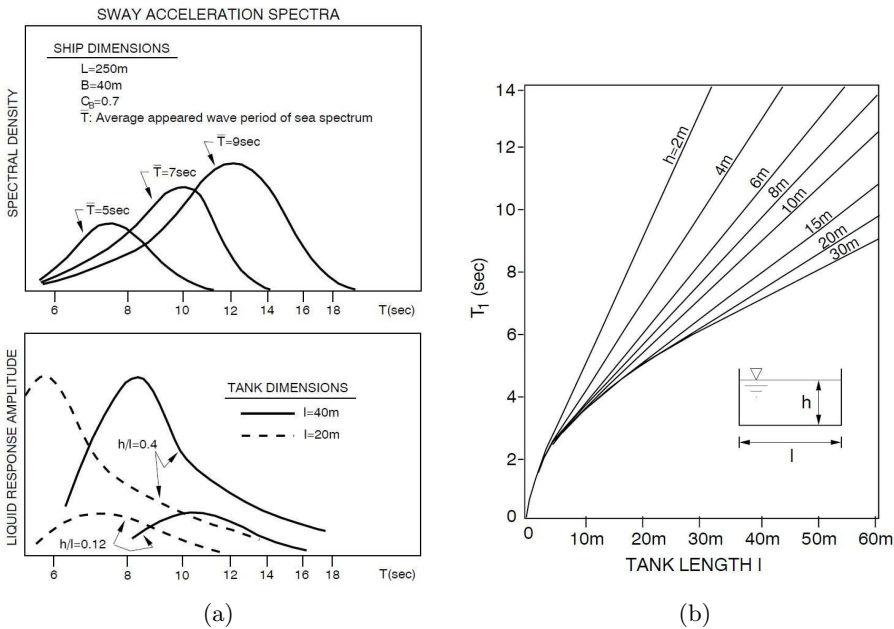


Figure 3.11: (a): Ship motions and transfer function of sloshing lateral forces versus period of oscillation [78]. (b): First mode natural period for rectangular tanks versus tank dimensions [5].

It shows that a peak response amplitude in the sloshing force might occur

in range of expected sway periods. As it can be seen from the right side of the Fig. 3.11, the increase in tank length increases the highest natural period of the fluid and, consequently, higher sea states and ship motions are needed to excite the sloshing around resonance ([5]). This graph also tells that it is not necessarily the most severe sea-state that causes the most severe sloshing.

The sloshing has been always of concern in design of liquefied natural gas (LNG) carriers, tankers, Floating Production and Storage Offloading (FPSO) units. Generally speaking, any ship carrying liquid in partially filled tanks, may experience violent sloshing [5]. The coupling of sloshing and ship motions are of concern in the analysis of many ships. The ship motions excite sloshing which in return influence back the ship motions. This is the whole concept of anti-roll tanks. If a tank is designed with good parameters in terms of dimensions and filling ratio in a way that its natural roll frequency coincides with ship roll natural frequency, it would counteract the growing of roll motion, acting as an extra roll-damping device. A detailed description of the anti-roll tank mechanism could be found in section 7.1. The coupling strategy used here is iterative, as illustrated by the flowchart in Fig. 3.12.

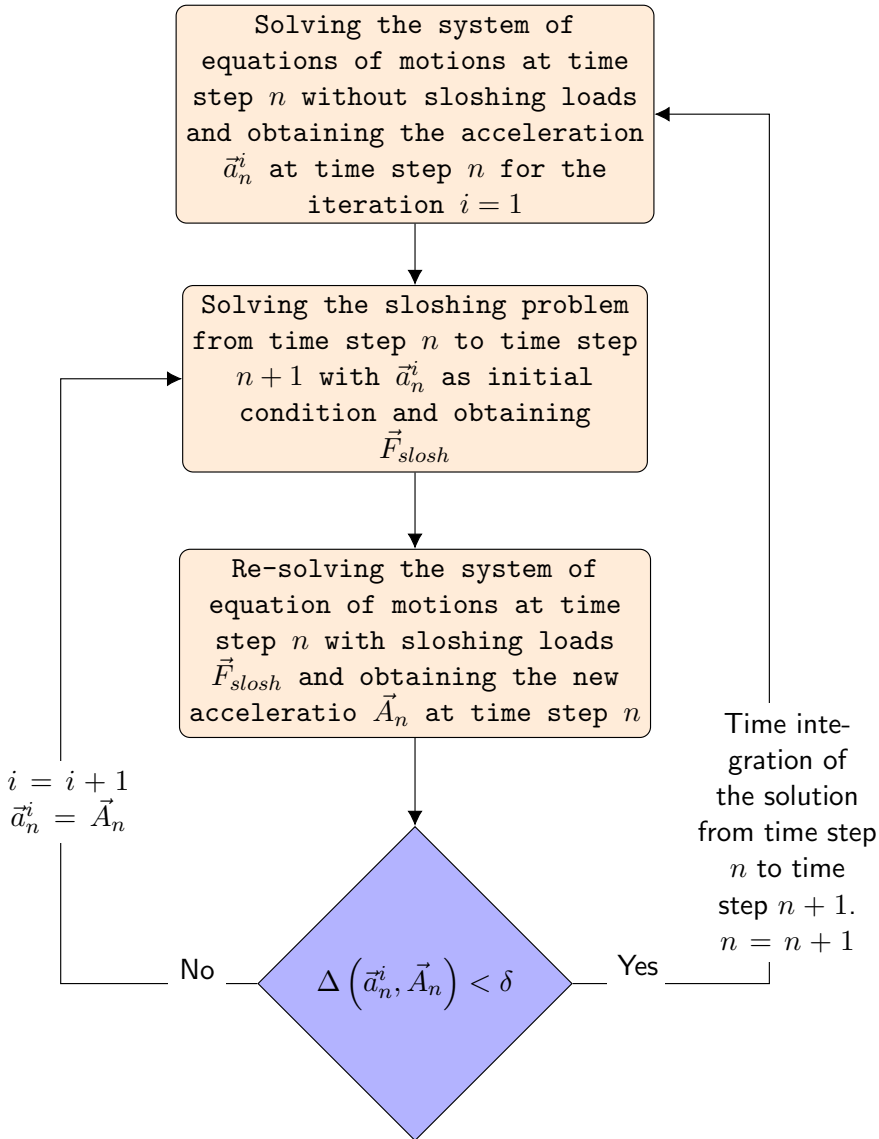


Figure 3.12: Flowchart of iterative coupling between seakeeping and sloshing solver.

For validating the coupling strategy shown in this flowchart, it would be wise to first use it for experiments involving limited number of degrees of freedom for the ship. A set of 2D experiments on a box-shaped ship section excited by regular beam sea have been conducted to study the effect of coupling with sloshing by Rognebakke [5]. Two identical tanks were mounted on the ship. The general configuration of the ship and the tanks is shown in Fig. 3.13.

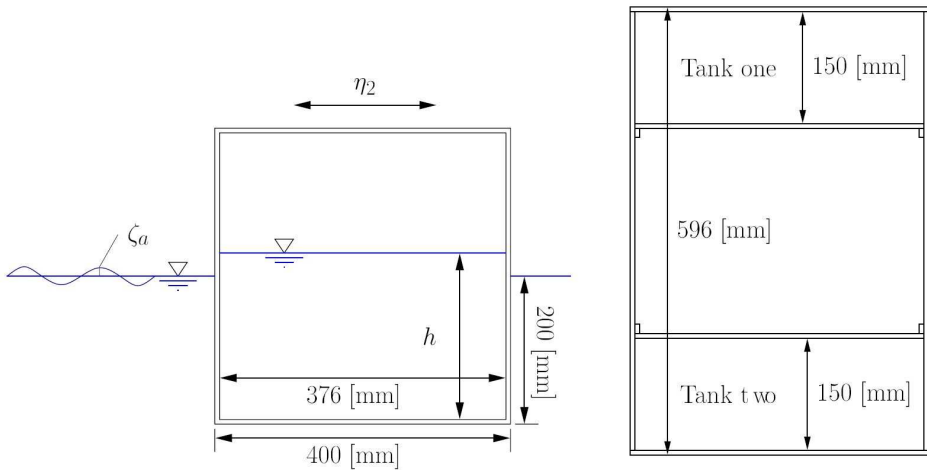


Figure 3.13: Ship section and mounted tanks, side and top view [5].

The experiments were performed at NTNU wave flume with overall length of 13.5m and 0.6m width and water depth of 1.03m. The ship section has 596mm length, which leaves 2mm clearance from the flume wall at each side. The breadth is 400mm and the draft is 200mm. The tanks have length of 376mm, width of 150mm and height of 288mm or 388mm in some experiments. The tank decks were movable to make the tank roof impact possible in case of need, but no tank roof impact was reported during the experiments though. In cases of different tanks filling ratio, the draft of 200mm is kept constant by adding extra weights on the ship in different cases of experiments. The ship section slides along two rails on top of low friction bearings where the bearings are slightly pre-tensioned. This gives a constant force of 2N against the motion. The ship section is restrained from drifting off by a spring with a total stiffness of 30.9N/m. It should also be noted that the eigenfrequency caused by the spring is well below the studied wave frequency. The relationship between wave frequency and

amplitude is shown in Fig. 3.14.

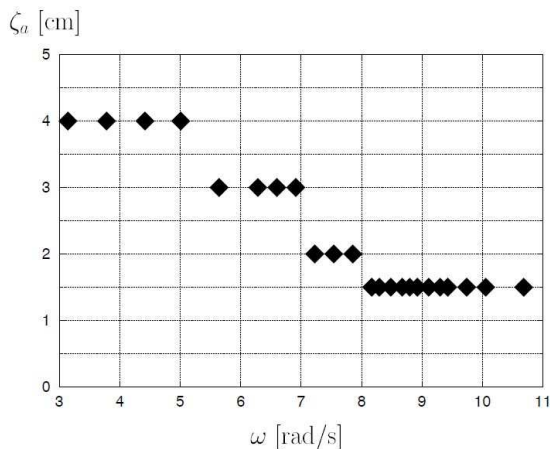


Figure 3.14: Wave frequency and amplitude relationship in the experiments by Rognebakke [5].

The measured and calculated transfer functions of the sway motion for the case with empty tanks (we can imagine the water in the tanks here as frozen and rigid) are given in Fig. 3.15 just to check the accuracy of measurements and simulations. A 1-DOF linear time domain code was used for the numerical simulations and as it could be seen, the results are in a good agreement with the experiments. Then we compared the experiments and numerical simulations for the case of two tanks with filling ratio $h = 184mm$. The numerical simulations of Rognebakke [5] are also shown in the figure, in which the non-linear analytical sloshing solver was coupled with a standard seakeeping code. The numerical simulations agree well with the experimental values also in this case.

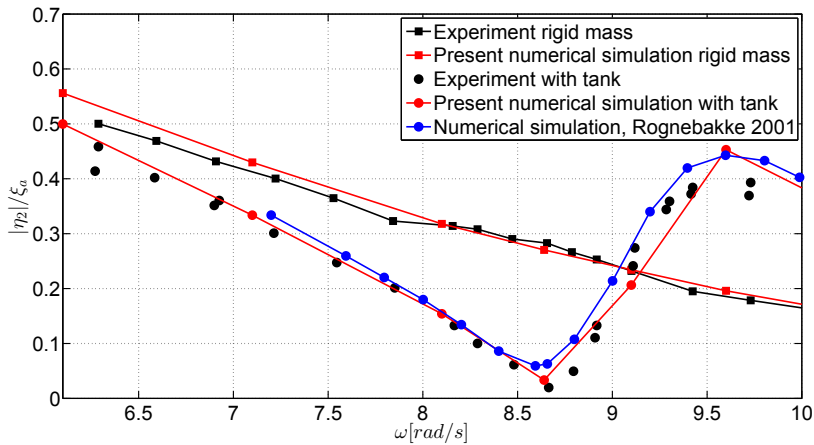


Figure 3.15: Sway RAO for the ship section without tanks (rigid mass) and with two tanks filled with $h = 184\text{mm}$ from present numerical seakeeping-sloshing coupled solver and from numerical and experimental studies by Rognbakke[5].

The figure shows a strong coupling of internal and external flows. The sloshing influence on sway motion in frequencies smaller than first natural sloshing frequency ($\omega_n = 8.65\text{rad/s}$) is a counteracting effect and the sway motion is smaller than in the rigid mass case. This trend continues until ω_n and at such frequency, the sloshing force has the biggest effect and makes the sway almost zero. For frequencies slightly larger than ω_n , the sway motion increases due to sloshing effects. This is related to the phase shift between sway exciting forces from external and internal flows. These phase shifts are clearly illustrated in Fig. 3.16, which provides snapshots from the experiments for the mentioned case. For example in part b, it is clear that the internal flow is counteracting the external flow forces.

Basically, sloshing acts as a frequency dependent restoring force on sway causing resonances. Furthermore, the combination of the linear sloshing force with the dynamics of the ship-section model causes zero sway motion at sloshing natural frequency (due to the infinite sloshing added mass at this frequency in linear theory), while in reality the sway motion will have a minimum sway motion different from zero in the vicinity of this frequency.

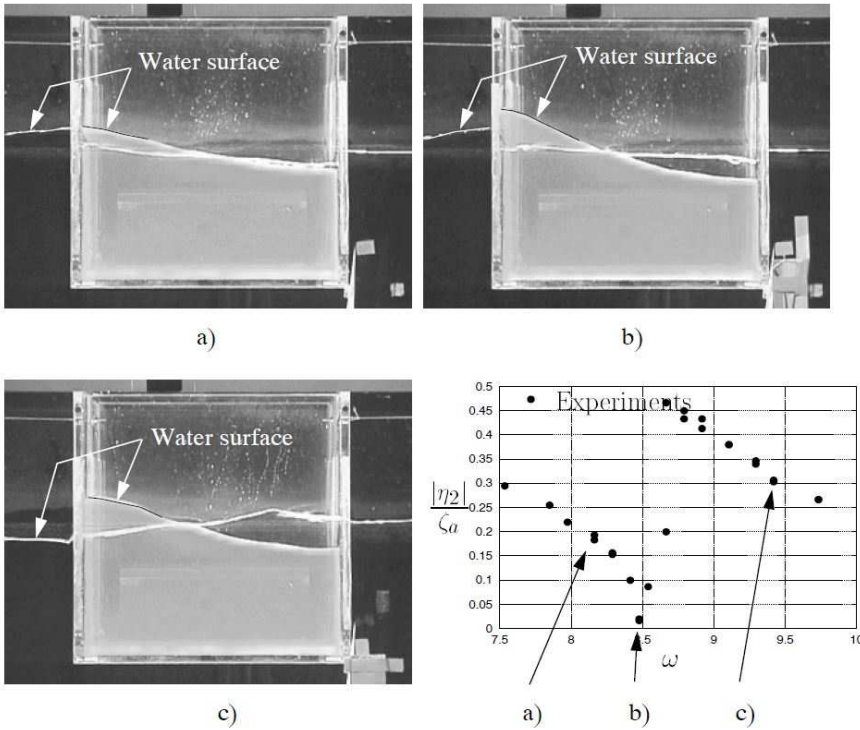


Figure 3.16: Wave frequency and amplitude relationship in the experiments by Rognebakke [5] (bottom right) and snapshots for three selected cases (top and bottom left).

3.3 Module of mooring cables calculations

In the physical investigations on a fishing vessel, described in chapters 6 and 7, in order to limit the mean horizontal motion (mean surge, sway and yaw) of the model, a mooring system of four elastic cables in a symmetrical configuration with respect to the longitudinal axis (V-shaped configuration) was placed at the water-plane level and fixed to the carriage as shown in Fig. 3.17. To perform numerical simulations consistent with the experimental investigations, the mooring-line system was modelled.

In the experiments, four load cells were attached between the carriage and the ends of the four elastic cables to measure the pretension (T_0) and the changes in the cable tension during the experiments. Using these data, the recorded ship motions and the cables configuration, the tension changes can be expressed in terms of cable length change. This process will be

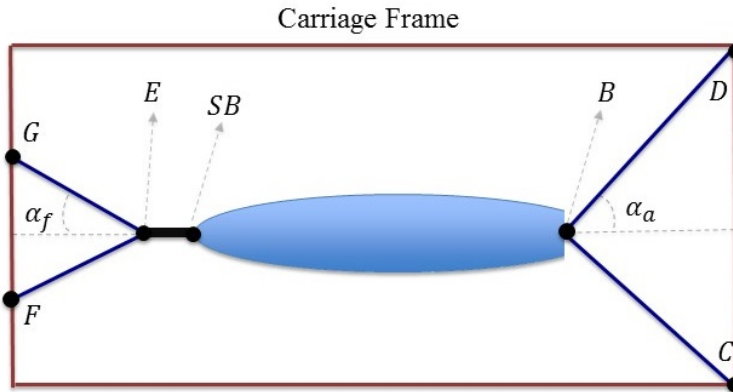


Figure 3.17: Top view of the cable general configuration in calm water.

explained in detail here.

Based on practical experiences, it is much more efficient for limiting the horizontal motion to have the $SB - E$ part as steel rigid part (shown in black in Fig. 3.17) and other parts as elastic cables (shown in blue in Fig. 3.17). In the aft part of the body, the elastic cables are instead directly attached to the ship hull, so there is no problem in finding the aft cables length change. By having the rigid ship-model motions, we can easily find them, while it is not that simple in the fore cables due to complexity of the configuration. At any time, we should find the exact position of joint E and then find the fore cables length change. A sketch of the cables configuration for a situation with ship-model motions is shown in Fig. 3.18.

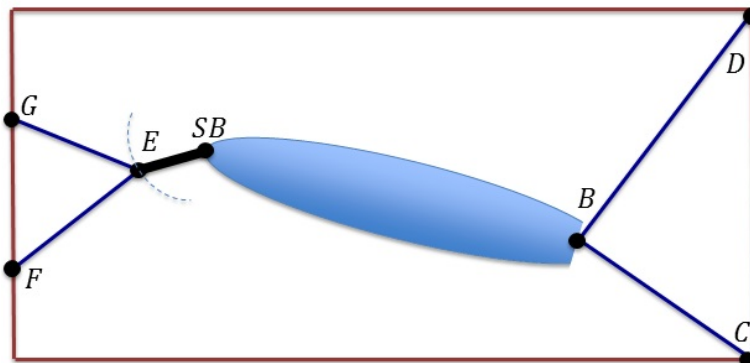


Figure 3.18: Top view of the cable configuration with an arbitrary motion of the ship model.

For finding the exact coordinates of the joint point of the fore elastic cables and the rigid steel cable, we can solve a system of four equations and four unknowns. The unknowns are the coordinates of the joint point E and the tension force in the steel part $F - E$. The four equations are equilibrium equations in forces in three directions in the joint point and also the fixed length of the steel part.

The unknowns are X_E, Y_E, Z_E (coordinates of the point E) and the steel part tension force F_E .

$$F_E (X_{SB} - X_E) = - \left[\frac{T_{EG}}{l_{EG}} (X_G - X_E) + \frac{T_{EF}}{l_{EF}} (X_F - X_E) \right] \quad (3.3)$$

$$F_E (Y_{SB} - Y_E) = - \left[\frac{T_{EG}}{l_{EG}} (Y_G - Y_E) + \frac{T_{EF}}{l_{EF}} (Y_F - Y_E) \right] \quad (3.4)$$

$$F_E (Z_{SB} - Z_E) = - \left[\frac{T_{EG}}{l_{EG}} (Z_G - Z_E) + \frac{T_{EF}}{l_{EF}} (Z_F - Z_E) \right] \quad (3.5)$$

$$\sqrt{(X_{SB} - X_E)^2 + (Y_{SB} - Y_E)^2 + (Z_{SB} - Z_E)^2} = l_{E-SB} \quad (3.6)$$

Here $T_{EG}, T_{EF}, l_{EG}, l_{EF}$ and l_{E-SB} are tension in cable EG , tension in cable EF , cable EG length, cable EF length and cable $E - SB$ length, respectively. The other parameters are points coordinates. For finding the solution of this system of equations, we used the Newton-Raphson Method. If we call the equations like:

$$\begin{aligned} f_1 (X_E, Y_E, Z_E, F_E) &= 0; \\ f_2 (X_E, Y_E, Z_E, F_E) &= 0; \\ f_3 (X_E, Y_E, Z_E, F_E) &= 0; \\ f_4 (X_E, Y_E, Z_E, F_E) &= 0; \end{aligned} \quad (3.7)$$

Then the solution would be:

$$\begin{bmatrix} X_E \\ Y_E \\ Z_E \\ F_E \end{bmatrix} = \begin{bmatrix} X_{E0} \\ Y_{E0} \\ Z_{E0} \\ F_{E0} \end{bmatrix} - [J (X_E, Y_E, Z_E, F_E)]^{-1} \begin{bmatrix} f_1 (X_{E0}, Y_{E0}, Z_{E0}, F_{E0}) \\ f_2 (X_{E0}, Y_{E0}, Z_{E0}, F_{E0}) \\ f_3 (X_{E0}, Y_{E0}, Z_{E0}, F_{E0}) \\ f_4 (X_{E0}, Y_{E0}, Z_{E0}, F_{E0}) \end{bmatrix} \quad (3.8)$$

where the first vector on the right hand side of the equation is the initial guess for the solution and the second term is the Jacobian matrix and is calculated as follows:

$$J(X_E, Y_E, Z_E, F_E) = \begin{bmatrix} \frac{\partial f_1}{\partial X_E} & \frac{\partial f_1}{\partial Y_E} & \frac{\partial f_1}{\partial Z_E} & \frac{\partial f_1}{\partial F_E} \\ \frac{\partial f_2}{\partial X_E} & \frac{\partial f_2}{\partial Y_E} & \frac{\partial f_2}{\partial Z_E} & \frac{\partial f_2}{\partial F_E} \\ \frac{\partial f_3}{\partial X_E} & \frac{\partial f_3}{\partial Y_E} & \frac{\partial f_3}{\partial Z_E} & \frac{\partial f_3}{\partial F_E} \\ \frac{\partial f_4}{\partial X_E} & \frac{\partial f_4}{\partial Y_E} & \frac{\partial f_4}{\partial Z_E} & \frac{\partial f_4}{\partial F_E} \end{bmatrix} \quad (3.9)$$

One should note that l_{EG} and l_{EF} are also functions of the unknown coordinates of the joint point and this fact should be considered in the calculation of the Jacobian matrix. This method is an iterative numerical method and a criterion should be set for the stopping point of the calculations. After having the coordinates of the joint point, we will have all the cable forces needed to put in the system of the equations of the ship. The other part related to this module is to find the relation of the cables tension against the cable length change. The general formula used for the cables looks like the one in Fig. 3.19 and is stated in Eq. 3.10.

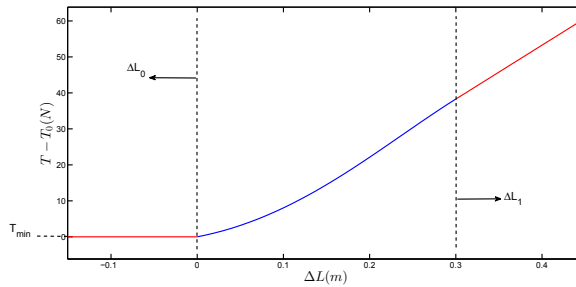


Figure 3.19: The tension versus cable length change.

$$T - T_0 = \begin{cases} T^{min} & \text{if } \Delta l < \Delta l_0 \\ f(\Delta l) & \text{if } \Delta l_0 < \Delta l < \Delta l_1 \\ g(\Delta l) & \text{if } \Delta l > \Delta l_1 \end{cases} \quad (3.10)$$

where T_0 is the pretension of the cables. Δl_0 is a lower limit where the cable tension becomes a fixed tension for values of Δl smaller than that. Δl_1 is a limit where the cable tension for the range of $(\Delta l_0, \Delta l_1)$ can be described with a polynomial function $f(\Delta l)$ and for values of Δl higher than Δl_1 , the tension gets linear ($g(\Delta l)$) in a way that its value and the slope are the same, respectively to the value of that function and related slope in Δl_1 .

Since the cables change a bit at any set of tests, the tension formula might be a bit different for different cases of experiments. The formulas for the cables tensions will be shown for different tests in the next chapters.

3.4 Weak-scatterer hypothesis formulation

In our time domain solver, the radiation-force coefficients and diffraction forces are calculated in frequency domain before starting the simulations (as in the simulations of the parametric rolling in C11 container-ship and will be shown in chapter 5). Based on [3], the weak-scatterer hypothesis for modifying the linear radiation and diffraction forces provides better solution in long and steeper waves. So a modification to the solver formulation is performed which is explained here. The main assumption for the weak-scatterer hypothesis ([3], [4]) is that the incident waves and body motions are large relative to the scattering and radiation wave effects (wavelength-to-ship length ratio sufficiently large). According to [3] and also investigating some experiments and numerical simulations with and without this modification, it was seen that using this modification gives the results in better agreement with the experiments. Therefore, we used this formulation for the experiment simulations in chapter 6 and 7 related to a fishing vessel. The formulation for this modification is as follows. The rigid body motions are solved in time domain and in a body-fixed frame (as explained in the chapter 2). The equations of motions could be written in a vector form as in [3]:

$$M \ddot{\eta} + \Omega \times M \dot{\eta} + A_{\infty} \dot{\beta} + \int_0^t K(t - \tau) \beta(\tau) d\tau = F^{FK} + F^{rest} + F^{grav} + F^{others} \quad (3.11)$$

where M is the generalized mass matrix, η_i are the six rigid degrees of freedom, Ω is the angular velocity vector ($\dot{\eta}_4, \dot{\eta}_5, \dot{\eta}_6$) and the upper dot means the time derivatives along the instantaneous body axes. The cross product of Ω and first three component of $M\dot{\eta}$ gives the first three components and the remaining give the second three components. A_{∞} is the infinite frequency added mass (as is explained in chapter 2) and K is the retardation function. The right-hand-side forces are non-linear Froude-Krylov, non-linear restoring, ship weight and other forces and moments, respectively. A simple model of water on deck and bottom slamming is used in the numerical simulations but the results do not show a big effect from them. More detail for these two parts could be found in [3]. The main corrections in this equation

are in the added mass and convolution integral terms. β is a six component vector and without weak-scatterer hypothesis correction, equals the $\dot{\eta}$ while using the weak-scatterer hypothesis, this vector is estimated in time from the body-boundary condition:

$$V_n(x, t) = (V_{ship} - V_{wave}) \cdot n \quad (3.12)$$

where V_{ship} and V_{wave} are the ship and incident wave velocities, and the V_n is the fluid-velocity along the ship hull normal vector n . This implies that scattering and radiation phenomena are considered together. According to [3], V_n is expressed in terms of N prescribed basis functions as follows:

$$V_n(x, t) = \sum_{i=1}^N \beta_i(t) \psi_i(t) \quad (3.13)$$

The body boundary condition 3.12 is enforced through a Minimum Least-Square approach along the instantaneous wetted surface of the body by defining $N=6$ and $\psi_i = n_i$ as the basis functions. This provides the equations to find the β vector in time. Now we have all the parameters for solving the equations of motions in time. We used the Runge-Kutta fourth order scheme to integrate the solution in time. More details about this method and its assumptions could be found in [3] and [4].

Chapter 4

SFH112 fishing vessel model and experimental set-up

4.1 Introduction

A comprehensive experimental investigation on the parametric rolling of a fishing vessel was carried out at the CNR-INSEAN basin No. 2 together with Claudio Lugni as the principal manager. The dimensions of this basin are: $length \times width \times depth = 220 \times 9 \times 3.6m$. The wave basin is equipped with a flap wave-maker, hinged at a height of 1.8 m from the bottom. The experiments performed on a scaled model (1:10) of a Norwegian fishing vessel. The model hull was made out of wood and was used for different types of experiments which will be explained in this chapter.

4.2 SFH112 fishing vessel model

The vessel model (INSEAN model C2575) is built at CNR-INSEAN in scale 1:10 and reproduces a medium sized Norwegian fishing vessel (SFH112). Bilge keels, skag and anti-roll tank have been used in the experiments. Both the bilge keels and the anti-roll tank are removable in order to estimate their separate contribution to the roll damping [79]. The body plan with skag and a 3D view of the C2575 model are shown in Figs. 4.1 and 4.2, while Tab. 4.1 reports the detailed geometric and hydrostatic properties.

Table 4.1: Detailed hull properties of the model scale of the SFH112 fishing vessel.

Length $L \equiv L_{pp}$	2.95m
Beam B	0.95m
Draft D	0.4m
Displacement ∇	657.3kg
Block Coefficient C_B	0.58
Longitudinal Center of Gravity (LCG) from AP (Aft Perpendicular)	1.412m
Verical Center of Gravity (VCG) above keel (KG)	0.43m
Transverse metacentric height GM_T	0.07m
Roll Radius of Gyration k_{xx}	$0.378B$
Pitch and Yaw Radius of Gyration k_{yy}, k_{zz}	$0.28L$
Natural roll period, T_{n4} (no tank)	2.97s
Natural roll period, T_{n4} (with tank)	3.064s
Tank length	0.95m
Tank height	0.14m
Tank width	0.051m
Tank filling depth	0.039m
Tank bottom position relative to calm water level	0.4 m
Tank bottom longitudinal position relative to COG	-0.38 m

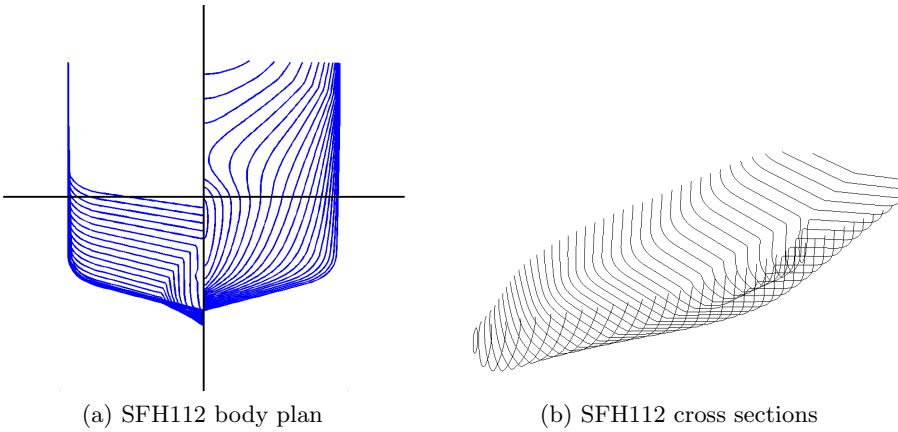


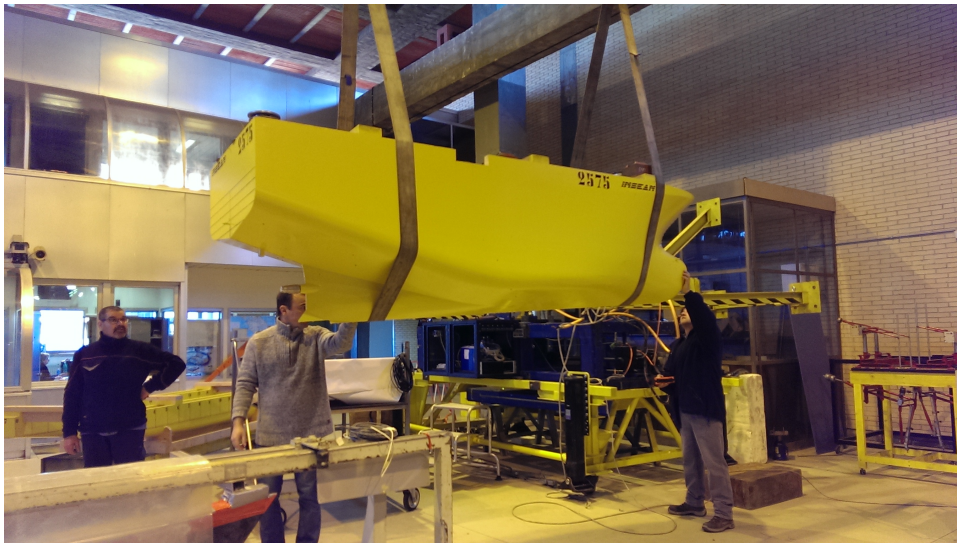
Figure 4.1: SFH112 fishing vessel body plan and cross sections.

Fishing vessels in Norway tend to become wider in order to increase the payload due to regulatory length limitations, so SFH112 vessel is also fairly wide. The midship region of the vessel lacks the uniform sections

seen on larger vessels and the body plan shows a vessel where the region of similarly shaped sections is short. This makes the vessel more vulnerable to parametric roll due to larger variation of the water-plane area in waves with wavelengths in the order of the ship length. The main characteristics of the model are shown in Tab. 4.1.



(a)



(b)

Figure 4.2: Pictures of the SFH112 model at CNR-INSEAN basin.

The incident wave system is measured by means of two different pairs of transducers (capacitance wire probe and finger probe) fixed to the carriage. The wave elevation recorded by a pair of sensors 16m ahead of the model, is the measure of the incident wave. A second pair of sensors, approximately 3m aside the COG of the ship-model, provides a wave elevation partially affected by the hull. In fact, the first pair (located in far upstream) can provide a good measure of the actual generated incident waves and the second pair account for the interaction with ship and the reflections from the tank walls. The rigid motions of the hull are measured with an inertial (MOTAN) and an optical (Krypton) system. The non-intrusive system Krypton gives the real-time measure of the rigid body motions: 3 CCD cameras detect the position of a reference system fixed to the body and identified through three infrared LEDs. This system allows a high spatial resolution, less than 1mm for the linear displacements and less than 0.05° for the angular degrees of freedom. The MOTAN is an inertial platform, which measures the accelerations and the angular velocities of a rigid model. In order to limit the mean horizontal motions (mean surge, sway and yaw) of the model, a mooring system of four elastic cables in a symmetrical configuration with respect to the longitudinal hull axis (V-shaped configuration) was placed at the water-plane level and fixed to the carriage (see sketch in Fig. 4.3).

In the experiments, four load cells were attached between the carriage and the ends of the four cables to measure the pretension (T_0) and the changes in the cable tension during the experiments. Using these data, the recorded ship motions and the cables configuration, the tension changes can be expressed in terms of cable length change. More details of the cables for any experiment sets will be given in chapters 6 and 7.

Three main categories of experiments were performed without tank during this campaign. They are listed below:

- The experiments of the bare hull with skeg in waves at Froude number $Fn = U/\sqrt{Lg} = 0$.
- The experiments of the bare hull with skeg in waves at Froude number $Fn=0.09$.
- The experiments of the bare hull with skeg in waves at Froude number $Fn=0.18$.

At the beginning of any experiment, decay tests in calm water and without forward speed were performed for having a better view of the damping for the different modes of the model and also the cable forces.

4.3 Mooring system

As explained in section 3.3, to limit the mean horizontal motion (mean surge, sway and yaw) of the model, a mooring system of four elastic cables in a symmetrical configuration with respect to the longitudinal axis (V-shaped configuration) was placed at the water-plane level and fixed to the carriage. The values used in the experiments for the cable angles are $\alpha_f = 25^\circ$ and $\alpha_a = 45^\circ$ as shown in Fig. 4.3.

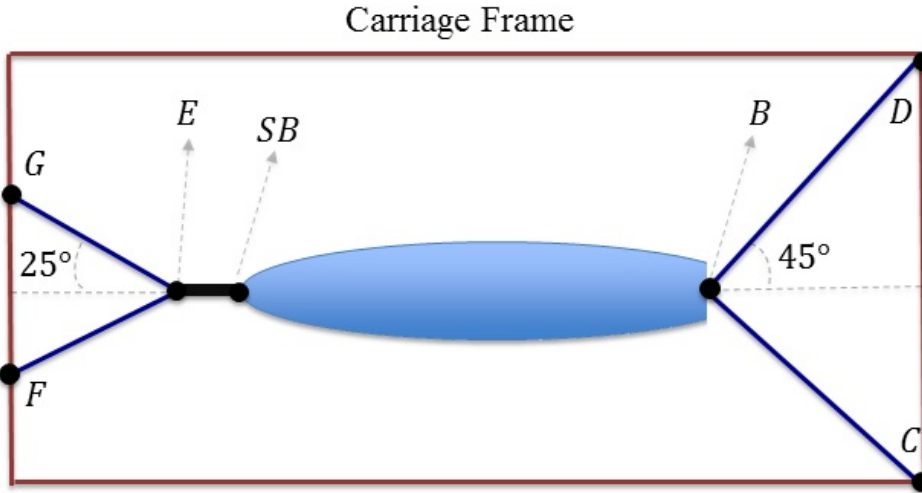


Figure 4.3: Top view of the experimental cable configuration in calm water.

The coordinates of the attachment points in the body frame coordinate system in calm water are listed in Tab. 4.2.

Table 4.2: Mooring cables nodes coordinates.

Node	x(m)	y(m)	z(m)
F	3.9057	0.82	0.05
G	3.9057	-0.82	0.05
E	2.1287	0.0	0.0
SB	1.8087	0.0	-0.0067
D	-2.379	-0.82	0.05
C	-2.379	0.82	0.05
B	-1.592	0.0	0.025

4.4 Anti-roll tank set-up

A passive free surface anti-roll tank is designed and mounted on the ship model and new tests were designed and performed to investigate its effect on the parametric rolling resonance. The tank is shaped as an elongated parallelepiped box (see Fig. 4.4) mounted $0.38m$ aft the longitudinal position of the centre of gravity of the ship model with skeg and without bilge keels. The tank is fixed to the model through a balance, designed at CNR-INSEAN using a Kistler load cells system, to measure the sloshing forces and moments of the tank on the ship model. The ballast on the model is compensated so to keep constant the hydrostatic properties after the tank installation. The length of the tank is the same as the ship model breadth, i.e. $95cm$. The tank height is $14cm$ and the filling depth is $3.9cm$. Four different widths corresponding to 3.0 , 4.0 , 5.1 and $8.1cm$ were investigated. The tests with tank were done only at zero forward speed. The ship model and the mounted tank on-board are illustrated in Fig. 4.4.

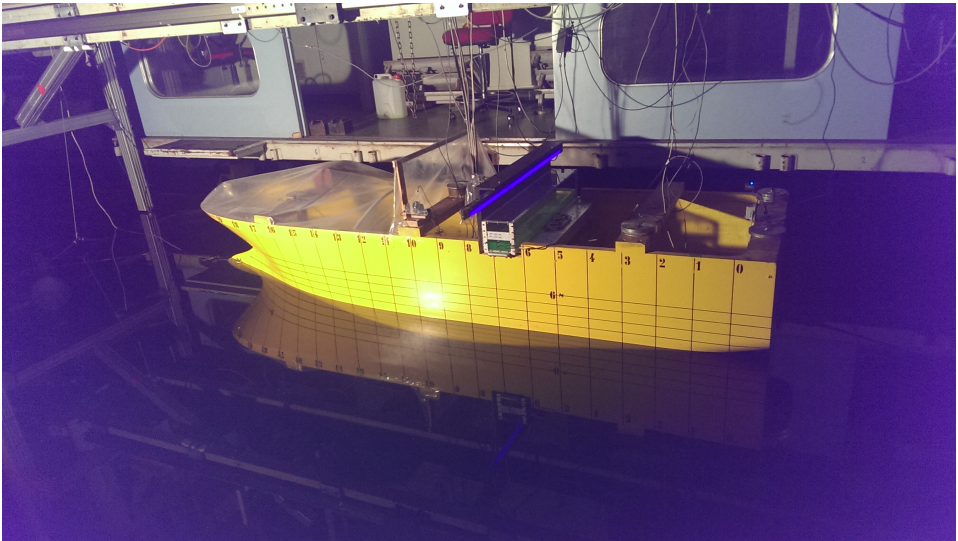


Figure 4.4: The ship model and the mounted free-surface anti-roll tank.

Before starting the experiments of the model and the mounted tank, a series of forced rolling experiments of the isolated tank were performed and the sloshing forces and moments were measured at a tank fixed coordinate system with its origin at the tank bottom. on the bottom of the tank was measured. As it was shown in chapter 3, these tests were used for validation of our sloshing numerical simulator.

Chapter 5

Experiments and numerical simulations (using strip theory) of parametric rolling in post-Panamax C11 class containership

In the first stages of this PhD work, a non-linear frequency domain numerical solver was developed where the motions are modelled in 5-DOF(excluding surge) and the radiation and diffraction problems were solved using a strip theory code [72]. The code was validated by comparing its results for a C11 class post-Panamax containership against the experimental results. The numerical and experimental results were in good agreement and related analysis was published and presented in OMAE2015 conference [12]. The experiments and numerical results are examined in this chapter.

5.1 Experimental set-up and numerical solver

5.1.1 Experimental set-up

A series of experiments for parametric rolling on a container ship model in regular (head and following sea) waves was performed during Hydralab III project in CEHIPAR (Canal de Experiencias Hidrodinamicas del Pardo) [80], Spain, which are used here for validation of our numerical method. The full-scale particulars for the post-Panamax C11 containership and its

bodyplan are shown in Tab. 5.1 and Fig. 5.1.

Table 5.1: Hull properties of C11 post-Panamax container ship.

Length between perpendiculars $L \equiv L_{pp}$	262m
Beam B	40m
Draft D	12.34m
Block Coefficient C_B	0.66
Vessel Displacement	76056ton
Vertical center of gravity (VCG) above keel	17.51m
Longitudinal center of gravity (LCG) from AP	124.54m
Transverse metacentric height GM_T	1.97m
Roll Radius of Gyration k_{xx}	$0.34B$
Pitch and Yaw Radius of Gyration k_{yy}, k_{zz}	$0.24L$

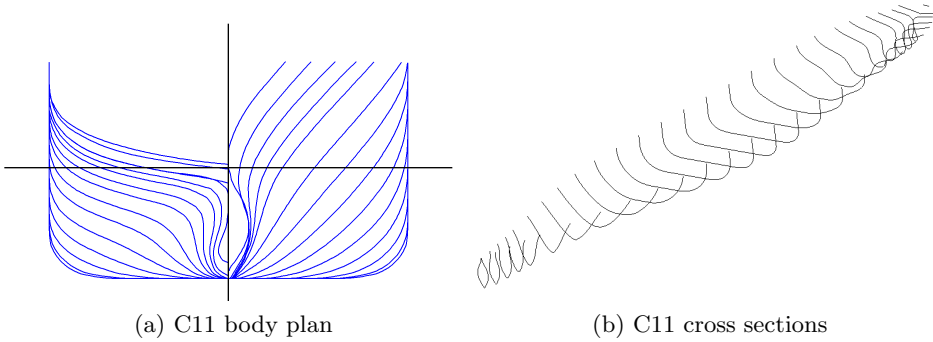


Figure 5.1: C11 Container ship body plan and cross sections.

The CEHIPAR towing tank is 150m long, 30m wide, has 5m depth and is equipped with a flap type wave maker at one side and an artificial beach to avoid wave reflection at the other side. The basin is equipped with a Computerized Planar Motion Carriage (CPMC). A schematic view of the basin is shown in Fig. 5.2 [38].

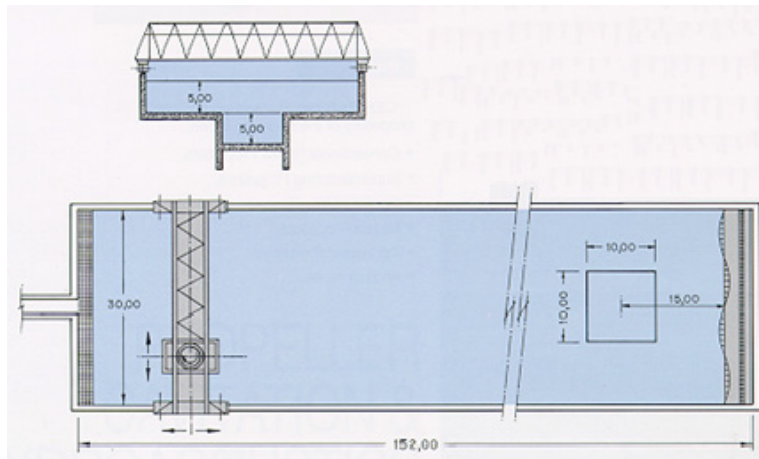


Figure 5.2: CEHIPAR basin with wave maker and wave beach and CPMC system [38].

Fig. 5.3 shows the ship model and the experimental set-up while performing the experiments.



Figure 5.3: C11 post-Panamax container ship model and the experimental set-up [38].

The experiments were performed on a model with scale of 1:65 in different scenarios, which are described in detail. A tuning was set for parameters so that parametric rolling could occur. Based on conditions that

were discussed in the previous sections, the frequency of excitation should be almost twice the roll natural frequency and, at the same time, the wave height should be higher than a threshold value and the roll damping should be lower than a limit. Besides, the running time should be long enough so that the building-up phase of the roll due to its instability can lead to steady-state conditions with the roll oscillating at its natural frequency. In the experiments examined, the wave length varies from 0.8 to 1.4 times of the ship length and the wave amplitude ranges between 3 and 5 m in full scale conditions. The full scale ship speeds in these experiments are 8 knots in head sea and 0 knot in following sea.

5.1.2 Numerical solver

Here, a numerical method based on linear potential-flow strip theory and non-linear Froude-Krylov and hydrostatic loads, modelling the vessel as a 5-DOF system and including viscous roll damping, is used to study parametric roll. In fact we solved the equations of motion as shown in Eq. 2.96, except for the Froude-Krylov and hydrostatic loads that are calculated from the integration of the pressure around the wetted surface of the ship at any time step. Inclusion of these two non-linear forces (calculated as explained in section 2.2.2) are essential to capture the parametric resonance.

In the roll damping part, we added linear equivalent viscous roll damping to the radiation roll damping. We used Ikeda semi-empirical formulation for calculating the viscous roll damping [81].

5.2 Results

Fig. 5.4 shows an example of parametric-roll occurrence from the model tests in [80] in terms of the time evolution of the wave elevation and of heave, roll and pitch for a given incident wave amplitude $\zeta_a = 3m$, wave period $T_w = 12.95s$ and ship forward speed $U = 8kn$. These values correspond to an incident-wave steepness $k\zeta_a = 0.072$, a calm water roll natural frequency to excitation frequency ratio $\omega_{4n}/\omega_e = 0.472$ and $\lambda/L_{pp} = 1$. Here λ and L_{pp} mean the incident wavelength and the ship length between perpendiculars, respectively.

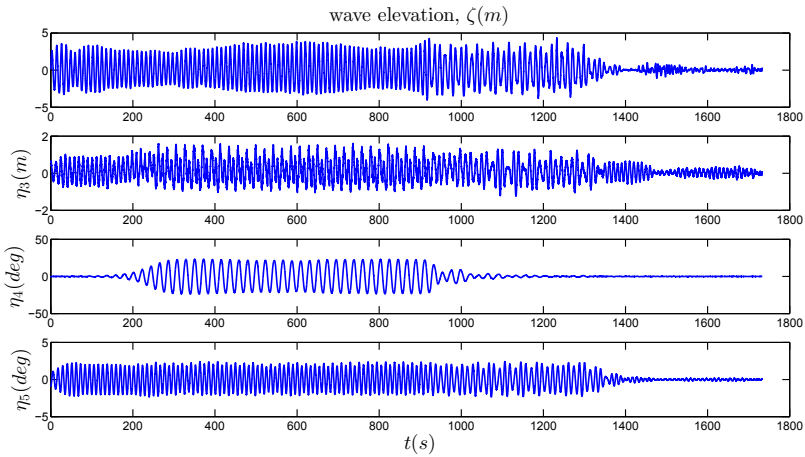


Figure 5.4: Development of parametric rolling in experiments in regular waves (Head sea, $\zeta_a = 3m$, $U = 8kn$, $T_w = 12.95s$) [80]

In this scenario, the maximum roll amplitude measured in experiments is 23.2° . For the same scenario, the numerical simulation was carried out and the results are given in Fig. 5.5 including all motions modeled by the developed solver.

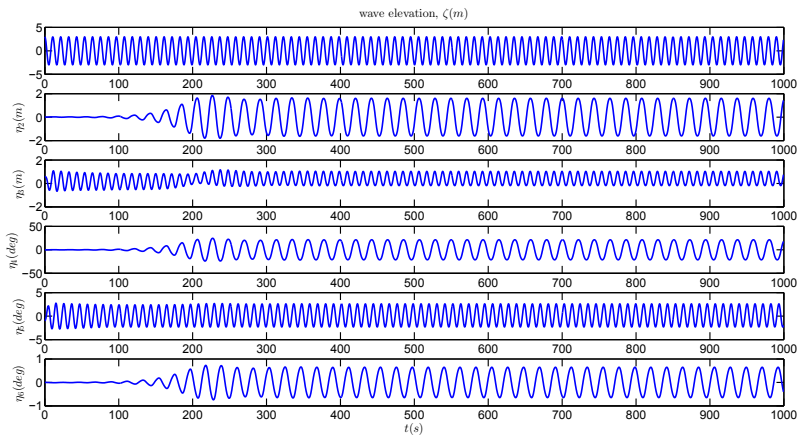


Figure 5.5: Development of parametric rolling in numerical simulations in regular waves (Head sea, $\zeta_a = 3m$, $U = 8kn$, $T_w = 12.95s$) [80].

The maximum numerical roll amplitude is 21.3 degrees.

In the next experiment examined, all the parameters are the same except

the wave amplitude which is changed to $4m$ ($k\zeta_a = 0.096$). We can see the effect of increasing the wave amplitude in Fig. 5.6.

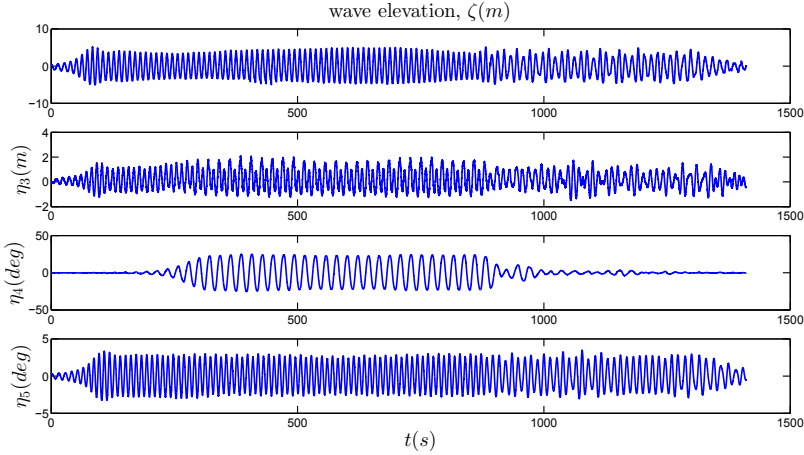


Figure 5.6: Development of parametric rolling in experiments in regular waves (Head sea, $\zeta_a = 4m$, $U = 8kn$, $T_w = 12.95s$) [80].

The maximum roll amplitude changes from 21.3 degrees for $\zeta_a = 3m$ to 25 degrees for $\zeta_a = 4m$. The same scenario with numerical simulations is shown in Fig. 5.7.

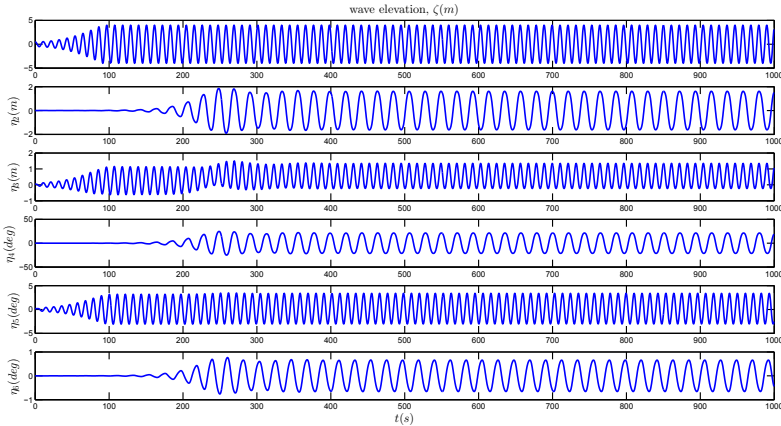


Figure 5.7: Development of parametric rolling in numerical simulations in regular waves (Head sea, $\zeta_a = 4m$, $U = 8kn$, $T_w = 12.95s$) [80].

The simulated results show 21.3° as the maximum roll amplitude, which

is in good agreement with experiments but it does not show an increase when comparing with previous scenario. Now we want to see how the ship would behave in another combination of parameters. For this scenario, the experiment was done for an incident wave amplitude $\zeta_a = 4m$, wave period $T_w = 14.19s$ and ship forward speed $U = 8kn$. These values correspond to an incident wave steepness $k\zeta_a = 0.08$, a calm water roll natural frequency to excitation frequency ratio $\omega_{4n}/\omega_e = 0.526$ and wavelength-to-ship length ratio $\lambda/L_{pp} = 1.2$ and the related measurements are shown in the Fig. 5.8.

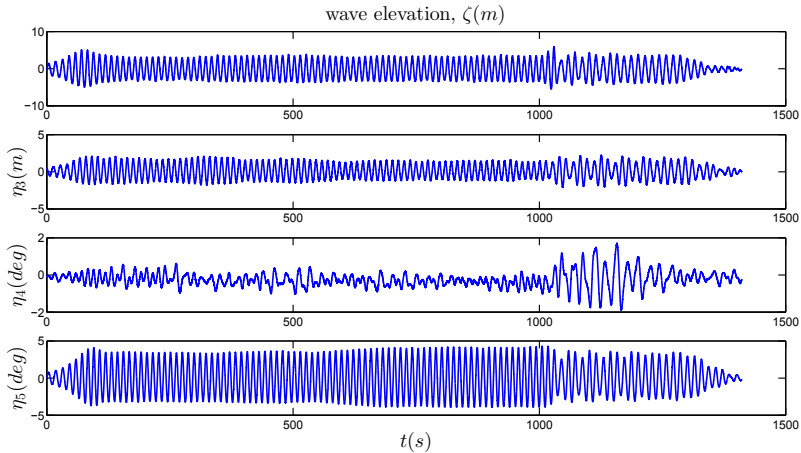


Figure 5.8: Development of parametric rolling in experiments in regular waves (Head sea, $\zeta_a = 4m$, $U = 8kn$, $T_w = 14.19s$) [80].

As it can be seen no parametric rolling occurred because of change of frequency of encounter conditions relative to roll natural frequency and the initial disturbance died out in time. The corresponding numerical results are provided in Fig. 5.9.

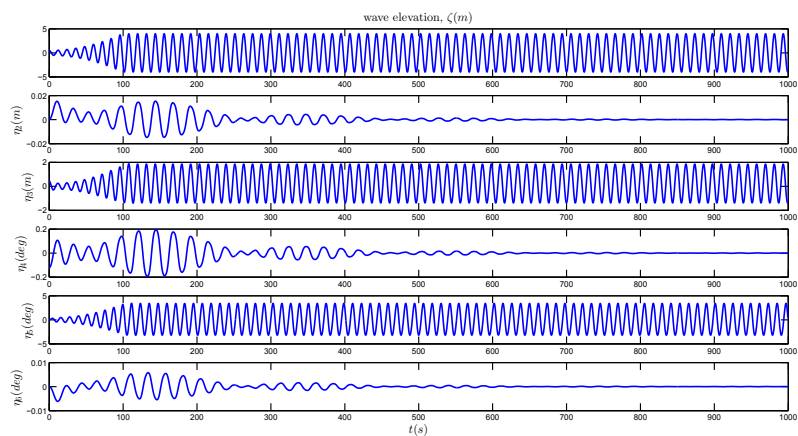


Figure 5.9: Development of parametric rolling in numerical simulations in regular waves (Head sea, $\zeta_a = 4m$, $U = 8kn$, $T_w = 14.19s$) [80].

Consistently with the experiments, also in this case there is no parametric resonance in roll. There are some other scenarios in the experiments and numerical simulations and the overall results can be seen in the Tab. 5.2.

Table 5.2: Occurrence of parametric roll (PR) in terms of roll amplitude from experiments in [80] and present method in head-sea regular waves.

Test No.	λ/L_{pp}	$\zeta_a(m)$	$T_w(s)$	$U(knots)$	$\eta_{4a}(^\circ)exp$	$\eta_{4a}(^\circ)sim$
5	0.8	3	11.59	8.0	31.0	38.5
6	1	3	12.95	8.0	23.2	21.3
7	1.2	3	14.19	8.0	2.0	No PR
8	1.4	3	15.33	8.0	0.5	No PR
9	0.8	4	11.59	8.0	32.8	40
10	1	4	12.95	8.0	25.0	21.3
11	1.2	4	14.19	8.0	1.7	No PR
12	1.4	4	15.33	8.0	0.8	No PR
13	0.8	5	11.59	8.0	35.7	40.5
14	1	5	12.95	8.0	27.3	20.4
15	1.2	5	14.19	8.0	1.3	No PR
16	1.4	5	15.33	8.0	0.6	No PR

The simulation results for the occurrence of parametric roll and for the values of steady-state roll amplitude are in good agreement with the experimental data. For the conditions in which the parametric rolling occurred the roll maximum amplitude is almost the same in experiments and simulations. As it can be seen in the experiments, for $T_w = 11.59$ and $12.95s$ the roll amplitude increases by increasing wave amplitude. For $T_w = 11.59s$ it goes from 31° for $\zeta_a = 3m$ to 32° for $\zeta_a = 4m$ and 35.7° for $\zeta_a = 5m$. This last value represents the largest amplitude observed in the head-sea tests. In six scenarios, there is no parametric resonance both in the model tests and in the simulations. More in detail, this occurs in tests with $T_w = 14.19$ and $15.33s$ ($\omega_{4n}/\omega_e = 0.526$ and 0.575) at all incident-wave steepnesses examined. The most severe cases did not occur for $\lambda/L_{pp} = 1$ but for 0.8 and the maximum roll amplitude for $\zeta_a = 5m$ reached 35.7° in experiments and 40.5° in simulations. These values are very high and dangerous for ships. Fig. 5.10 examines the initial transient phase leading to the build-up of the parametric resonance from one experimental case and the corresponding numerical simulation. The roll time history is synchronized with the evolution of the incident-wave elevation.

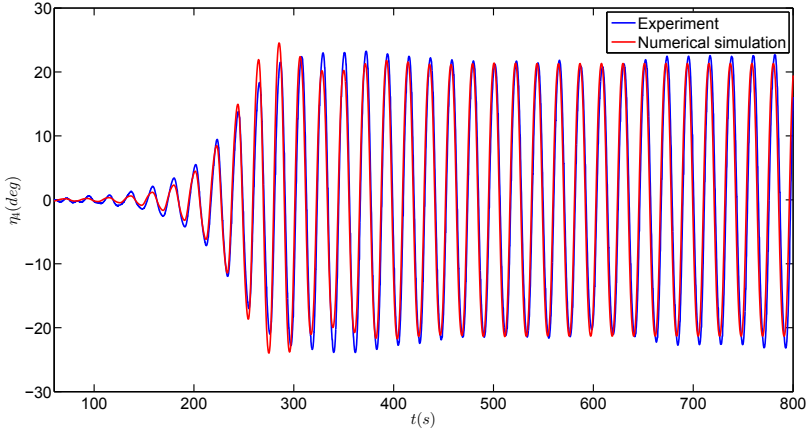


Figure 5.10: Comparison of development of parametric rolling in experiments [80] and numerical simulations in regular waves (Head sea, $\zeta_a = 3m$, $U = 8kn$, $T_w = 12.95s$).

There is good agreement between the two results. The differences could be due to a non-perfectly regular behavior of the incident waves in the experiments. However, we have no possibilities to assess experimental error sources.

As it was told before, one of the objective of this model is to identify dangerous zones for parametric rolling by producing polar diagrams. Due to the time limit, the solver was not developed for solving the ship motions in irregular waves. By developing that part of the solver, one can reproduce polar diagrams for different sea states. Those diagrams would be of high importance and value for the ship masters in order to avoid the dangerous zones in terms of the parametric rolling. Here the polar diagrams for regular waves for selected wave periods and wave amplitudes are shown in the Figs. 5.11 to 5.13.

In the polar diagrams, the radial coordinate is the ship speed in knots, and the angular coordinate is the wave heading. 180° corresponds to the head sea waves. The toolbar on the right of the figures represents the steady-state roll amplitude in degrees. The heading intervals are considered as 15° and the interval in speed is $2knots$. For each polar diagram 117 simulations were performed for a time duration of $2000s$. With these polar diagrams one can identify which speed and heading combinations, within the chosen values, can be dangerous regarding parametric rolling.

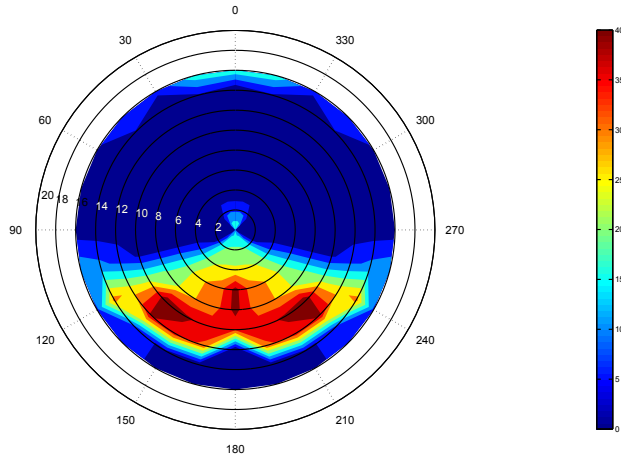


Figure 5.11: Numerical polar plot for roll (degree) in regular waves versus heading and forward speed in knots ($GM = 1.97m$, $\zeta_a = 3m$, $T_w = 11.59s$).

The first polar plot is in Fig. 5.11 and is for $\zeta_a = 3m$ and $T_w = 11.59s$. As it can be seen, we have a weak amplification at head sea (180° heading) with no forward speed but it becomes higher with increasing forward speed, it will have the maximum amplification at around $8knots$ and starts to reduce after that vanishing at around $12knots$. In bow sea, the maximum roll amplitude occurs in a forward speed between 10 and $12knots$ and vanishes at around $14knots$. In beam sea there is no parametric rolling observed. In following sea we have small amplification at zero forward speed, then it vanishes at around $2knots$ and it seems it starts again at $16knots$. The next polar diagram in Fig. 5.12 is for the same wave period but with amplitude of $4m$.

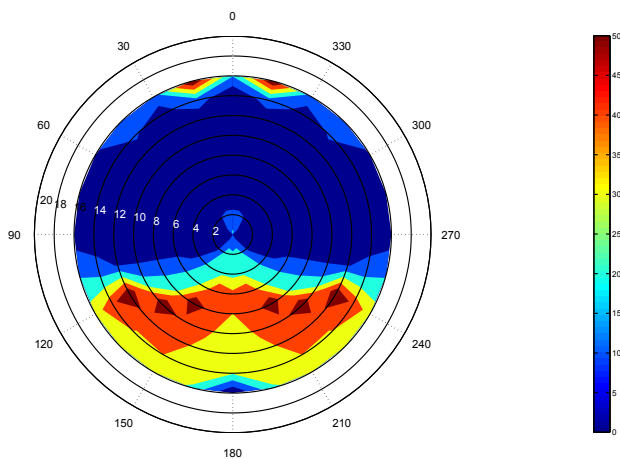


Figure 5.12: Numerical polar plot for roll (degree) in regular waves versus heading and forward speed in knots ($GM = 1.97m$, $\zeta_a = 4m$, $T_w = 11.59s$).

As it can be seen, by increasing the wave amplitude, the danger zone in head sea widens and the speed at which the parametric rolling vanishes increases. The parametric rolling zone in following sea seems also to start at lower speeds. We can also see some danger zones at heading of 15° in speed of $16knots$ while we do not see a very high danger in the same area for wave amplitude of $3m$. The highest roll amplitude observed is also greater in the larger wave-amplitude case and so the capsizing risk is higher.

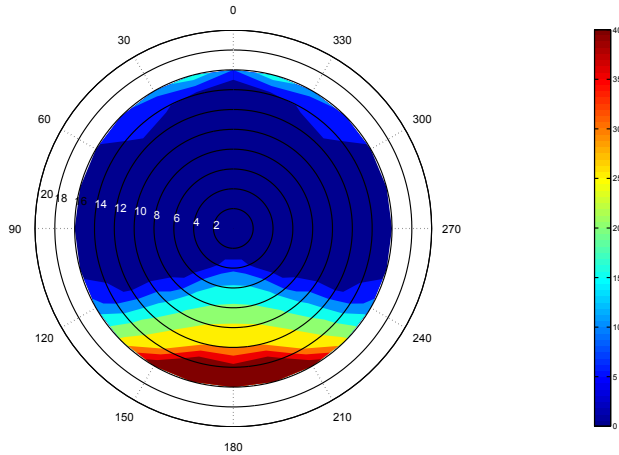


Figure 5.13: Numerical polar plot for roll (degree) in regular waves versus heading and forward speed in knots ($GM = 1.97m$, $\zeta_a = 3m$, $T_w = 12.95s$).

The last polar diagram is shown in Fig. 5.13 for a higher wave period than in the previous two figures. We see that at zero forward speed there is no parametric rolling in any heading while we observed some small amplification for shorter incident-wave period. The situation in following sea with higher speeds is almost the same in the two cases. In head sea, it is clear that the strong amplification starts at higher speeds than in figure 5.11. For instance, at speed of $10knots$ the roll amplitude is around 35 degrees for $T_w = 11.59s$ while in the same condition the amplitude is around 25 degrees for $T_w = 12.95s$. From these polar plots, there are more dangerous zones in head and bow sea than in following and beam sea, at least in the studied situations and in the operational conditions. The ship masters should avoid these situations by ship handling tactics based on forward speed and heading or a combination of them. As it can be seen from the results, reducing the forward speed not always brings the ship out of parametric rolling area and sometimes increasing the speed might be more useful in this regard. The damping plays an important role in the occurrence of parametric roll. Here the basic damping is calculated at the encounter frequency due to the fact that in this numerical analysis we do not use a convolution integral formulation. The quadratic viscous damping is small relative to the wave radiation damping. For example, the total damping ratio at roll amplitude of 20 degrees for $T_w = 12.95s$, head sea and $U = 8kn$ is around 8% and for $T_w = 11.59s$ is around 9.6%. Unluckily free-decay tests are not available

from the experiments in [80] to assess the roll damping used in our simulations. Therefore, a sensitivity analysis has been performed on the influence of damping on the parametric roll. We added a linear damping as a fraction of critical damping to the system to find the threshold damping that can prevent parametric resonance. The results are shown in Fig. 5.14.

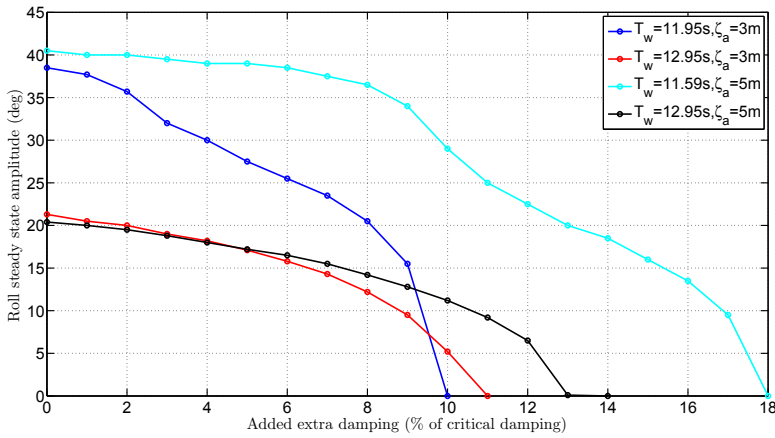


Figure 5.14: The effect of added damping on parametric roll occurrence and roll amplitude for Head sea waves and $U = 8$ knots.

It is clear that the needed damping for higher wave amplitude is larger. For the studied incident waves, with additional damping between 10% and 18% of the critical damping we can avoid parametric resonance in roll. These results suggest that the use of other damping devices (like bilge keels or anti-roll tank) might avoid the parametric roll. We also did a sensitivity test on the effect of freeboard on parametric roll. By increasing and decreasing the freeboard by 5%, we did not see much difference in rolling amplitude. In fact the difference was less than 1° .

A set of experiments ([80]) were also done for $GM = 0.99m$ in following sea waves and without forward speed. The results from the model tests and the simulations are shown in Tab. 5.3.

Table 5.3: Occurrence of parametric roll (PR) in terms of roll amplitude from experiments in [80] and present method in following-sea regular waves and $GM = 0.99m$

Test No.	λ/L_{pp}	$\zeta_a(m)$	$T_w(s)$	$U(knots)$	$\eta_{4a}(^\circ)exp$	$\eta_{4a}(^\circ)sim$
309	0.8	3	11.59	0.0	35.79	Cap
310	1	3	12.95	0.0	35.79	Cap
311	1.2	3	14.19	0.0	31.53	29.6
312	1.4	3	15.33	0.0	25.96	22.5
313	0.8	4	11.59	0.0	35.74	Cap
314	1	4	12.95	0.0	38.20	Cap
315	1.2	4	14.19	0.0	34.07	Cap
316	1.4	4	15.33	0.0	26.35	24.5

Here, Cap means capsizing. From the comparison, the numerical predictions are a bit conservative in terms of roll amplitude. In three conditions, the agreement is good but in other conditions, which lead to high roll amplitudes, the simulation shows capsizing while the experiments did not record such critical event. A possible experimental error source is wave reflection from tank walls, which is more important in zero forward speed cases.

5.3 Conclusion

The solver has been validated against model experiments in regular incident waves on a post-Panamax C11 class container ship, without bilge keels and without anti-roll tank. The results showed good agreement with a tendency of the developed solver to give conservative results in some examined scenarios. The conditions for parametric-roll occurrence, in terms of incident-wave frequency and amplitude and ship speed, as well as the experienced roll amplitudes are almost the same in experiments and simulations. Furthermore, we speculated about the influence of wave reflection from tank walls at zero forward speed in following waves. A sensitivity study on the influence of the roll damping and the free-board on the parametric roll was performed numerically. By adding damping in the range between 10% to 18% of the critical damping, we could avoid parametric resonance in roll for the examined incident waves. For the studied cases, the free-board seems to have a small effect on parametric rolling. The proposed numerical tool could be used to obtain critical conditions in regard of parametric rolling. Therefore, it could be the starting point to design dedicated model tests or more

complex numerical investigations.

Besides, it could also be used for producing polar diagrams, which show dangerous combinations of wave heading, wave amplitude and ship speed in regular waves in regard of parametric rolling. The seakeeping analysis of the ships in the real sea states should be modelled by solvers in irregular waves. Using these solvers, one can produce polar diagrams in which the dangerous combination of ship speed and heading in different sea states in terms of parametric rolling could be shown. Such diagrams are highly valuable for ship-masters aboard ships to avoid such dangerous instability zones. Using those diagrams, enables them to be aware of the risk of parametric rolling and helps them to take the precautionary actions. Due to the time limits, we did not develop our solver further to solve the ship motions in the irregular seas and instead we provided selected polar diagram in regular waves.

Chapter 6

Experiments and numerical simulations on a fishing vessel in cases without anti-roll tank

In this chapter we investigate the parametric rolling of the fishing vessel introduced in chapter 4. The typical fishing vessels are blunt bodies with low length to beam ratio and this is also true for the examined ship model. This invalids the basic strip-theory assumption that the vessel is slender. So, numerically, we developed a 3D solver for this part as explained in chapter 2. Experimentally, three sets of model tests have been performed before installation of an anti-roll tank. The tests have been performed in CNR-INSEAN basin No. 2 (Rome, Italy), during June and July 2014 and January and February 2015. The basin dimensions, the experimental set up and the ship model were described in detail in chapter 4. First set of experiments was performed at Froude number $F_n=0$ and the second and third round of tests were carried out at $F_n=0.09$ and $F_n=0.18$. In order to limit the mean horizontal motions (mean surge, sway and yaw) of the model, a mooring system of four elastic cables in a symmetrical configuration with respect to the longitudinal hull axis (V-shaped configuration) was placed at the water-plane level and fixed to the carriage. The detailed description of this mooring system, as used in the experiments and as modelled numerically, is provided in chapters 4 and 3, respectively. The tests were performed in regular waves generated in the basin in the vicinity of parametric resonance instability area. These three sets of tests are described

and compared against numerical simulation in this chapter. All six modes of motions for test cases are compared and presented in this chapter. The six modes of motions are shown in each figure and since a long simulation time is presented, the visibility for comparing the motions became limited in some cases. Therefore, a higher visibility for comparison are provided in appendix C.

6.1 Cases at $\text{Fn}=0$

As we know, the parametric resonance can occur when the natural roll frequency (ω_{n4}) is half of the incident wave frequency. So these tests were performed varying the frequency ratio $\frac{\omega_{n4}}{\omega_e}$ from 0.46 to 0.54. The other condition for occurrence of parametric rolling is that the wave height should be high enough. So a wave steepness $k\zeta_a$ range of 0.1 to 0.25 was considered.

6.1.1 Cable identification and wave characteristics

The experiments performed at $\text{Fn}=0$ are shown in Tab. 6.1.

Table 6.1: The test cases at $\text{Fn}=0$. A cell with symbol X indicates that the corresponding test was not performed.

$k\zeta_a \downarrow, \frac{\omega_{n4}}{\omega_e} \rightarrow$	0.46	0.47	0.48	0.49	0.50	0.51	0.52	0.53	0.54
0.1	X	X	C459	C479	C457	C501	C468	C480	X
0.15	X	C464	C463	C462	C461	C460	C469	C481	C482
0.20	C473	C472	C471	C470	C466	C465	C474	C484	C499
0.25	C493	C490	C483	C491	C492	C495	C496	C497	C500

For starting the numerical simulations, we have to do the cable identifications for the four cables. In the experiments, four transducers measured the cables tensions in time. By knowing these tensions, the positions of cables attachments to the model and the vessel rigid motions in time we can plot the graph of cables tension $T(N)$ versus cables length variation $\Delta L(m)$ and extract the cable identifications. This is important for the numerical model of the cables, performed as explained in chapter 3. Before each set of experiments, free-decay tests in calm water were performed for having the cable configuration exactly before the tests. For the cases mentioned

in Tab. 6.1, three sets of decay tests in calm water were performed. For instance, the surge decay tests of C451, C476 and C486 were performed and used for cable identifications. Here we show and explain the surge decay test C451. The time series of the ship-model motions are shown in Fig. 6.1. As it can be seen from this graph, all the motions except surge, are small. However, in the process of extracting the cables identifications, all motions are considered in the cables length variation calculations.

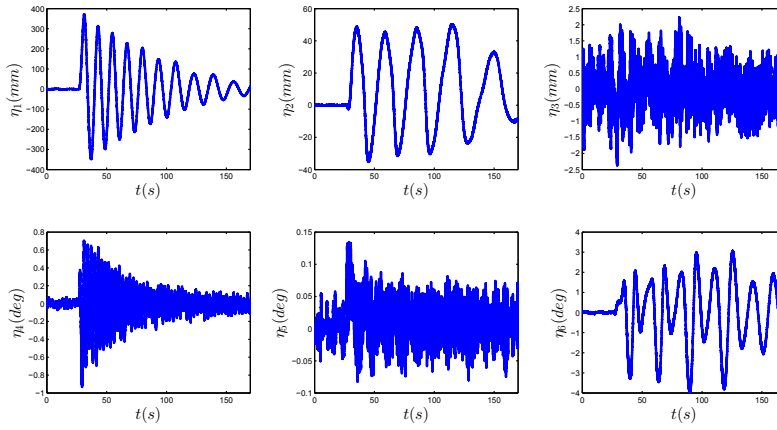


Figure 6.1: 6-DOF fishing-vessel motions in time for surge decay test C451.

The cables length variation in time and also the cables tension in time are shown in Figs. 6.2 and 6.3.

As it can be seen from Fig. 6.3, all the cables have a pretension. Now if we remove the pretension and just plot the cable tension against cable length variation, we can extract the cables identifications. This is given in Fig. 6.4

The pretension value for the cable aft and port side is negative, which is non-physical. It seems that the transducer in that cable had a problem in the experiments. So we can not trust the value from that sensor. To cover this information lack, we assumed a perfect left-right symmetry of the cables. Therefore, from now on we just consider the cables of the starboard side and use the same for those in the port side. By considering these cables and fitting some fourth order curves, we obtain the cable identifications. The main model-test points and the related identification are shown in Fig. 6.5.

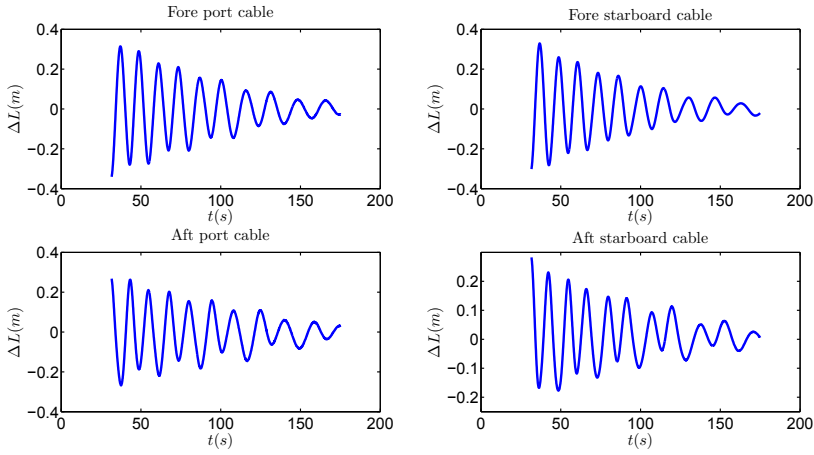


Figure 6.2: Cables length variation in time for surge decay test C451.

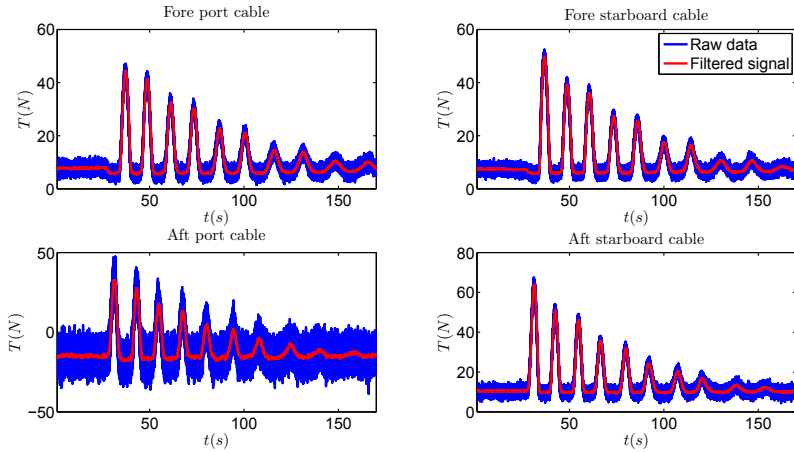


Figure 6.3: Cables tension in time for surge decay test C451.

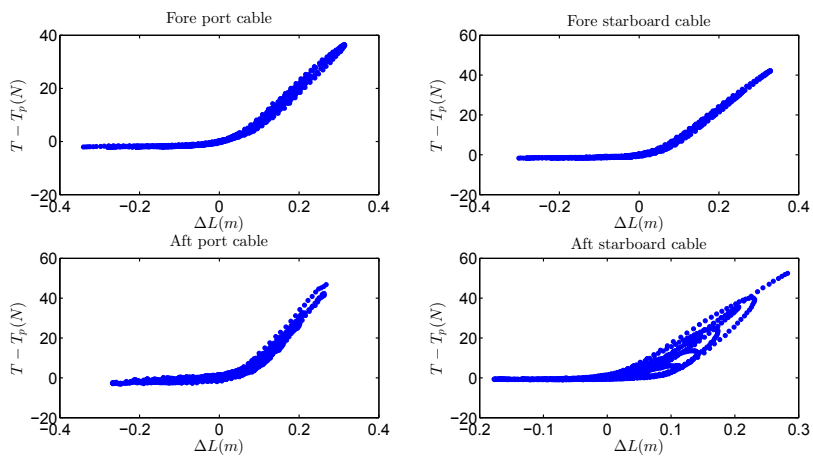


Figure 6.4: Cables tension versus length variation for surge decay test C451.

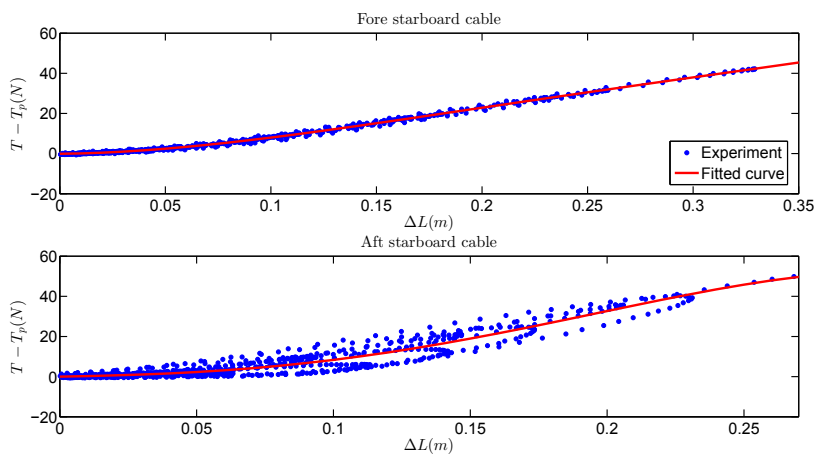


Figure 6.5: Cables tension versus length variation and related identification for surge decay test C451.

For instance, the tension law used for the fore cables of case C451 is as follows:

$$T-T_0 = \begin{cases} 10.994\Delta l + 940.575\Delta l^2 - 2567.357\Delta l^3 + 2404.848\Delta l^4; \Delta l_0 < \Delta l < \Delta l_1 \\ T_{min}; \Delta l < \Delta l_0 \end{cases} \quad (6.1)$$

where $T_0 = 5.3732N$ is the pretension and $T_{min} = 0$ as explained in Fig. 3.19, $\Delta l_0 = 0$ and $\Delta l_1 = 0.25m$. Moreover, the tension law for $\Delta l > \Delta l_1$ is a linear fit to the curve at Δl_1 .

The tension law for the aft cables is as follows:

$$T-T_0 = \begin{cases} 52.916\Delta l - 490.090\Delta l^2 + 10833.444\Delta l^3 - 27828.920\Delta l^4; \Delta l_0 < \Delta l < \Delta l_1 \\ T_{min}; \Delta l < \Delta l_0 \end{cases} \quad (6.2)$$

where $T_0 = 10.4487N$, $T_{min} = 0$, $\Delta l_0 = 0$ and $\Delta l_1 = 0.15m$ and the tension law for $\Delta l > \Delta l_1$ is a linear fit to the curve at Δl_1 .

Now we have the cables and we can start doing the numerical simulations for surge decay C451 case and compare them to the experiments. The results are given in Fig. 6.6.

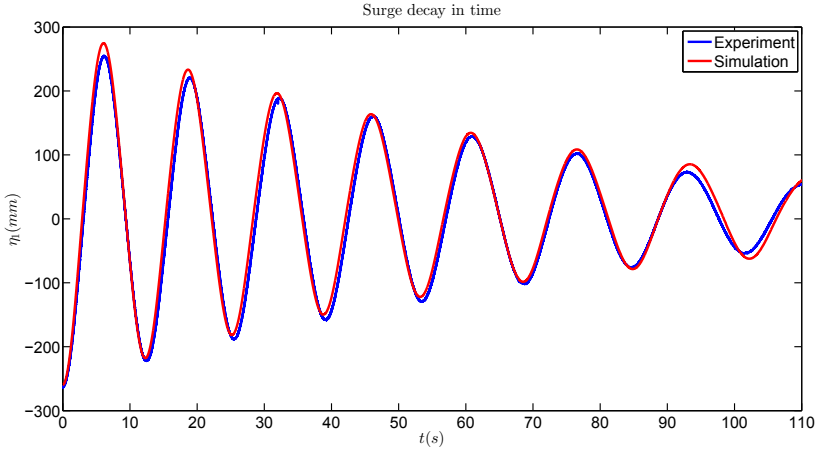


Figure 6.6: Comparison of numerical and experimental results for C451 surge decay test.

This figure shows a good agreement between numerical and experimental result in surge decay, which shows that the cables have been modelled in a satisfactory way.

The other parameters extracted from the experiments, are the viscous damping coefficients. The following viscous damping coefficients (extracted from the decay tests) were used to get the similar damping level in numerical simulations as in experiments. In all simulations of motions of this fishing vessel, the viscous damping is extracted from the surge decay tests. The obtained linear (visc,lin) and quadratic (visc,non-lin) viscous damping coefficients in model scale are as follows:

$$B_{11}^{visc,lin} = 20.92 \text{ Ns/m}, \quad B_{11}^{visc,non-lin} = 0.0 \quad (6.3)$$

$$B_{22}^{visc,lin} = 39.14 \text{ Ns/m}, \quad B_{22}^{visc,non-lin} = 0.0 \quad (6.4)$$

$$B_{44}^{visc,lin} = 1.2344 \text{ Nms}, \quad B_{44}^{visc,non-lin} = 10.1206 \text{ Nms}^2 \quad (6.5)$$

$$B_{66}^{visc,lin} = 65.0383 \text{ Nms}, \quad B_{66}^{visc,non-lin} = 0.0 \quad (6.6)$$

Now we can compare the simulations in roll decay test and check if the numerical model of the roll damping is correct. The comparison is documented in Fig. 6.7.

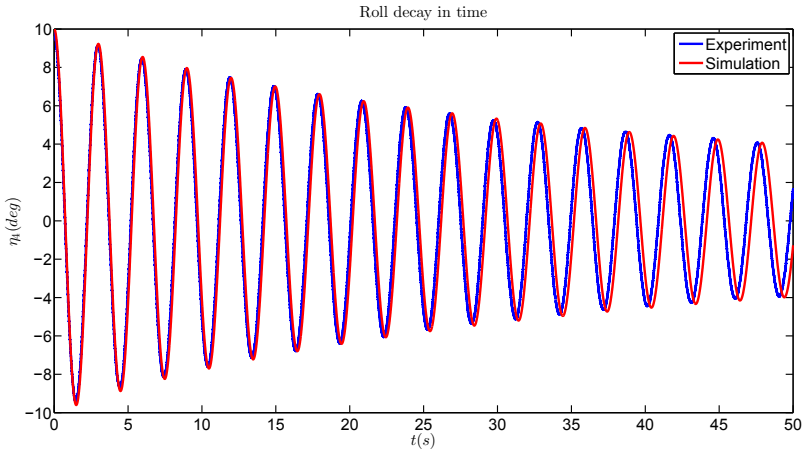


Figure 6.7: Comparison of numerical and experimental results for C450 roll decay test.

This figure also shows that the roll damping level in the numerical simulation is in agreement with the experimental value. Unfortunately the sway and yaw decay tests could not be reproduced in the numerical simulations. One reason could be the fact that we do not have the exact data for all four cables from the experiments. Alternatively, we also implemented a linear sway and yaw restoring in the numerical model while the cable forces are used for the other modes of motions. The results for these two methods are shown in Figs. 6.8 and 6.9.

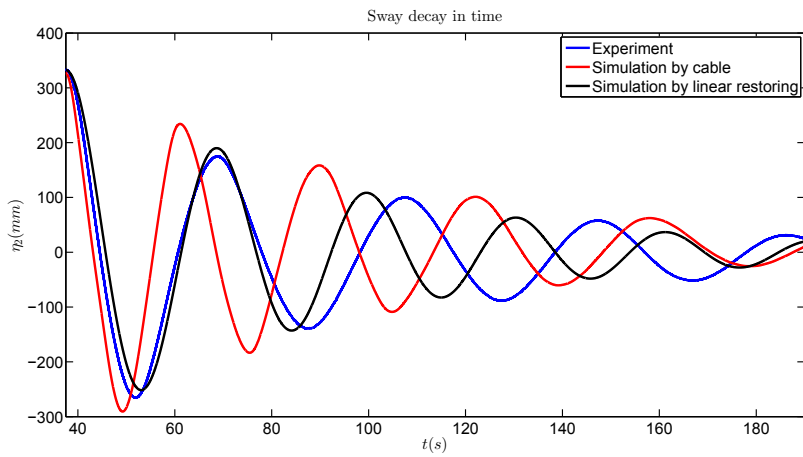


Figure 6.8: Comparison of numerical and experimental results for sway decay test.

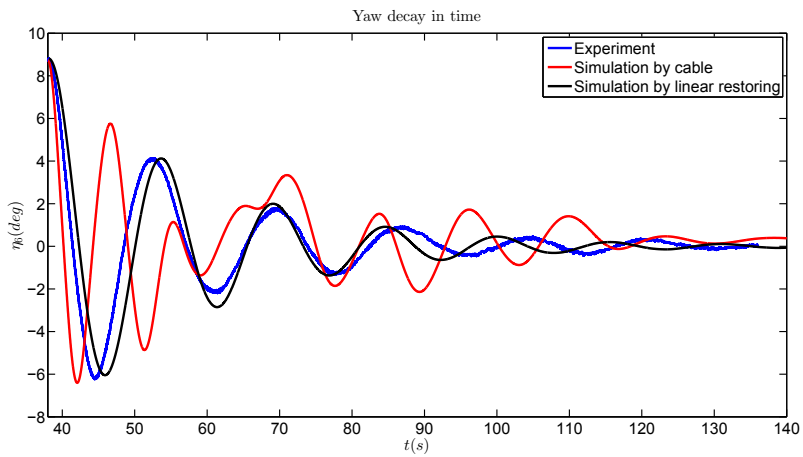


Figure 6.9: Comparison of numerical and experimental results for Yaw decay test.

As it can be seen from these two figures, even using the linear restoring loads could not reproduce the experimental decay tests. Besides, we did the final simulations based on these two methods and it showed that the final results in terms of occurrence of parametric rolling and the steady state value in case of occurrence do not change. So from now on, we will use the extracted cables for all numerical simulations for all the test cases in waves.

Since the prescribed incident waves and the actual waves generated in the basin might be a bit different due to experimental errors, we performed FFT (Fast Fourier Transform) of the actual incident waves in the experiments and use only the first component to identify the wave period and wave amplitude for the numerical simulations. We should note that we must do the FFT for large enough number of periods (we used 10 periods) and also use some parts of the waves after the transient parts and before any important ship motion starts, to ensure nearly steady-state conditions with limited wave reflection effects. Fig. 6.10 shows a sample result of this FFT procedure for test case C457.

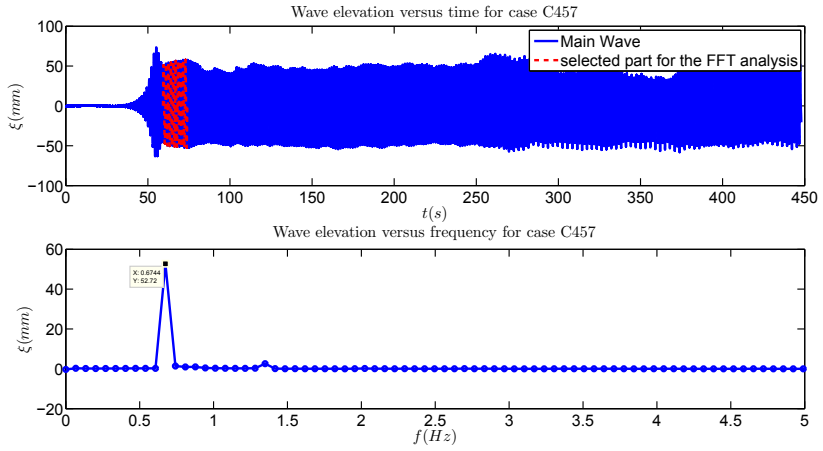


Figure 6.10: Wave elevation in time for C457 test and the FFT analysis of its selected part.

The top subplot shows the wave elevation in time. The selected part for the FFT is also marked with red color. The results of the FFT for the selected part are shown in the bottom subplot.

6.1.2 Numerical and experimental results

After the FFT for all mentioned test cases, and after all cables and all damping-coefficients identifications, the simulations for all cases can be performed. They are discussed in this section. First the results of FFT analysis are shown in the Tab. 6.2.

Table 6.2: Test cases at $Fn = 0$. The frequency ratio $\frac{\omega_{n4}}{\omega_e}$ and the steepness $k\zeta_a$, refer to the prescribed incident waves. In each cell, three elements are given vertically, as follows: the first label indicates the case number, the second value is the wave period in seconds and the last value is the actual incident-wave steepness. A cell with only X indicates that the corresponding test was not performed.

$k\zeta_a \downarrow, \frac{\omega_{n4}}{\omega_e} \rightarrow$	0.46	0.47	0.48	0.49	0.50	0.51	0.52	0.53	0.54	
0.1	X	X	C459 1.432 0.091	C479 1.461 0.098	C457 1.483 0.096	C501 1.518 0.094	C468 1.550 0.093	C480 1.571 0.107	X	
			C464 1.404 0.143	C463 1.432 0.143	C462 1.462 0.136	C461 1.491 0.143	C460 1.518 0.137	C469 1.553 0.131	C481 1.578 0.144	C482 1.598 0.154
0.15	X	C473 1.369 0.197	C472 1.397 0.182	C471 1.426 0.152	C470 1.450 0.198	C466 1.491 0.173	C465 1.510 0.191	C474 1.549 0.188	C484 1.582 0.182	C499 1.595 0.190
		C493 1.387 0.207	C490 1.406 0.214	C483 1.431 0.230	C491 1.465 0.216	C492 1.480 0.229	C495 1.509 0.227	C496 1.538 0.216	C497 1.555 0.241	C500 1.587 0.221

Tab. 6.3 shows the experimental and numerical results for roll-motion amplitude in nearly steady-state conditions in all studied cases.

Table 6.3: Test cases at $Fn = 0$, as given in Tab. 6.2. For each examined case, the experimental (Exp) and numerical (Num) roll-motion amplitudes in nearly steady-state conditions are given in degrees. A roll angle with a F shows that the roll steady-state value is obtained by forcing the model with a small roll angle after a while. NOF means that parametric roll did not happen even with triggering the roll motion.

$k\zeta_a \downarrow, \frac{\omega_{n4}}{\omega_e} \rightarrow$	0.46	0.47	0.48	0.49	0.50	0.51	0.52	0.53	0.54
0.10 Exp	X	X	C459 NOF	C479 21.1	C457 18.27	C501 15.24	C468 12.5	C480 NOF	X
Num	X	X	3.8	19.2	18.9	16.75	12.9	11.0	X
0.15 Exp	X	C464 NOF	C463 23.66	C462 22.2	C461 20.76	C460 17.11	C469 16.0	C481 12.5	C482 NOF
Num	X	14.0	21.8	20.5	18.9	17.4	14.5	11.8	7.7
0.20 Exp	C473 NOF	C472 19.2	C471 25.13	C470 22.52	C466 20.7	C465 17.0	C474 16.05	C484 10.5F	C499 5.0F
Num	26.9	25.0	22.4	20.7	18.25	16.0	13.0	9.9	5.3
0.25 Exp	C493 NOF	C490 20.0	C483 24.6	C491 21.4	C492 18.1	C495 15.0	C496 13.7	C497 10.0F	C500 NOF
Num	25.7	24.1	21.0	18.5	16.0	15.5	12.0	11.0	NOF

From the table, for most of the cases, the numerical and experimental results agree.

For 6 cases (C473, C493, C464, C459, C480 and C482), highlighted in grey in the table, the two results are somehow different. In the other cases the results are the same in terms of occurrence of PR and the roll amplitudes are also in an acceptable agreement. The comparison of two cases is shown below and then the reason of differences for the 6 highlighted cases is discussed.

The numerical and experimental incident waves and corresponding results of vessel motions for the case C457 are shown in Figs. 6.11. From the figure, the results are in a good agreement in all modes except in sway and yaw. The numerical and experimental cable tensions for case C457 are shown in Fig. 6.12, showing similar behaviours and values. In general, in the examined head-sea waves, the surge motion is characterized by an important negative mean value leading to a drift of the vessel toward the stern. As a result, the fore cables are tensioned and show an oscillatory behaviour, while those in the aft of the vessel experience only the pretension. The experimental cable tensions have a high frequency and quite high amplitude

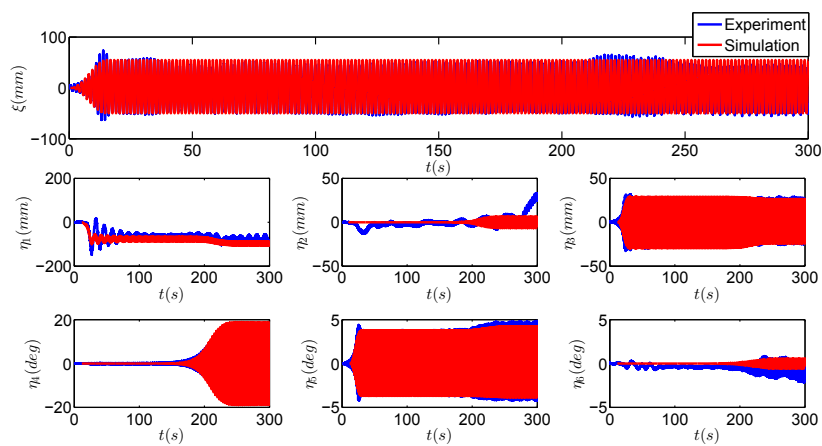


Figure 6.11: Comparison of experimental and numerical incident waves and model motions in all six degrees of freedom for case C457.

noise though.

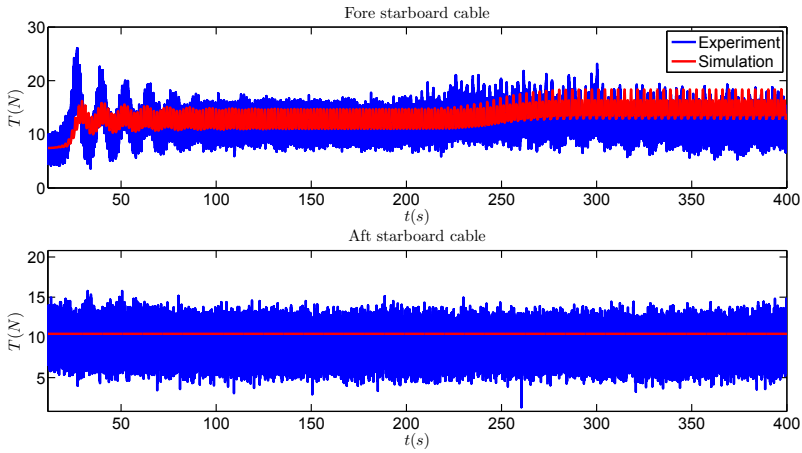


Figure 6.12: Comparison of experimental and numerical values for mooring cables tensions in case C457.

The motions in sway and yaw are a bit different, and it might be due to the fact that we use exactly symmetric cables for port and starboard while it is not like that in the experiments. Besides, the reflection of waves from the tank walls in the experiments might be important. Although, one should note that both of these motions are quite small when compared to other modes of motions. The transient phase of surge motions is also a bit different in experiment and numerical simulations, which is consistent with the differences observed in Fig. 6.12 for the fore cable tensions.

The comparison between numerical and experimental values for vessel motions and cable forces for case C483 is shown in Figs. 6.13 and 6.14. The agreement between the two results is satisfactory. It should be borne in mind that the important parameter in the PR analysis is its occurrence and steady-state roll amplitude. In a practical case, the build-up phase of the roll motion would also matter to characterize the time scale for PR to reach critical roll angles. However, in the experiments, this build-up phase is much affected by the used set up. In the experiments, the cables configuration and also other asymmetric effects could trigger the PR while in the numerical simulation, the cables are exactly symmetric and there are not the same disturbances as in the experimental set-up.

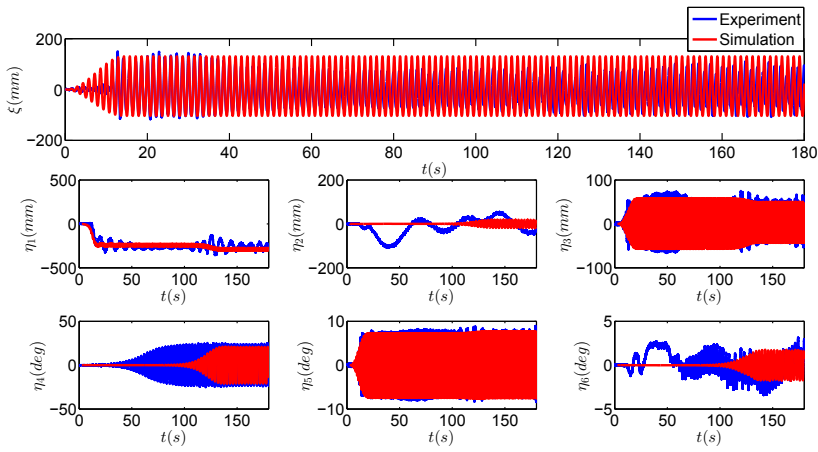


Figure 6.13: Comparison of experimental and numerical incident waves and model motions in all six degrees of freedom for case C483.

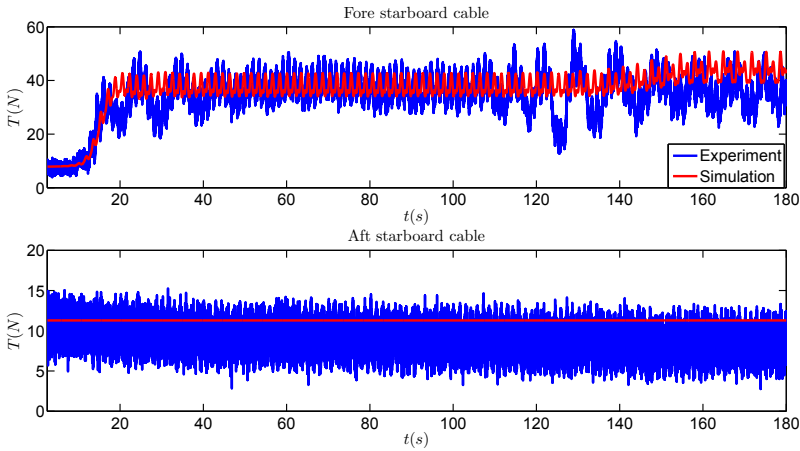


Figure 6.14: Comparison of experimental and numerical values for mooring cables tensions in case C483.

To have a better idea of the ship-instability tendency in the experimental cases, we superimpose the stability diagram from the experimental and numerical studies to the Mathieu instability diagram based on uncoupled roll equation of motion.

First we explain the uncoupled roll motion and the Mathieu equation. Let us assume a ship in head-sea regular waves. In these conditions, there is no exciting roll moment for the ship. We disregard the sway and yaw motion coupling to the roll and only consider the indirect effect of the incident waves and of heave and pitch motions on the transverse metacentric height (similarly as shown in Fig. 1.6), leading to time changes in the roll restoring coefficient, i.e.:

$$C_{44}(t) = \rho g \nabla (\overline{GM}_m + \delta \overline{GM} \sin(\omega_e t + \beta)). \quad (6.7)$$

Here ρ is the water density, g is the gravity acceleration, ∇ is the ship displacement, \overline{GM}_m is the metacentric height mean value and $\delta \overline{GM}$ is the amplitude of metacentric-height change induced by incident waves, and heave and pitch motions. ω_e is the encounter frequency and β is the phase of the metacentric-height variation relative to the incident waves. Under these assumptions, we can write the roll equation of motion as follows [82]:

$$(I_{44} + A_{44}) \ddot{\eta}_4 + B_{44} \dot{\eta}_4 + \rho g \nabla (\overline{GM}_m + \delta \overline{GM} \sin(\omega_e t + \beta)) \eta_4 = 0 \quad (6.8)$$

Here I_{44} is roll moment of inertia, A_{44} is the roll added mass and B_{44} is the linear roll damping. Eq. 6.8 is an approximated roll-motion equation because sway and yaw coupling are disregarded and only the linear roll damping is used. Besides, in reality, the metacentric variation is not exactly sinusoidal. Eq. 6.8 can be rewritten as:

$$\ddot{\eta}_4 + 2\xi \omega_n \dot{\eta}_4 + \omega_n^2 \left(1 + \frac{\delta \overline{GM}}{\overline{GM}_m} \sin(\omega_e t + \beta)\right) \eta_4 = 0. \quad (6.9)$$

where ω_n is the uncoupled roll natural frequency:

$$\omega_n = \sqrt{\frac{\rho g \nabla \overline{GM}_m}{I_{44} + A_{44}}} \quad (6.10)$$

ξ is the damping ratio, defined as:

$$\xi = \frac{B_{44}}{2\sqrt{(I_{44} + A_{44}) \rho g \nabla \overline{GM}_m}}. \quad (6.11)$$

In the classical Mathieu equation $\xi = 0$. This equation shows instability behaviour depending on the values of the involved incident-wave and ship parameters. It means that, a small perturbation from the equilibrium may result in strongly increased motion in time, if the system is in the instability area. The instability areas can be expressed as a function of ω_n/ω_e , $\frac{\delta GM}{GM_m}$ and the damping ratio ξ . The damped Mathieu instability diagrams for different values of $\xi\omega_n/\omega_e$ are shown in the Fig. 6.15 ([82]).

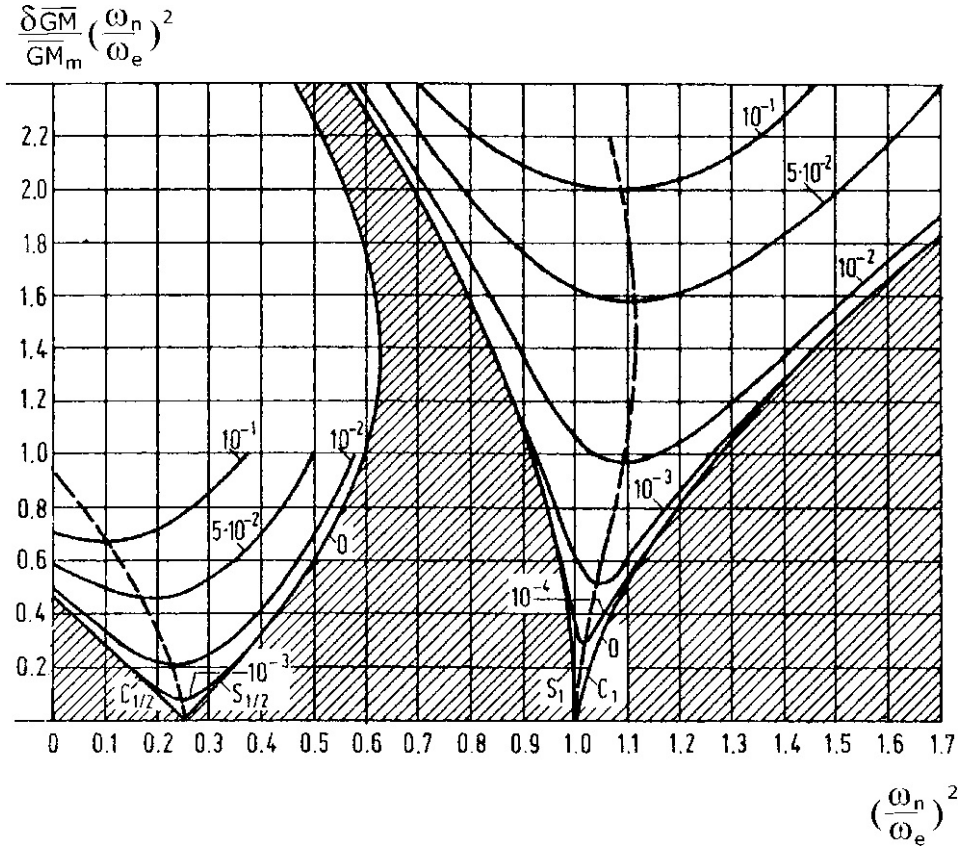


Figure 6.15: Stability diagram for the Eq. 6.9. Shaded areas represent stable domain for zero damping equation. The lines show different values of the $\xi\omega_n/\omega_e$.

Now if we calculate the metacentric-height variation in the SFH112 fishing vessel for the mentioned waves in the Tab. 6.2, then we can superimpose each experiment case as a point in the Mathieu-instability diagram. The results are shown in Fig. 6.16.

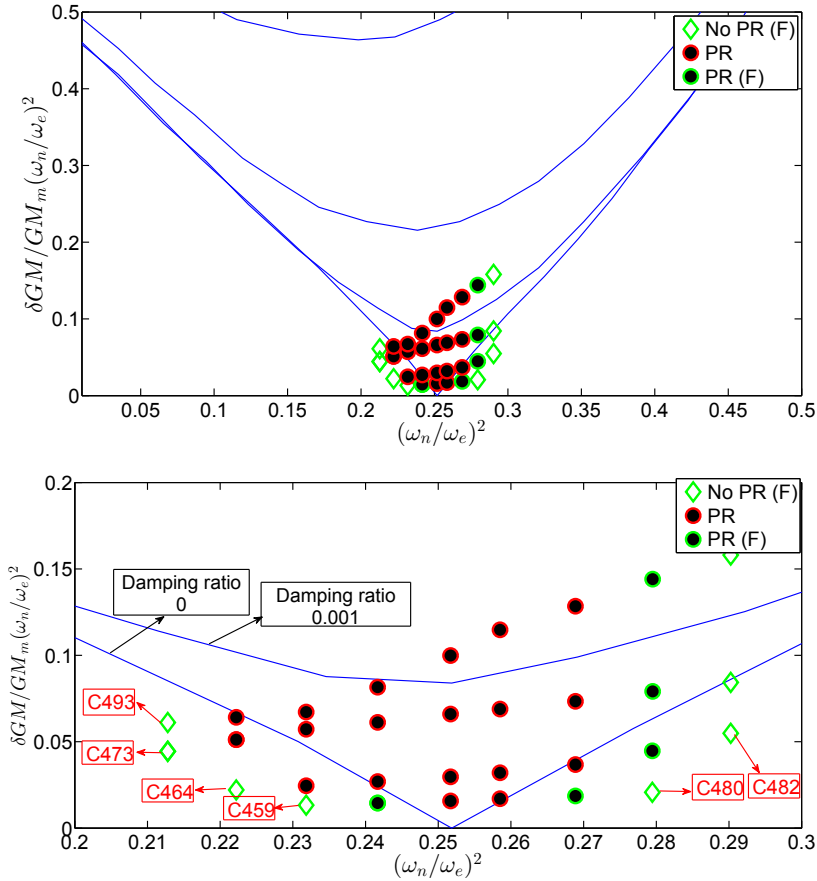


Figure 6.16: Mathieu instability diagram for uncoupled roll (solid lines) and experimental cases (symbols). Main plot (top), Enlarged view (bottom).

Symbol PR indicates cases in which parametric roll occurs. PR(F) means PR occurs but a forced roll should be introduced in the system, and No PR (F) means PR does not occur even by initiating a roll motion. The experimental damping ratio ($\xi \frac{\omega_n}{\omega_e}$) for the examined cases is between 0.0014 and 0.0016. As it can be seen here, it is obvious that the instability borders are a bit different than those in the Mathieu instability diagram, and this is because the Mathieu equation is for an uncoupled roll equation and the GM variation is considered as sinusoidal while in reality the roll motion is coupled with other modes of motion and the GM variation in time is not exactly sinusoidal. As we can see from this figure, all the test cases with differences in numerical and experimental data, are at the instability

borders. At the stability border, the stability behaviour is highly sensitive to the damping value and excitation level and other parameters. So by a smallest change in these parameters, we can go in the stability zone or get off that zone.

The comparison of roll motion for the cases with different results are shown below in Figs. 6.17 to 6.22.

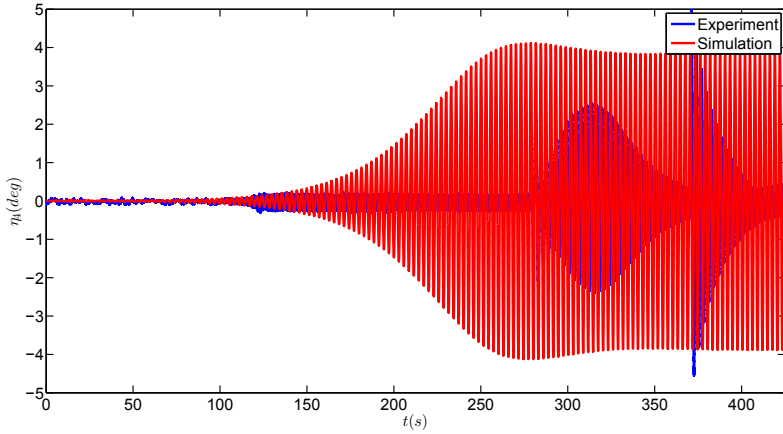


Figure 6.17: Comparison of roll motion for experiment and numerical simulation for case C459.

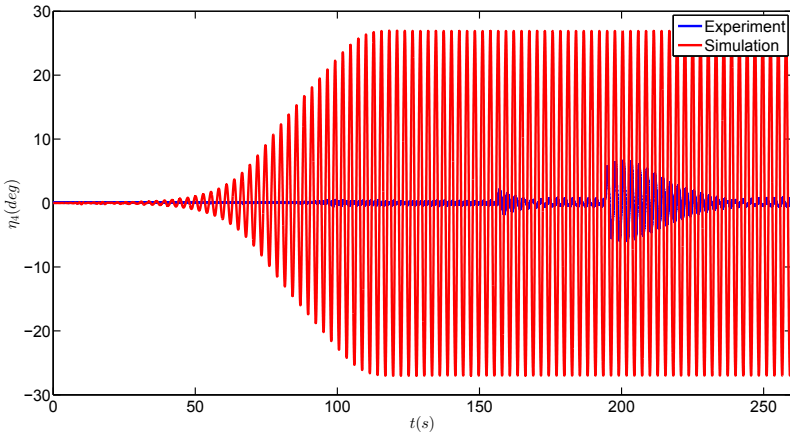


Figure 6.18: Comparison of roll motion for experiment and numerical simulation for case C473.

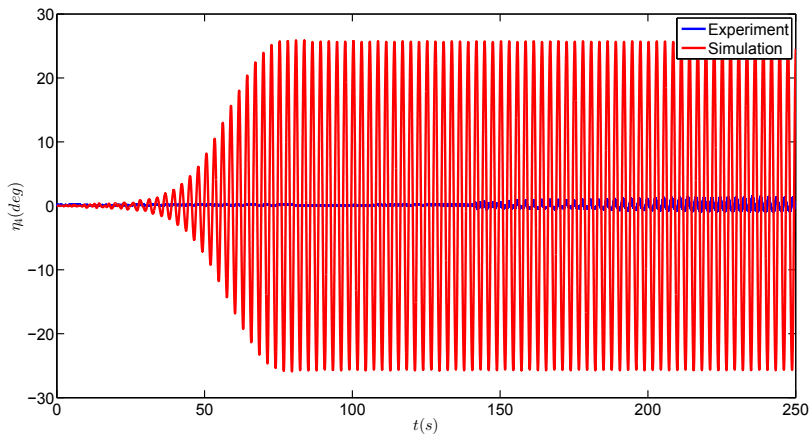


Figure 6.19: Comparison of roll motion for experiment and numerical simulation for case C493.

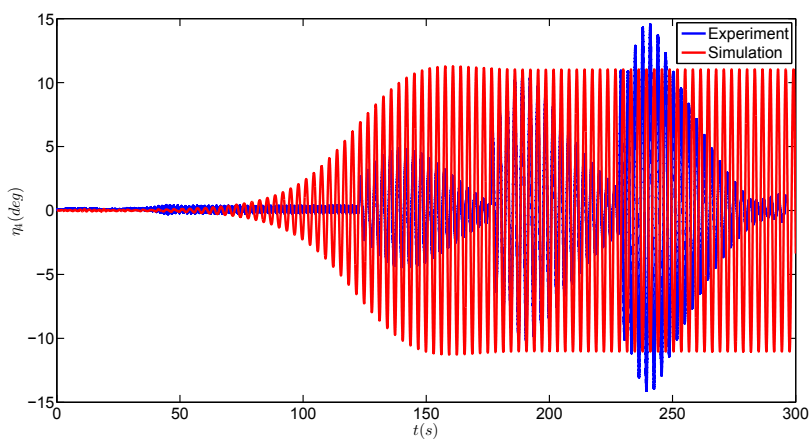


Figure 6.20: Comparison of roll motion for experiment and numerical simulation for case C480.

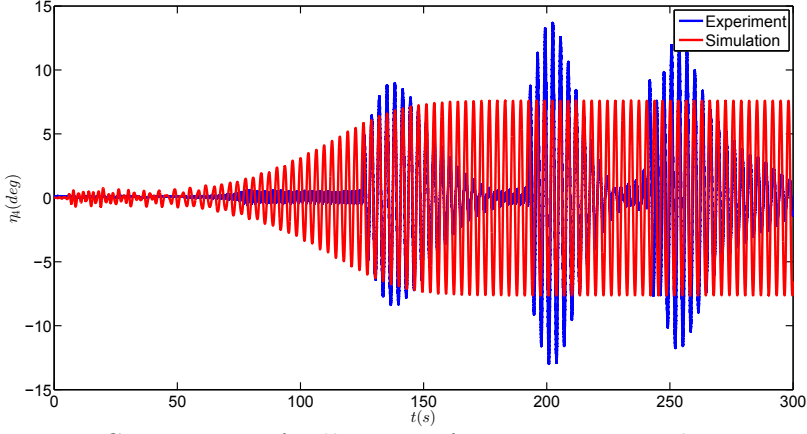


Figure 6.21: Comparison of roll motion for experiment and numerical simulation for case C482.

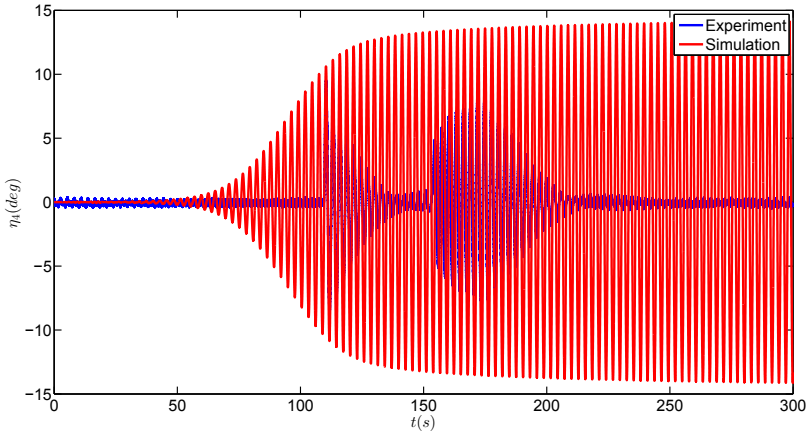


Figure 6.22: Comparison of roll motion for experiment and numerical simulation for case C464.

6.2 Cases at $\text{Fn}=0.09$

The tests for this part were performed for the frequency ratio $\frac{\omega_{n4}}{\omega_e}$ from 0.45 to 0.50 with forward speed of $U = 0.488\text{m/s}$ which corresponds to $\text{Fn} = 0.09$. The wave steepness $k\zeta_a$ varies between 0.1 to 0.25.

6.2.1 Cable identification and wave characteristics

The experiments performed at $F_n=0.09$ are shown in Tab. 6.4

Table 6.4: The test cases at $F_n=0.09$. A cell with symbol X indicates that the corresponding test was not performed.

$k\zeta_a \downarrow, \frac{\omega_{n4}}{\omega_e} \rightarrow$	0.45	0.46	0.47	0.48	0.49	0.50
0.1	X	X	C521	C538	X	X
0.15	C537	C536	C522	C533	C534	C535
0.20	X	X	X	C539	X	X

Because the different tests were performed at different times, sometimes after returning the ship model to the water after a while, the cable configuration was not exactly the same for all tests. Therefore, free-decay tests in the different degrees of freedom were performed before the tests in waves. Before starting the simulations, we need to analyse the decay tests to get the correct cable configuration. The surge decay C530 is used for the cable identification in a similar process as done in the previous section. Related experimental ship motions are shown in Fig. 6.23.

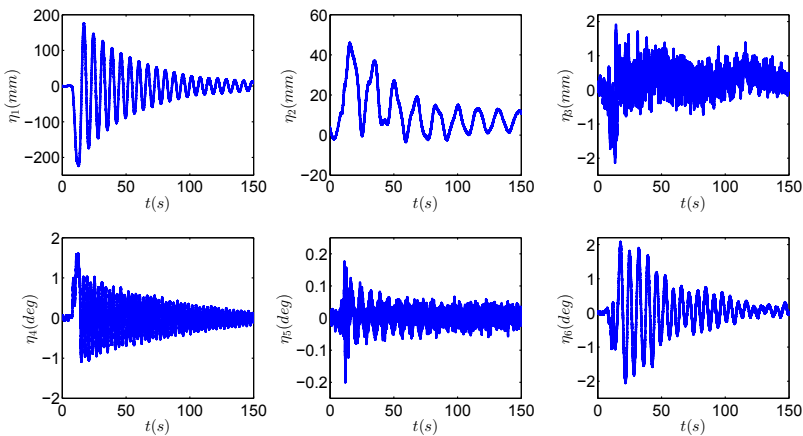


Figure 6.23: 6-DOF fishing-vessel motions in time for surge decay test C530.

The tension law identified for the fore cables of case C530 is as follows:

$$T-T_0 = \begin{cases} 151.085\Delta l + 14.3576\Delta l^2 - 330.4319\Delta l^3 + 1976.8406\Delta l^4; \Delta l_0 < \Delta l < \Delta l_1 \\ T_{min}; \Delta l < \Delta l_0 \end{cases} \quad (6.12)$$

where $T_0 = 30.8N$ is the pretension and $T_{min} = -23.8N$ as explained in Fig. 3.19, $\Delta l_0 = -0.2m$ and $\Delta l_1 = 0.2m$. Moreover, the tension law for $\Delta l > \Delta l_1$ is a linear fit to the curve at Δl_1 .

The tension law used for the aft cables is as follows:

$$T-T_0 = \begin{cases} 300.5010\Delta l - 381.2196\Delta l^2 - 4052.0581\Delta l^3 - 3814.8616\Delta l^4; \Delta l_0 < \Delta l < \Delta l_1 \\ T_{min}; \Delta l < \Delta l_0 \end{cases} \quad (6.13)$$

where $T_0 = 32.8606N$ is the pretension and $T_{min} = -23.66N$, $\Delta l_0 = -0.12m$ and $\Delta l_1 = 0.13m$. Moreover, the tension law for $\Delta l > \Delta l_1$ is a linear fit to the curve at Δl_1 .

The experimental data for the cable tensions and the related cable identifications are shown in Fig. 6.24.

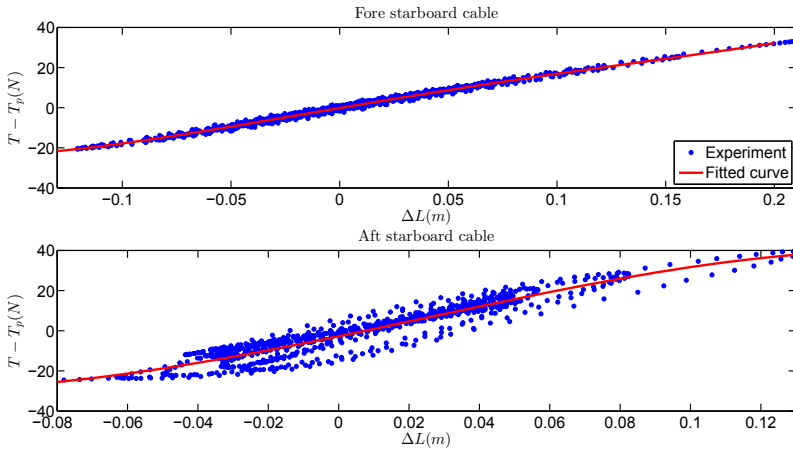


Figure 6.24: Cable identification comparison of case C530.

As it can be seen in the figure, the experimental tension data are a bit scattered for the aft cable. It might be due to a small change of cable attachment (i.e. of the cable to the carriage) in the aft part during the experiments.

The surge motion and corresponding cable tensions during surge decay C530 are given in Figs. 6.25 and 6.26, showing a global good agreement

between experiments and numerical results. Similar agreement is shown by Fig. 6.27 for the roll motion during the roll decay C529.

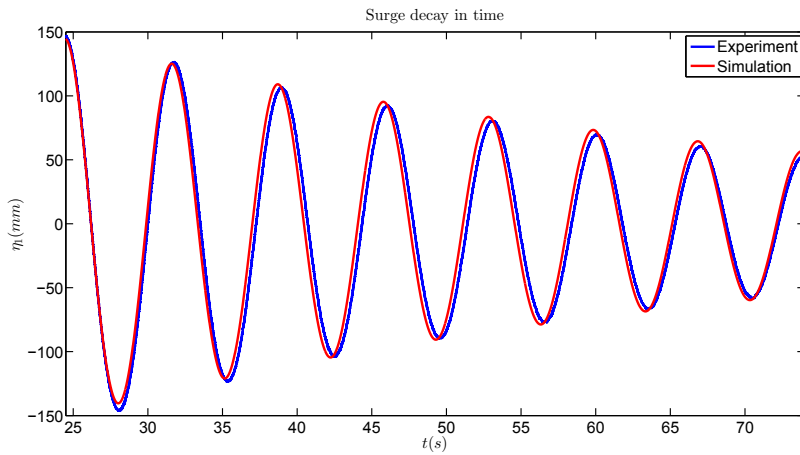


Figure 6.25: Comparison of surge decay C530.

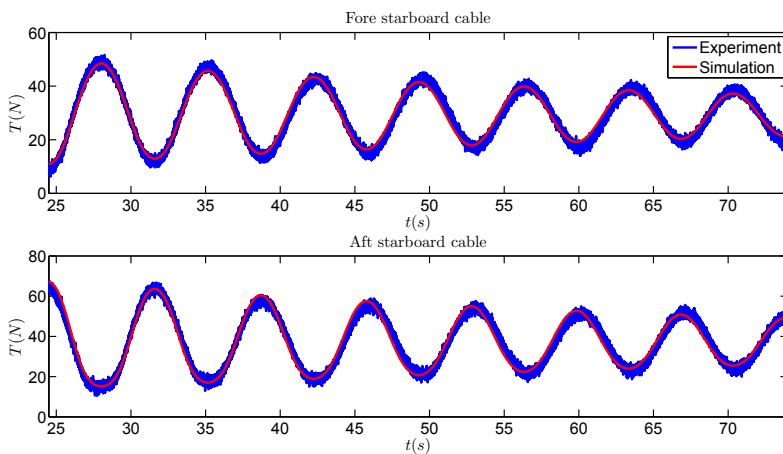


Figure 6.26: Comparison of cable tensions in surge decay C530.

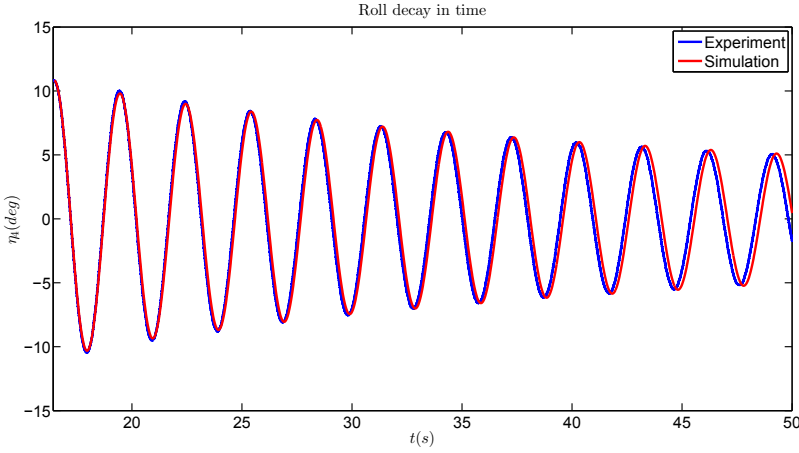


Figure 6.27: Comparison of roll decay C529.

The linear and quadratic damping coefficients used in the numerical simulations of these cases are as follows:

$$B_{11}^{visc,lin} = 25.41 \text{ N s/m}, \quad B_{11}^{visc,non-lin} = 26.1075 \text{ N s}^2/\text{m}^2 \quad (6.14)$$

$$B_{22}^{visc,lin} = 39.14 \text{ N s/m}, \quad B_{22}^{visc,non-lin} = 0.0 \quad (6.15)$$

$$B_{44}^{visc,lin} = 1.2344 \text{ N m s}, \quad B_{44}^{visc,non-lin} = 10.1206 \text{ N m s}^2 \quad (6.16)$$

$$B_{66}^{visc,lin} = 65.0383 \text{ N m s}, \quad B_{66}^{visc,non-lin} = 0.0 \quad (6.17)$$

As done for the previous cases without forward speed, the generated incident wave in the experiments have been analysed due to possible differences between nominal and generated waves. So using the same procedure as explained in the previous sections we estimated the first component from the FFT analysis of the incident wave series. A sample of this FFT analysis is shown in Fig. 6.28.

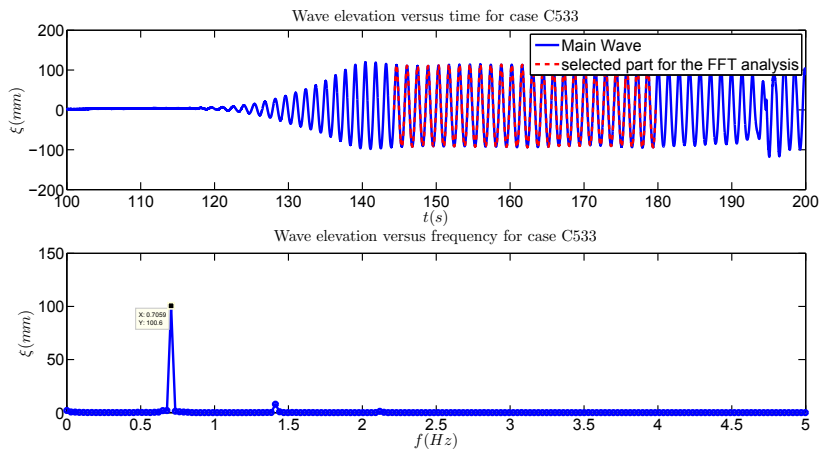


Figure 6.28: FFT analysis of incident wave for case C533.

6.2.2 Numerical and experimental results

The experimental and numerical results of all cases at $Fn=0.09$ are discussed in this section. The test cases and the wave characteristics according to the FFT analysis are shown in Tab. 6.5.

Table 6.5: Test cases at $Fn = 0.09$. The frequency ratio $\frac{\omega_{n4}}{\omega_e}$ and the steepness $k\zeta_a$ refer to the prescribed incident waves. In each cell, three elements are given vertically, as follows: the first label indicates the case number, the second value is the wave period in seconds and the last value is the actual incident-wave steepness. A cell with only X indicates that the corresponding test was not performed.

$k\zeta_a \downarrow, \frac{\omega_{n4}}{\omega_e} \rightarrow$	0.45	0.46	0.47	0.48	0.49	0.50
			C521 1.65	C538 1.68		
0.1	X	X	0.0976	0.0972	X	X
	C537 1.59	C536 1.62	C522 1.65	C533 1.68	C534 1.71	C535 1.74
0.15	0.1404	0.1418	0.1427	0.1426	0.1428	0.1428
				C539 1.68		
0.20	X	X	X	0.1838	X	X

The experimental and numerical results for roll-motion amplitude in nearly steady-state conditions in all studied cases are given in Tab. 6.6.

Table 6.6: Test cases at $Fn=0.09$, as given in Tab. 6.5. For each examined case, the experimental (Exp) and numerical (Num) roll-motion amplitudes in nearly steady-state conditions are given in degrees. A roll angle with a F shows that the roll steady-state value is obtained by forcing the model with a roll angle after a while. NOF means that parametric roll did not happen even with triggering the roll motion.

$k\zeta_a \downarrow, \frac{\omega_{n4}}{\omega_e} \rightarrow$	0.45	0.46	0.47	0.48	0.49	0.50
0.10 Exp	X	X	C521 NO	C538 23.5F	X	X
Num	X	X	30.0	25.6	X	X
0.15 Exp	C537 NOF	C536 24.0F	C522 16.5F	C533 22.5F	C534 18.5F	C535 NOF
Num	30.0	24.5	23.0	22.4	20.5	19.3
0.20 Exp	X	X	X	C539 15.3F	X	X
Num	X	X	X	19.0	X	X

As it can be seen, the overall results are in good agreement, but for three cases: C521, C537 and C535, for which the numerical and experimental PR results are different. These three cases are shown and discussed first.

It seems that these cases are again at the instability border similarly to the cases at $Fn=0$. For the numerical simulation of case C521, the PR starts to grow when the experiment time is over. The numerical simulation at the end of the experiment time is less than 1 degree. The comparison of motions for this case is shown in the Fig. 6.29 and the cable tension comparison is shown in Fig. 6.30.

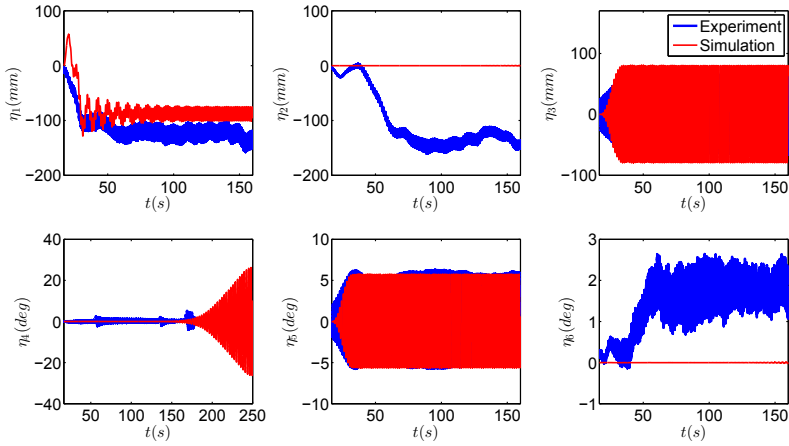


Figure 6.29: Comparison of motions for case C521.

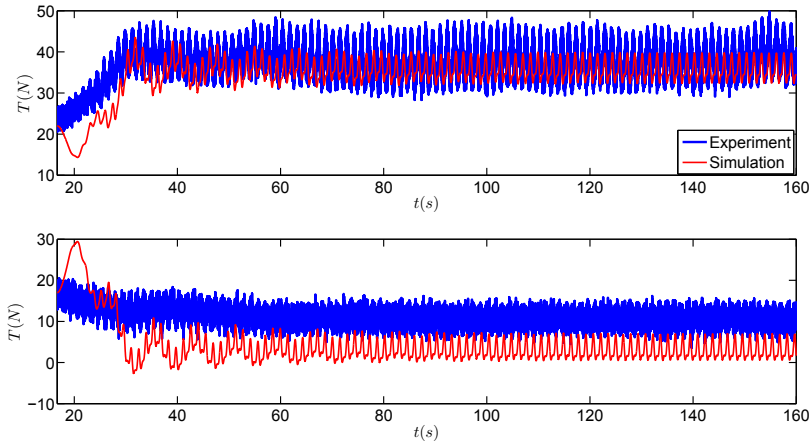


Figure 6.30: Comparison of cable tensions for case C521 (Top: fore starboard cable tension. Bottom: aft starboard cable tension).

The same trend happens for case C537 but, the numerical roll motion at the end of the experiments is around 4 degree. The comparison of motions and cable tensions are shown in the Figs. 6.31 and 6.32.

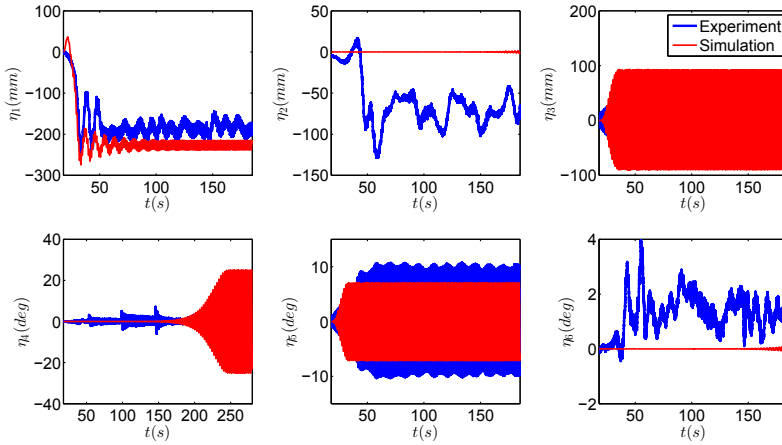


Figure 6.31: Comparison of motions for case C537.

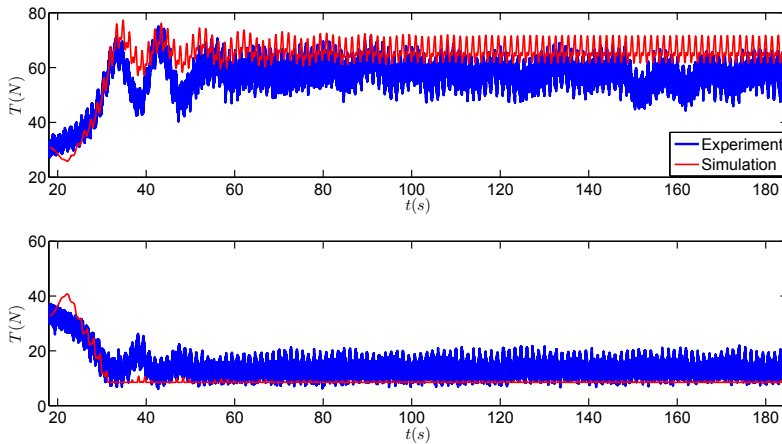


Figure 6.32: Comparison of cable tensions for case C537 (Top: fore starboard cable tension. Bottom: aft starboard cable tension).

For case C535, the pitch motion reduces strangely without reaching the steady state value. This reduction in pitch can avoid PR occurrence in the experiments. Checking the experimental video for this case also did not help to find the reason of this pitch reduction. The comparison of motions and cable tensions for the case C535 are shown in the Figs. 6.33 and 6.34.

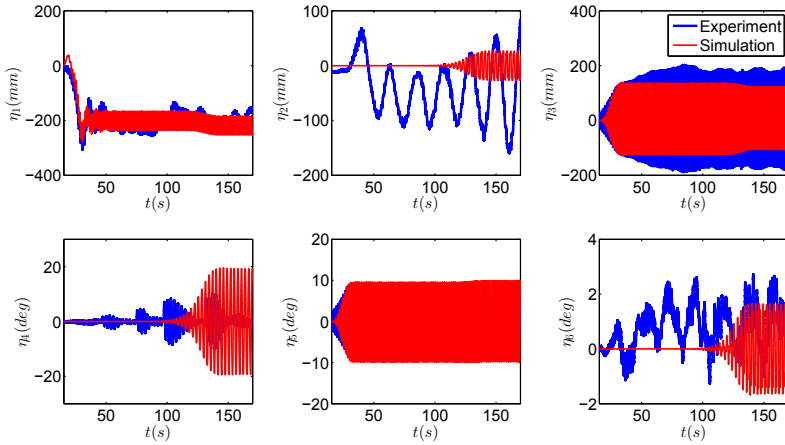


Figure 6.33: Comparison of motions for case C535.

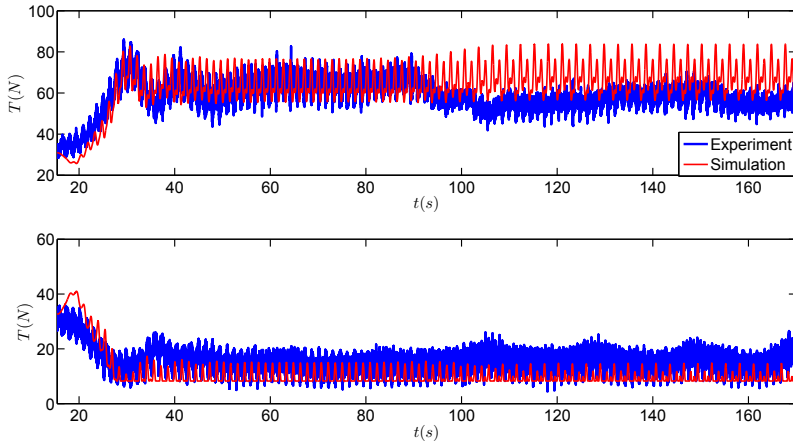


Figure 6.34: Comparison of cable tensions for case C535 (Top: fore starboard cable tension. Bottom: aft starboard cable tension).

For having a better picture of the position of these cases in the instability diagram, a numerical study was performed for several cases with different wave frequency ratios $\frac{\omega_{nA}}{\omega_e}$ ranging from 0.40 to 0.51 and $k\zeta_a$ in the range from 0.05 to 0.20. Based on the restoring variation in these cases (as explained in the case for Froude number $\text{Fn}=0$) and on the numerical results of roll motion (PR or NOPR), Fig. 6.35 is obtained.

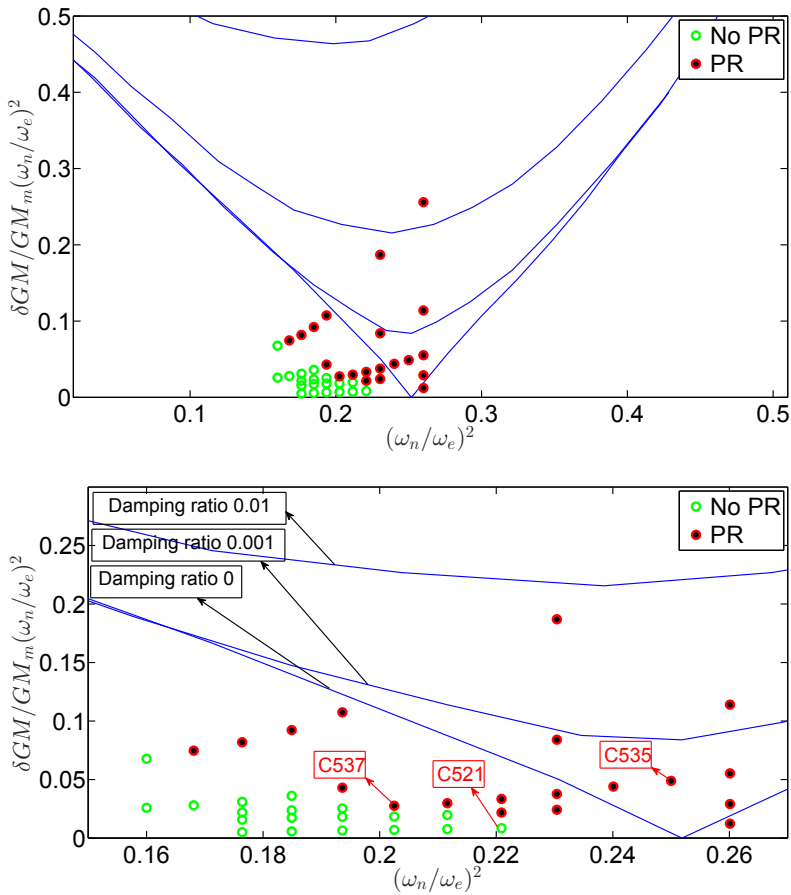


Figure 6.35: Mathieu instability diagram for uncoupled roll (solid lines) and numerical cases (symbols). Main plot (top), Enlarged view (bottom).

As it can be seen from this figure, the cases C537 and C521 are clearly at the stability border. But the case C535 seems to be well inside the instability region. That is because for all cases with higher frequency ratio ($\frac{\omega_n}{\omega_e} = 0.51$) and all wave steepnesses, PR was observed. This shows that according to the numerical simulation, this case should experience PR in the experiments as well.

The comparison of the numerical simulations and experimental results shows a good agreement for the other cases in terms of PR occurrence and roll steady-state amplitude. The motions and cables tension comparison for the remaining cases are shown in the Figs. 6.36 to 6.45.

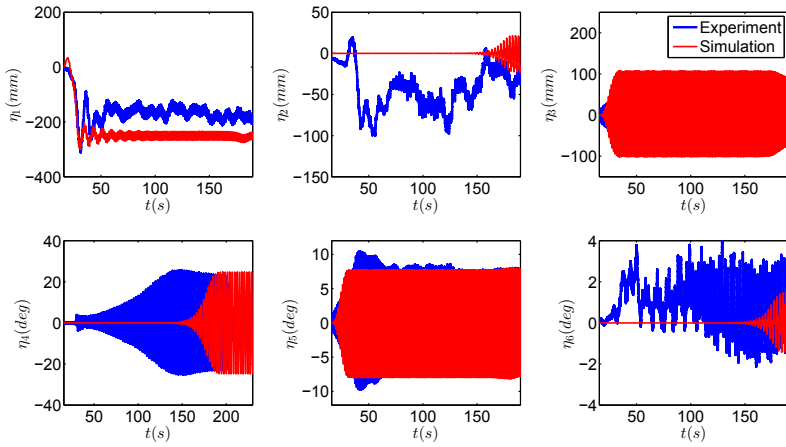


Figure 6.36: Comparison of motions for case C536.

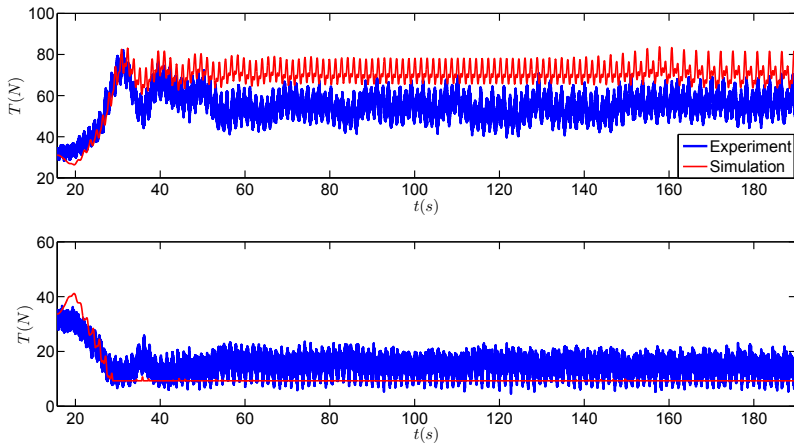


Figure 6.37: Comparison of cable tensions for case C536 (Top: fore starboard cable tension. Bottom: aft starboard cable tension).

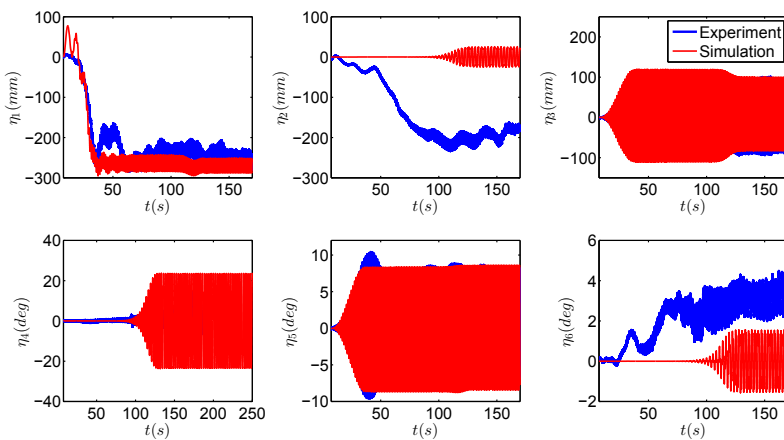


Figure 6.38: Comparison of motions for case C522.

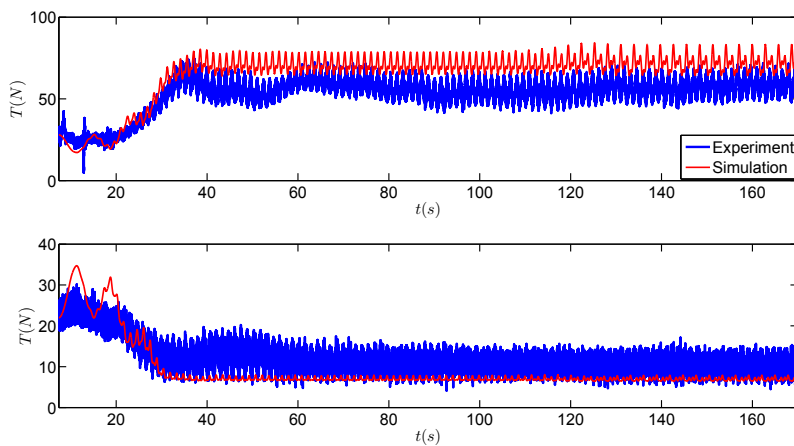


Figure 6.39: Comparison of cable tensions for case C522 (Top: fore starboard cable tension. Bottom: aft starboard cable tension).

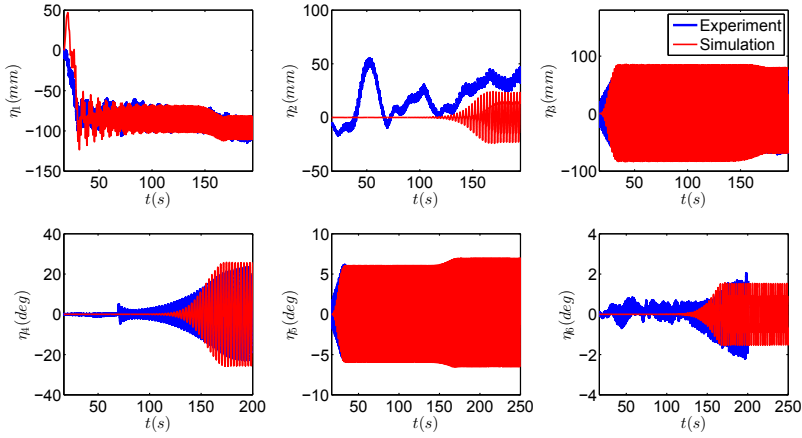


Figure 6.40: Comparison of motions for case C538.

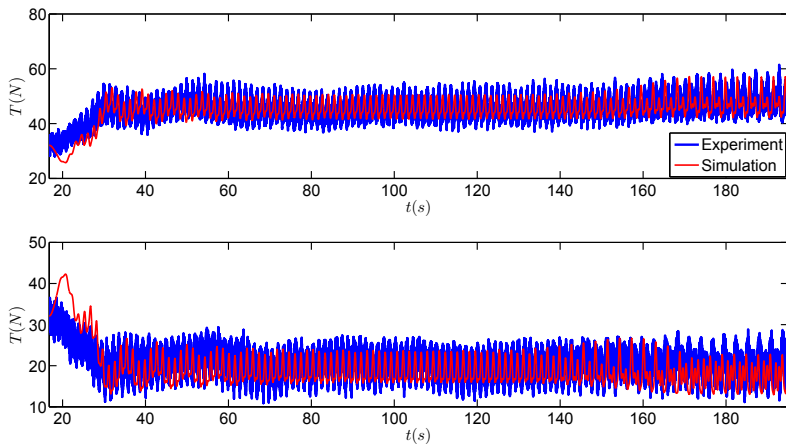


Figure 6.41: Comparison of cable tensions for case C538 (Top: fore starboard cable tension. Bottom: aft starboard cable tension).

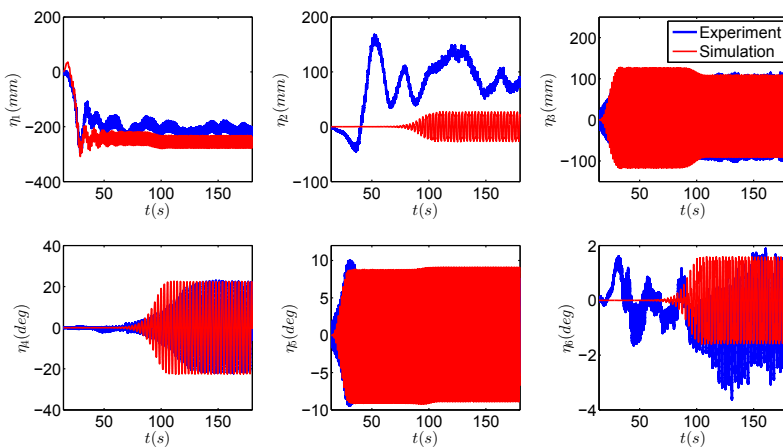


Figure 6.42: Comparison of motions for case C533.

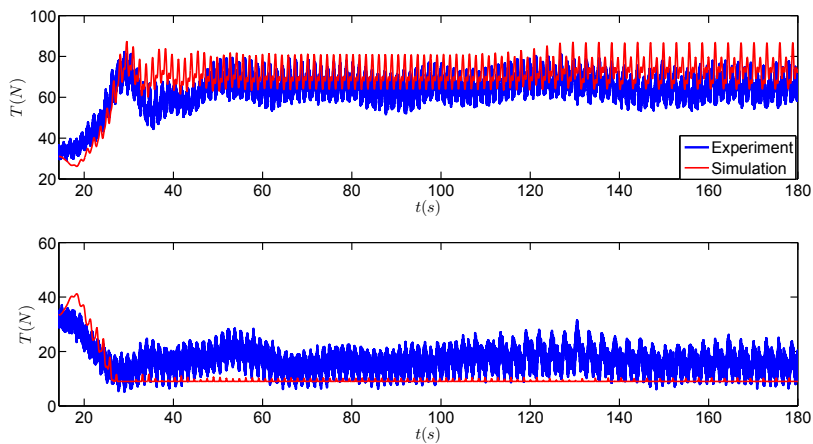


Figure 6.43: Comparison of cable tensions for case C533 (Top: fore starboard cable tension. Bottom: aft starboard cable tension).

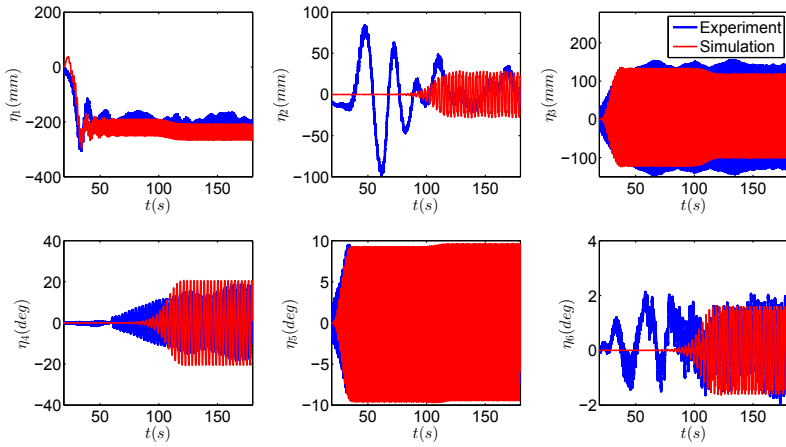


Figure 6.44: Comparison of motions for case C534.

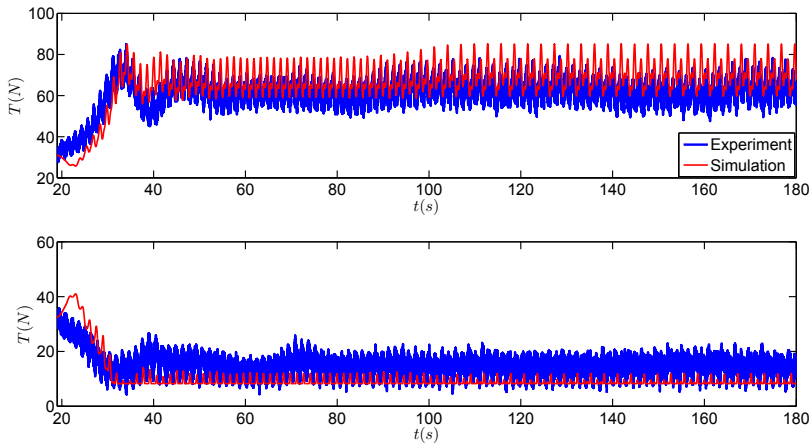


Figure 6.45: Comparison of cable tensions for case C534 (Top: fore starboard cable tension. Bottom: aft starboard cable tension).

6.3 Cases at $Fn=0.18$

The tests for this part is performed for the frequency ratio $\frac{\omega_{n4}}{\omega_e}$ from 0.43 to 0.50 with forward speed of $U = 0.976m/s$ which corresponds to $Fn = 0.18$. The wave steepness $k\zeta_a$ varies between 0.10 to 0.15.

6.3.1 Cable identification and wave characteristics

The experiments performed at $Fn = 0.18$ are shown in Tab. 6.9.

Table 6.7: The test cases at $Fn = 0.18$. A cell with symbol X indicates that the corresponding test was not performed.

$k\zeta_a \downarrow, \frac{\omega_{n4}}{\omega_e} \rightarrow$	0.43	0.44	0.45	0.46	0.47	0.48	0.49	0.50
0.1	X	X	X	X	X	C548	X	X
0.15	C555	C554	C551	C550	C549	C545	C552	C553

The viscous damping coefficients used for these tests are similar to those used for cases at $Fn = 0.09$. As for the cables, it was realized that the first examined case C545 was characterized by cable tensions not suitable to limit the horizontal motions of the vessel. Therefore, the pretension was increased for the other cases in waves. It means that two sets of cables were identified to model numerically, respectively, case C545 and the other cases at this Froude number.

The same procedure as explained previously was used for the cables identifications. For the first set of cables, the tension law identified for the fore cables in the test C545 is as follows:

$$T-T_0 = \begin{cases} 141.085\Delta l + 14.3576\Delta l^2 - 230.4319\Delta l^3 + 1976.8406\Delta l^4; \Delta l_0 < \Delta l < \Delta l_1 \\ T_{min}; \Delta l < \Delta l_0 \end{cases} \quad (6.18)$$

where $T_0 = 42.02N$ is the pretension and $T_{min} = -23.8N$ as explained in Fig. 3.19, $\Delta l_0 = -0.2m$ and $\Delta l_1 = 0.2m$. Moreover, the tension law for $\Delta l > \Delta l_1$ is a linear fit to the curve at Δl_1 .

The tension law used for the aft cables is as follows:

$$T-T_0 = \begin{cases} 280.5010\Delta l + 281.2196\Delta l^2 - 3552.0581\Delta l^3 - 3814.8616\Delta l^4; \Delta l_0 < \Delta l < \Delta l_1 \\ T_{min}; \Delta l < \Delta l_0 \end{cases} \tag{6.19}$$

where $T_0 = 27.0N$ is the pretension and $T_{min} = -23.66N$ as explained in Fig. 3.19, $\Delta l_0 = -0.12m$ and $\Delta l_1 = 0.1m$.

For the second set of cables, the tension law remains as for the first set for the fore cables. Instead, the tension law for the aft cables differs and is as follows:

$$T-T_0 = \begin{cases} 50.982\Delta l + 551.683\Delta l^2 + 2884.489\Delta l^3 - 9000.0\Delta l^4; \Delta l_0 < \Delta l < \Delta l_1 \\ T_{min}; \Delta l < \Delta l_0 \end{cases} \tag{6.20}$$

where $T_0 = 16.50N$ is the pretension and $T_{min} = -23.66N$ as explained in Fig. 3.19, $\Delta l_0 = 0$ and $\Delta l_1 = 0.1m$.

As done for the cases at $Fn=0$ and 0.09 , the characteristics of the incident waves generated in the experiments were identified through a FFT process. The nominal and actual incident-wave parameters for the examined cases at $Fn=0.18$ are shown in Tab. 6.8.

Table 6.8: Test cases at $Fn = 0.18$. The frequency ratio $\frac{\omega_{n4}}{\omega_e}$ and the steepness $k\zeta_a$ refer to the prescribed incident waves. In each cell, three elements are given vertically, as follows: the first label indicates the case number, the second value is the wave period in seconds and the last value is the actual incident-wave steepness. A cell with only X indicates that the corresponding test was not performed.

$k\zeta_a \downarrow, \frac{\omega_{n4}}{\omega_e} \rightarrow$	0.43	0.44	0.45	0.46	0.47	0.48	0.49	0.50
						C548 1.88		
0.1	X	X	X	X	X	0.0969	X	X
	C555 1.73	C554 1.76	C551 1.79	C550 1.82	C549 1.86	C545 1.89	C552 1.92	C553 1.92
0.15	0.1422	0.1424	0.1429	0.1427	0.1421	0.1428	0.1432	0.1429

At this stage all required information was available to perform the numerical simulations in free decay and waves conditions and to compare them against the corresponding test data. Figs. 6.46 and 6.47 examine, respectively, the surge-decay case C542 and the roll-decay case C541.

The roll-decay comparison shows that the level of damping used in the numerical simulation is in agreement with the experimental data. In the surge decay, the surge natural frequency seems quite similar in numerics and experiments, which shows the cables have been identified correctly. On the other hand, the surge amplitude is overestimated a bit after a couple of oscillations. We could not fix that with changing the linear and quadratic damping coefficients. The reason for this disagreement has not been ruled out.

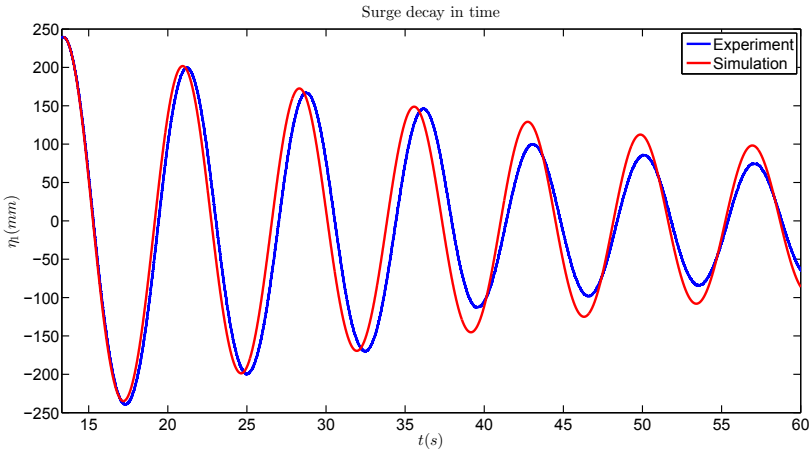


Figure 6.46: Comparison of surge decay C542.

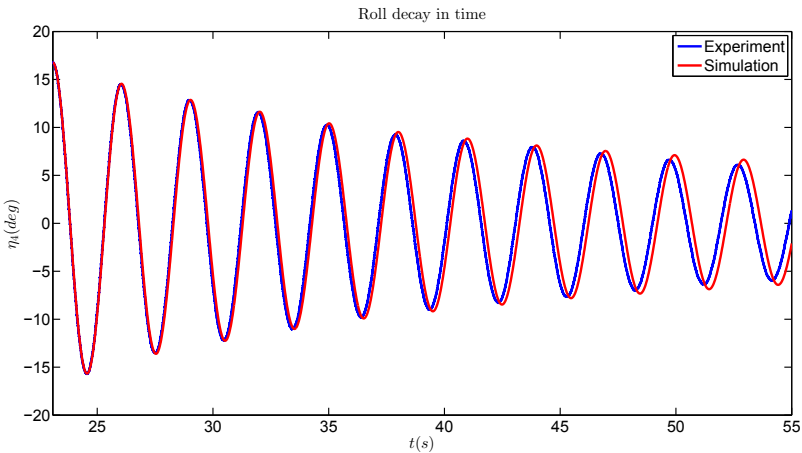


Figure 6.47: Comparison of roll decay C541.

6.3.2 Numerical and experimental results

Before starting the simulations of the test cases at $Fn = 0.18$, by checking the videos of experiments, it was clearly observed that the model had a negative small sinkage (rising up) and a small trim angle (bow up) with this forward speed. After checking the snapshots from the videos of experiments, a sinkage and trim values were identified and used in the simulations. One snapshot of the experiment C551 is shown in Fig. 6.48.



Figure 6.48: Sinkage and trim of the model in test C551.

The distance between each two waterlines in the model is 5cm. Based on the thickness of the blue lines (shown in the figure), the sinkage is around 8 mm up. The trim appears a small value bringing the bow up, a value of 0.5° (bow up) was considered in the numerical simulations, together with the identified sinkage.

The resulting numerical results for all examined cases at Fn 0.18 are shown in Tab. 6.9.

Table 6.9: Test cases at $Fn = 0.18$, as given in Tab 6.8. For each examined case, the experimental (Exp) and numerical (Num) roll-motion amplitudes in nearly steady-state conditions are given in degrees. A roll angle with a F shows that the roll steady-state value is obtained by forcing the model with a roll angle after a while. *NOF* means that parametric roll did not happen even with triggering the roll motion.

$k\zeta_a \downarrow, \frac{\omega_{n4}}{\omega_e} \rightarrow$	0.43	0.44	0.45	0.46	0.47	0.48	0.49	0.50
0.10 Exp						C548		
Num	X	X	X	X	X	21.1F	X	X
0.15 Exp	C555	C554	C551	C550	C549	C545	C552	C553
Num	NOF	14.5F	18.5F	20.6F	18F	NOF	9F	NOF
	27.5	27.0	26.5	25.6	23.0F	20.2	15.0F	NOF

From the table, the numerical and experimental results disagree in terms of PR occurrence for two cases, i.e. C555 and C545. In the other cases, the numerics predicts well the PR occurrence but the roll amplitude tends to over-predict the experimental value. A detailed analysis of the individual cases is presented next.

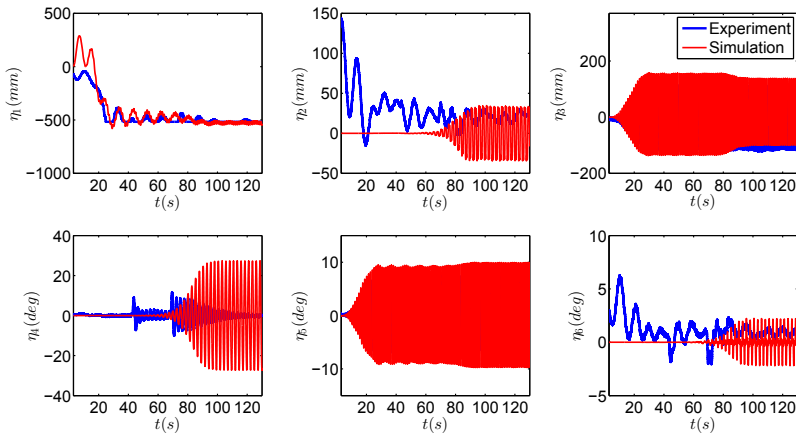


Figure 6.49: Comparison of motions for case C555.

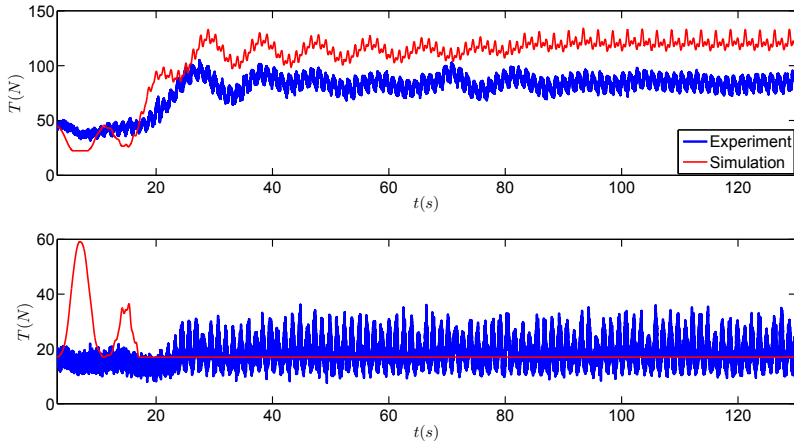


Figure 6.50: Comparison of cable tensions for case C555 (Top: fore starboard cable tension. Bottom: aft starboard cable tension).

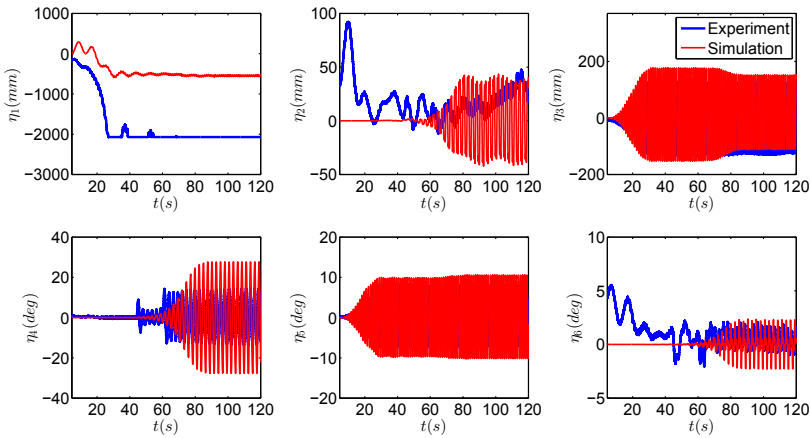


Figure 6.51: Comparison of motions for case C554.

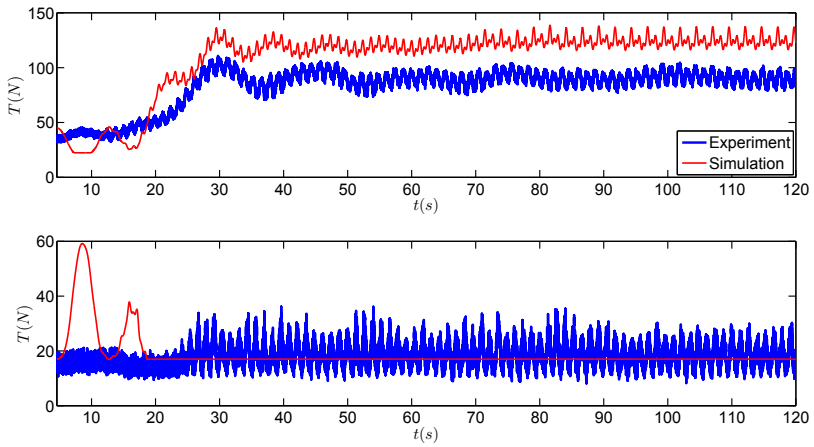


Figure 6.52: Comparison of cable tensions for case C554 (Top: fore starboard cable tension. Bottom: aft starboard cable tension).

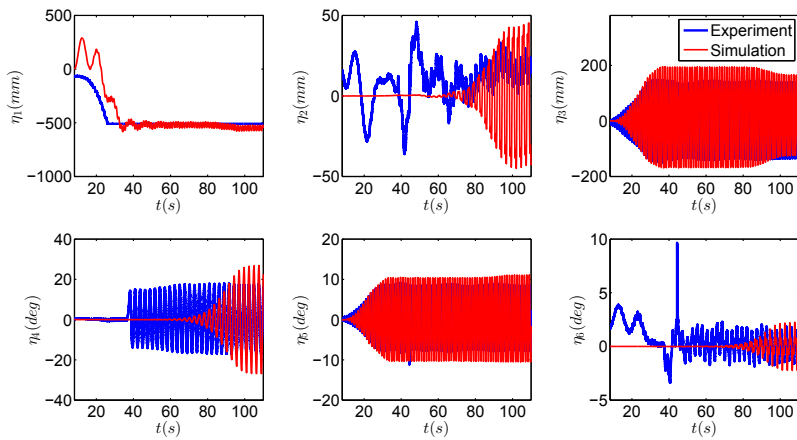


Figure 6.53: Comparison of motions for case C551.

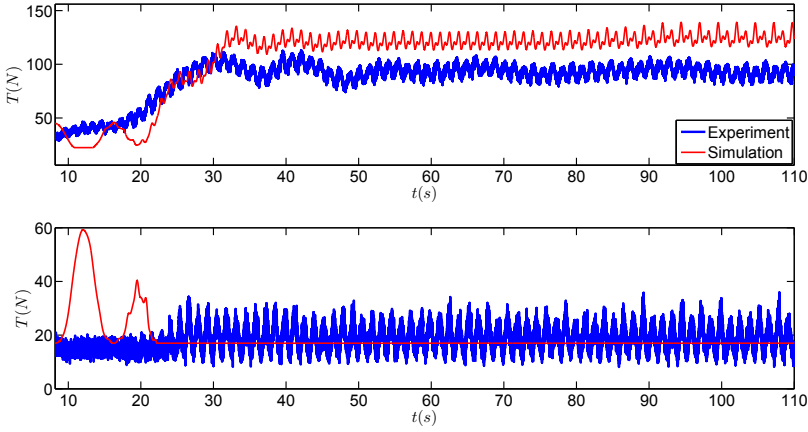


Figure 6.54: Comparison of cable tensions for case C551 (Top: fore starboard cable tension. Bottom: aft starboard cable tension).

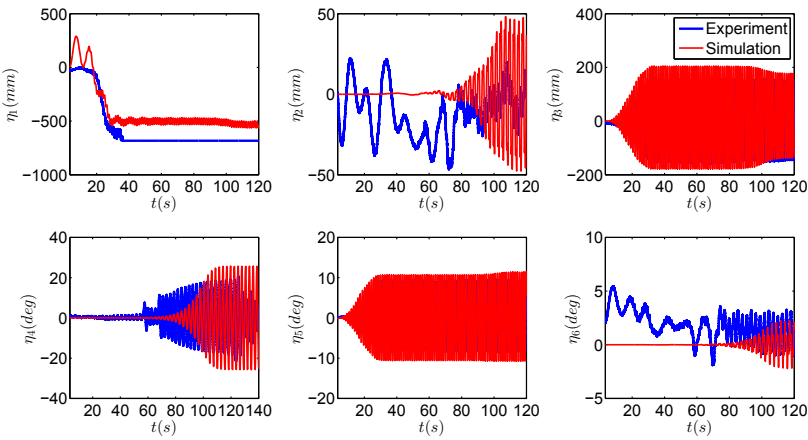


Figure 6.55: Comparison of motions for case C550.

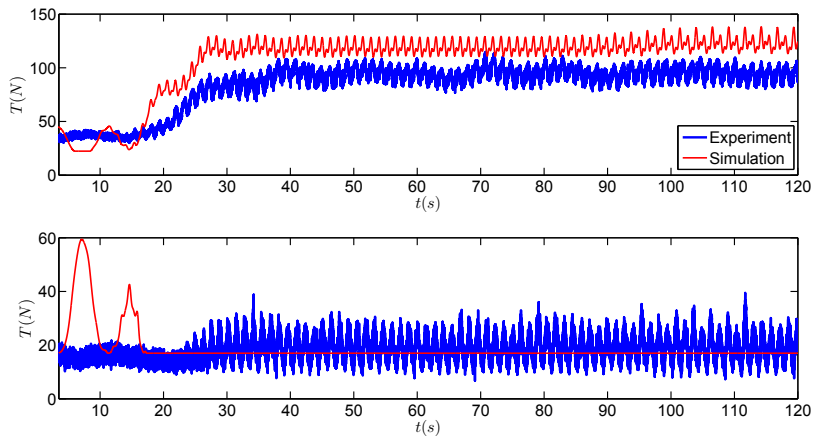


Figure 6.56: Comparison of cable tensions for case C550 (Top: fore starboard cable tension. Bottom: aft starboard cable tension).

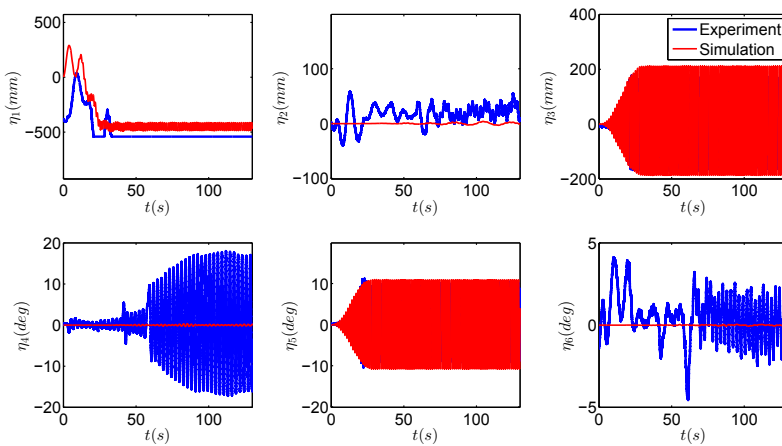


Figure 6.57: Comparison of motions for case C549.

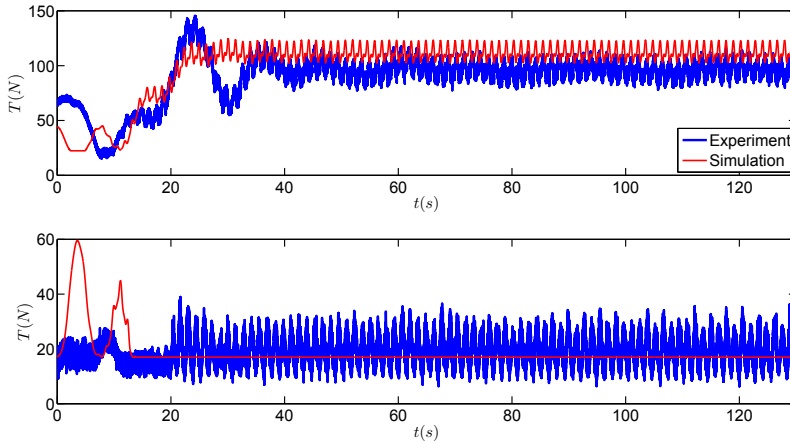


Figure 6.58: Comparison of cable tensions for case C549 (Top: fore starboard cable tension. Bottom: aft starboard cable tension).

Figs. 6.49 and 6.50 present the comparison for the motions and cable tensions for case 555. This corresponds to the lowest examined wave-frequency ratio. Experimentally no PR is observed, even with triggering the roll motion. Numerically, a PR with amplitude 27.5° develops at a time later than when the roll motion is triggered without PR in the experiments. Considering the nominal-wave parameters for simplicity, in this case the wave-frequency ratio is $\frac{\omega_{n4}}{\omega_e} = 0.43$ and the wave steepness is $k\zeta_a = 0.15$. From now on, we refer to the nominal wave characteristics of the cases for the simplicity.

At the same wave steepness and increasing the nominal wave frequency ratio to $\frac{\omega_{n4}}{\omega_e} = 0.44$ and 0.45 , the PR is observed experimentally after forcing a roll motion. Therefore we can say that the left instability border for the nominal wave steepness $k\zeta_a = 0.15$, is at a frequency ratio between 0.43 and 0.44 . This suggests that the difference in PR occurrence for case C555 might be due to the case being close to the instability border and therefore to a greater sensitivity of the vessel behaviour to the involved roll damping.

Figs. 6.51 and 6.52 present the comparison for the motions and cable tensions for case 554 with nominal wave-frequency ratio $\frac{\omega_{n4}}{\omega_e} = 0.44$ and the nominal wave steepness $k\zeta_a = 0.15$. In this case, a PR with value of 14.5° is observed experimentally with a forced roll motion. In the numerical simulations, a PR with value 27.0° occurs, without the need of forcing the roll motion. The reason for the large difference in steady-state roll amplitude lies in the complicated non-linearities involved for this wave-body interac-

tion case, which are not fully handled in the proposed numerical model. At this forward speed and wave parameters, huge amount of wave breaking in the ship bow and huge bottom slamming and bow flare slamming and even water on deck are observed experimentally. Fig. 6.59 shows snapshots of water on deck phenomenon and bottom and bow flare slamming in the experimental case C554.

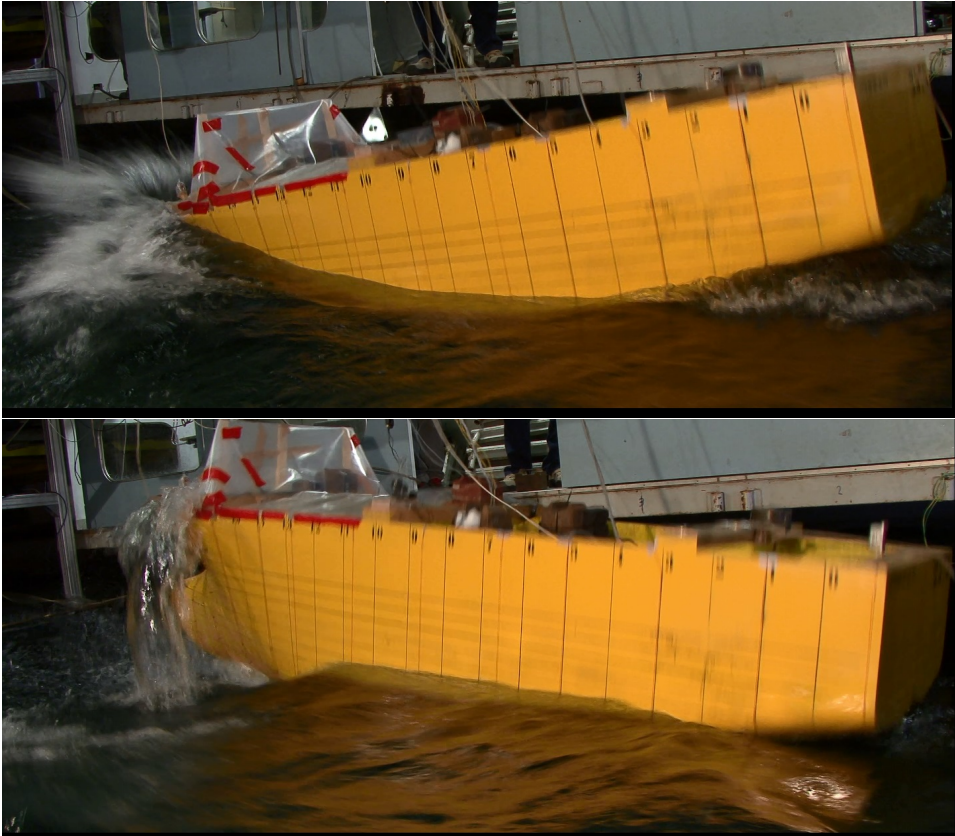


Figure 6.59: Snapshots of experiment case C554. Top: Bottom and bow flare slamming. Bottom: Water on deck phenomenon.

Besides, the combination of large roll, heave and pitch motions, makes some slamming phenomenon to occur asymmetrically above the waterline of the vessel. All these non-linearities of course have big effect on the roll amplitude and have to be modelled with more sophisticated numerical methods.

At case C551 and C550, with Figs. 6.53 and 6.54, and Figs. 6.55 and 6.56, present the comparison for the motions and cable tensions, respectively

for cases C551 and C550. These cases correspond to nominal wave-frequency ratio $\frac{\omega_{n4}}{\omega_e} = 0.45$ and 0.46 and the wave steepness $k\zeta_a = 0.15$. For them, we observe the PR occurrence in the experiments after a forced roll motion. The numerical results show the PR occurrence without forcing a roll motion, with larger value than experimentally. In both cases PR developed at a time later than when the roll motion is triggered in the corresponding experiments. Forcing the roll motion in the numerical simulations gives the same amplitude for the PR as obtained without any triggering mechanism (not shown here).

Figs. 6.57 and 6.58 present the comparison for the motions and cable tensions for case 549, with nominal wave-frequency ratio $\frac{\omega_{n4}}{\omega_e} = 0.47$ at the same wave steepness as for the cases with $\text{Fn} = 0.18$ examined so far. In this case, a PR with amplitude of 18° is observed in the experiments with a triggered roll motion. Numerically, the simulation performed without forcing the roll motion predicts no PR occurrence (see roll time history in Fig. 6.57). Then we tried to trigger a roll motion in this case as it was done in the experiments. This was done enforcing a Gaussian roll moment for a very short time to reproduce a similar forced roll motion as in the model tests. By doing so, a PR with amplitude of 18° builds up. This value is relatively close to the experimental results, as shown in Fig. 6.60.

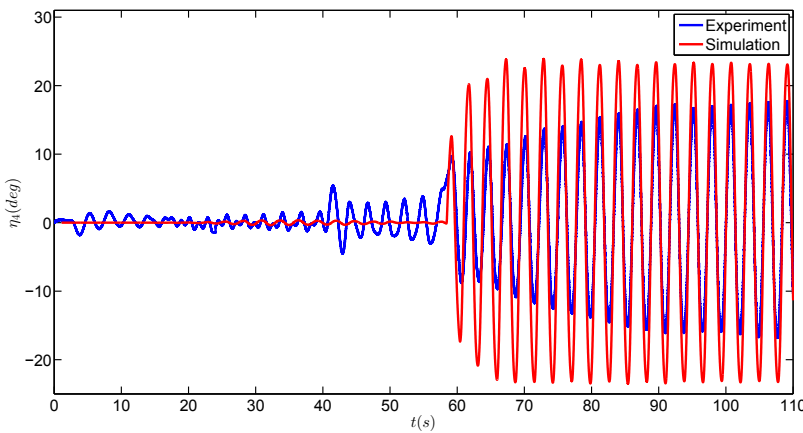


Figure 6.60: Comparison of forced roll motion for case C549.

Figs. 6.61 and 6.62 present the comparison for the motions and cable tensions for case C548, with nominal wave-frequency ratio $\frac{\omega_{n4}}{\omega_e} = 0.48$ and the wave steepness $k\zeta_a = 0.10$. In this case, a PR with amplitude of 21° is observed experimentally after triggering a roll motion. The numerical

simulations also show a PR with amplitude of 25° . Figs. 6.63 and 6.64 present the comparison for the motions and cable tensions for case C545, with larger nominal wave steepness, i.e. $k\zeta_a = 0.15$, and the same nominal wave frequency ratio as for C548. For case C545, experimentally no parametric resonance is observed even after triggering the parametric roll. Numerically the PR occurs on a long time scale. Slightly after the numerical PR starts to develop, experimentally something happened as indicated by a sign change in surge (t about 75 s), that goes from a saturated negative value to a large positive value. Shortly after, large sway oscillations are triggered, coupled with yaw. It is hard from the vessel motions to identify the physical phenomenon occurred in the model tests, but its excitation of sway and yaw motions could be responsible for preventing the PR occurrence in the experiments. As a result, we cannot conclude about the PR occurrence in the experiments for this case.

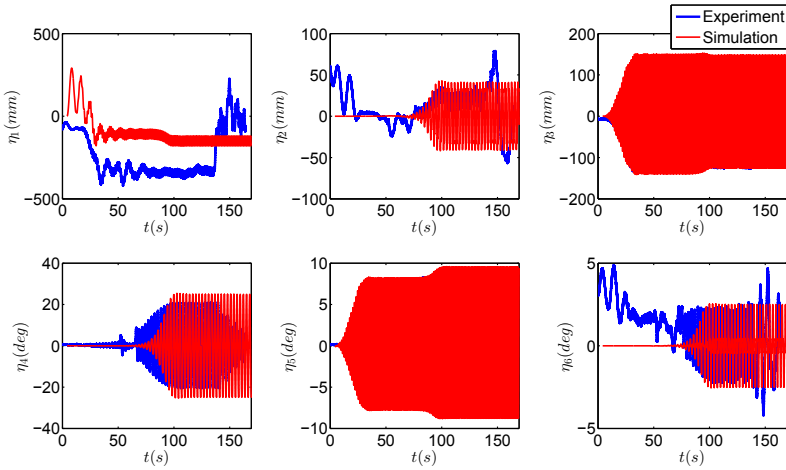


Figure 6.61: Comparison of motions for case C548.

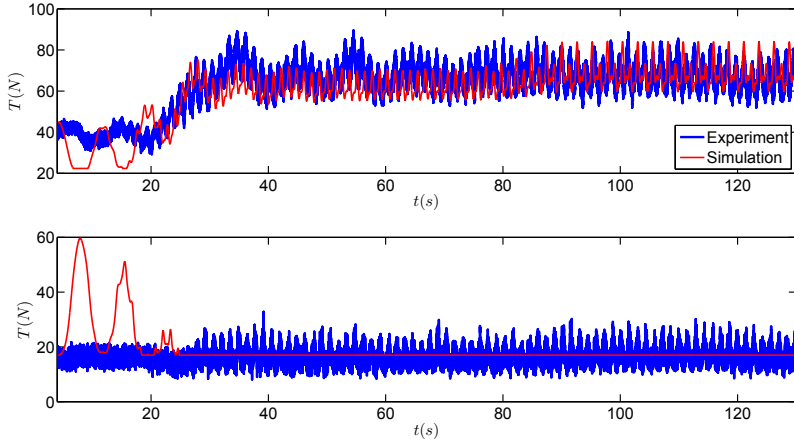


Figure 6.62: Comparison of cable tensions for case C548 (Top: fore starboard cable tension. Bottom: aft starboard cable tension).

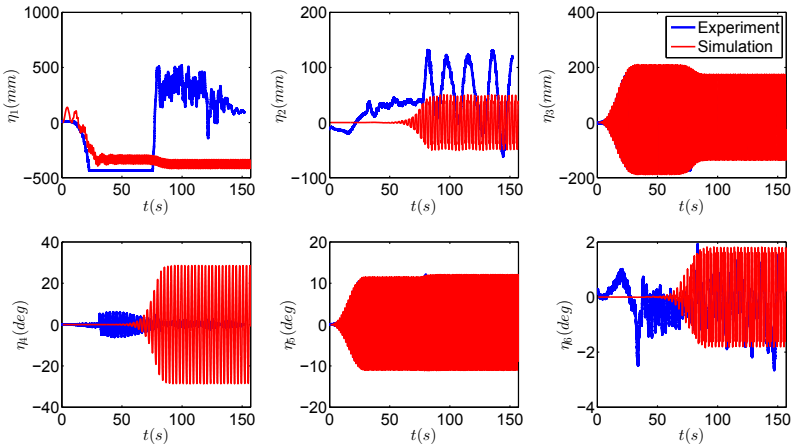


Figure 6.63: Comparison of motions for case C545.

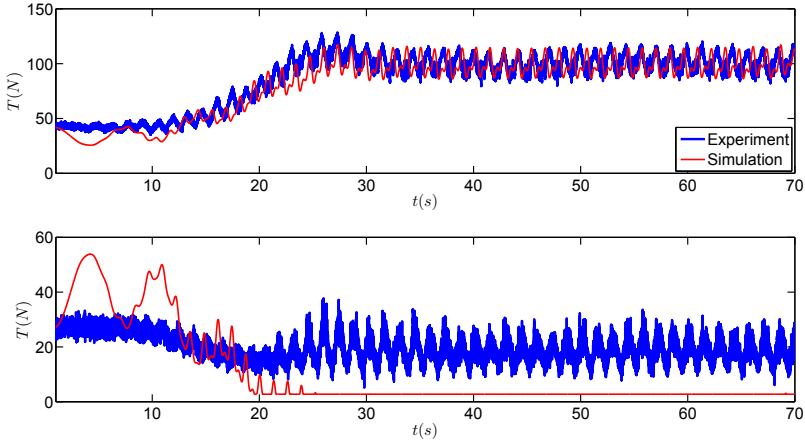


Figure 6.64: Comparison of cable tensions for case C545 (Top: fore starboard cable tension. Bottom: aft starboard cable tension).

Figs. 6.65 and 6.66 present the comparison for the motions and cable tensions for case C552, with nominal wave frequency ratio $\frac{\omega_{n4}}{\omega_e} = 0.49$ and the nominal wave steepness $k\zeta_a = 0.15$. In this case, experimentally a triggered roll motion leads to a PR with amplitude around 9° . The numerical simulation, without a roll-forcing mechanism, indicates no parametric roll. However, triggering a roll motion as in the experiments leads to PR occurrence with amplitude 15° , as shown in Fig. 6.67.

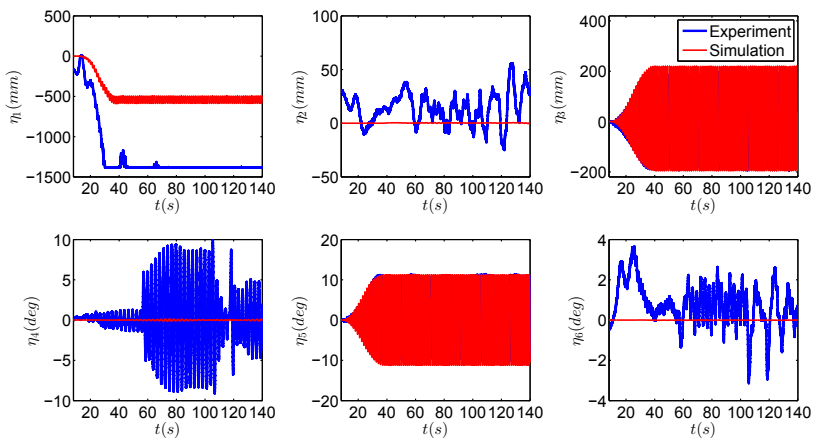


Figure 6.65: Comparison of motions for case C552.

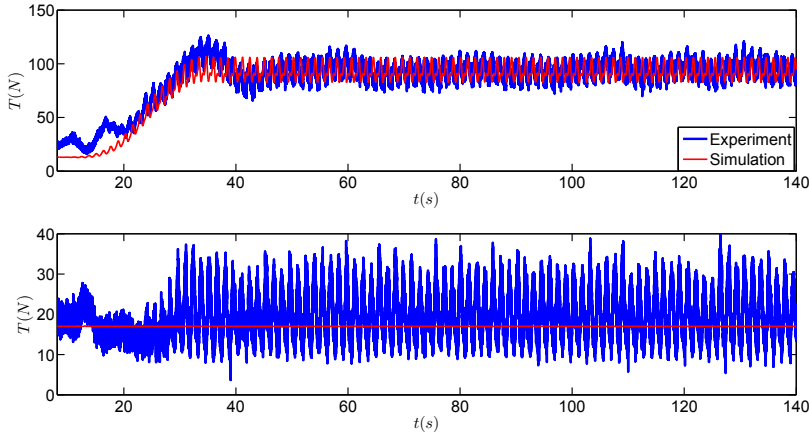


Figure 6.66: Comparison of cable tensions for case C552 (Top: fore starboard cable tension. Bottom: aft starboard cable tension).

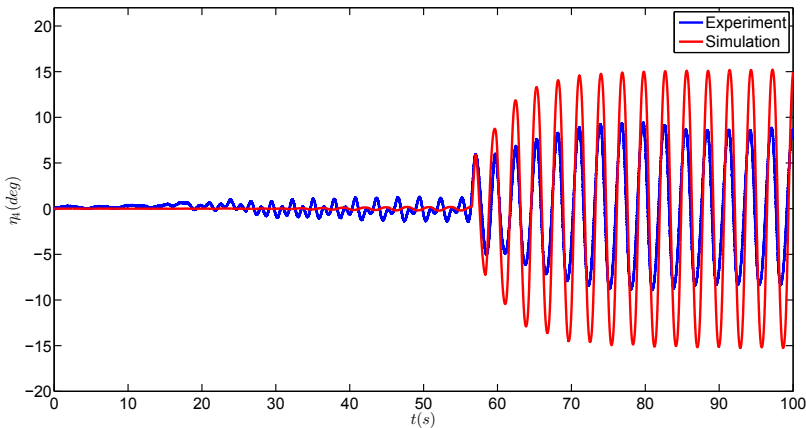


Figure 6.67: Comparison of forced roll motion for case C552.

Figs. 6.68 and 6.69 present the comparison for the motions and cable tensions for case C553, representing the last examined case in this section. This is with nominal wave-frequency ratio $\frac{\omega_{n4}}{\omega_e} = 0.50$ and the nominal wave steepness $k\zeta_a = 0.15$. The experimental results show no PR even with forcing a roll motion. The forced roll motion is damped out after some oscillations.

The numerical results without forcing a roll motion showed no paramet-

ric resonance. They were then repeated enforcing a roll motion similarly as forced in the experiments. The new results are presented in Fig. 6.70 and confirmed no PR for this case. Because case C553 is associated with no PR and case C552 has a PR with small amplitude, it seems that the instability border is somewhere between frequency ratio $\frac{\omega_{n4}}{\omega_e} = 0.49$ and 0.50.

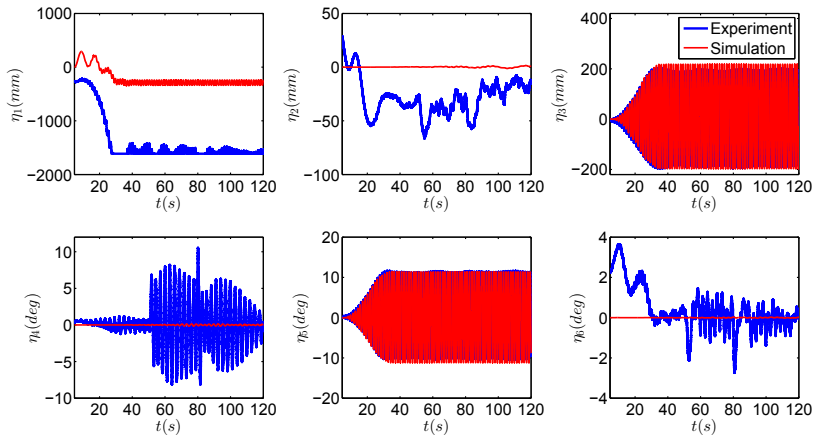


Figure 6.68: Comparison of motions for case C553.

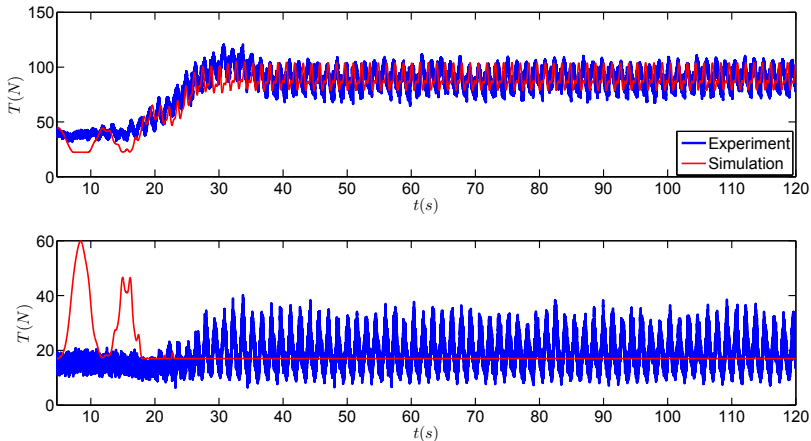


Figure 6.69: Comparison of cable tensions for case C553 (Top: fore starboard cable tension. Bottom: aft starboard cable tension).

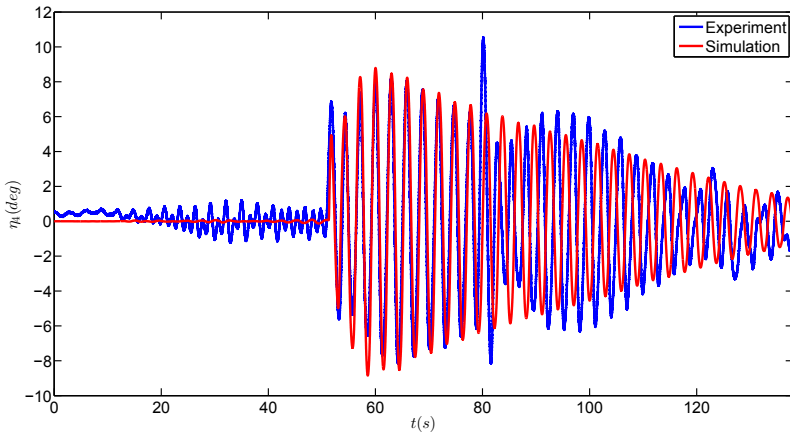


Figure 6.70: Comparison of forced roll motion for case C553.

In all of these cases, the sensor of surge motion in the experiments is saturated so we can not compare the values in surge motions directly. But from the cables tensions comparison it seems that the surge drifts in cases C550, C551, C554 and C555 are over-predicted in the numerical simulations.

6.4 Conclusion

Experimental results for the fishing vessel SFH112 without forward speed ($Fn = 0$) and with two different forward speeds ($Fn = 0.09$ and $Fn = 0.18$) are presented. The tests were performed with different wave periods and steepnesses. The numerical simulations were also performed and the results are compared against the experimental results. Before doing the simulations, the mooring cables tensions were identified from the surge decay tests. The viscous damping coefficients are also obtained from the decay tests. As a check, the surge and roll decays were simulated and compared against the experiments, with globally a good agreement. Then after doing the FFT on the incident wave profiles in the experiments, the simulations were performed for all cases and the general comparison with experimental results shows a satisfactory agreement, but there are some cases in which the results are different in terms of PR occurrence. In $Fn = 0$, plotting the Mathieu instability diagram for the uncoupled roll equation shows that all the cases with disagreement in PR occurrence are at the instability border. PR is an instability phenomenon. Near the instability borders, its occurrence is very sensitive to the involved parameters. Even small differences between the

numerical model and the experimental condition could lead on-off change in the PR occurrence. The comparisons of all six degrees of freedom for all examined cases show that the motions are the same except for sway and yaw. One reason could be the differences in the cable systems, i.e. the cables used in the numerical simulations are exactly symmetrical in port and starboard side while it is not exactly like that in the experiments. Besides, the wave reflections from the tank walls especially at $Fn=0$, not accounted for in the simulations, might have some effects also. The transient phase in the surge motion is also different in the numerical and experimental results. One should also note that in the roll motion, the steady state value is important and the transient phase should not be compared, due to different perturbations in the lateral directions in the numerical and experimental setting which highly affect the PR build up time. The cables tensions are also compared for all examined wave cases.

In a second part of the chapter, the results for the cases with $Fn = 0.09$ are compared and presented. Similar to the cases without forward speed, first we did the FFT of the incident waves. Then we extracted the viscous damping and the cables identifications from the roll and surge decay tests. By doing the numerical simulations for surge and roll decay tests and comparing them against the experiments, the identification process was correct. The comparison of the cases in waves showed that, the numerical and experimental results for three cases differ in terms of PR occurrence. We ran some more cases for a wider range of frequencies and wave steepness to do a numerical study on the instability borders. By doing so, as it was shown in the Fig. 6.35, two of the three cases seem to be at the instability border. For them, the value of the numerical roll motion in the time range of experiments is very small and the main build up starts after the experimental time recordings. Besides, in the experiment case C535, it was observed that the pitch motion decreases in amplitude strangely without reaching a steady-state value. This reduction in pitch might have some effects in avoiding PR and anyway indicates the occurrence of some phenomenon in the tests that is not reproduced in the numerical simulations. The results in the stability diagram also proved it because the point corresponding to case C535 looked to be well inside the instability zone. Moreover, the numerical simulations seem to over predict the surge drift. That is why the cable tensions are also different a bit in the numerical simulations and experiments. For other cases, the general trend of agreement is similar to the cases at $Fn = 0$.

In the last part of the chapter, we performed and presented the results for the cases with $Fn = 0.18$. We first extracted the viscous damping and cable identifications from the surge and roll decay tests. Checking the videos

of these set of experiments, a sink (up) and trim (bow up) in the experiments were detected in the ship model before it was reached by incident waves. The values of the sink and trim were small and guessed from the experimental videos as 8mm sink (up), equal to 2% of the ship draft and 0.5° as trim value (bow up). These values were used in the numerical simulations.

The results showed that in terms of PR occurrence all cases except cases C555 and C545 show reasonable agreement between the experiments and the numerical results. It was shown that case C555 is at the instability border and in case C545 some phenomenon, not reproduced in the numerical simulations, occurred in the experiments leading to sudden change in sign of the mean value in surge motion and triggering an oscillatory sway motion. In terms of PR steady-state amplitude, the amplitudes agreement was not good in some cases. This is due to the large non-linear phenomena observed in the tests. The large vertical motions made lots of wave breaking at the ship bow and water on deck was also observed in some of the experiments. Besides, the bottom and bow flare slamming are also important in these cases and need to be modelled with sophisticated numerical models. The combination of roll with heave and pitch motions also brought to asymmetric slamming events.

To understand the level of non-linearities in the experiments, we tried to compare the linear RAO of heave and pitch motions against the experimental results for the cases with mentioned two forward speeds. We used the linear RAO for these two motions based on our 3D hybrid method frequency-domain code and then superimposed the experimental results on it. The comparison is shown in Figs. 6.71 and 6.72.

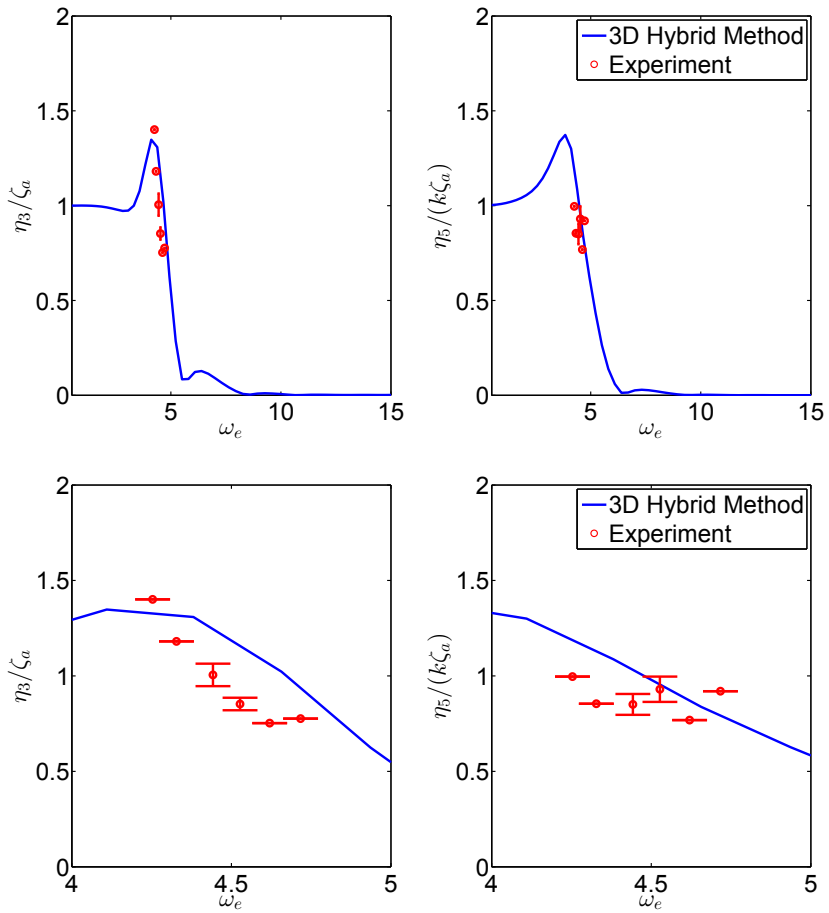


Figure 6.71: Comparison of numerical linear RAO against the experimental results for the fishing vessel SFH112 in head-sea waves for $Fn = 0.09$. Top: Main plot. Bottom: Enlarged view.

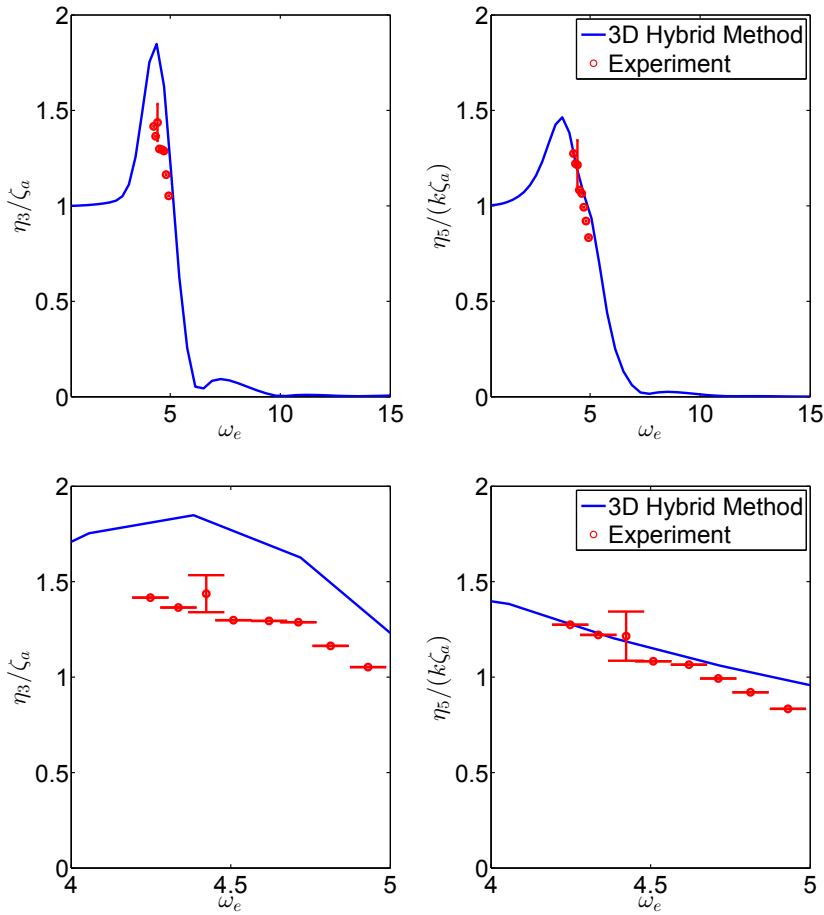


Figure 6.72: Comparison of numerical linear RAO against the experimental results for the fishing vessel SFH112 in head-sea waves for $Fn = 0.18$. Top: Main plot. Bottom: Enlarged view.

We showed only heave and pitch motions because the linear RAO for sway, roll and yaw are almost zero for longitudinal waves. Besides the surge motion in the experiments is far from regularly oscillating due to the coupling to the sway and yaw through mooring system. The heave and pitch experimental results were obtained selecting a window of several periods after transient part of the motions and before the build up of a parametric roll. There are some cases which were repeated in the experiments and also some cases were performed with the same frequency ratio and different wave steepnesses. The error bar in the experimental results in the figure simply shows the variation of the motions amplitudes in these repetitions. A more sophisticated error analysis on the experimental data is presented in appendix B. The comparison indicates that the numerical results over-predict the heave and pitch motions in the shown cases.

But there are some numerical and experimental error sources that might have influenced the results (the shown RAO and also the PR results) in this chapter. In the experiments, the heave and pitch motions are not very regularly oscillating even in the steady-state phase for all cases. That is partly due to the incident wave which is not perfectly regular because of reflection of waves from the tank walls. There are many non-linearities connected to the breaking waves at the ship bow observed for many cases (especially for cases with forward speed), to the bottom and bow flare slamming and even to water on deck in some cases. Small misalignments from the head sea waves in the experiments might also have some influences.

Besides, in the numerical side, the interaction between the local steady flow and unsteady flow is ignored in the numerical solver. It might have some effects on the results especially for this ship which does not have a slender body. Furthermore, the non-linearities that are included in the numerical solver are simplified. Also local wave elevation is not considered in the wetted surface of the body in time.

Chapter 7

Experiments and numerical simulations for a fishing vessel with anti-roll tank at $F_n=0$

In order to check the anti-roll tank effects in parametric rolling, a tank with length $l = 95\text{cm}$ and filling depth $h = 3.9\text{cm}$ was designed and installed on the ship model. Different tank widths have been used in order to study the influence on the roll damping provided by the tank. The different tanks used in the experiments are as follows:

- Tank width=3.0 cm, tank water depth=3.9 cm.
- Tank width=4.0 cm, tank water depth=3.9 cm.
- Tank width=5.1 cm, tank water depth=3.9 cm.
- Tank width=8.1 cm, tank water depth=3.9 cm.

The tank position and set-up have been described in section 4.4. Some forced roll oscillation experiments on the isolated tank were performed before the main experiments of the ship with tank. In the isolated tank tests, the centre of roll was 0.4 m below the tank bottom and forces and moments were measured in a body-fixed reference frame centred at the tank bottom. The experimental and numerical simulation results for the isolated tank are presented in section 3.1.1.3.

As discussed in chapter 3, the comparison of numerical and experimental tank loads show that there is acceptable agreement for the sway force

while the roll moment is under-predicted numerically by around 25%. The differences are probably due to the fact that these cases are performed at the resonance frequency and as observed in the experiments, there are significant tank roof impacts that make the flow very violent and create pronounced splashes and non-linearities that cannot be captured correctly by the sloshing solver. Furthermore, pressures at the tank roof will directly influence roll moments but not directly influence sway force. Numerical convergence and conservation of fluid mass were checked in the simulations.

7.1 Free surface anti-roll tank mechanism

The free surface anti-roll tank could provide extra roll damping at certain frequencies and this could help to avoid the parametric rolling resonance of the ship. Here we simply explain the mechanism of this system and the parameters that could make the extra damping higher or lower. For simplicity, we just consider that the tank only experiences roll motion. The anti-roll tank mechanism is that it uses the transfer of water from one side of the ship to the other side with, a certain phase lag with respect to the rolling motion of the vessel, as a mean to provide a counteracting moment. The tank moment can formally be written as:

$$M_r = M_r \sin(\omega t + \varepsilon_r) \quad (7.1)$$

Here M_r and ε_r are the tank roll moment amplitude and phase lag with respect to the tank motion (here we can say ship roll motion), respectively. ω is also the rolling frequency of the tank. $M_r \sin \varepsilon_r$ is the amplitude of the tank moment component out of phase with the tank roll motion and $M_r \cos \varepsilon_r$ is the amplitude of the component in phase with respect to the tank roll motion. The component out of phase with the tank motion is in fact 180° out of phase with respect to the tank roll velocity. Therefore, this component could be regarded as a damping term. To have a maximum damping from the tank, it is desired to have the phase angle $|\varepsilon_r| = 90^\circ$.

Many parameters influence the fluid motion in the tank and consequently its roll moment. Some of them are the geometry and the dimension of the tank, its position with respect to the axis of rotation, the amount of liquid carried in it, and the ship motions which the tank is subjected to (both as amplitude and frequency) [61].

Theoretically, at natural sloshing frequency, the roll moment has a phase lag of -90° compared with the oscillatory motion of the tank. Water depth is one of the most important parameters of the tank. Because for a certain

tank length (which is equal to the ship breadth in our case), the only possibility to change the sloshing natural frequency is changing the tank water depth. It is clear that at or near this natural frequency, the water transfer is largest and circumstances are most favourable for roll damping [61].

But one should note that this is a complex phenomenon and normally the actual sloshing natural frequency is different than the theoretical sloshing natural frequency. The actual sloshing frequency is a function of the tank length, tank water depth, tank height, position of the rotation point and roll amplitude. By increasing the roll amplitude and decreasing the h/l ratio (water depth-to-tank length ratio), the actual sloshing frequency would deviate from the theoretical value and therefore the phase angle of the sloshing moment would differ from -90° . The tank roll moment amplitude and the phase angle for different tank dimensions were presented and discussed in section 3.1.1.2. It can be seen that the actual sloshing frequency, ω_a (where the $\varepsilon_r = -90^\circ$) is shifted from the theoretical sloshing frequency, ω_1 as explained here.

Van den Bosch et al. [61] did several forced roll experiments on a tank with tank length $l = 1m$ to study these relations. Some of these tests were shown in section 3.1.1.2 and were simulated by our numerical solver. The effect of h/l ratio of the tank and the rotation point position relative to the tank bottom on the actual sloshing frequency is shown in the Fig. 7.1.

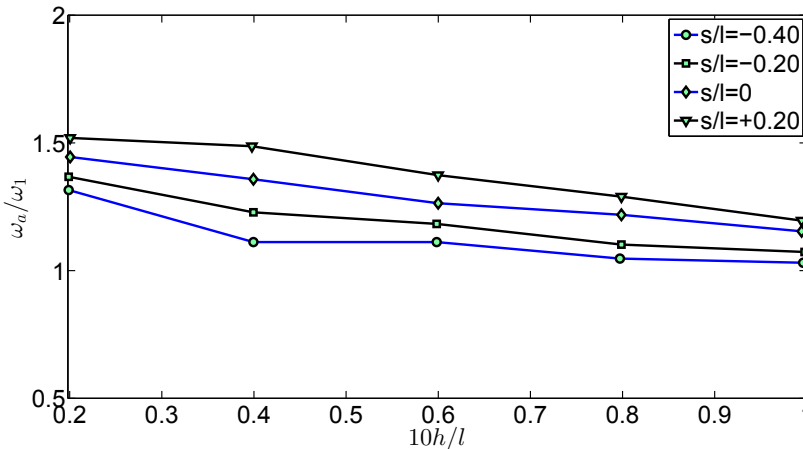


Figure 7.1: Ratio ω_a/ω_1 as a function of h/l and s/l . $\phi_a = 0.10rad$, [61].

ω_a is the actual sloshing frequency where the phase angle $\varepsilon_r = -90^\circ$ and ω_1 is the theoretical sloshing frequency. s is the distance from the axis of rotation to the tank bottom and it is positive if the tank bottom is situated

above this axis. As can be seen from this figure, the actual and theoretical sloshing frequencies get closer with increasing the h/l ratio of the tank. In terms of the s/l ratio of the tank, it seems that the ω_a and ω_1 get closer if the tank is situated below the axis of rotation. The ratio ω_a/ω_1 gets closer to 1 by increasing the value of $|s/l|$.

The amplitude of roll motion has also an effect on the ω_a/ω_1 ratio, as shown in Fig. 7.2.

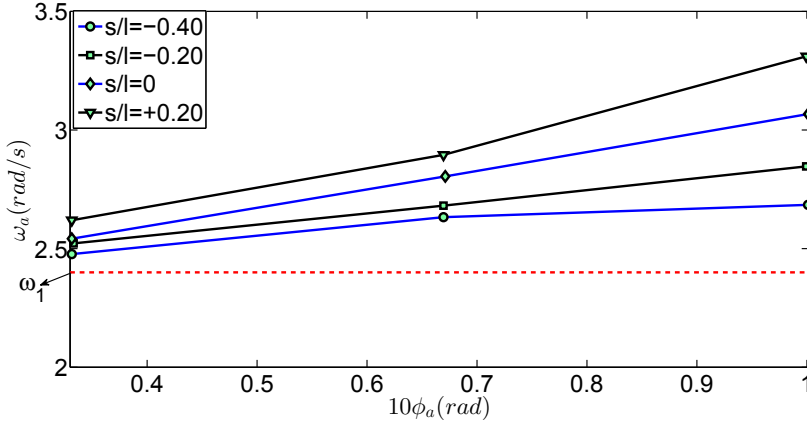


Figure 7.2: ω_a as a function of ϕ_a and s/l . $h/l = 0.06$, [61].

Fig. 7.2 shows that ω_a deviates from ω_1 with increasing the roll amplitude. The effect of s/l is similar, as shown in Fig. 7.1.

It is also evident that the flow pattern is two dimensional in a plane normal to x-axis (ship length axis). So the tank moment is proportional to the tank width and the phase difference ε_r will not be influenced.

7.2 Roll decay tests and cable identifications

In Figs. 7.3 to 7.6, the comparison of numerical and experimental results for roll-decay tests for the fishing vessel with different tank sizes on-board are shown. The water depth in all cases is 3.9cm while the tank width varies.

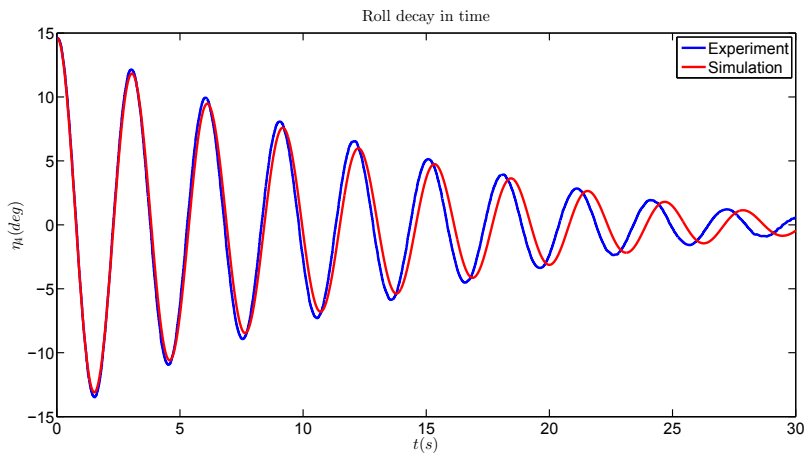


Figure 7.3: Roll decay test for ship with tank (tank width=3.0cm and tank water depth=3.9cm).

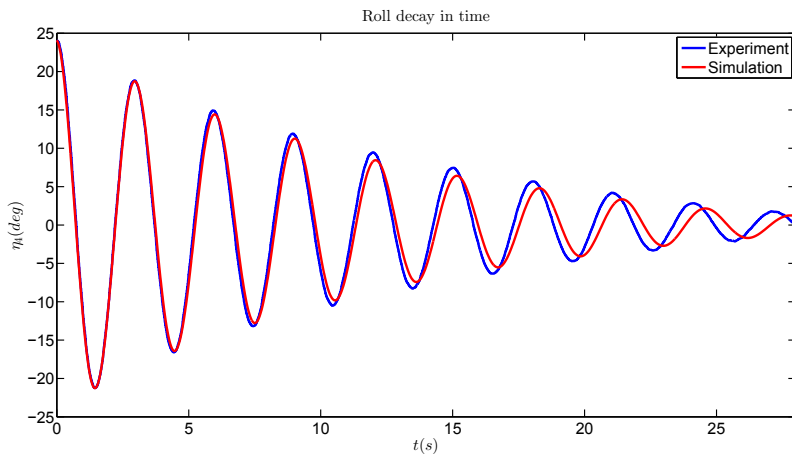


Figure 7.4: Roll decay test for ship with tank (tank width=4.0cm and tank water depth=3.9cm).

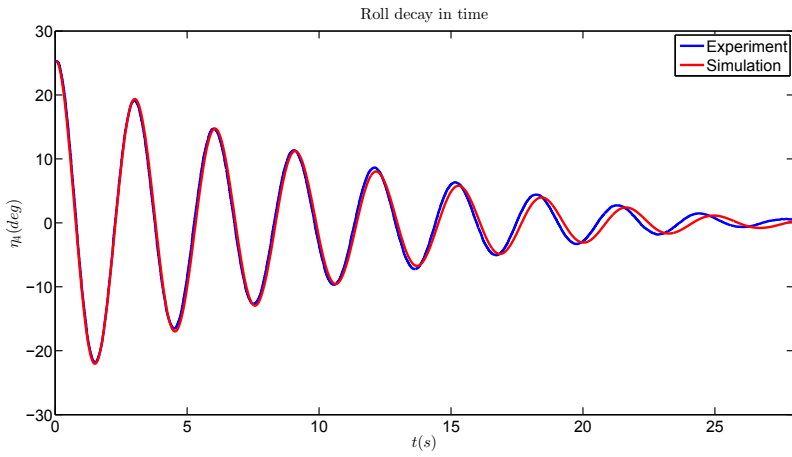


Figure 7.5: Roll decay test for ship with tank (tank width=5.1cm and tank water depth=3.9cm).

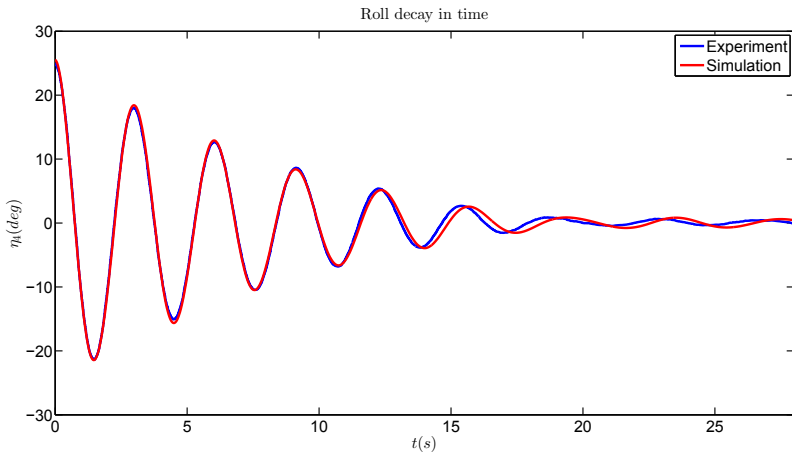


Figure 7.6: Roll decay test for ship with tank (tank width=8.1cm and tank water depth=3.9cm).

From the figures, it can be seen that the damping level provided by the tank is captured very well by the numerical solver. But the natural roll period looks to be overestimated after five or six oscillations. This overestimation seems higher in Fig. 7.3, for the tank with smallest width. This figure shows around 1.5% overestimation after eight oscillations. It should be noted that in all these cases, big tank-roof impacts were observed in the experiments. So lots of splashes and non-linearities happened for all these cases not modelled properly in the numerical solver, as shown by the numerical water evolution inside the tank. These differences might cause the overestimation in the roll natural period.

For having a better picture of the damping level provided by these tanks compared to the case without tank, Fig. 7.7 shows a comparison of the numerical simulation of roll decays with initial roll angle of 25° and with different cases.

We used the numerical simulation for this comparison, because it is important to have the same initial roll angle, and this is hard to find in the experimental data.

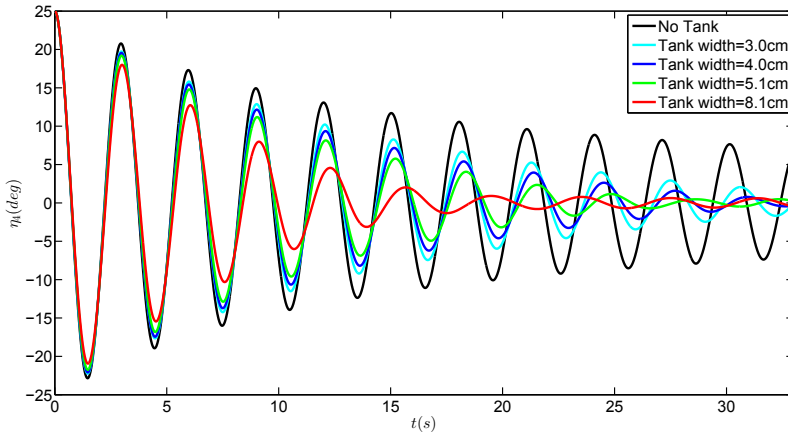


Figure 7.7: Roll-decay simulations for ship with different tank dimensions.

As it can be seen from Fig. 7.7, the tank has a big effect in the roll damping. It can be seen that while after 10 oscillations, the roll amplitude is around 8° in case without tank, it is less than 2° for all other cases with tank. The relation of the damping level and the tank width is also clear in this figure. It can also be seen that the damping due to the tank is not linear and that is why the roll frequency has changed in cases with tanks and this change increases with tank width. This non-linearity of the damping

provided by the tanks has been also observed in the experiments by Bosch et al. [61] which has been mentioned and discussed before in section 3.1.1.2.

Similarly as for the fishing vessel without tank, also for the model with on-board tank, we identified the cable tensions. The tension law for fore cables in this case is as follows:

$$T-T_0 = \begin{cases} 25.3792\Delta l + 935.2816\Delta l^2 - 2573.407\Delta l^3 + 2013.876\Delta l^4; \Delta l_0 < \Delta l < \Delta l_1 \\ T_{min}; \Delta l < \Delta l_0 \end{cases} \quad (7.2)$$

where $T_0 = 4.10N$ is the pretension and $T_{min} = 0$ as explained in Fig. 3.19, $\Delta l_0 = 0$ and $\Delta l_1 = 0.25m$. Moreover, the tension law for $\Delta l > \Delta l_1$ is a linear fit to the curve at Δl_1 .

The tension law for the aft cables is as follows:

$$T-T_0 = \begin{cases} 140.982\Delta l + 451.683\Delta l^2 + 1584.489\Delta l^3 - 6000.0\Delta l^4; \Delta l_0 < \Delta l < \Delta l_1 \\ T_{min}; \Delta l < \Delta l_0 \end{cases} \quad (7.3)$$

where $T_0 = 6.93N$ is the pretension and $T_{min} = 0$ as explained in Fig. 3.19, $\Delta l_0 = 0$ and $\Delta l_1 = 0.25m$.

We then performed the simulations in waves. It should be mentioned that due to the high damping level from the tanks, PR did not occur both in the experiments and numerically without triggering an initial roll angle. After the triggering, PR built up in some cases and reached a steady-state value. In some other cases, the triggered roll angle damped out after some oscillations. As it is discussed and shown in [68], it was observed that the phasing between the roll and heave motions is important in the PR occurrence. It was also observed that the heave and pitch motion phases are mutually dependent, so fixing numerically the phasing of the initial forced roll with the heave motion as in the experiments, will provide the correct phasing between roll and pitch motions, i.e. consistent with the experiments. To achieve this, numerically we enforced a roll moment to the system in the predefined time interval based on the phasing in the experiments. But it was not that straightforward and was performed with two parameters as input, connected with the magnitude of roll moment and its duration, and we had to repeat some cases for several simulations and tuning the two input parameters for the forced roll moment so to achieve a good agreement in the initial roll angle and related phase. Since the simulations in the cases with tank were far more time consuming than those without tank, we tried the best to achieve a similar forced roll angle but it is not the same in all examined cases.

We analyze the test cases with different tank sizes in the following sections.

7.3 Tank width=3.0 cm, tank water depth=3.9 cm

In this section, the simulations for the cases with tank width=3.0cm and water depth=3.9cm are compared against the experiments. Similar to simulations for the cases without tank in the previous chapter, the FFT analysis on the incident waves recorded in the experiments was performed first to identify the actual incident waves. The cases and the wave characteristics are shown in Tab. 7.1.

Table 7.1: Test cases with tank width=3.0cm and tank water depth=3.9cm at $Fn=0$. The frequency ratio $\frac{\omega_{n4}}{\omega_e}$ and the steepness $k\zeta_a$ refer to the prescribed incident waves. In each cell, three elements are given vertically, as follows: the first label indicates the case number, the second value is the wave period in seconds and the last value is the actual incident-wave steepness. A cell with only X indicates that the corresponding test was not performed.

$k\zeta_a \downarrow, \frac{\omega_{n4}}{\omega_e} \rightarrow$	0.48	0.49	0.50	0.51	0.52	0.53
0.05	X	X	C733 1.50 0.050	X	X	X
			C730 1.50 0.101			
0.10	X	X	C729 1.45 0.152	X	X	X
			C728 1.48 0.147			
0.15	0.152	0.147	C721 1.50 0.152	0.147	0.148	C727 1.60 0.145
			C731 1.51 0.183			
0.20	X	X	C732 1.51 0.23	X	X	X

The numerical and experimental parametric-roll results for all the cases with this tank are shown in Tab. 7.2.

Table 7.2: Test cases as given in Table 7.1. For each examined case, the experimental (Exp) and numerical (Num) roll-motion amplitudes in nearly steady-state conditions are given in degrees together with the initial forced roll amplitude. NoPR= no PR occurrence.

$k_{Sa} \downarrow, \frac{\omega_{n4}}{\omega_e} \rightarrow$	0.48	0.49	0.50
Exp 0.05			C733 ($\eta_4(0) = 12.00^\circ \rightarrow NoPR$)
Num 0.05	X	X	($\eta_4(0) = 11.35^\circ \rightarrow NoPR$)
Exp 0.10			C730 ($\eta_4(0) = 16.20^\circ \rightarrow PR10^\circ$)
Num 0.10	X	X	($\eta_4(0) = 14.50^\circ \rightarrow PR16.3^\circ$)
Exp 0.15			C721 ($\eta_4(0) = 10.50^\circ \rightarrow PR15.0^\circ$)
Num 0.15	C729 ($\eta_4(0) = 15.5^\circ \rightarrow NoPR$) ($\eta_4(0) = 11.50^\circ \rightarrow NoPR$)	C728 ($\eta_4(0) = 14.5^\circ \rightarrow PR19.0^\circ$) ($\eta_4(0) = 12.50^\circ \rightarrow PR20.3^\circ$)	($\eta_4(0) = 10.35^\circ \rightarrow PR19.0^\circ$)
Exp 0.20			C731 ($\eta_4(0) = 12.10^\circ \rightarrow PR15.0^\circ$)
Num 0.20	X	X	($\eta_4(0) = 9.0^\circ \rightarrow PR18.0^\circ$)
Exp 0.25			C732 ($\eta_4(0) = 9.14^\circ \rightarrow PR12.5^\circ$)
Num 0.25	X	X	($\eta_4(0) = 8.0^\circ \rightarrow PR14.5^\circ$)

Continuation of Tab. 7.2

$k\zeta_a \downarrow, \frac{\omega_{m4}}{\omega_e} \rightarrow$	0.51	0.52	0.53
Exp 0.05			
Num 0.05	X	X	X
Exp 0.10			
Num 0.10	X	X	X
Exp 0.15			
Num 0.15	C723 ($\eta_4(0) = 13.8^\circ \rightarrow PR12.5^\circ$) ($\eta_4(0) = 12.90^\circ \rightarrow PR17.5^\circ$)	C726 ($\eta_4(0) = 10.67^\circ \rightarrow PR12.2^\circ$) ($\eta_4(0) = 10.75^\circ \rightarrow PR15.5^\circ$)	C727 ($\eta_4(0) = 17.2^\circ \rightarrow NoPR$) ($\eta_4(0) = 15.60^\circ \rightarrow PR13.8^\circ$)
Exp 0.20			
Num 0.20	X	X	X
Exp 0.25			
Num 0.25	X	X	X

The information in the table for nominal $k\zeta_a = 0.05$ and frequency ratio 0.50 for instance shows that in the test C733, with triggering a forced roll motion of 12.5° , no parametric roll occurred. In the numerical simulation also the roll motion of 11.35° could not trigger the parametric resonance in roll. With increasing the wave steepness to 0.10, the parametric resonance with steady-state value of 10° is obtained by forcing a 16.20° roll motion. A parametric roll of 16.3° is also obtained from forced roll motion of 14.5° in the numerical simulations.

The comparison of numerical and experimental roll-motion time histories of the mentioned cases is shown in Figs. 7.8 to 7.17.

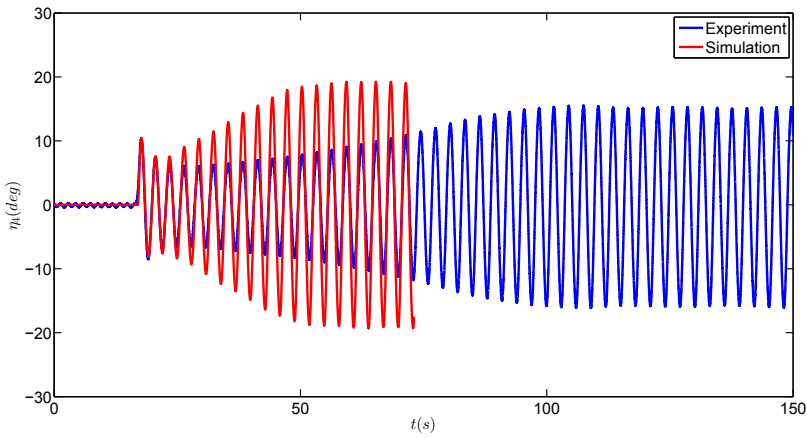


Figure 7.8: Comparison of numerical simulation and experimental results of roll motion for case C721.

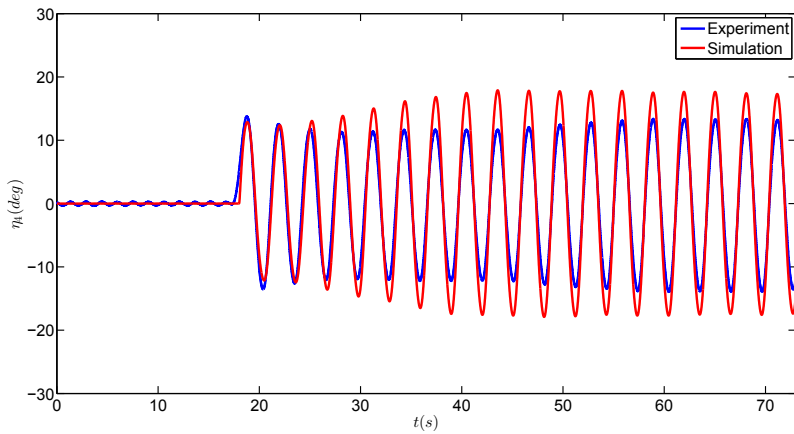


Figure 7.9: Comparison of numerical simulation and experimental results of roll motion for case C723.

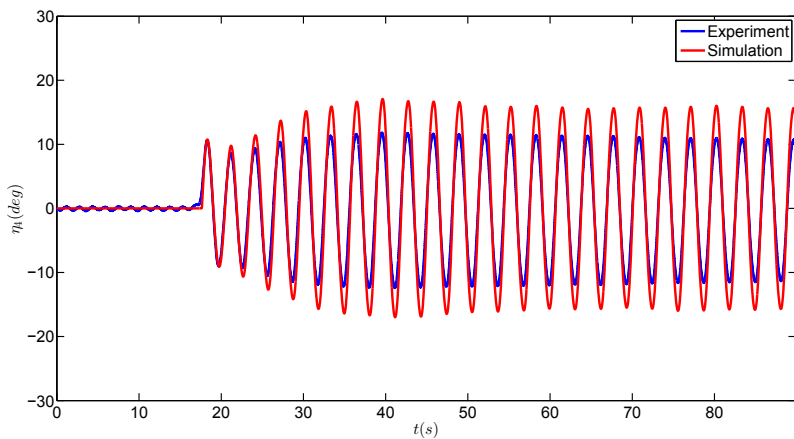


Figure 7.10: Comparison of numerical simulation and experimental results of roll motion for case C726.

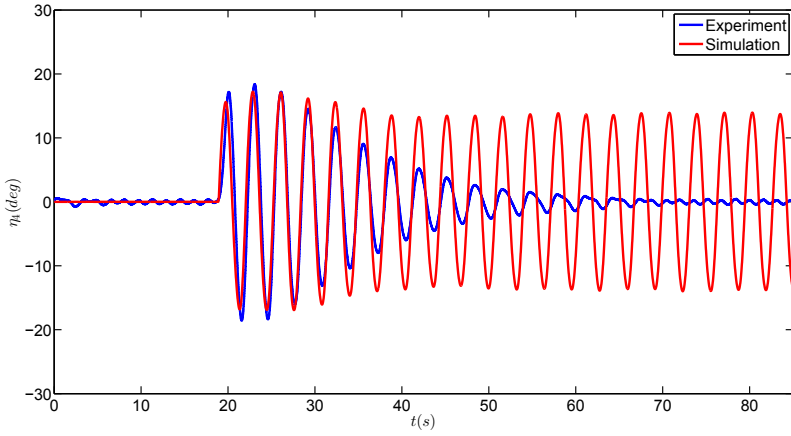


Figure 7.11: Comparison of numerical simulation and experimental results of roll motion for case C727.

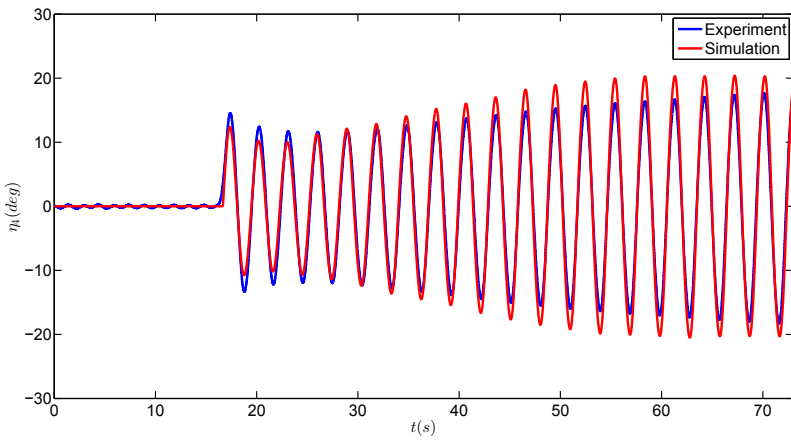


Figure 7.12: Comparison of numerical simulation and experimental results of roll motion for case C728.

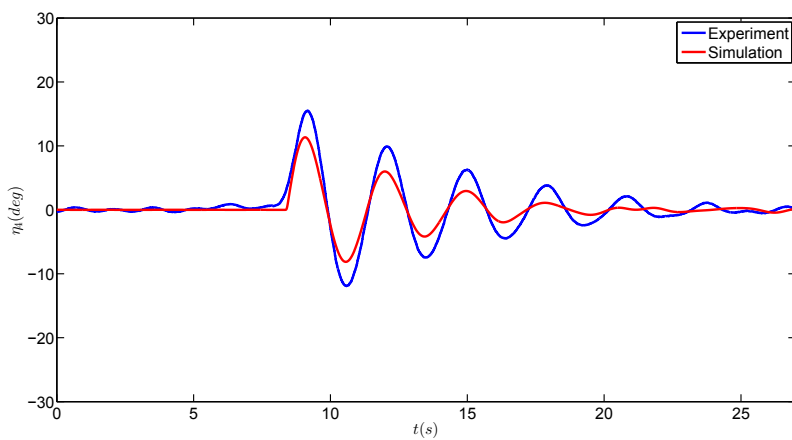


Figure 7.13: Comparison of numerical simulation and experimental results of roll motion for case C729.

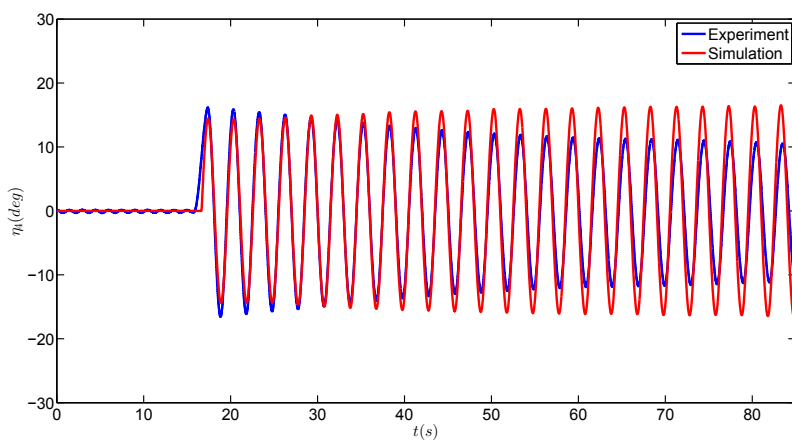


Figure 7.14: Comparison of numerical simulation and experimental results of roll motion for case C730.

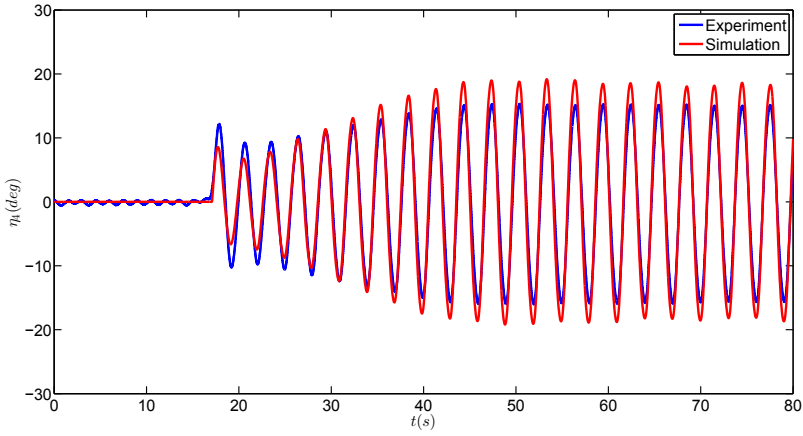


Figure 7.15: Comparison of numerical simulation and experimental results of roll motion for case C731.

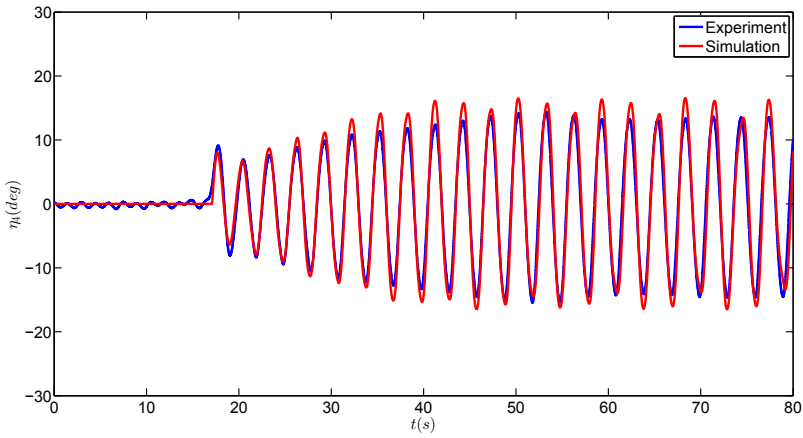


Figure 7.16: Comparison of numerical simulation and experimental results of roll motion for case C732.

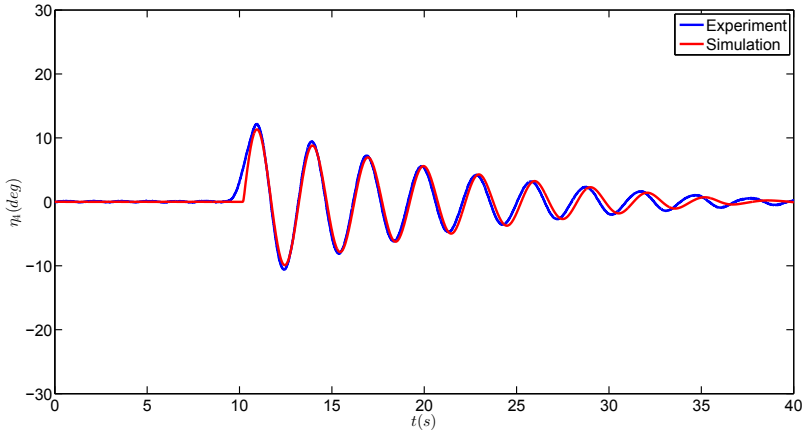


Figure 7.17: Comparison of numerical simulation and experimental results of roll motion for case C733.

From these figures, the PR occurrence and the PR roll amplitude is captured by the numerical simulations for all cases except C727.

In the experimental case C727, a forced roll motion of 17.2° could not result in PR while in the numerical simulation, triggering a forced roll of 15.6° results in PR with steady-state amplitude of 13.8° . By looking at the Tabs. 7.1 and 7.2, it can be seen that the case C727 is in the far right of the experimental table. Using the nominal wave parameters, we can see that for the wave steepness $k\zeta_a = 0.15$, PR occurred experimentally with frequency ratio $\frac{\omega_{n4}}{\omega_e} = 0.49$ to 0.52 . No PR was observed instead for frequency ratio $\frac{\omega_{n4}}{\omega_e} = 0.48$ and 0.53 . This indicates that these two cases are at the stability border for wave steepness $k\zeta_a = 0.15$. It means that we expect no PR also in cases with higher frequency ratio than case C727 and lower frequency ratio than C729 and the same wave steepness. The numerical simulations captured the left stability border of frequency ratio at wave steepness $k\zeta_a = 0.15$ at case C729 but not the right stability border at case C727.

By looking at the experimental case C733, with frequency ratio $\frac{\omega_{n4}}{\omega_e} = 0.50$, and nominal wave steepness $k\zeta_a = 0.05$, no PR was observed. It seems that the wave steepness is not enough for overcoming the roll damping for getting the vessel into the instability zone. By increasing the wave steepness to $k\zeta_a = 0.10$, we see that a PR with steady-state amplitude of 10° occurs. With increasing the wave steepness to higher values the PR always occurred on all examined cases. So it shows us that the case C733 is the lower

stability border in the wave steepness for the frequency ratio $\frac{\omega_{n4}}{\omega_e} = 0.50$. Even though it is in the stability border, the numerical simulation is able to provide a similar result for this case as in the experiment.

Since the numerical simulation for the cases with tank is time consuming (due to the sloshing CFD solver), the simulation is performed until the roll motion achieves a steady-state amplitude. Only this PR parameter is compared with the experiments, while the build-up phase of the PR is not taken as a part of the solver assessment, based on the discussion in the previous chapter.

7.4 Tank width=4.0 cm, tank water depth=3.9 cm

In this section, we analyze the results for the cases with tank width=4.0cm and water depth=3.9cm. First the FFT analysis of the incident waves in the experiments is performed and the wave characteristics are shown in Tab. 7.3.

Table 7.3: Test cases with tank width=4.0cm and tank water depth=3.9cm at $Fn=0$. The frequency ratio and the steepness $k\zeta_a$ refer to the prescribed incident waves. In each cell, three elements are given vertically, as follows: the first label indicates the case number, the second value is the wave period in seconds and the last value is the actual incident-wave steepness. A cell with only X indicates that the corresponding test was not performed.

$k\zeta_a \downarrow, \frac{\omega_{n4}}{\omega_e} \rightarrow$	0.48	0.49	0.50	0.51	0.52	0.53	
0.10	X	X	C744 1.52 0.102	X	X	X	
	C742 1.46 0.154	C739 1.49 0.151	C735 1.53 0.140	C736 1.55 0.134	C737 1.58 0.127	C738 1.61 0.136	
	0.20	X	X	C743 1.52 0.171	X	X	X
0.25		X	X	C745 1.53 0.21	X	X	X

The experimental and numerical parametric-roll results of the cases with

this tank are shown in Tab. 7.4.

Table 7.4: Test cases as given in Tab. 7.3. For each examined case, the experimental (Exp) and numerical (Num) roll-motion amplitudes in nearly steady-state conditions are given in degrees together with the initial forced roll amplitude. NoPR= no PR occurrence.

$k_{S\alpha} \downarrow \frac{\omega_{n4}}{\omega_e} \rightarrow$	0.48	0.49	0.50
Exp 0.10			C744 ($\eta_4(0) = 14.20^\circ \rightarrow NoPR$)
Num 0.10	X	X	($\eta_4(0) = 12.10^\circ \rightarrow NoPR$)
Exp 0.15	($\eta_4(0) = 15.38^\circ \rightarrow NoPR$)	($\eta_4(0) = 11.60^\circ \rightarrow PR12.30^\circ$)	C735 ($\eta_4(0) = 13.40^\circ \rightarrow NoPR$)
Num 0.15	($\eta_4(0) = 15.60^\circ \rightarrow NoPR$)	($\eta_4(0) = 13.10^\circ \rightarrow PR19.30^\circ$)	($\eta_4(0) = 12.80^\circ \rightarrow PR17.50^\circ$)
Exp 0.20			C743 ($\eta_4(0) = 14.50^\circ \rightarrow PR15.0^\circ$)
Num 0.20	X	X	($\eta_4(0) = 11.65^\circ \rightarrow PR16.90^\circ$)
Exp 0.25			C745 ($\eta_4(0) = 7.50^\circ \rightarrow PR15.0^\circ$)
Num 0.25	X	X	($\eta_4(0) = 9.7^\circ \rightarrow PR16.0^\circ$)

Continuation of Tab. 7.4

$k\zeta_a \downarrow, \omega_e \rightarrow$	0.51	0.52	0.53
Exp 0.10			
Num 0.10	X	X	X
Exp 0.15			
Num 0.15	C736 ($\eta_4(0) = 13.23^\circ \rightarrow PR10.0^\circ$) ($\eta_4(0) = 12.90^\circ \rightarrow PR15.88^\circ$)	C737 ($\eta_4(0) = 18.50^\circ \rightarrow PR11.50^\circ$) ($\eta_4(0) = 18.0^\circ \rightarrow PR13.50^\circ$)	C738 ($\eta_4(0) = 12.5^\circ \rightarrow NoPR$) ($\eta_4(0) = 12.20^\circ \rightarrow PR13.0^\circ$)
Exp 0.20			
Num 0.20	X	X	X
Exp 0.25			
Num 0.25	X	X	X

It can be seen that in all cases (except two of them), the PR occurrence and the PR amplitude are in acceptable agreement.

The comparison of the numerical and experimental roll-motion time histories for these cases is shown in Figs. 7.18 to 7.26.

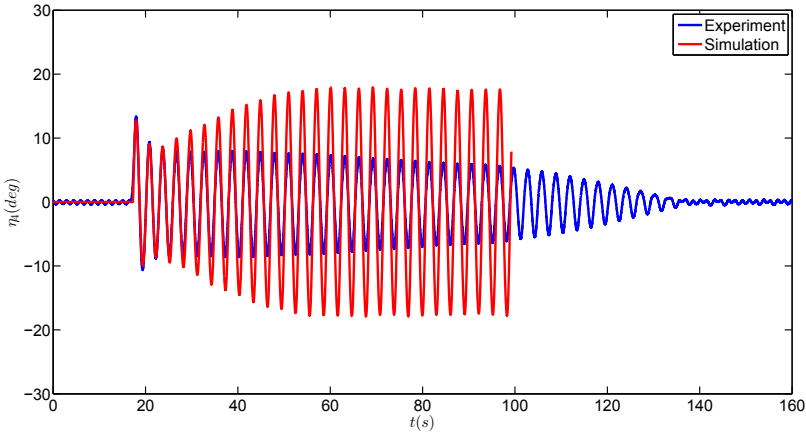


Figure 7.18: Comparison of numerical simulation and experimental results of roll motion for case C735.

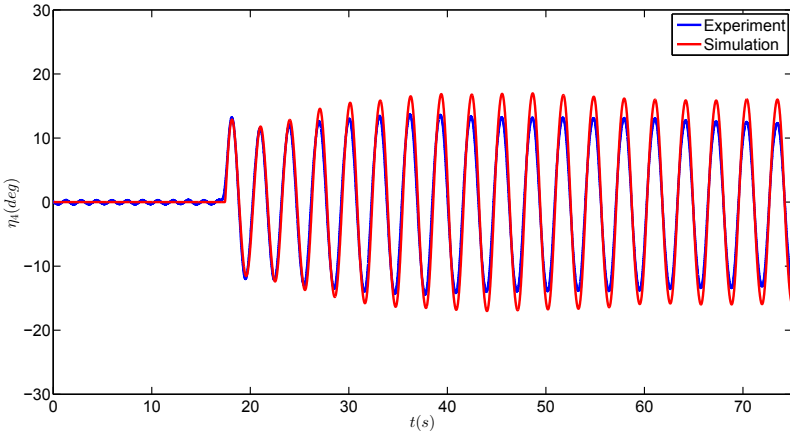


Figure 7.19: Comparison of numerical simulation and experimental results of roll motion for case C736.

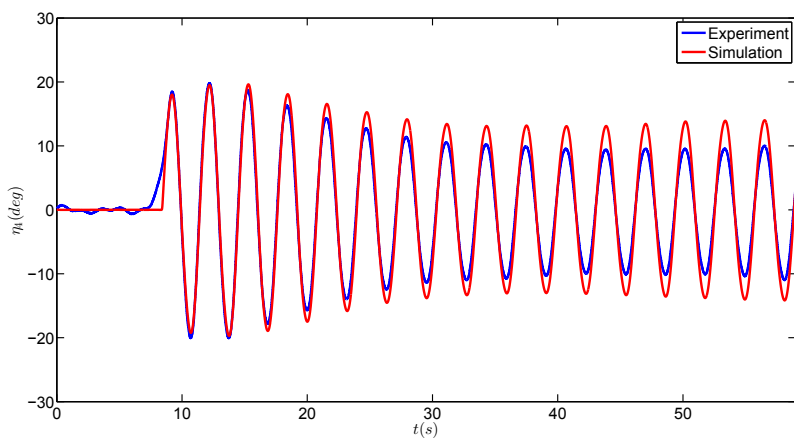


Figure 7.20: Comparison of numerical simulation and experimental results of roll motion for case C737.

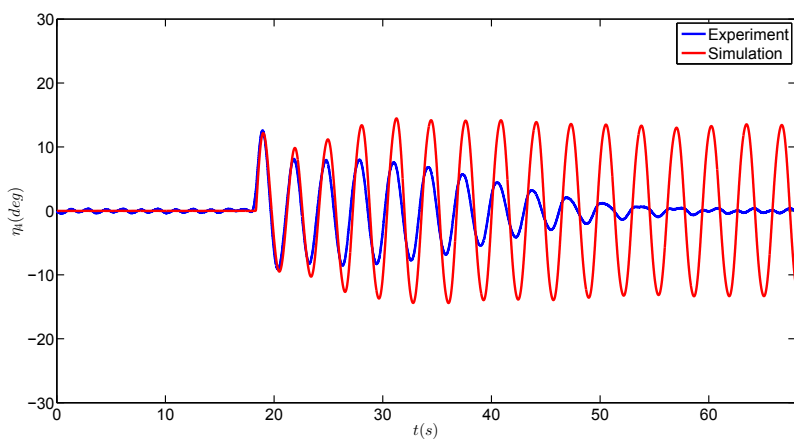


Figure 7.21: Comparison of numerical simulation and experimental results of roll motion for case C738.

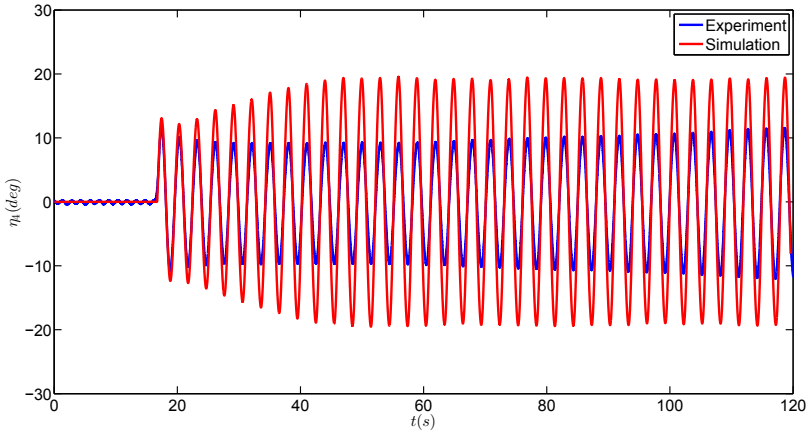


Figure 7.22: Comparison of numerical simulation and experimental results of roll motion for case C739.

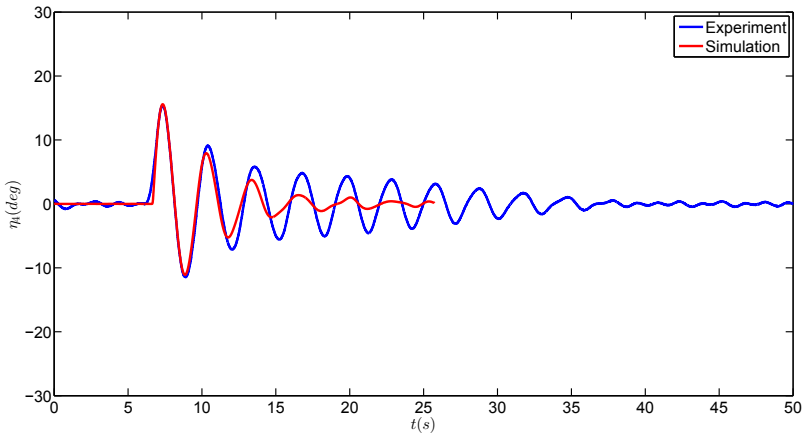


Figure 7.23: Comparison of numerical simulation and experimental results of roll motion for case C742.

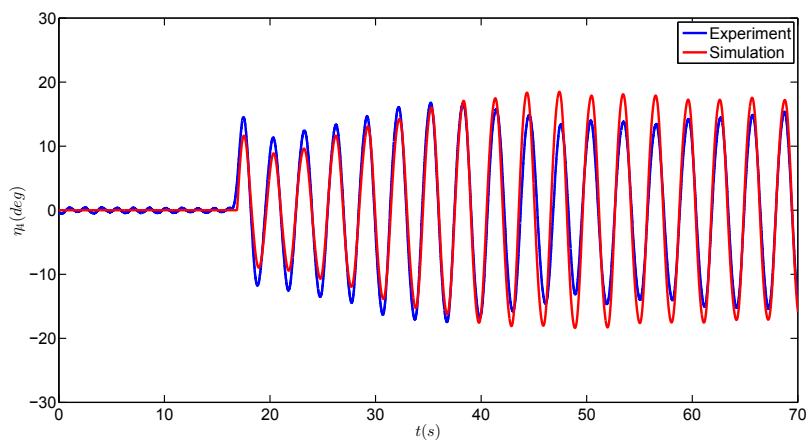


Figure 7.24: Comparison of numerical simulation and experimental results of roll motion for case C743.

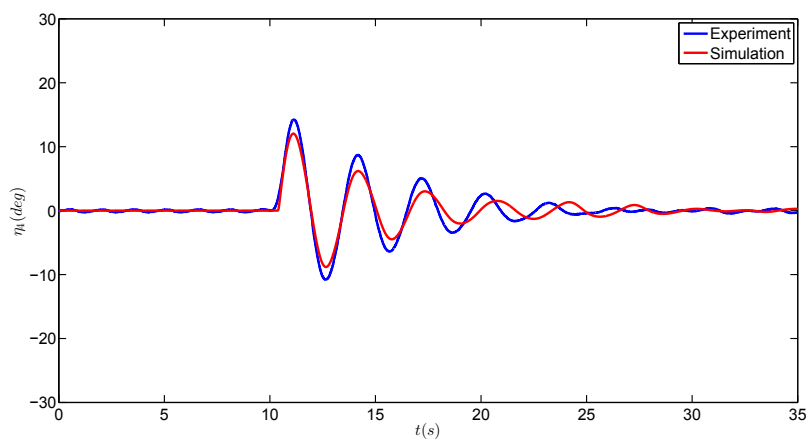


Figure 7.25: Comparison of numerical simulation and experimental results of roll motion for case C744.

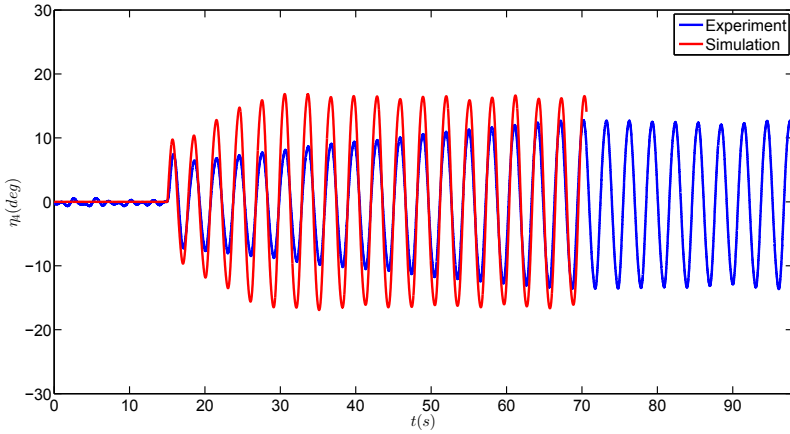


Figure 7.26: Comparison of numerical simulation and experimental results of roll motion for case C745.

We can see that the PR occurrence is captured in all cases by the numerics expect for cases C735 and C738. We try to explain why it is like that.

By looking at the table of experimental results (Tabs. 7.3 to 7.4), for the case C744 with nominal frequency ratio $\frac{\omega_{n4}}{\omega_e} = 0.50$ and nominal wave steepness $k\zeta_a = 0.10$ we see that no PR occurred in the experiments. It means that either the wave is not steep enough for triggering the PR or the roll damping is too high. Fig 7.25 shows that the forced roll motion of 14.2° is damped out in less than five oscillations. So we expect to get the PR by increasing the wave steepness. By increasing the nominal wave steepness to $k\zeta_a = 0.15$ at the same nominal frequency ratio, we get case C735. From the roll time history in Fig. 7.18, also in this case there is no parametric resonance and a forced roll of 13.4° is damped out in time. However, the experimental roll shows that the case must be close to the instability border because the decay in time is not as fast as for case C744, even though the roll is forced with similar initial amplitude. In fact, for case C735, it takes more than 35 oscillations for the roll to be damped out. The fact that many oscillations are needed for the roll to die out might be also due to the incident wave in the experiments. Because if the wave changes the amplitude, it bring the ship out of the instability zone. With increasing the wave steepness to $k\zeta_a = 0.20$ we get case C743. In this case, the same level of forced roll motion as for cases C744 and C735 leads to a PR of almost 15.0° as could be seen in Fig. 7.24. So these three cases

clearly show that case C735 is at the instability border. As it was mentioned before, the results at the border are very sensitive to involved parameters and the experimental and numerical uncertainties might be enough to take the case into or out of the instability zone. The numerical result for case C744 is out of instability zone as for the experiments. It also shows a PR result with steady-state value of 16.9° for case C743, which again is similar to experiments. But for case C735, it is different from the experimental results and shows a PR with steady-state value of 17.5° .

For finding the right limit in nominal frequency ratio of the instability region for the cases with nominal wave steepness of $k\zeta_a = 0.15$, we should check the results for cases C736, C737 and C738. We can see that case C736, with lowest frequency ratio among the three, PR was observed with a steady-state value of 10.0° . By increasing the frequency ratio to $\frac{\omega_{n4}}{\omega_e} = 0.52$, PR with a steady-state value of 11.5° was still observed. In case C738 with frequency ratio $\frac{\omega_{n4}}{\omega_e} = 0.53$, the forced roll motion of 12.5° was damped out after 10 oscillations. It shows that this case is at the instability border and one can expect not to see any PR for frequency ratios higher than 0.53. The numerical results for cases C736 and C737 showed PR similar as in the experiments. But in case C738, the numerical results are different than experiments. The reason could be explained again as the case being at the instability border.

7.5 Tank width=5.1 cm, tank water depth=3.9 cm

In this section, we analyze the results for the cases with tank width=5.1cm and water depth=3.9cm. The cases and the wave characteristics (after doing the FFT on the incident waves in experiments) are shown in Tab. 7.5.

Table 7.5: Test cases with tank width=5.1cm and tank water depth=3.9cm at $Fn=0$. The frequency ratio and the steepness $k\zeta_a$ refer to the prescribed incident waves. In each cell, three elements are given vertically, as follows: the first label indicates the case number, the second value is the wave period in seconds and the last value is the actual incident-wave steepness. A cell with only X indicates that the corresponding test was not performed.

$k\zeta_a \downarrow, \frac{\omega_{n4}}{\omega_e} \rightarrow$	0.48	0.49	0.50	0.51	0.52
			C751 1.53		
0.10	X	X	0.096	X	X
		C750 1.50	C746 1.53	C772 1.56	C773 1.59
0.15	X	0.135	0.134	0.137	0.147
		C776 1.46	C755 1.50	C752 1.53	C753 1.55
0.20	0.186	0.172	0.186	0.184	0.185
		C759 1.47	C757 1.50	C756 1.53	C758 1.59
0.25	0.220	0.221	0.220	X	0.230

The experimental and numerical parametric-roll results of the cases with this tank is shown in Tab. 7.6.

Table 7.6: Test cases as given in Tab. 7.5. For each examined case, the experimental (Exp) and numerical (Num) roll-motion amplitudes in nearly steady-state conditions are given in degrees together with the initial forced roll amplitude. NoPR= no PR occurrence.

$k\zeta_a \downarrow, \frac{\omega_{n4}}{\omega_c} \rightarrow$	0.48	0.49	0.50
Exp 0.10			C751 ($\eta_4(0) = 21.10^\circ \rightarrow$ NoPR)
Num 0.10	X	X	($\eta_4(0) = 22.0^\circ \rightarrow$ NoPR)
Exp 0.15			C746 ($\eta_4(0) = 21.0^\circ \rightarrow$ PR11.50°)
Num 0.15	X		($\eta_4(0) = 22.10^\circ \rightarrow$ PR15.50°)
Exp 0.20			C752 ($\eta_4(0) = 20.0^\circ \rightarrow$ PR14.5°)
Num 0.20	C776 ($\eta_4(0) = 20.17^\circ \rightarrow$ PR17.5°) ($\eta_4(0) = 16.70^\circ \rightarrow$ PR20.0°)	C755 ($\eta_4(0) = 18.50^\circ \rightarrow$ NoPR) ($\eta_4(0) = 13.50^\circ \rightarrow$ NoPR)	($\eta_4(0) = 20.10^\circ \rightarrow$ PR16.30°)
Exp 0.25			C756 ($\eta_4(0) = 10.67^\circ \rightarrow$ PR13.30°)
Num 0.25	C759 ($\eta_4(0) = 21.0^\circ \rightarrow$ NoPR) ($\eta_4(0) = 18.50^\circ \rightarrow$ NoPR)	C757 ($\eta_4(0) = 12.50^\circ \rightarrow$ NoPR) ($\eta_4(0) = 15.40^\circ \rightarrow$ NoPR)	($\eta_4(0) = 11.90^\circ \rightarrow$ PR13.50°)

Continuation of Tab. 7.6

$k\zeta_a \downarrow \frac{\omega_{n4}}{\omega_e} \rightarrow$	0.51	0.52	0.53
Exp 0.10			
Num 0.10	X	X	
Exp 0.15			
Num 0.15	C772 ($\eta_4(0) = 18.70^\circ \rightarrow PR12.50^\circ$) ($\eta_4(0) = 24.30^\circ \rightarrow PR14.30^\circ$)	C773 ($\eta_4(0) = 23.10^\circ \rightarrow NoPR$) ($\eta_4(0) = 21.3^\circ \rightarrow PR14.0^\circ$)	
Exp 0.20			
Num 0.20	C753 ($\eta_4(0) = 17.30^\circ \rightarrow PR12.50^\circ$) ($\eta_4(0) = 12.80^\circ \rightarrow PR15.0^\circ$)	C754 ($\eta_4(0) = 16.0^\circ \rightarrow NoPR$) ($\eta_4(0) = 15.50^\circ \rightarrow PR12.2^\circ$)	
Exp 0.25			
Num 0.25	X	C758 ($\eta_4(0) = 10.0^\circ \rightarrow NoPR$) ($\eta_4(0) = 9.0^\circ \rightarrow NoPR$)	

The comparison of numerical and experimental roll-motion time histories for the mentioned cases is shown in the Figs. 7.27 to 7.40.

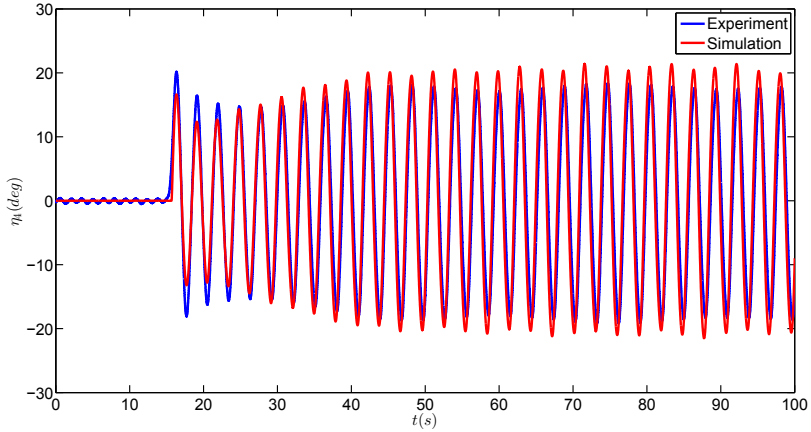


Figure 7.27: Comparison of numerical simulation and experimental results of roll motion for case C776.

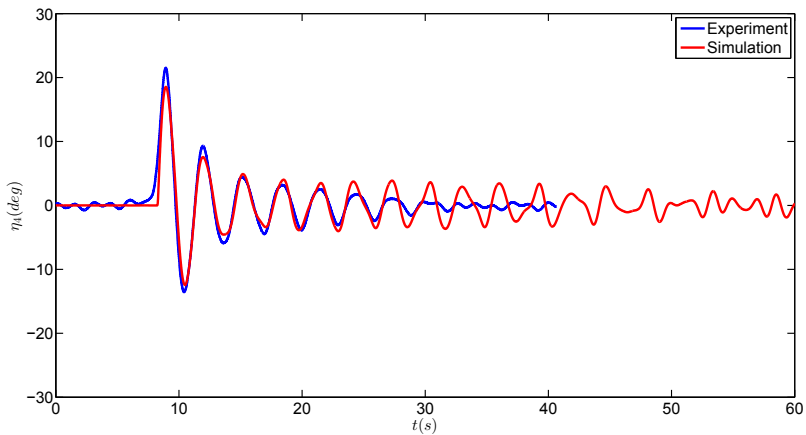


Figure 7.28: Comparison of numerical simulation and experimental results of roll motion for case C759.

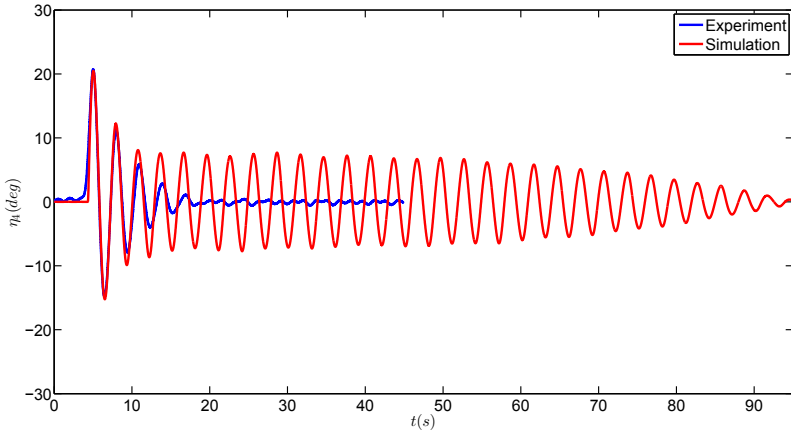


Figure 7.29: Comparison of numerical simulation and experimental results of roll motion for case C750.

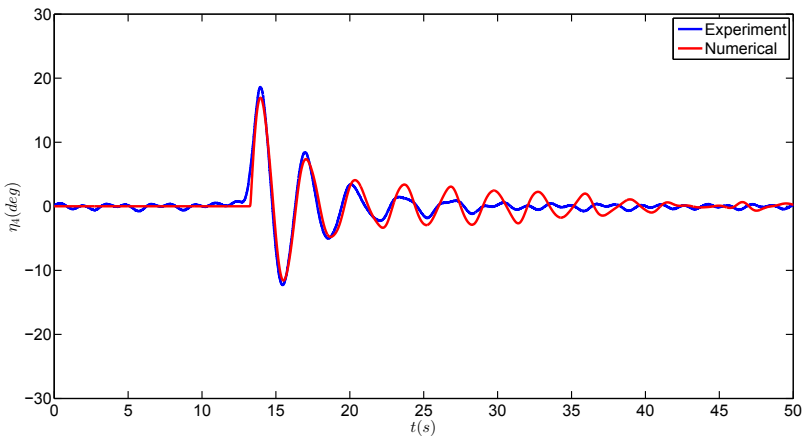


Figure 7.30: Comparison of numerical simulation and experimental results of roll motion for case C755.

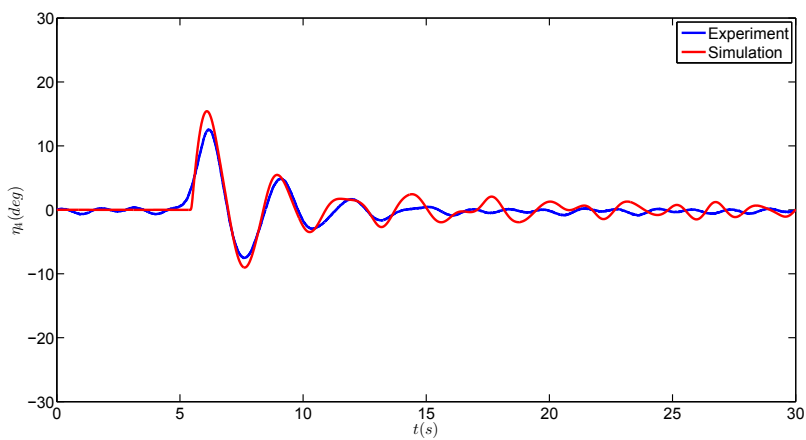


Figure 7.31: Comparison of numerical simulation and experimental results of roll motion for case C757.

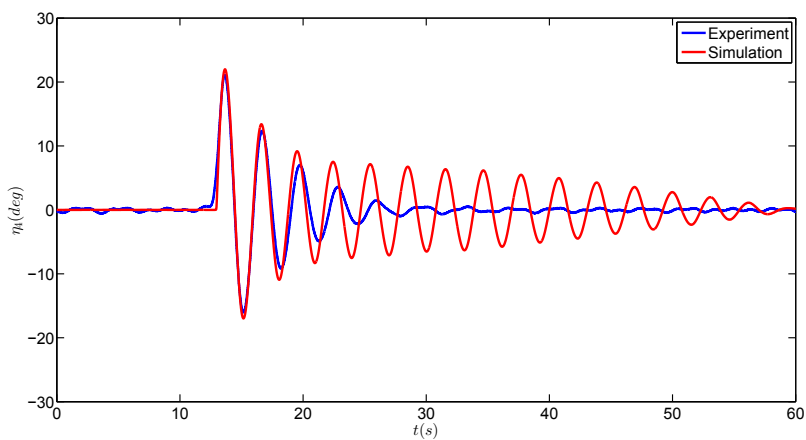


Figure 7.32: Comparison of numerical simulation and experimental results of roll motion for case C751.

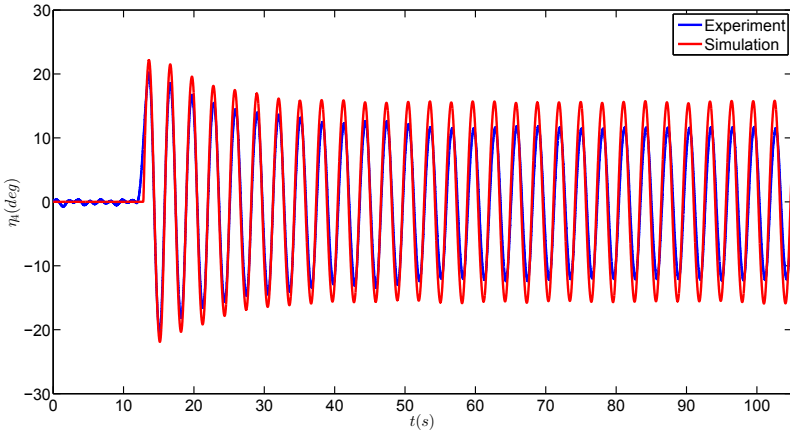


Figure 7.33: Comparison of numerical simulation and experimental results of roll motion for case C746.

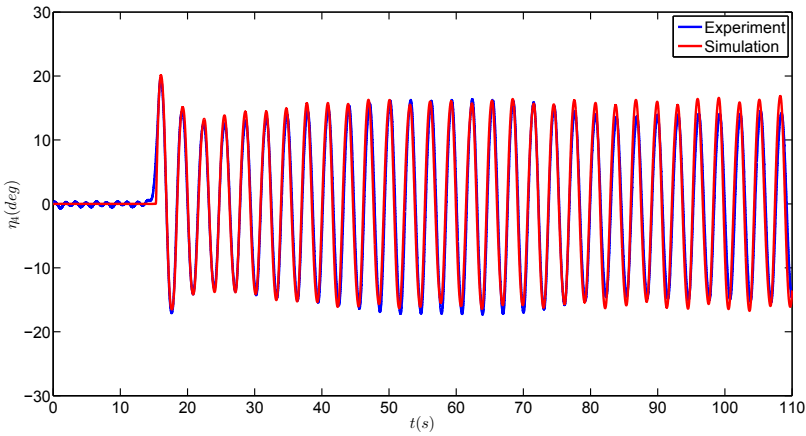


Figure 7.34: Comparison of numerical simulation and experimental results of roll motion for case C752.

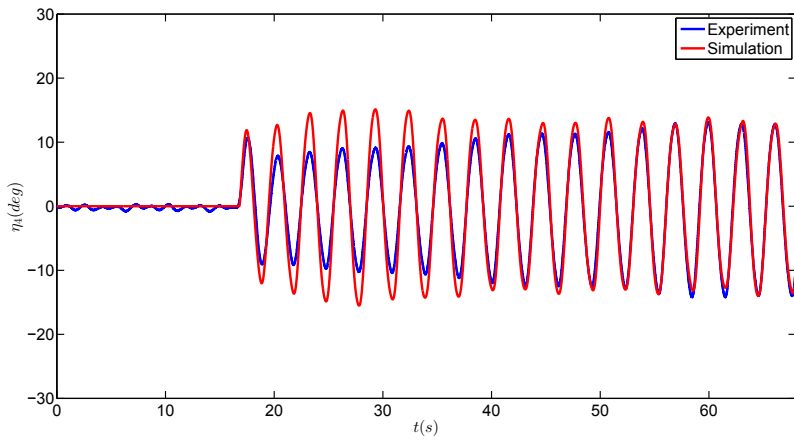


Figure 7.35: Comparison of numerical simulation and experimental results of roll motion for case C756.

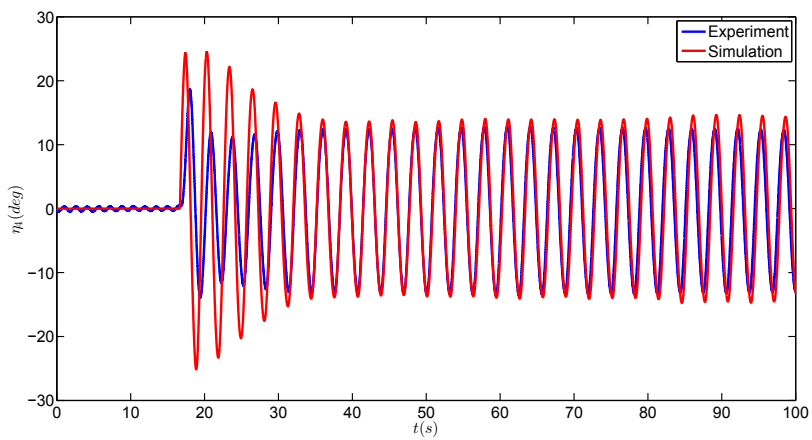


Figure 7.36: Comparison of numerical simulation and experimental results of roll motion for case C772.

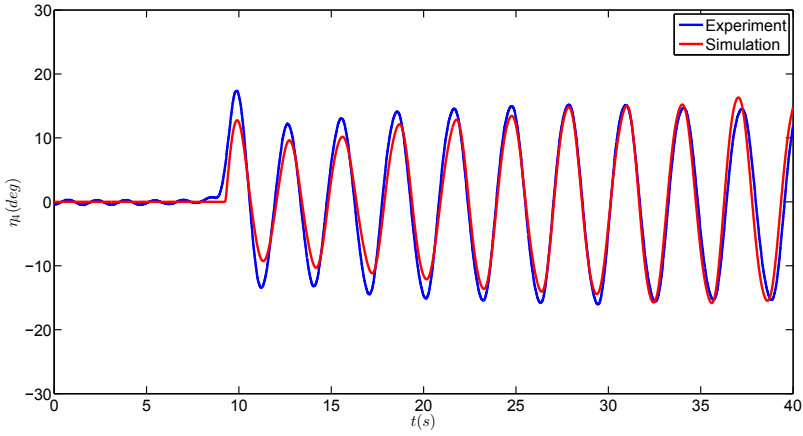


Figure 7.37: Comparison of numerical simulation and experimental results of roll motion for case C753.

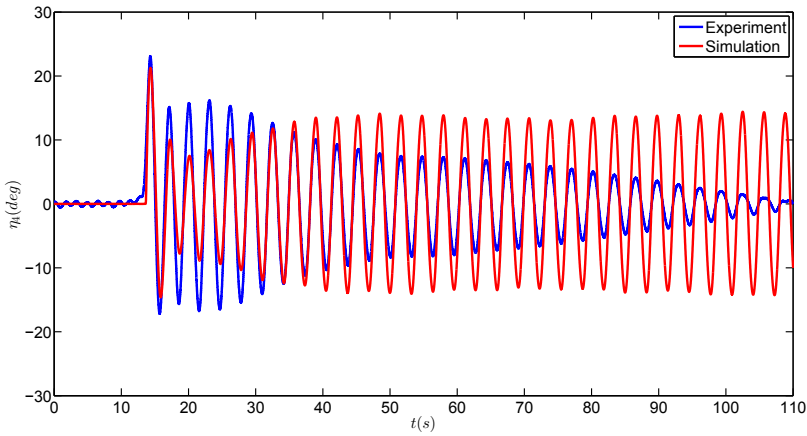


Figure 7.38: Comparison of numerical simulation and experimental results of roll motion for case C773.

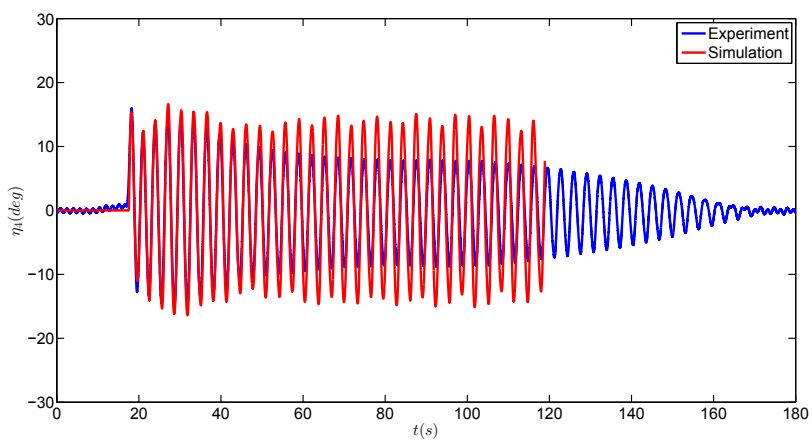


Figure 7.39: Comparison of numerical simulation and experimental results of roll motion for case C754.

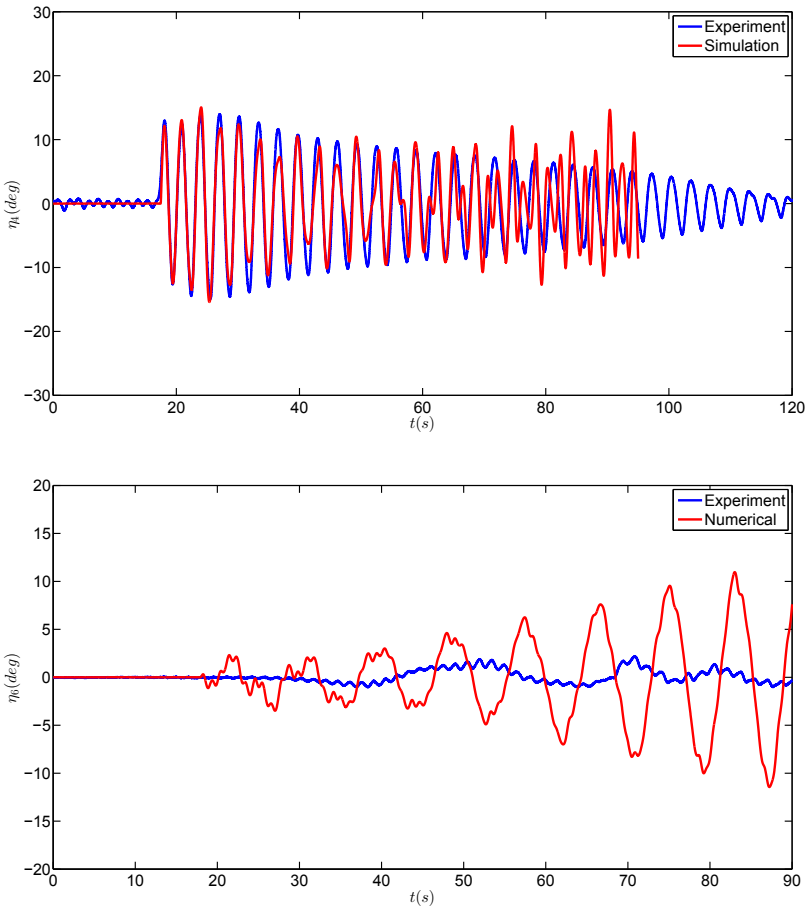


Figure 7.40: Comparison of numerical simulation and experimental results of roll (top figure) and yaw motion (bottom figure) for case C758.

First we explain a phenomenon observed in the numerical result for the case C758 and afterwards, we explain the other results of Tab. 7.6. As it can be seen from the top part of the Fig. 7.40, the numerical roll motion seems to decrease first in the amplitude and then increase again with a frequency twice the roll natural frequency. This increase is not the PR and is due to the coupling to the yaw motion which is shown in the bottom part of Fig. 7.40. It seems that the resonance of the yaw motion (associated with the modelled mooring system) is excited numerically causing the yaw motion to increase. So for eliminating the coupling effect from yaw into the roll motion in this case, the yaw mode of motion was disabled in the solver and the case was rerun. The new results are shown in Fig. 7.41 and it can be seen that the previous increase in roll is now eliminated. Now both experiment and numerical results show no PR occurrence.

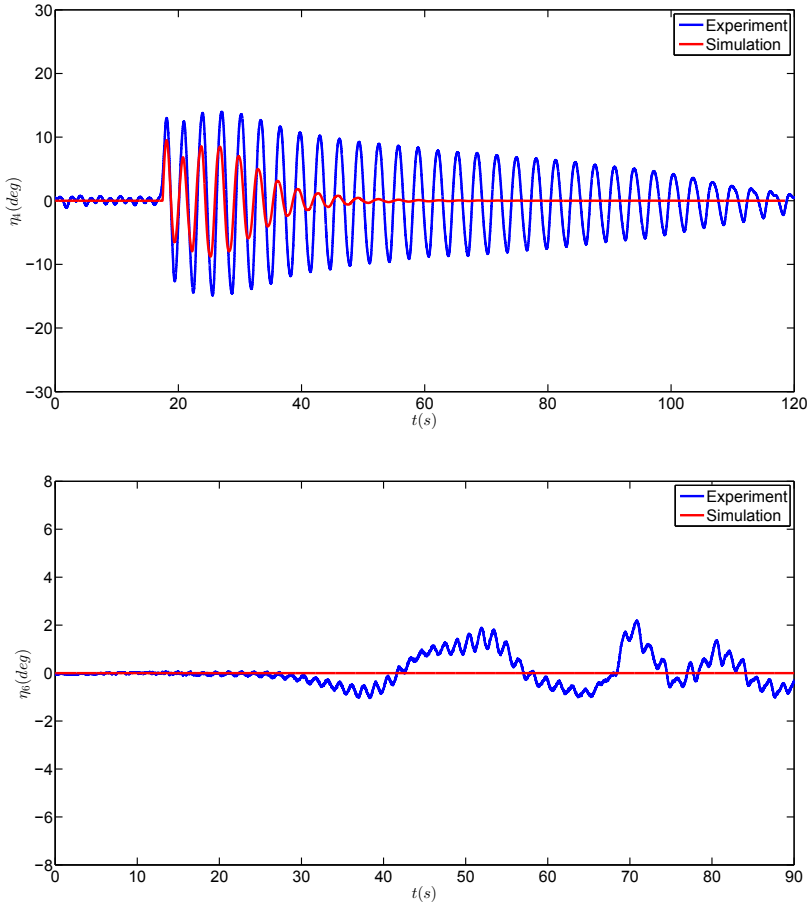


Figure 7.41: Comparison of numerical simulation (with disabled yaw mode) and experimental results of roll (top figure) and yaw motion (bottom figure) for case C758.

Concerning the other cases of this section, cases C754 and C773 highlight differences in PR occurrence while there is consistent in PR occurrence, between numerics and experiments, for the remaining cases.

If we look at the cases with nominal wave steepness $k\zeta_a = 0.15$, PR does not occur for the nominal wave frequency ratio $\frac{\omega_{n4}}{\omega_e} = 0.49$, i.e. for case C750. By increasing the frequency ratio to 0.50 and keeping the same $k\zeta_a$, we get case C746. For this we see that a triggered roll motion with amplitude of 21° leads to PR with steady-state amplitude of 11.5° . This shows that the left instability border at this wave steepness is at a nominal wave frequency

ratio between $\frac{\omega_{n4}}{\omega_e} = 0.49$ to 0.50 . By increasing the frequency ratio to 0.51 we get case C772 for which a PR is observed with amplitude 12.5° . Now increasing the frequency ratio to 0.53 in the experiments, the vessel goes out of the instability zone and no PR occurs. The triggered roll motion with amplitude 23.1° is in fact damped out after 30 oscillations as can be seen in Fig. 7.38. This shows that this case is out of the instability zone but close to the instability border. The numerical simulation shows instead a PR with an amplitude of 14.0° differently from the experimental results. Now if we look at the experimental cases with nominal wave steepness $k\zeta_a = 0.20$ and the wave frequency ratio in the range of $\frac{\omega_{n4}}{\omega_e} = 0.50$ to 0.53 , we see the trend of the results as we expected. A PR with amplitude of 14.5° is observed in case C752 and a PR with amplitude 12.5° in case C753. But no PR is observed for case C754, which is at frequency ratio 0.53 . This shows that this case is at the instability border. As can be seen from Fig. 7.39, the triggered roll for this case takes many oscillations to be damped out and this indicates that this case is out of the instability zone but close to the border. The numerical result for this case shows a PR with amplitude of 12.2° differently from the experimental results.

But trying to find the left instability border of the cases with nominal wave steepness $k\zeta_a = 0.20$, one strange behaviour is observed. For nominal wave frequency ratio 0.50 , i.e for case C752, we observe a PR. Decreasing the frequency ratio to 0.49 , i.e. for case C755, there is no PR experimentally. This might indicate that the instability border is somewhere between frequency ratio 0.49 and 0.50 . But the test C776 with frequency ratio 0.48 , is associated with a PR with amplitude 17.5° , while we expected no PR in this case. The numerical simulation also shows the same behaviour. One reason for this phenomenon could be the fact that in addition to the frequency ratio and the wave steepness, there are some other parameters that influence the PR occurrence here. For example, since the PR does not occur spontaneously for the cases with the tank, a forced roll motion should be triggered at the ship. The amplitude of this triggered roll motion and also the roll-heave phasing are also important in the PR occurrence.

7.6 Tank width=8.1 cm, tank water depth=3.9 cm

In this section, we analyze the results for the cases with tank width=8.1cm and water depth=3.9cm. The cases and the wave characteristics (obtained from FFT of the incident wave in the experiments) are shown in Tab. 7.7.

Table 7.7: Test cases with tank width=8.1cm and tank water depth=3.9cm at $Fn=0$. The frequency ratio and the steepness $k\zeta_a$ refer to the prescribed incident waves. In each cell, three elements are given vertically, as follows: the first label indicates the case number, the second value is the wave period in seconds and the last value is the actual incident-wave steepness. The cell with only X indicates that the corresponding test was not performed.

$k\zeta_a \downarrow, \frac{\omega_{n4}}{\omega_e} \rightarrow$	0.49	0.50	0.51
		C779 1.55	C780 1.58
0.15	X	0.149	0.143
	C777 1.52	C788 1.55	C785 1.58
0.20	0.185	0.193	0.197
	C786 1.52	C787 1.55	C783 1.58
0.25	0.238	0.235	0.251

The experimental and numerical parametric-roll results of the cases with this tank is shown in Tab. 7.8.

Table 7.8: Test cases as given in Tab. 7.7. For each examined case, the experimental (Exp) and numerical (Num.) roll-motion amplitudes in nearly steady-state conditions are given in degrees together with the initial forced roll amplitude. NoPR= no PR occurrence.

$k\zeta_a \downarrow, \frac{\omega_{n4}}{\omega_c} \rightarrow$	0.49	0.50	0.51
Exp 0.15			C780 ($\eta_4(0) = 19.54^\circ \rightarrow$ NoPR)
Num 0.15	X C777	C779 ($\eta_4(0) = 20.9^\circ \rightarrow$ NoPR) C788 ($\eta_4(0) = 19.30^\circ \rightarrow$ NoPR)	($\eta_4(0) = 16.35^\circ \rightarrow$ NoPR) C785 ($\eta_4(0) = 20.3^\circ \rightarrow$ NoPR)
Exp 0.20	($\eta_4(0) = 17.50^\circ \rightarrow$ NoPR)	($\eta_4(0) = 19.84^\circ \rightarrow$ NoPR)	($\eta_4(0) = 16.50^\circ \rightarrow$ NoPR)
Num 0.20	($\eta_4(0) = 15.25^\circ \rightarrow$ NoPR)	($\eta_4(0) = 17.60^\circ \rightarrow$ NoPR)	($\eta_4(0) = 16.50^\circ \rightarrow$ NoPR)
Exp 0.25	C786 ($\eta_4(0) = 22.3^\circ \rightarrow$ NoPR)	C787 ($\eta_4(0) = 20.90^\circ \rightarrow$ PR13.7°)	C783 ($\eta_4(0) = 18.70^\circ \rightarrow$ NoPR)
Num 0.25	($\eta_4(0) = 16.10^\circ \rightarrow$ NoPR)	($\eta_4(0) = 20.20^\circ \rightarrow$ NoPR)	($\eta_4(0) = 18.10^\circ \rightarrow$ NoPR)

The comparison of the numerical and experimental roll-motion time histories for the mentioned cases is shown in Figs. 7.42 to 7.49.

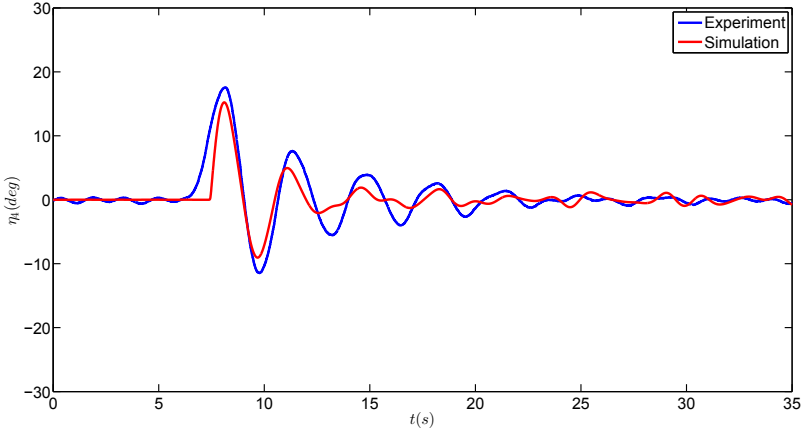


Figure 7.42: Comparison of numerical simulation and experimental results of roll motion for case C777.

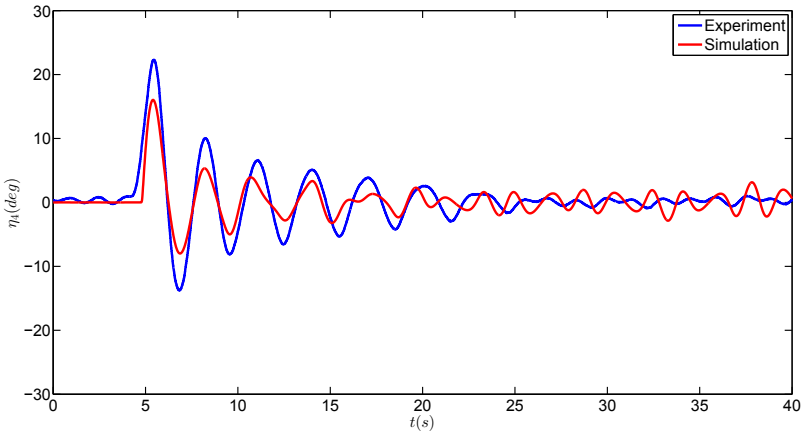


Figure 7.43: Comparison of numerical simulation and experimental results of roll motion for case C786.

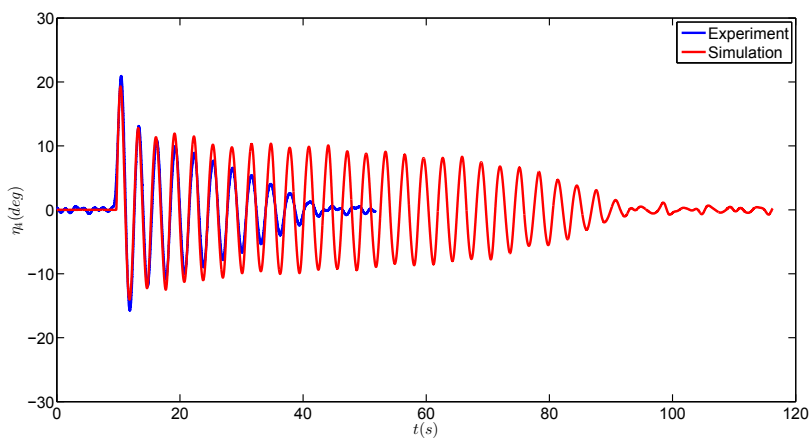


Figure 7.44: Comparison of numerical simulation and experimental results of roll motion for case C779.

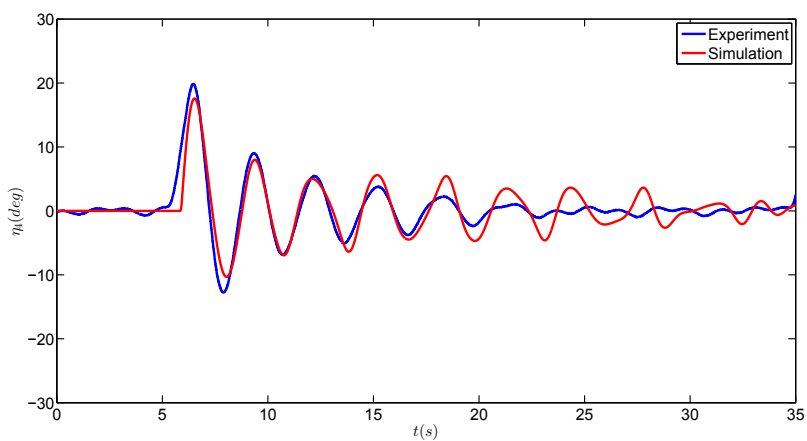


Figure 7.45: Comparison of numerical simulation and experimental results of roll motion for case C788.

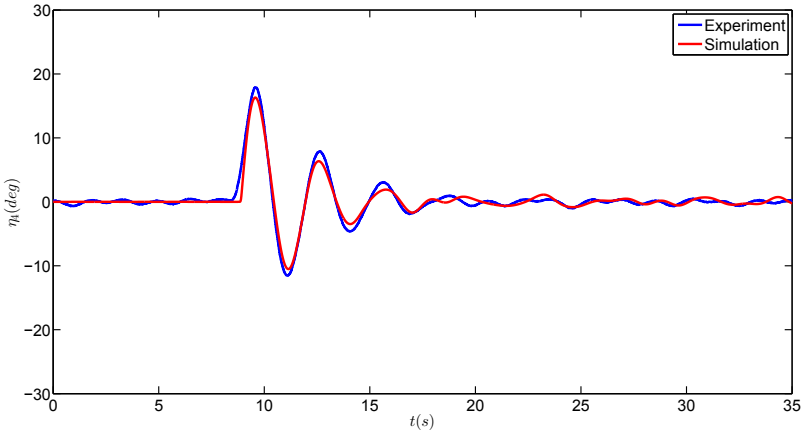


Figure 7.46: Comparison of numerical simulation and experimental results of roll motion for case C780.

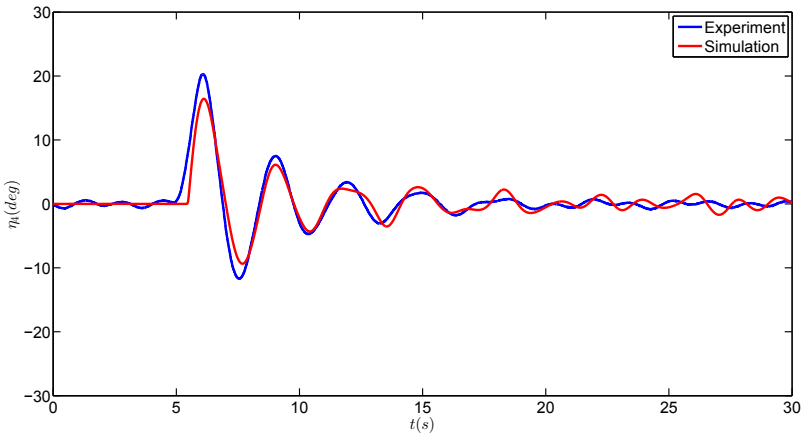


Figure 7.47: Comparison of numerical simulation and experimental results of roll motion for case C785.

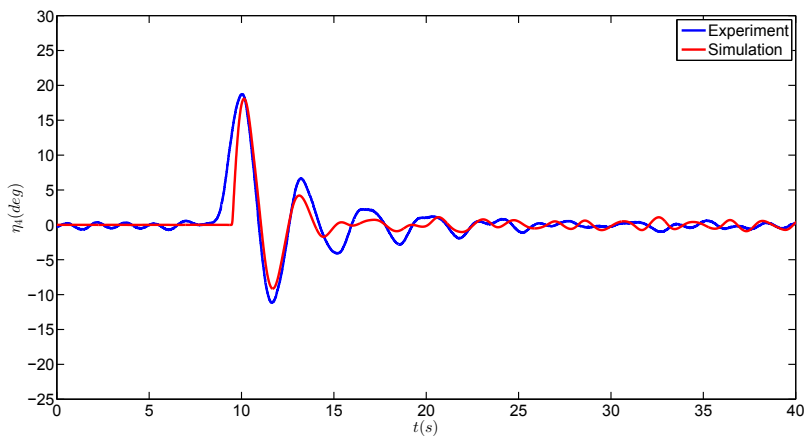


Figure 7.48: Comparison of numerical simulation and experimental results of roll motion for case C783.

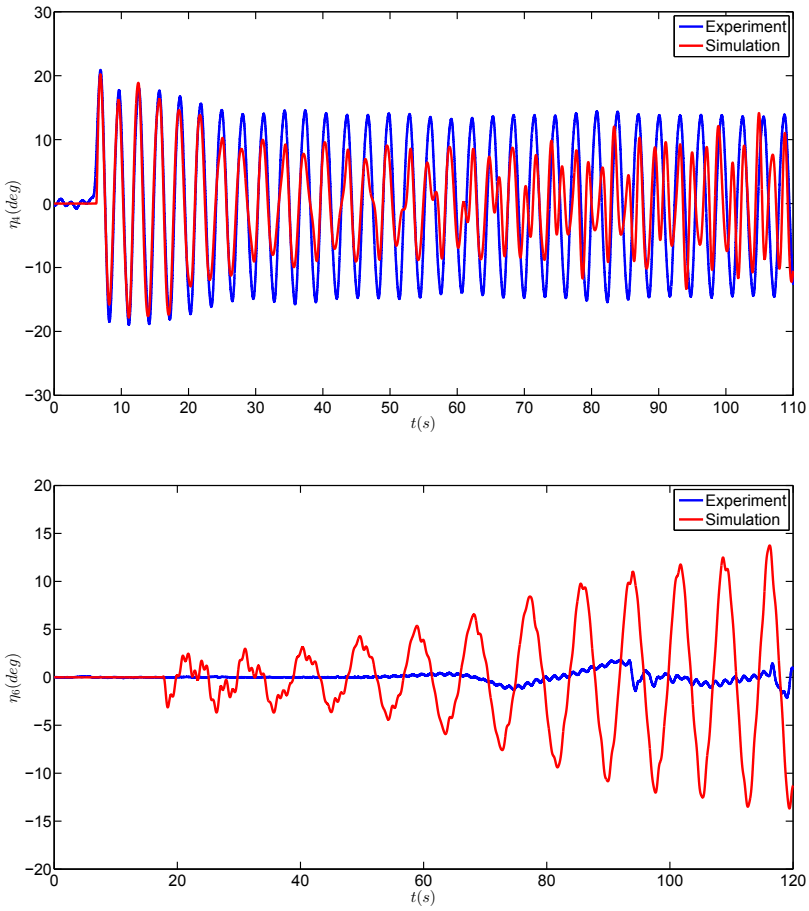


Figure 7.49: Comparison of numerical simulation and experimental results of roll (top figure) and yaw motion (bottom figure) for case C787.

Because the tank width for the cases of this section is quite large, we expect to get a substantial roll-damping effect from the tank. In the experimental cases, triggering the roll motion with big amplitudes even around 20° did not result in PR and damped out after some oscillations in all cases except for case C787. Case C787 has the highest tested nominal wave steepness $k\zeta_a = 0.25$ and nominal frequency ratio $\frac{\omega_{nd}}{\omega_e} = 0.50$. This case is in the center of the instability zone and with a high incident wave steepness leading to a PR occurrence. Triggering a roll motion of amplitude 20.9° resulted in a PR with amplitude 13.7° . The numerical simulation shows no PR for all cases without PR experimentally. Case C787 deserves a more in-depth discussion.

Examining the roll for this case (top plot of Fig. 7.49), one could be tempted to say that also numerically there is a PR as in the experiments. But this is not exactly true. Similarly to case C758, previously discussed, the numerical roll motion of case C787 decreases first and then increases in amplitude with a frequency twice the roll natural frequency. This feature is not documented by the experimental roll and suggests a different phenomenon occurring in the numerical case. This increase does not correspond to a PR and seems to be due to the coupling to the yaw motion, which is shown in the bottom part of Fig. 7.49. It seems that the resonance of the yaw is excited leading to an increase in this motion. So as we did for case C758 in the previous section, for eliminating the coupling effect from yaw into the roll motion in case C758, the yaw mode was disabled in the solver and the case was rerun. The new results are shown in Fig. 7.50. In this case numerically there is no PR, differently from the experiments.

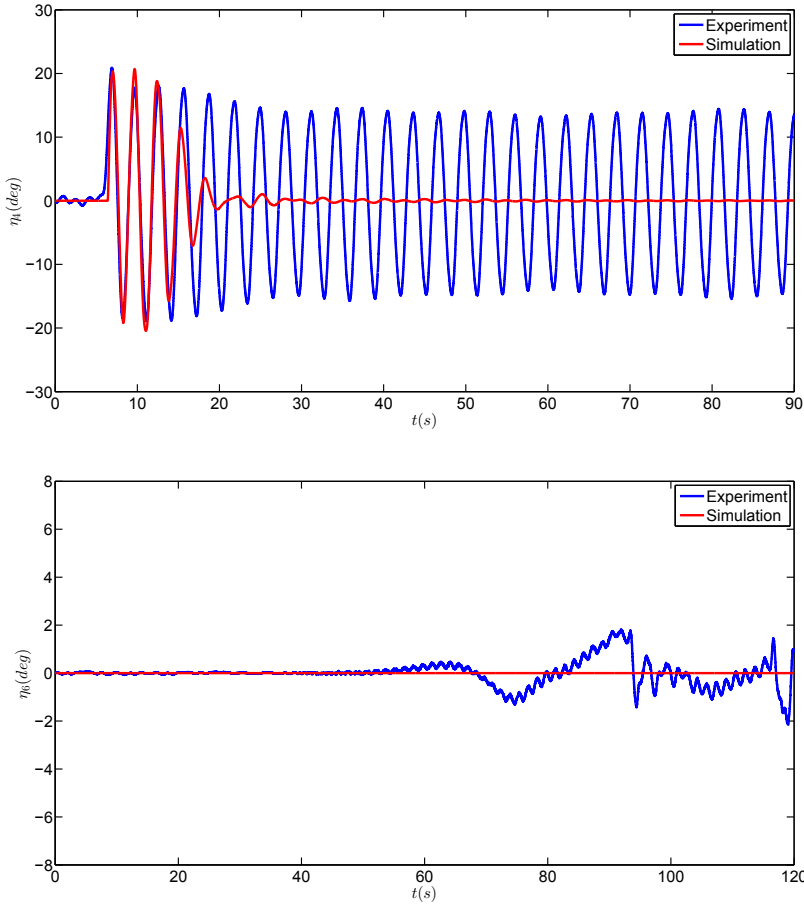


Figure 7.50: Comparison of numerical simulation (with disabled yaw mode) and experimental results of roll (top figure) and yaw motion (bottom figure) for case C787.

7.7 Conclusion

Experiments and numerical simulations are performed and presented to investigate the effect of different sizes of an anti-roll free surface tank on parametric resonance in roll motion for a fishing vessel. A tank with different tank widths (3.0 cm, 4.0 cm, 5.1 cm and 8.1 cm), with 3.9 cm as tank water depth and 95 cm as the tank length, has been used in the experiments. At the beginning of this chapter, the roll decay tests for all the tank sizes have been simulated using the numerical solver and the comparison of ex-

periment and numerical results was presented. The comparison shows that the results are in good agreement and therefore the damping level from the tank could be obtained from the numerical solver. Then the effectiveness of the tank in providing roll damping is shown by comparing different roll decay tests with and without tank and with the same initial roll angle.

Selected tests in each tank size have been simulated and discussed. As explained before, due to the high damping level from the tank, PR did not occur spontaneously in the experiments. So, a forced roll motion was triggered in all the test cases which resulted in PR in some cases and in no PR in others. In the numerical simulations, we tried to reproduce the same conditions as in the experiments. So, first the tests have been tested without triggering the roll motion and no PR occurred in all cases. Then we triggered a roll motion similarly as in the experiments. The triggered roll amplitude and the phasing of roll motion and heave motion (at the trigger time) is important for the PR occurrence. We tried to have the same triggering in the simulation cases by imposing a roll moment to the system at the correct time. Although there might be some differences in the triggered roll amplitude, since the numerical triggering process was not that straightforward. The roll amplitude and phasing was tuned by using two parameters as input in the simulations and after each run, we had to repeat the cases with updated values of parameters, if the tuning of the initial forcing-roll conditions was not good enough. We had to do this process several times in some cases to get an acceptable roll amplitude and phasing in the numerical simulations. To show the importance of the roll phasing in some cases, Fig. 7.51 shows a numerical study for one case with different phasing in two simulations.

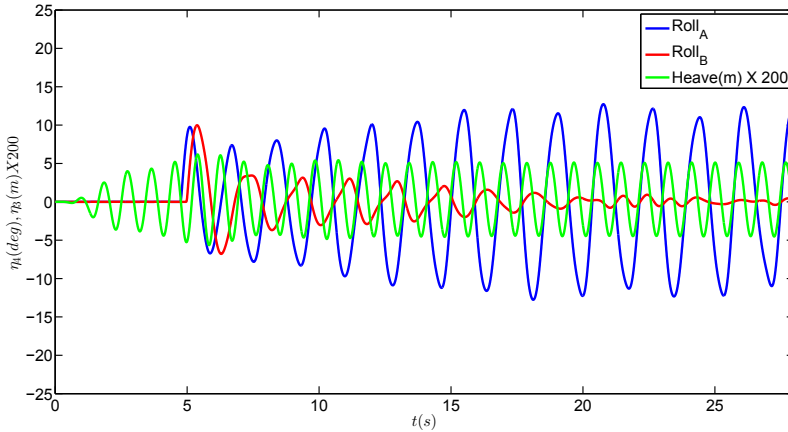


Figure 7.51: Numerical study on the effect of forced roll-heave phasing on roll motion in time for $\frac{\omega_{n4}}{\omega_e} = 0.5$ and $k\zeta_a = 0.25$ for the ship model with tank width=5.1cm.

As it can be seen, the same forced roll amplitude but with different phasing relative to heave, results in totally different numerical roll behaviour. In one case ($Roll_A$), PR occurs while in the other one ($Roll_B$), the forced roll motion is totally damped out.

All the presented and compared results in this chapter are for the cases with the same roll-heave phasing. As it was discussed and showed, in all test cases with different tank widths, the numerical results in terms of PR occurrence were mostly similar to the experiments except for some cases near the instability border. Totally 41 test cases were examined, among them 35 were captured by the numerical solver and only 6 cases showed different results in terms of PR occurrence when compared against the experiments.

For an overall picture of the effectiveness of the tanks in avoiding parametric rolling, Tab. 7.9 compares the experimental results for cases with and without tank at Froude number $Fn = 0$ for nominal wave frequency ratio $\frac{\omega_{n4}}{\omega_e} = 0.5$ and nominal wave steepness $k\zeta_a$ ranging from 0.10 to 0.25.

NoPRF means that no PR was observed even with forcing a roll motion. This frequency ratio was selected for this table because the experiments with and without tank were performed for different $k\zeta_a$ values at this frequency. Besides, this frequency seems to be in the center of the instability region. It can be seen that in cases without tank, PR occurred for all examined wave steepnesses spontaneously, i.e. without triggering any roll motion. For cases with tanks, PR was not observed at all spontaneously, i.e. without

Table 7.9: The comparison of experimental results for cases without and with tank at $Fn=0$ for frequency ratio $\frac{\omega_{n4}}{\omega_e} = 0.5$.

$k\zeta_a \downarrow$	No tank	tank width =3.0 cm	tank width =4.0 cm	tank width =5.1 cm	tank width =8.1 cm
0.10	PR 18.27	PR 10.0F	NoPRF	NoPRF	X
0.15	PR 20.76	PR 15.0F	NoPRF	PR 11.5F	NoPRF
0.20	PR 20.70	PR 15.0F	PR 14.5F	PR 14.5F	NoPRF
0.25	PR 18.10	PR 12.5F	PR 15.0F	PR 13.3F	PR 13.7F

triggering roll motion. But with forcing a roll motion, PR was observed only in some cases. For case with tank width=3.0cm, forced PR was observed at all wave steepnesses. Increasing the tank width to 4.0cm, the forced PR vanished at the two smallest wave steepnesses. By increasing the tank width to 5.1cm, the results are more or less similar except at wave steepness 0.15. The reason of this might be due to the amplitude of forced roll motion. A forced PR with amplitude 11.5° was observed at wave steepness $k\zeta_a = 0.15$ and with tank width 5.1cm after a forced roll motion of almost 21.0° with a tank width 4.0cm, the forced roll was around 13.0° and was damped out. By increasing the tank width even more to 8.1cm, a PR only occurred at the highest tested wave steepnesses.

One should also note that Tab. 7.9 just shows an overall picture of the PR for different cases. It would have been more informative and precise if we could show all cases with the same roll-heave phasing in the table. But it is not possible since the roll-heave phasing is not necessarily the same at all cases. Such analysis could be done numerically and is suggested as future investigation.

The performed analysis suggests that a well-designed anti-roll free surface tank could easily avoid the parametric rolling phenomena. It was shown that in most of the cases the parametric rolling could be avoided in longitudinal seas and it only happens in some cases if an initial roll angle more than a threshold value is imposed on the model at the correct phasing. The performed numerical simulations also showed that the conditions in which the parametric rolling occurred are in agreement with the experiments. Some cases only at the instability border had different results in terms of PR occurrence when compared to the experiments. As it was discussed before, for cases at the instability border, a small difference in parameters (due

to experimental and numerical uncertainties) could bring the ship in the instability zone or take the ship out of it. Besides, there are some other parameters that might be important and were not considered in the simulations. For instance, as it was shown that forced roll-heave phasing is important, forced roll-yaw phasing might also be important in PR. But on the practical side, it is so difficult (if not impossible) to reproduce all the phasing of the experiments in the numerical simulations.

There are some other numerical and experimental error sources that might have influenced the results in this chapter. In the experiments, the heave and pitch motions are not very regularly oscillating even in the steady-state phase for all cases. That is partly due to the incident wave, which is not perfectly regular because of reflection of waves from the tank walls. There are many non-linearities connected to the breaking waves at the ship bow, the bottom and bow flare slamming and even water on deck in some cases. Small misalignments from the head sea waves in the experiments might also have some influences. There are also many non-linearities connected to the sloshing phenomenon inside the tank. Since the tank water depth-to-the tank length ratio $h/l = 0.04$ is particularly small, the tank roof impact and the dry tank bottom was observed in almost all cases of the experiments. Many splashes occurred in connection to the tank roof impact.

Besides, on the numerical side, the interaction between the local steady flow and unsteady flow, for the cases with forward speed, is ignored in the numerical solver. It might have some effects on the results especially for the studied ship, which does not have a slender hull. Furthermore, the non-linearities that are included in the numerical solver are simplified. Also, the local wave elevation is not considered in the wetted surface of the hull in time. Furthermore, the test cases are performed at or near the sloshing resonance frequency of the tank, and as observed in the experiments, there are significant tank roof impacts that make the flow very violent and create pronounced splashes and non-linearities not captured correctly by our CFD sloshing solver.

Chapter 8

Summary and further work

The parametric resonance in roll motion has been studied in regular waves numerically and experimentally. This study was performed with numerical simulations on a Norwegian fishing vessel and a container ship and dedicated experimental tests on a typical Norwegian fishing vessel, which has a bluff hull with small length-to-beam ratio. Numerical solvers with different level of sophistication were developed and used for the two different ships. The effect of forward speed and anti-roll tank are also studied. The solvers were validated against experimental results. The different numerical solvers developed in this thesis are outlined first.

8.1 Numerical solvers

Different numerical solvers with different level of sophistication were developed and used in the numerical study of the parametric rolling in this thesis. First, we used a linear seakeeping formulation with some non-linear modifications (as explained in chapter 2), which are necessary for capturing the parametric rolling phenomenon. In this solver, the motions were modelled in a 5-DOF (excluding surge) system and the radiation and diffraction problem were solved using a 2D strip theory code [72]. The 2D code was validated in chapter 2 for motions of a 2D semi-circular section. In this solver, the Froude-Krylov and restoring loads are calculated in time where the dynamic incident wave pressure and the hydrostatic pressure are integrated on the wetted hull surface up to the incident wave surface and accounting for the body motions. These two loads are calculated in time, but we can not consider this solver as a complete time-domain code, because the memory effect of radiation loads has not been considered in the formulation. This solver showed good capability in capturing PR in ships with certain slender

hulls. For cases with more bluff bodies with higher beam-to-length ratio, where the 3D effects are more important, we can not use the strip theory any more. That is why we developed further another simulator to study the bluff bodies like fishing vessels. We used the so-called hybrid method to solve the radiation and diffraction problem in cases with forward speed based on the solutions of cases without forward speed from a 3D code. The Froude-Krylov and restoring forces are calculated in time with integrating the incident wave dynamic pressure and hydrostatic pressure on the wetted surface of the ship up to the incident wave elevation and accounting for the body motions. The cable tensions of the mooring system, modeled to reproduce the experimental set-up for the fishing vessel, are also calculated in time. The memory effect of radiation forces are considered through the convolution integral, so we can consider this solver as a complete time-domain simulator. A simple model of water on deck and bottom slamming is also used in the numerical simulations but the results do not show a big effect from them for the fishing vessel examined here. More detail for these two parts could be found in [3]. The effect of using the weak-scatterer assumption in modifying the radiation and diffraction loads is also modelled and studied. This solver is a 3D 6-DOF time-domain code with weak-scatterer assumption.

For studying the effect of a simple anti-roll tank, a sloshing solver was also introduced and customized. The sloshing in the anti-roll tank is numerically simulated as a 2D problem by Computational Fluid Dynamics (CFD) based on the finite volume method, in which water and air are assumed as incompressible and the viscous flow to be laminar. The Volume of Fluid (VOF) technique is used to capture the air-water interface. The solver is customized based on our needs from the “Open source Field Operation And Manipulation”, known in short as Open-FOAM, which is an open source package in fluid mechanics. The coupling between the seakeeping and the sloshing-tank solver was performed iteratively, as explained in chapter 3.

8.2 Different ships studied

The parametric rolling for a C11 post-Panamax container ship in regular waves is studied numerically using the 5-DOF solver explained above. Twelve cases in head sea waves with forward speed $U = 8kn$ were simulated. The wave length-to-ship length ratio λ/L_{pp} for these cases varied between 0.8 to 1.4. All 12 cases were simulated correctly according to the results obtained from the simulator as was shown in Tab. 5.2. In six cases, no PR occurred and in other cases PR occurred with different steady-state roll

angle which was simulated with an acceptable agreement with available experiments. Eight cases were also checked in following-sea waves and without forward speed. The λ/L_{pp} is in the same range as for the head-sea cases. PR occurred in all cases in the experiments. In the numerical simulations, we also predicted PR in all cases and in 3 cases the steady-state roll value was similar to the experimental results. In 5 cases with the highest roll in the experiments, the simulator showed a capsize in the numerical simulations as was documented in the Tab. 5.3. The solver showed good agreement with the experiments with a tendency of the developed solver to give conservative results in some examined scenarios. The conditions in which the parametric rolling occurred with largest documented amplitude are almost the same in experiments and simulations. Furthermore, we speculated about the influence of wave reflection from experimental tank walls at zero forward speed in following waves.

After the C11 post-Panamax container-ship, we investigated the parametric rolling in a fishing vessel. The typical fishing vessels are blunt bodies with high beam-to-length ratio. The fishing vessel studied here has also a high beam-to-length ratio. This ratio for this fishing vessel is 0.32 while it was 0.15 for the studied C11 container ship (more than 2 times larger). This suggests that 3D effects should be important for this vessel and we can not use the strip theory solver for it. For having a better picture, the RAOs for heave and pitch of this fishing vessel for $Fn = 0$, $Fn = 0.09$ and $Fn = 0.18$ in head-sea waves are shown in Figs. 8.1 to 8.3. The interesting area for our study is the one between the two vertical dashed black lines in the figures.

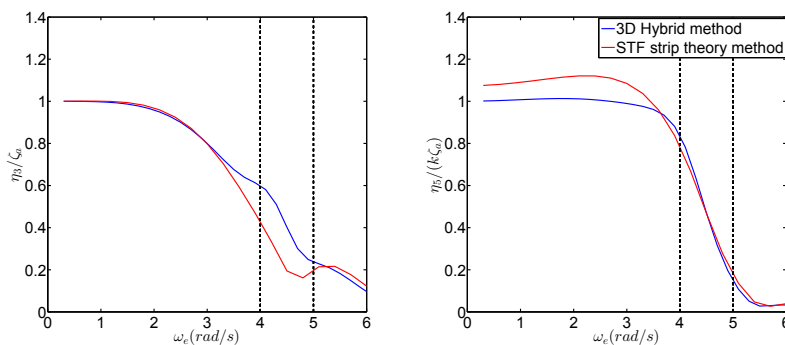


Figure 8.1: Comparison of RAOs in heave and pitch calculated by STF strip theory and 3D hybrid method for fishing vessel SFH112 with $Fn = 0$ in head-sea waves.

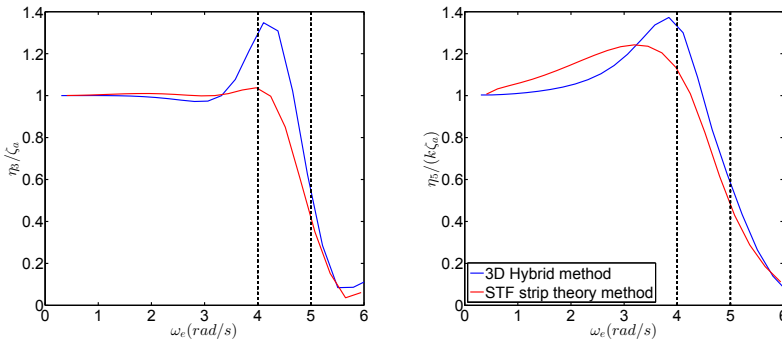


Figure 8.2: Comparison of RAOs in heave and pitch for fishing vessel SFH112 with $Fn = 0.09$ and head-sea waves, with STF strip theory and 3D hybrid method.

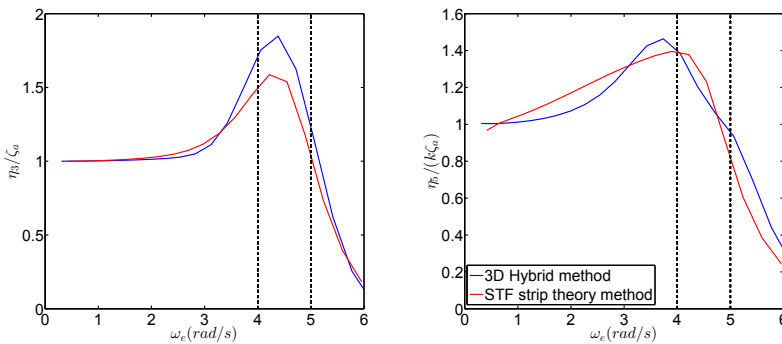


Figure 8.3: Comparison of RAOs in heave and pitch for fishing vessel SFH112 with $Fn = 0.18$ and head-sea waves, with STF strip theory and 3D hybrid method.

From these figures, the 3D effects are important as expected. It seems that the 3D effects are more important in heave motion than in pitch motion for the range of frequencies of our interest. Since the heave and pitch motions are important in PR, we must use the 3D method to capture the PR phenomenon correctly. The fishing vessel without and with anti-roll tank have been studied numerically and experimentally in head-sea regular waves. For the ship model without anti-roll tank, three set of tests with $Fn = 0$, $Fn = 0.09$ and $Fn = 0.18$ have been studied. Detailed summary of the results for each examined Fn is given in the following.

8.2.1 Cases without tank and $F_n = 0$

The parametric resonance could occur where the natural roll frequency, ω_{n4} is around half of the excitation frequency ω_e , in this case coinciding with the incident-wave frequency. So these tests were designed and performed for the frequency ratio $\frac{\omega_{n4}}{\omega_e}$ from 0.46 to 0.54 to be in the instability zone. The other condition for occurrence of parametric rolling is that the wave height should be high enough. So a wave steepness $k\zeta_a$ range of 0.1 to 0.25 was considered for this set of tests.

Before doing the simulations, the mooring cables identification was extracted from the surge-decay experiments. The mooring system was used to limit the horizontal motions in the tests. So one cable identification was extracted for the fore cables and one for the aft cables. The viscous damping coefficients are also obtained from the decay tests. Then the surge and roll decays were simulated and compared against experiments which showed a good agreement. It was noted also that the sway and yaw could not be reproduced numerically probably due to the small difference in cables and also the wave reflection from the tank walls. Trying a linear restoring coefficient for sway and yaw also did not help much with the decay tests.

A Fast-Fourier Transform (FFT) of the incident-wave elevations in the experiments was performed and the first harmonic component was extracted and used in the simulations. The comparisons of the numerical and experimental results for all cases were shown in chapter 6 documenting a good agreement.

There are some cases in which the results are different in terms of PR occurrence. From 32 cases totally, the results in 26 cases were the same in numerical and experimental estimations in terms of PR occurrence. The roll steady-state amplitude showed also an acceptable agreement. For the remaining 6 cases, the numerical results were different from the experiments in terms of PR occurrence. Plotting the Mathieu instability diagram based on the 1-DOF roll equation of motion, showed that the six points corresponding to these 6 cases are close to the instability border. It means that for the cases well inside or outside the instability zone, the numerical and experimental results agree. PR as an instability phenomenon is highly sensitive to all parameters especially near the instability borders and the ship could get in or out of the instability zone by even a very small change in the parameters. The differences in PR occurrence, which occur at the instability border, are probably due to uncertainties in the numerical simulations and experiments. From the Mathieu instability diagram, it is clear that the instability border is different in the experiments. The reason is that the Mathieu instability diagram is for a 1-DOF equation with harmonic

restoring variation while apparently for these experiments the ship behaves strongly as a 6-DOF system in the context of PR occurrence and the roll was coupled to other modes of motions. In addition, the restoring variation for the ship is not exactly harmonic as assumed in the Mathieu equation. The effect of the coupling of motions on the instability border is discussed in [38].

The comparison between experimental and numerical results of all six degrees of freedom for all cases at $Fn = 0$, showed that the motions are in the same order except for sway and yaw. One reason could be the difference in cable systems (the cables used in the numerical simulations are port-starboard symmetric while it is not like that in experiments) and the wave reflections from the experimental tank walls which are not accounted for in the simulations. The transient part in surge motion is also different in numerical and experimental results. One should also note that in roll motion, the steady-state value is important and the transient phase should not be compared since the level of transverse disturbances are not the same in the actual physical experimental conditions and in the ideal numerical conditions. The cables tensions have also been compared in selected cases.

The effect of using weak-scatterer assumption in the numerical simulation is assessed with running the numerical simulations with and without it for cases without tank at $Fn = 0$. The comparison of results are shown in Tab. 8.1.

Table 8.1: Test cases at $Fn = 0$, as given in Tab. 6.2. For each examined case, the experimental (*Exp*), numerical with weak-scatterer assumption (*Num WS*) and numerical without weak-scatterer assumption (*Num NoWS*) roll-motion amplitudes in nearly steady-state conditions are given in degrees. A roll angle with a *F* shows that the roll steady-state value is obtained by forcing the model with a small roll angle after a while. *NOF* means that parametric roll did not occur even with triggering the roll motion.

$k\zeta_a \downarrow, \frac{\omega_{n4}}{\omega_c} \rightarrow$	0.46	0.47	0.48	0.49	0.50	0.51	0.52	0.53	0.54
0.10 <i>Exp</i>			C459	C479	C457	C501	C468	C480	
Num WS	X	X	NOF	21.1	18.27	15.24	12.5	NOF	
Num NoWS	X	X	3.8	19.2	18.9	16.75	12.9	11.0	X
			3.7	18.0	16.5	10.5	NOF	NOF	X
0.15 <i>Exp</i>		C464	C463	C462	C461	C460	C469	C481	C482
Num WS	X	NOF	23.66	22.2	20.76	17.11	16.0	12.5	NOF
Num NoWS	X	14.0	21.8	20.5	18.9	17.4	14.5	11.8	7.7
		5.2	18.5	16.5	5.0	NOF	NOF	NOF	NOF
0.20 <i>Exp</i>	C473	C472	C471	C470	C466	C465	C474	C484	C499
Num WS	NOF	19.2	25.13	22.52	20.7	17.0	16.05	10.5F	5.0F
Num NoWS	26.9	25.0	22.4	20.7	18.25	16.0	13.0	9.9	5.3
	NOF	25.0	19.0	12.2	NOF	NOF	NOF	NOF	NOF
0.25 <i>Exp</i>	C493	C490	C483	C491	C492	C495	C496	C497	C500
Num WS	NOF	20.0	24.6	21.4	18.1	15.0	13.7	10.0F	NOF
Num NoWS	25.7	24.1	21.0	18.5	16.0	15.5	12.0	11.0	NOF
	27.0	25.0	20.0	NOF	NOF	NOF	NOF	NOF	NOF

The cells with different roll amplitudes (difference more than 5°) for results using with and without weak-scatterer assumption are marked with the grey shading. As it can be seen from this table, the weak scatterer assumption shows high importance for higher frequency ratios (longer waves) and steeper waves. This is in agreement also with its main assumptions. It can be seen that only for frequency ratio 0.48, it can capture all experimental results, correctly. For other cases, its results are different from experiments, either in all or some of the cases. For 3 cases near the instability border (C473, C480 and C482), the results with solver without weak-scatterer assumption are in agreement with experimental results, while the solver with weak-scatterer assumption are not. But looking at all the tested cases in the table, results using weak-scatterer assumption show far closer results to the experiments than results without weak-scatterer.

To check the effect of coupling of other motions on the PR, we simulated some cases without tank at $Fn = 0$ with different degrees-of-freedom. We used our main solver with weak-scatterer assumption and disabled the horizontal motions and simulate the cases only with roll, heave and pitch motions. In order to isolate the effect of surge motion only, we simulate all cases one more time with disabling the sway and yaw modes only. We did all these simulations only for the cases with frequency ratios between 0.48 and 0.52 where we got the numerical results in agreement with experiments before. The results are shown in Tab. 8.2.

Table 8.2: Test cases at $Fn = 0$, as given in Tab. 6.2. For each examined case, the experimental (Exp), numerical results with 6-DOF model (Num), numerical results with roll, heave and pitch modes free only (Num 345) and numerical results with surge, roll, heave and pitch modes free only (Num 1345) roll-motion amplitudes in nearly steady-state conditions are given in degrees. A roll angle with a F shows that the roll steady-state value is obtained by forcing the model with a small roll angle after a while. NOF means that parametric roll did not happen even with triggering the roll motion.

$k\zeta_a \downarrow, \frac{\omega_{n4}}{\omega_e} \rightarrow$	0.48	0.49	0.50	0.51	0.52
0.10 Exp	C459	C479	C457	C501	C468
Num	NOF	21.1	18.27	15.24	12.5
Num 345	3.8	19.2	18.9	16.75	12.9
Num 1345	4.5	14.0	13.0	8.5	NOF
	4.5	16.6	16.2	13.5	10.0
0.15 Exp	C463	C462	C461	C460	C469
Num	23.66	22.2	20.76	17.11	16.0
Num 345	21.8	20.5	18.9	17.4	14.5
Num 1345	12.5	10.0	NOF	NOF	NOF
	17.8	16.5	14.0	12.0	7.7
0.20 Exp	C471	C470	C466	C465	C474
Num	25.13	22.52	20.7	17.0	16.05
Num 345	22.4	20.7	18.25	16.0	13.0
Num 1345	12.0	NOF	NOF	NOF	NOF
	18.0	13.2	11.5	5.5	NOF
0.25 Exp	C483	C491	C492	C495	C496
Num	24.6	21.4	18.1	15.0	13.7
Num 345	21.0	18.5	16.0	15.5	12.0
Num 1345	NOF	NOF	NOF	NOF	NOF
	12.3	9.3	NOF	NOF	NOF

In case of all horizontal motions disabled, it seems that the couplings of horizontal motions gets more important in PR for longer and steeper waves. For instance for frequency ratio 0.48, for wave steepness up to 0.2, PR is captured in all cases (although with different roll amplitudes), but in wave steepness 0.25, no PR was observed numerically. A same trend could be seen in frequency ratio 0.49, but here no PR was observed in wave steepness 0.2 and 0.25 and this trend goes on until no PR was observed in all wave steepnesses in frequency ratio 0.52. So it is clearly observed that the coupling of horizontal motions gets higher importance with increasing the wave length and steepness.

The numerical results with surge motion enabled could recover PR in some cases that were not captured without surge, sway and yaw. For instance for frequency ratio 0.48, PR could be captured in all tested wave steepnesses (even though the amplitude is different from the experiments). A same trend could be seen for frequency ratio 0.49 also.

Therefore, these results show that although without sway and yaw and only with surge motion included, in some moderate steep and not so long waves, PR could be captured (with slightly different roll amplitude), but all horizontal motions are important for PR specially for longer and steeper waves.

8.2.2 Cases without tank and $F_n=0.09$

The tests for the ship without tank and with $F_n = 0.09$ were performed for the frequency ratio $\frac{\omega_{n4}}{\omega_e}$ from 0.45 to 0.50. The wave steepness $k\zeta_a$ was varied between 0.1 to 0.20. The higher steepness ($k\zeta_a = 0.25$) was dangerous for the model due to excitation of high vertical motions, and therefore not analyzed in forward speed.

9 cases totally were studied and for six of them, the numerical and experimental results were in agreement while for remaining three cases there was a difference in PR occurrence. In two of these cases (C537 and C521), no PR were observed experimentally while PR were observed in the numerical simulations. The amplitude of the numerical roll motion in the time range of experiments was very small and the main build up started after the experiment time recording. For the third case C535, experimentally it was observed that the pitch motion decreases in amplitude strangely without reaching a steady-state value. This reduction in pitch might have some effects in avoiding PR. We could not find the exact reason of this pitch motion behaviour in the test.

To see where these cases are in the instability diagram, numerical simulations were performed for some scenarios and then a stability diagram was

plotted accordingly. From this, cases C537 and C521 are clearly near the instability border. Case C535 seems not to be near the instability border, and looks to be well inside the instability region.

8.2.3 Cases without tank and $Fn=0.18$

Finally, the tests without tank and with $Fn = 0.18$ were performed for the frequency ratio $\frac{\omega_{n4}}{\omega_e}$ from 0.43 to 0.50. The wave steepness $k\zeta_a$, was varied between 0.10 to 0.15. Due to the high forward speed and large vertical motions, it was dangerous for the model to do the tests with higher wave steepnesses.

By checking the videos of the tests at this forward speed, a sink (rise up) and trim (bow up) was clearly observed in the experiments (when the model was towed before hitting the incident waves). The values of sink and trim were estimated as $8mm$ (2% of the draft) and 0.5° , respectively, from the experiment videos and were considered in the numerical simulations.

There were totally 9 cases and the results in 7 of them showed an agreement in terms of PR occurrence. The numerical PR steady-state amplitude is not so close to the experimental values in some cases. This is probably due to the big non-linearities connected to the wave breaking at ship bow, pronounced water on deck and bottom and bow flare slamming in the experiments. In two cases, the results are different in terms of PR occurrence. It was discussed and showed that one of these cases, C555, seems to be close to the instability border. But this does not seem the case for C545.

For some experimental cases, the PR was not observed to build up spontaneously without triggering a forced roll motion. We checked if the PR amplitude could be affected by the triggering process and so we studied numerically the phenomenon both without and with triggering the roll motion and found the same steady-state PR amplitude in some cases (such as cases C545 and C553), while in some other cases the results were different (such as cases C549 and C552).

8.2.4 Cases with tank at $Fn=0$

The effect of free-surface anti-roll tank on the parametric roll was studied numerically and experimentally.

Two types of experiments were performed regarding the tanks. One was with the tank in isolated conditions and forced to oscillate in roll with the axis of rotation 0.4m below the tank bottom. The loads due to the sloshing were measured in a body-fixed reference frame centred at the tank bottom.

These experiments were used to validate the numerical solver for sloshing simulations and the results were shown in chapter 3.

From the comparison, there is an acceptable agreement for the sway force while the roll moment is under-predicted in the numerical simulations by around 25%. The differences are probably due to the fact that these cases are performed at the resonance frequency and, as observed in the experiments, there are significant tank roof impacts that make the flow very violent and create pronounced splashes and non-linearities not captured correctly by the sloshing solver. Furthermore, pressures at the tank roof will directly influence the roll moment but not directly the sway force. Numerical convergence and conservation of fluid mass were checked in the simulations. Two other different experimental data from the literature were also used in the chapter 3 for further validation of the sloshing code.

The second type of experiments examined the fishing vessel with on-board tank in regular incident head-sea waves. These tests were performed with different tank dimensions, and different wave conditions. These are dedicated PR experiments on the fishing vessel that were carried out to understand the physics and occurrence of parametric rolling on the fishing vessel. These tests were also used for validation of the numerical coupled solver. A simple rectangular tank was used with a length equal to the ship beam, draft of 3.9 cm and different tank width (3.0, 4.0, 5.1 and 8.1 cm). The anti-roll tank set-up is shown and discussed in section 4.4. Considering the tank dimensions and also checking the videos of the experiments, it could be considered a 2D tank.

For validation of the seakeeping-sloshing tank coupled solver, first the 1-DOF sway motion of a 2D ship section with two tanks on-board were considered and the simulations for the RAO (Response Amplitude Operator) for the sway motion were performed and compared against the experiments from [5] in chapter 3. The results were in good agreement with the experiments, confirming that our method can solve the problem at the sloshing resonance frequency more accurately than the non-linear potential solver presented in [5].

The use of a simpler non-iterative, i.e. weak, coupling strategy was also examined. The results in Fig. 8.4 highlight a strong coupling phenomenon and the suitability of the proposed iterative-coupling strategy.

After that, we tried to validate our simulator in a model with 6-DOF for the fishing vessel.

The anti-roll free surface tank mechanism is explained in section 7.1. It discussed the tank moment from the tank and the way it acts against the roll motion. It was shown and discussed that some part of this moment acts

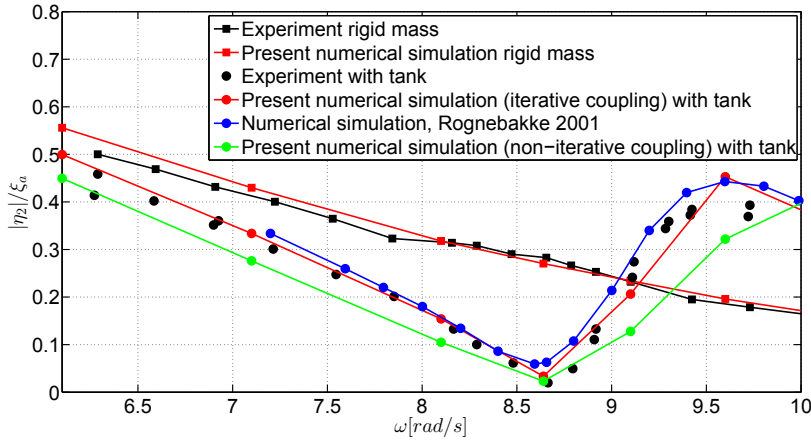


Figure 8.4: The effect of iteration in coupling of sloshing and seakeeping solver. Sway RAO for the ship section without tanks (rigid mass) and with two tanks filled with $h = 184\text{mm}$ from present numerical seakeeping-sloshing coupled solver and from numerical and experimental studies by Rognebakke [5].

as an extra damping to the system. The roll decay tests for all the tank sizes were simulated using the numerical solver and compared against the experiments. The comparison showed that the results are in good agreement and therefore the damping level from the tank could be captured by the numerical solver. The effectiveness of the tanks in roll damping was examined by comparing different roll decays simulations with and without tank, with the same initial roll angle. This confirmed a non-linear roll moment from the anti-roll tanks.

Due to the high damping level from the tanks, PR did not occur spontaneously in the experiments with on-board tanks. So a forced roll motion was triggered for all test cases and only a part of them resulted in a PR occurrence. In the numerical simulations, we tried to take the exact conditions for the experiments into account. So first the simulations were performed without triggering the roll motion and no PR occurred in all cases. Then we triggered a roll motion similarly as done in the experiments. The triggered roll amplitude and the phasing between roll and heave motions (at the trigger time) is important in PR occurrence. We tried to have the same triggering in the simulation cases by imposing the correct roll moment to the system at the correct time. However, there might be some differences in the triggered roll amplitude, since the numerical triggering process was

not that straightforward. To show the importance of the roll phasing, Fig. 7.51 showed a numerical study for one case with different phasing in two simulations. It showed that in one case a PR was build up and in another case, the triggered roll motion damped out after some oscillations. Since the simulations were time-consuming in the coupled cases, they were only performed until the roll motion achieved a steady-state value.

The instability region for the tests with different tank widths are observed in the experiments. It was also observed that increasing the tank width, shrinks the instability region in the tested area. For the highest value of tank width, PR was not observed at all even with triggering large roll motions. The simulation results show good agreement in capturing PR cases and also the PR amplitude. Out of 41 cases examined, 35 cases were captured by the numerical simulations. It was shown that for most of the cases with different results, the case is near instability border.

8.3 Conclusion

As final note, we can say that the agreement of the numerical results and the experimental data is good for all tests, with and without anti-roll tank. It was observed that at cases close to the instability border, the PR occurrence is very sensitive to all parameters and even small differences between experimental and numerical set-ups could lead to a difference in PR occurrence for the corresponding results. The seakeeping-sloshing tank coupled solver was capable of predicting the counteracting roll moment from the anti-roll tank. Therefore this solver could be used further for parametric rolling instability of vessels in design or operational stages. The coupled solver could also be used for general seakeeping analysis of all types of vessels with or without tanks on-board (from tankers to LNG carriers). Furthermore, the complete experimental data presented here, could be a good benchmark for investigating the parametric roll in fishing vessels and also for studying the effect of anti-roll tanks in the roll motion. Besides, it is a good data set for validating numerical tools for other researchers.

The performed analysis also suggests that a well-designed anti-roll free surface tank could easily avoid the parametric-rolling phenomena. It was shown that in most of the cases the parametric rolling could be avoided in longitudinal seas and it only happens in some cases if an initial roll angle more than a threshold value is imposed on the model at the correct phasing. There are some numerical and experimental uncertainties that might have influenced the results in some cases.

In the experiments, the incident waves are not perfectly regular due to

the reflection of waves from the tank walls. The cable attachment position to the carriage in the experiments might have moved a bit during the experiments and this affects the extracted cable identifications. There are many non-linearities connected to the breaking waves at the ship bow observed for many cases (especially for cases with forward speed), to the bottom and bow flare slamming and even to water on deck in some cases. Large variation in the wetted area in the aft part of the fishing vessel is also noticed. Small misalignments from the head-sea waves in the experiments might also have some influences.

Besides, on the numerical side, the interaction between the local steady flow and unsteady flow is ignored in the numerical solver, for the cases with forward speed. It might have some effects on the results especially for this fishing vessel, which is not slender. Furthermore, the non-linearities included in the numerical solver are highly simplified. Also local wave elevation is not considered when estimating the wetted surface of the body in time.

Furthermore, the test cases with the tank, are performed at or near the sloshing resonance frequency of the tank, and as observed in the experiments, there are significant tank roof impacts that make the flow very violent and create pronounced splashes and non-linearities not captured correctly by our CFD sloshing solver.

There are some other parameters that might be important and were not considered in the numerical simulations. For instance, it was shown that forced roll-heave phasing is important for PR occurrence. Similarly, forced roll-yaw phasing might be important. But in practical side, it is rather difficult (if not impossible) to reproduce properly all phasing of the experiments in the numerical simulations.

8.4 Recommendation for further work

The present study can be pursued in many different perspectives both experimentally and numerically. Some recommendations for further research steps are as follows:

- Studies about the effect of sway and yaw coupling to the roll motion and their effects on PR could be done. The effect of surge excursion on PR is also interesting in longitudinal seas.
- Since the fishing vessels are rather blunt, it should be very enlightening to account for the interactions between local steady flow and unsteady flow and study their effects in PR occurrence at forward

speed. Besides, the local steady flow could be considered in calculating the non-linear Froude-Krylov and restoring forces.

- In this thesis, some polar diagrams were produced for the C11 container ship using the STF code (which is fast) for regular waves. Due to the time limits and the various subjects to study, no polar diagrams were produced for the examined fishing vessels using time domain 3D code (which is slower than STF code). It could be a good idea to develop the solver first for irregular waves and then to produce different polar diagrams for PR occurrence for different vessels and sea states.
- A numerical and experimental study on the parametric rolling in the oblique seas.
- A more in-depth study of the sloshing tank and its interaction with the vessel motions, to investigate further the importance of roll-heave phasing in the PR occurrence.
- A simpler mooring system (e.g. with a linear tension law or without the steel part in bow part which makes the computation complicated) could be used in the experiments.

References

- [1] Nils Salvesen, EO Tuck, and Odd Faltinsen. Ship motions and sea loads. *Trans. SNAME*, 78(8):250–287, 1970.
- [2] WE Cummins. The impulse response function and ship motions. Technical report, David Taylor Model Basin Washington DC, 1962.
- [3] Marilena Greco, Claudio Lugni, and Odd Magnus Faltinsen. Can the water on deck influence the parametric roll of a fpso? a numerical and experimental investigation. *European Journal of Mechanics-B/Fluids*, 47:188–201, 2014.
- [4] Jacek S Pawlowski and Don W Bass. A theoretical and numerical model of ship motions in heavy seas. *SNAME Transaction*, 99, 1991.
- [5] Olav Rognebakke. Sloshing in rectangular tanks and interaction with ship motions. *PhD thesis, Norwegian University of Science and Technology (NTNU), Trondheim, Norway*, 2002.
- [6] William N France, Marc Levadou, Thomas W Treacle, J Randolph Paulling, R Keith Michel, and Colin Moore. An investigation of head-sea parametric rolling and its influence on container lashing systems. *Marine Technology*, 40(1):1–19, 2003.
- [7] Christian Holden. Modeling and control of parametric roll resonance. 2011.
- [8] Cargolaw.com, 2017.
- [9] Stephen Carmel. Study of parametric rolling event on a panamax container vessel. *Transportation Research Record: Journal of the Transportation Research Board*, (1963):56–63, 2006.
- [10] Thor Fossen and Henk Nijmeijer. *Parametric resonance in dynamical systems*. Springer Science & Business Media, 2011.

-
- [11] William N France, Marc Levadou, Thomas W Treakle, J Randolph Paulling, R Keith Michel, and Colin Moore. An investigation of head-sea parametric rolling and its influence on container lashing systems. *In SNAME annual meeting*, 2001.
- [12] Isar Ghamari, Odd M Faltinsen, and Marilena Greco. Investigation of parametric resonance in roll for container carrier ships. In *ASME 2015 34th International Conference on Ocean, Offshore and Arctic Engineering*. American Society of Mechanical Engineers, 2015.
- [13] William Froude. *On the rolling of ships*. Institution of Naval Architects, 1861.
- [14] Otto Grim. Rollschwingungen, stabilitat und sicherheit im seegang. *Schiffstechnik*, 1:10–21, 1952.
- [15] JE Kerwin. Notes on rolling in longitudinal waves. *International Shipbuilding Progress*, 2(16):597–614, 1955.
- [16] J Randolph Paulling. On unstable ship motions resulting from nonlinear coupling. *Journal of Ship Research*, 3:36–46, 1959.
- [17] A Bruce Dunwoody. Roll of a ship in astern seas—metacentric height spectra. *Journal of ship research*, 33(3), 1989.
- [18] AB Dunwoody. Roll of a ship in astern seas—response to gm fluctuations. *Journal of ship research*, 33(4), 1989.
- [19] Naoya Umeda, Masami Hamamoto, Yoshifumi Takaishi, Yutaka Chiba, Akihiko Matsuda, Wataru Sera, Shiro Suzuki, Konstantinos Spyrou, and Kenji Watanabe. Model experiments of ship capsize in astern seas. *Journal of the Society of naval Architects of Japan*, 1995(177):207–217, 1995.
- [20] NE Sanchez and AH Nayfeh. Nonlinear rolling motions of ships in longitudinal waves. *International Shipbuilding Progress*, 37(411), 1990.
- [21] IG Oh, AH Nayfeh, and DT Mook. A theoretical and experimental investigation of indirectly excited roll motion in ships. *Philosophical Transactions of the Royal Society of London A: Mathematical, Physical and Engineering Sciences*, 358(1771):1853–1881, 2000.
- [22] Masami Hamamoto and James P Panjaitan. A critical situation leading to capsize of ships in astern seas. *Journal of the Society of Naval Architects of Japan*, 1996(180):215–221, 1996.

- [23] Abdul Munif and Naoya Umeda. Modeling extreme roll motions and capsizing of a moderate-speed ship in astern waves. *Journal of the Society of Naval Architects of Japan*, 2000(187):51–58, 2000.
- [24] N PEREZ M and C SANGUINETTI V. Experimental results of parametric resonance phenomenon of roll motion in longitudinal waves for small fishing vessels. *International Shipbuilding Progress*, 42(431):221–234, 1995.
- [25] MAS Neves, NA Pérez, and L Valerio. Stability of small fishing vessels in longitudinal waves. *Ocean Engineering*, 26(12):1389–1419, 1999.
- [26] Marcelo AS Neves. On the excitation of combination modes associated with parametric resonance in waves. In *Proceedings of the 6th International Ship Stability Workshop*, 2002.
- [27] Marcelo AS Neves and Claudio A Rodríguez. An investigation on roll parametric resonance in regular waves. *International shipbuilding progress*, 54(4):207–225, 2007.
- [28] Jianbo Hua. A study of the parametrically excited roll motion of a roro-ship in following and heading waves. *International shipbuilding progress*, 39(420):345–366, 1992.
- [29] Jianbo Hua, Wei-Hui Wang, and Jiang-Ren Chang. A representation of gm-variation in waves by the volterra system. *Journal of Marine Science and Technology*, 7(2):94–100, 1999.
- [30] Alberto Francescutto. An experimental investigation of parametric rolling in head waves. *Transaction-American Society of Mechanical Engineers Journal of Offshore Mechanics and Arctic Engineering*, 123(2):65–69, 2001.
- [31] Alberto Francescutto, Gabriele Bulian, and Claudio Lugni. Nonlinear and stochastic aspects of parametric rolling modeling. *Marine Technology*, 41(2):74–81, 2004.
- [32] M Palmquist and C Nygren. Recordings of head-sea parametric rolling on a pctc. *Annex in IMO SLF*, 47, 2004.
- [33] KJ Spyrou. Design criteria for parametric rolling. *Oceanic Engineering International*, 9(1):11, 2005.

-
- [34] ITTC 2006. Recommended procedures and guidelines—testing and extrapolation methods loads and responses, stability predicting the occurrence and magnitude of parametric rolling, 2006.
- [35] Marc Levadou and Guilhem Gaillarde. Operational guidance to avoid parametric roll. In *Proc. Int. Conf. on Design and Operation of Container Ships*, pages 75–86, 2003.
- [36] YS Shin, VL Belenky, JR Paulling, KM Weems, Wm Lin, Kevin McTaggart, Kostas J Spyrou, Thomas W Treacle, Marc Levadou, Bruce L Hutchison, et al. Criteria for parametric roll of large containerships in longitudinal seas. *Transactions-Society of Naval Architects and Marine Engineers*, 112:14–47, 2004.
- [37] M Lövstadt and J Bloch Helmers. Decision support for the ships crew by dnv active operator guidance system based on wasim. *Proc. German Society of Naval Architects*, 98:33–39, 2004.
- [38] Anton Turk. *Coupled nonlinear parametric resonance model for container ships*. PhD thesis, Tehnički fakultet, Sveučilište u Rijeci, 2012.
- [39] Stefan Krüger, Ralf Hinrichs, and Heike Cramer. Performance based approaches for the evaluation of intact stability problems. In *Proc. PRADS*, 2004.
- [40] Stefan Krueger. Evaluation of the cargo loss of a large container vessel due to parametric roll. *TU Hamburg-Harburg*, 2006.
- [41] S Silva, TA Santos, and C Guedes Soares. Parametrically excited roll in regular and irregular head seas. *International Shipbuilding Progress*, 52(1):29–56, 2005.
- [42] Marc Levadou and Riaan Vant Veer. Parametric roll and ship design. pages 307–330, 2011.
- [43] Leigh S McCue, Bradley L Campbell, and William F Belknap. On the parametric resonance of tumblehome hullforms in a longitudinal seaway. *Naval Engineers Journal*, 119(3):35–44, 2007.
- [44] KJ Spyrou, I Tigkas, G Scanferla, N Pallikaropoulos, and N Themelis. Prediction potential of the parametric rolling behaviour of a post-panamax containership. *Ocean Engineering*, 35(11):1235–1244, 2008.

- [45] Vadim L Belenky, Kenneth M Weems, Woei-Min Lin, and J Randolph Paulling. Probabilistic analysis of roll parametric resonance in head seas. In *Contemporary Ideas on Ship Stability and Capsizing in Waves*, pages 555–569. Springer, 2011.
- [46] G Bulian, C Lugni, and A Francescutto. A contribution on the problem of practical ergodicity of parametric roll in longitudinal long crested irregular sea. In *7th International Ship Stability Workshop*, pages 101–117, 2004.
- [47] Gabriele Bulian, Alberto Francescutto, and Claudio Lugni. On the nonlinear modeling of parametric rolling in regular and irregular waves. *International Shipbuilding Progress*, 51(2, 3):173–203, 2004.
- [48] N Umeda. Benchmark testing of numerical prediction on capsizing of intact ships in following and quartering seas. In *Proc 5th Int Workshop on Stability and Operational Safety of Ships, Trieste, Italy, 12-13 Sept 2001*, pages 6–1, 2001.
- [49] Naoya Umeda, Hirotada Hashimoto, Dracos Vassalos, Shinichi Urano, and Kenji Okou. Nonlinear dynamics on parametric roll resonance with realistic numerical modelling. *International shipbuilding progress*, 51(2, 3):205–220, 2004.
- [50] Abdul Munif and Naoya Umeda. Numerical prediction on parametric roll resonance for a ship having no significant wave-induced change in hydrostatically-obtained metacentric height. *International shipbuilding progress*, 53(3):183–203, 2006.
- [51] Marilena Greco and Claudio Lugni. Numerical study of parametric roll on a fishing vessel. In *ASME 2013 32nd International Conference on Ocean, Offshore and Arctic Engineering*. American Society of Mechanical Engineers, 2013.
- [52] American Bureau of Shipping (ABS). Guide for the assessment of parametric roll resonance in the design of container carriers, 2004.
- [53] Lloyds Register (LR). Head-sea parametric rolling of container ships, marine services information sheet, 2003.
- [54] Bureau Veritas (BV). Parametric roll - bureau veritas approach, technical note, 2005.

- [55] IMO 2005. Document SLF48/4/12. On the development of performance-based criteria for ship stability in longitudinal waves , submitted by Italy, 11 July 2005.
- [56] IMO 2006, 49th session. Revision of the intact stability code, subcommittee on stability and load lines and on fishing vessels safety.
- [57] IMO 2007. Revised guidance to the master for avoiding dangerous situations in adverse weather and sea conditions, resolution msc.1/circ.1228, International Shipbuilding Progress27, 139-142.
- [58] IMO 2008a. Document SLF51/4/1. Report of the intersessional correspondence group on intact stability, submitted by Germany, 10 April 2008, London, UK.
- [59] IMO 2008b. Resolution MSC.267(85). Adoption of the international code on intact stability, 2008 (2008 is code) , Adopted on 4 December 2008, London, UK.
- [60] ITTC 2005. Proceedings of 24th international towing tank conference, report of the stability in waves committee, 2005.
- [61] JJ Van Den Bosch and JH Vugts. *Roll damping by free surface tanks*. TNO, 1966.
- [62] Ahmed F Abdel Gawad, Saad A Ragab, Ali H Nayfeh, and Dean T Mook. Roll stabilization by anti-roll passive tanks. *Ocean Engineering*, 28(5):457–469, 2001.
- [63] YS Shin, VL Belenky, WM Lin, KM Weems, AH Engle, Kevin McTaggart, Jeffrey M Falzarano, Bruce L Hutchison, Miroslaw Gerigk, and Stefan Grochowalski. Nonlinear time domain simulation technology for seakeeping and wave-load analysis for modern ship design. authors' closure. *Transactions-Society of Naval Architects and Marine Engineers*, 111:557–583, 2003.
- [64] N Umeda, H Hashimoto, S Minegaki, and A Matsuda. Preventing parametric roll with use of devices and their practical impact. In *Proc. of the 10th International Symposium on Practical Design of Ships and Other Floating Structures, PRADS*, pages 693–698, 2007.
- [65] Osama A Marzouk and Ali H Nayfeh. Control of ship roll using passive and active anti-roll tanks. *Ocean engineering*, 36(9):661–671, 2009.

- [66] Marcelo AS Neves, Jorge A Merino, and Claudio A Rodríguez. A nonlinear model of parametric rolling stabilization by anti-roll tanks. *Ocean Engineering*, 36(14):1048–1059, 2009.
- [67] M Greco and C Lugni. 3-d seakeeping analysis with water on deck and slamming. part 1: Numerical solver. *Journal of Fluids and Structures*, 33:127–147, 2012.
- [68] Isar Ghamari, Odd M Faltinsen, Marilena Greco, and Claudio Lugni. Parametric resonance of a fishing vessel with and without anti-roll tank: An experimental and numerical study. In *ASME 2017 36th International Conference on Ocean, Offshore and Arctic Engineering*. American Society of Mechanical Engineers, 2017.
- [69] Maxime Thys. Theoretical and experimental investigation of a free running fishing vessel at small frequency of encounter. *PhD thesis, Norwegian University of Science and Technology (NTNU), Trondheim, Norway*, 2013.
- [70] Chang-Ho Lee. *WAMIT theory manual*. Massachusetts Institute of Technology, Department of Ocean Engineering, 1995.
- [71] JMJ Journée. Hydromechanic coefficients for calculating time domain motions of cutter suction dredges by cummins equations. *Delft University of Technology, Ship Hydromechanics Laboratory, Mekelweg, 2628(2)*, 1993.
- [72] Renato Skejic. Maneuvering and seakeeping of a single ship and of two ships in interaction. *PhD thesis, Norwegian University of Science and Technology (NTNU), Trondheim, Norway*, 2008.
- [73] RW Yeung. The transient heaving motion of floating cylinders. *Journal of engineering mathematics*, 16(2):97–119, 1982.
- [74] Sōichi Itō. *Study of the transient heave oscillation of a floating cylinder*. PhD thesis, Massachusetts Institute of Technology, 1977.
- [75] WE Smith. *Computation of pitch and heave motions for arbitrary ship forms*. Nederlands Scheepsstudiecentrum TNO, 1967.
- [76] Reza Firoozkoohi. Experimental, numerical and analytical investigation of the effect of screens on sloshing. *PhD thesis, Norwegian University of Science and Technology (NTNU), Trondheim, Norway*, 2013.

-
- [77] Odd Magnus Faltinsen and Alexander N Timokha. *Sloshing*. Cambridge University Press, 2009.
- [78] OM Faltinsen. A nonlinear theory of sloshing in rectangular tanks. *Journal of Ship Research*, 18(4), 1974.
- [79] KG Aarsæther, D Kristiansen, B Su, and C Lugni. Modelling of roll damping effects for a fishing vessel with forward speed. In *ASME 2015 34th International Conference on Ocean, Offshore and Arctic Engineering*. American Society of Mechanical Engineers, 2015.
- [80] S Ribeiro E Silva, C Guedes Soares, Anton Turk, Jasna Prpic-Orsic, and Emre Uzunoglu. Experimental assessment of the parametric rolling on a c11 class containership. In *HYDRALAB III Joint User Meeting*, 2010.
- [81] Yoshiho Ikeda, Yoji Himeno, and Norio Tanaka. A prediction method for ship roll damping. *Report of the department of naval architecture, University of Osaka Prefecture*, 405, 1978.
- [82] Odd M Faltinsen. *Hydrodynamics of high-speed marine vehicles*. Cambridge university press, 2005.
- [83] M Greco, B Bouscasse, and C Lugni. 3-d seakeeping analysis with water on deck and slamming. part 2: Experiments and physical investigation. *Journal of fluids and structures*, 33:148–179, 2012.

Appendix A

Retardation function formulation

A.1 Integrals in the retardation formulation

In the formulation used in the retardation function calculation, the following integrals have been utilized:

$$\int_a^{\infty} \frac{\cos(\omega t)}{\omega^2} d\omega = \frac{1}{a} \cos(at) - t \left[\frac{\pi}{2} - \int_0^{at} \frac{\sin(x)}{x} dx \right] \quad (\text{A.1})$$

$$\int_a^{\infty} \frac{\sin(\omega t)}{\omega^3} d\omega = \frac{1}{2a^2} \sin(at) + \frac{t}{2} \int_a^{\infty} \frac{\cos(\omega t)}{\omega^2} d\omega \quad (\text{A.2})$$

For calculation of retardation function one should note the following hints:

- The last integral in the right hand side of Eq. A.1 is solved numerically.
- The integral on the right hand side of the Eq. A.2 could be expressed by Eq. A.1.
- In the numerical integration of retardation function, for high frequencies, the term $\cos(\omega t)$ is highly oscillating and the time variable t should be discretized according to the frequency, otherwise one could get wrong retardation values.

A.2 Retardation functions for the fishing vessel SFH112

The retardation functions calculated for the SFH112 fishing vessel at $F_n = 0$ are shown in Figs. A.1 and A.2.

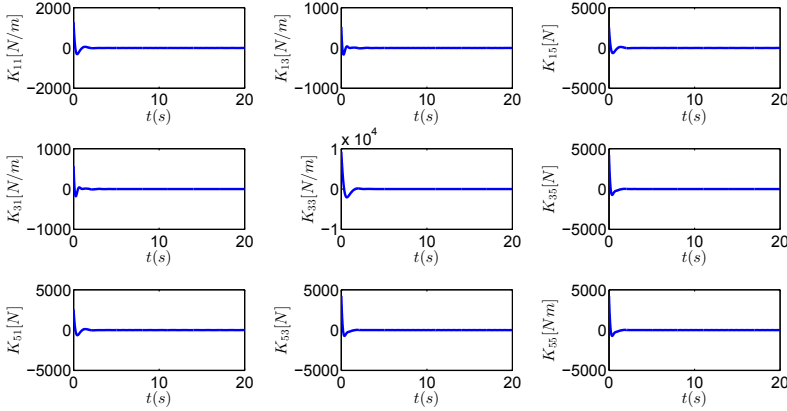


Figure A.1: Retardation functions for surge, heave and pitch motions for $F_n=0$ based on an extension of $B_{ij} = \frac{c_1}{\omega_e^2}$ for $\omega_e > 10.5 \frac{\text{rad}}{\text{s}}$.

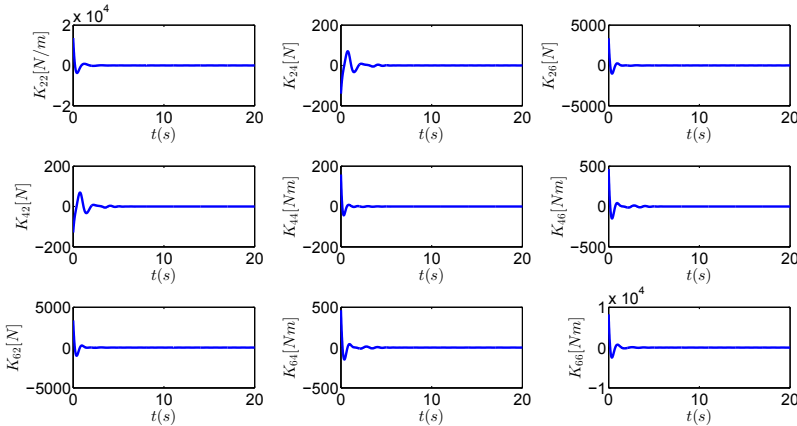


Figure A.2: Retardation functions for sway, roll and yaw motions for $F_n=0$ based on an extension of $B_{ij} = \frac{c_1}{\omega_e^2}$ for $\omega_e > 10.5 \frac{\text{rad}}{\text{s}}$.

The damping extension for the frequencies higher than $10.5 \frac{rad}{s}$ is based on the $B_{ij} = \frac{c_1}{\omega_e^2}$ formula. The extensions for all damping modes are shown in the Figs. A.3 and A.4.

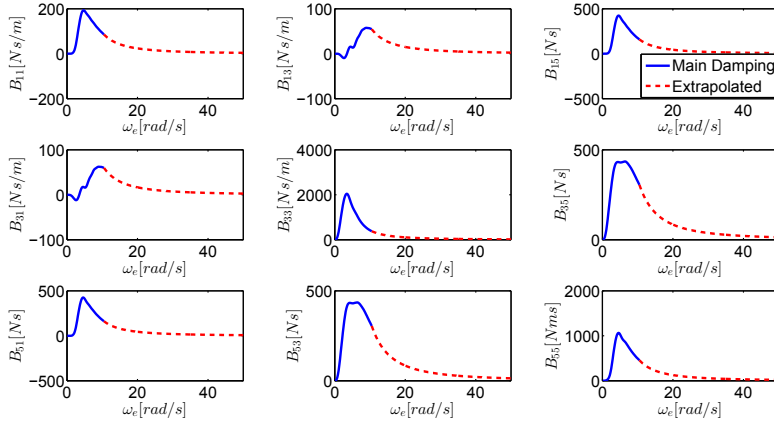


Figure A.3: Damping curve extension for surge, heave and pitch motions for $Fn=0$ based on an extension of $B_{ij} = \frac{c_1}{\omega_e^2}$ for $\omega_e > 10.5 \frac{rad}{s}$.

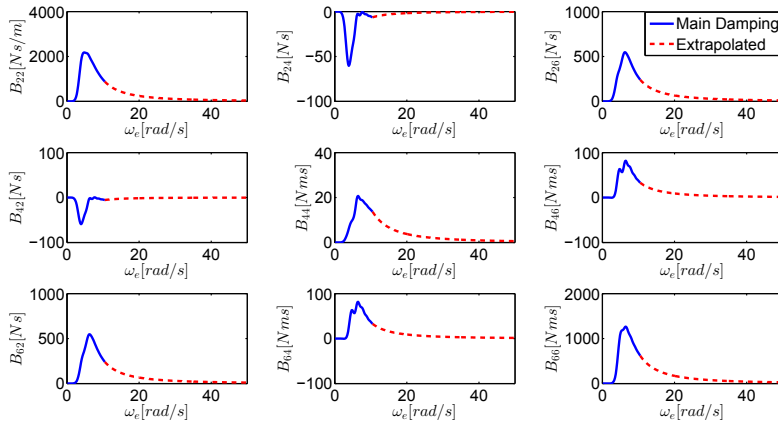


Figure A.4: Damping curve extension for sway, roll and yaw motions for $Fn=0$ based on an extension of $B_{ij} = \frac{c_1}{\omega_e^2}$ for $\omega_e > 10.5 \frac{rad}{s}$.

After the calculation of the retardation functions, we can check the results by recalculating the damping curves using obtained retardation func-

tions (as explained in chapter 2). The comparison of the original curves for the main damping coefficients and corresponding recalculated curves is shown in Figs. A.5 and A.6.

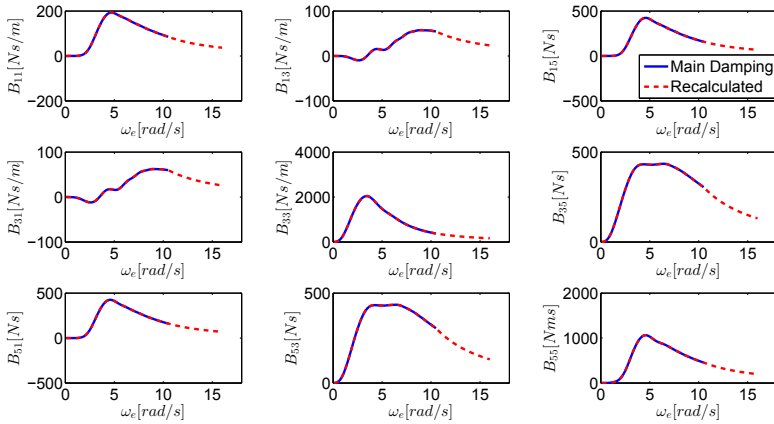


Figure A.5: Comparison of main damping curves for surge, heave and pitch motions and the recalculated damping curves from the retardation functions for the SFH112 fishing vessel at $Fn = 0$.

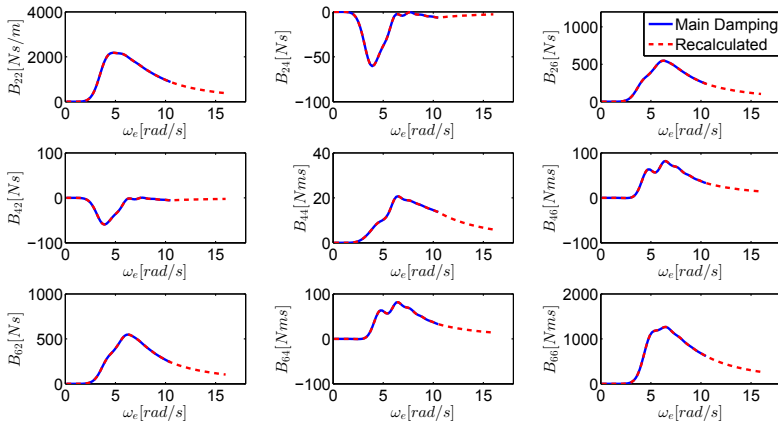


Figure A.6: Comparison of main damping curves for sway, roll and yaw motions and the recalculated damping curves from the retardation functions for the SFH112 fishing vessel at $Fn = 0$.

Appendix B

Experimental uncertainties

Some aspects of the uncertainties in the dedicated experiments carried out during this PhD research on the PR on a fishing vessel are studied and explained in this appendix.

B.1 Instrument precision

The incident wave system is measured by means of two different transducers fixed to the carriage: a finger (Kenek) and a capacitance wire probe. The Kenek is a non-intrusive instrument with an accuracy of 0.1mm and a maximum range of measurement $\pm 150\text{mm}$. The capacitance wave probe, developed at CNR-INSEAN, ensures an accuracy of the order of the wire diameter 0.5mm and a range of measurement of $\pm 300\text{mm}$. Because of the intrusive wire, this probe is suitable for station-keeping and low forward speed.

The wave elevation recorded by a pair of sensors 4m ahead of the model is used as a measure of the undisturbed incident wave and will be indicated as incident wave in the following text.

The rigid motions of the hull are measured with an inertial (MOTAN) and an optical (Krypton) system. The non-intrusive Krypton system provides real-time measure of the rigid motions using three infrared LEDs to identify a reference system fixed to the body and three CCD cameras to record the LED positions in time. This system enables tracking at a high spatial resolution of less than 1mm for the linear displacements and less than 0.05° for the angular degrees of freedom. The MOTAN is an inertial platform that measures the accelerations and the angular velocities of a rigid model. Numerical integration could recover the motion of the body in post-processing with an error around 1mm for the linear displacements and

0.15° for the rotational degrees of freedom [83].

B.2 Error analysis: Repeatability error

Tab. B.1 summarizes the test matrix for the fishing vessel without tank at $Fn = 0$. In each cell, for each test case, the actual values (the values of first harmonic based on FFT results) for wave frequency ratio ($\frac{\omega_{n4}}{\omega_e}$) and wave steepness ($k\zeta_a$) are shown. The nominal values are also shown in the left column and upper row of the table.

Table B.1: The nominal and actual wave frequency ratio ($\frac{\omega_{n4}}{\omega_e}$) and steepness ($k\zeta_a$) for test cases at $Fn=0$.

$k\zeta_a \downarrow, \frac{\omega_{n4}}{\omega_e} \rightarrow$	0.46	0.47	0.48	0.49	0.50	0.51	0.52	0.53	0.54
			C459	C479	C457	C501	C468	C480	
			0.482	0.492	0.499	0.511	0.522	0.529	
0.1	X	X	0.091	0.098	0.096	0.094	0.093	0.107	X
		C464	C463	C462	C461	C460	C469	C481	C482
		0.473	0.482	0.492	0.502	0.511	0.523	0.531	0.538
0.15	X	0.143	0.143	0.136	0.143	0.137	0.131	0.144	0.154
	C473	C472	C471	C470	C466	C465	C474	C484	C499
	0.461	0.470	0.480	0.488	0.502	0.508	0.521	0.533	0.537
0.20	0.197	0.182	0.152	0.198	0.173	0.191	0.188	0.182	0.190
	C493	C490	C483	C491	C492	C495	C496	C497	C500
	0.467	0.473	0.482	0.493	0.498	0.508	0.518	0.524	0.534
0.25	0.207	0.214	0.230	0.216	0.229	0.227	0.216	0.241	0.221

In this section, an error analysis is presented to give a global estimation of the maximum error expected for each quantity. Only the repeatability error is estimated. An accurate estimation of the repeatability error requires the test to be repeated several times, which is time consuming and unlikely to be performed for each test condition. A single physical condition, corresponding to the nominal parameters of wave frequency ratio 0.51 and wave steepness 0.10 and $Fr = 0$, is selected (the test case is marked with a grey highlight in the table). The test is repeated 4 times and each run lasts for at least 30 cycles after the steady-state regime has been reached (test cases C489, C494, C498, C501). The parametric rolling occurred in all cases with roll steady state value of 15.4°, 15.25°, 15.01° and 15.24°, respectively. The error analysis of the heave, roll and pitch motions is performed in this section. The incident wave profile and ship motions in the four repetitions of

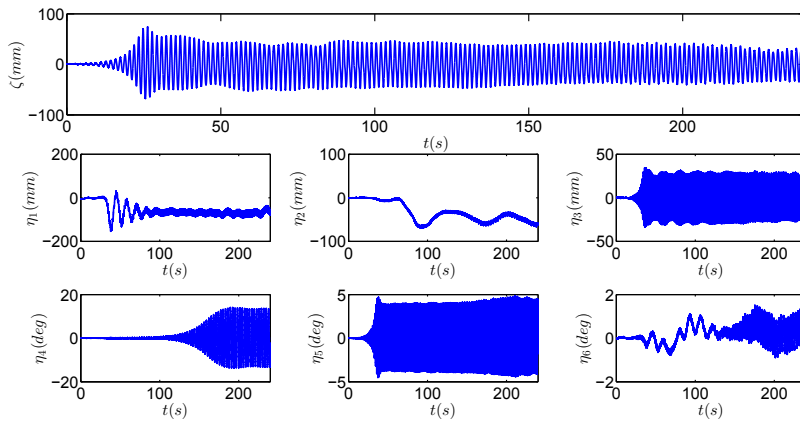


Figure B.1: Experimental incident wave profile and ship motions in cases C489.

this test are shown in Figs. B.1 to B.4.

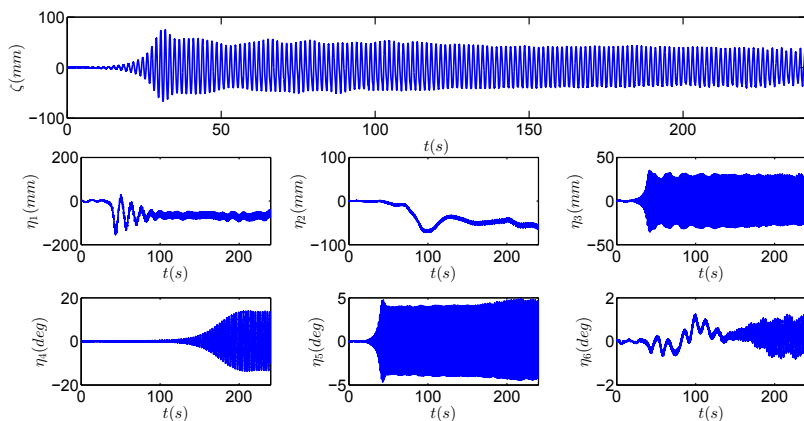


Figure B.2: Experimental incident wave profile and ship motions in cases C494.

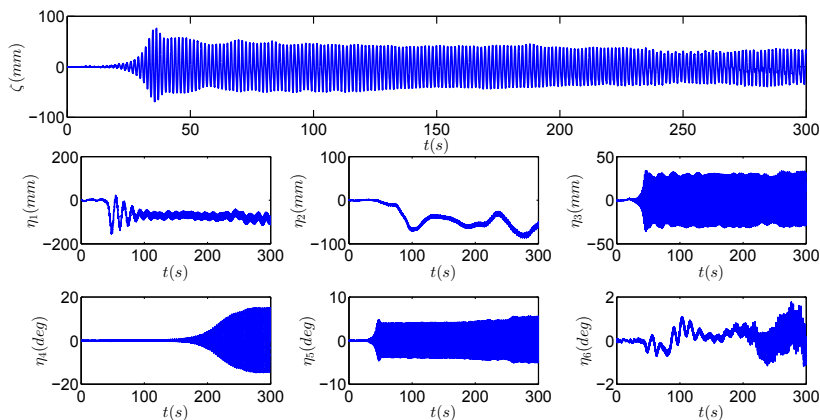


Figure B.3: Experimental incident wave profile and ship motions in cases C498.

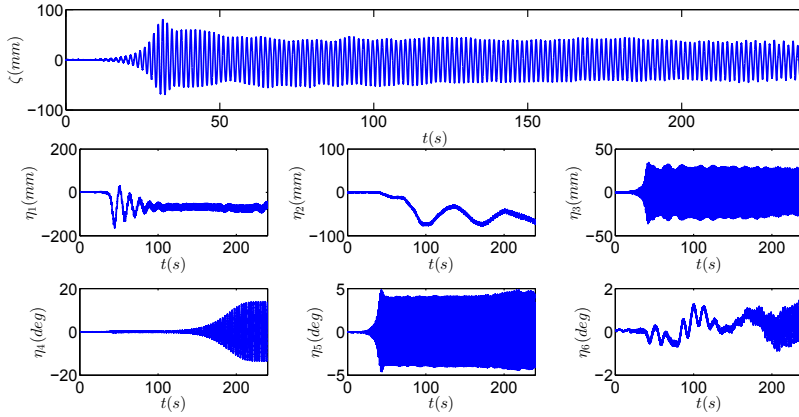


Figure B.4: Experimental incident wave profile and ship motions in cases C501.

Assuming that the variable for which we want to perform the uncertainty analysis is constant in time (for instance, the mean added resistance in waves, R_{aw}), this would involve the estimate of the average and standard deviation of the variable over N repeated tests, as follows:

$$\bar{R}_{aw} = \frac{1}{N} \sum_{i=1}^N R_{aw,i} \quad (\text{B.1})$$

$$S_{R_{aw}} = \sqrt{\frac{1}{N-1} \sum_{i=1}^N (R_{aw,i} - \bar{R}_{aw})^2} \quad (\text{B.2})$$

In contrast, the uncertainty of the time history of the oscillatory quantities, e.g. the incident wave profile and hull motions, requires the following procedure as described in [83], when assuming regular incident waves and nearly steady-state conditions:

- for each run the steady-state signal is divided into at least 10 temporal windows, each one long two incident-wave periods;
- the mean value on each window is subtracted;
- at each time instant, the mean and the standard deviation, accounting for the samples coming from all the windows, are estimated.

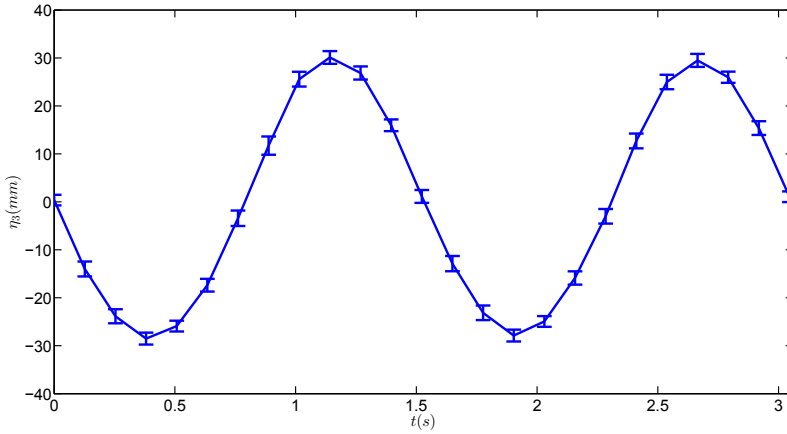


Figure B.5: Repeatability analysis for the case with nominal wave frequency ratio $\frac{\omega_{n4}}{\omega_e} = 0.51$ and wave steepness $k\zeta_a = 0.10$; mean time history of the heave motion together with the error bar (\pm two times of the standard deviation).

In this procedure, the windowing process has a small uncertainty estimated to be approximately two time steps in the data acquisition (i.e. approximately 0.0036 s here).

For the incident wave train measured through the first couple of wave transducers on the front of the ship, the expected wave period is 1.518s. This period corresponds to the mean period calculated from the repeatability analysis. The mean time history of the heave, roll and pitch motions together with the error bar giving the standard deviation of the measurements, are shown in Fig. B.5 to B.7.

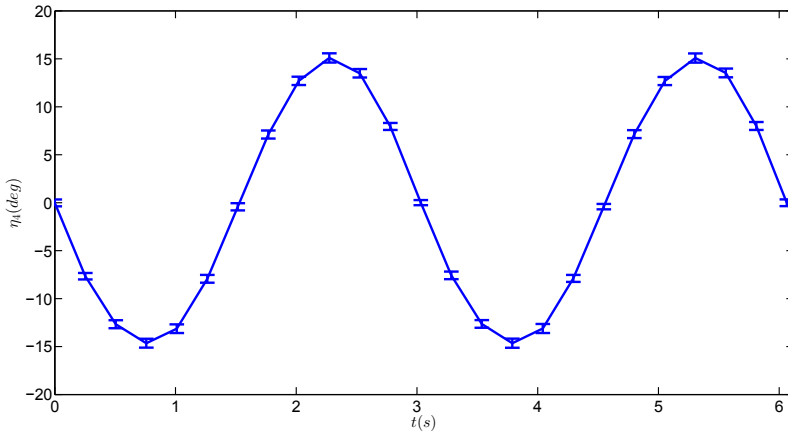


Figure B.6: Repeatability analysis for the case with nominal wave frequency ratio $\frac{\omega_{n4}}{\omega_e} = 0.51$ and wave steepness $k\zeta_a = 0.10$; mean time history of the roll motion together with the error bar (\pm two times of the standard deviation).

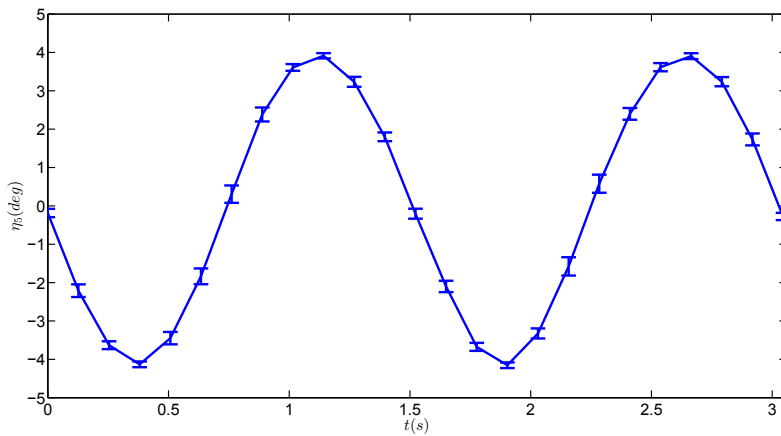


Figure B.7: Repeatability analysis for the case with nominal wave frequency ratio $\frac{\omega_{n4}}{\omega_e} = 0.51$ and wave steepness $k\zeta_a = 0.10$; mean time history of the pitch motion together with the error bar (\pm two times of the standard deviation).

For the cases considered, the mean standard deviations associated with the heave, roll and pitch motions are approximately 1.62%, 0.3% and 0.3% of the motion amplitudes, respectively.

This process is not an appropriate process for the incident wave profiles. The wave profiles as could be seen from the Figs. B.1 to B.4, are affected by unavoidable seiching modes of the basin which are very long waves and make the signal less repeatable. These seiching modes do not influence the motions so much. Since the seiching modes are associated with low frequencies, they do not influence the first harmonics of the waves. So we did the FFT analysis of the incident wave profile for these 4 repetitions and got the first harmonic of the waves and calculated the mean value and standard deviations for the first harmonic. Although it might be too few runs and therefore calculation of standard deviation might not be reliable, we tried it for just the first harmonic. Figs. B.8 to B.11 show the incident wave profiles, the selected window for the FFT analysis and their FFT analyses.

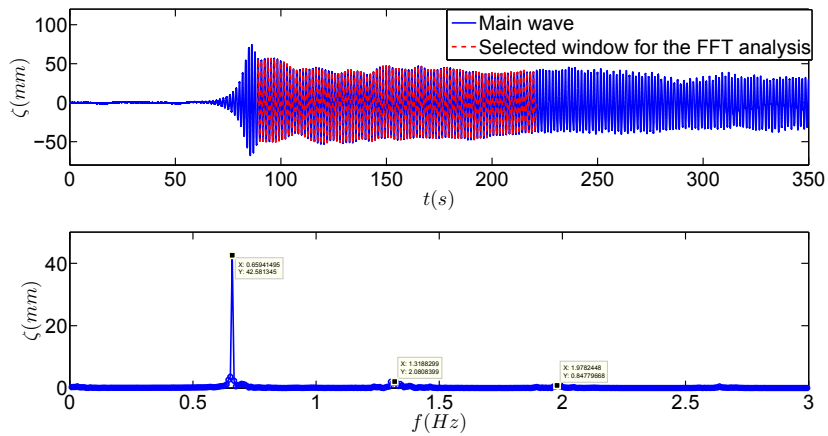


Figure B.8: FFT analysis for the incident wave profile for the case C489.

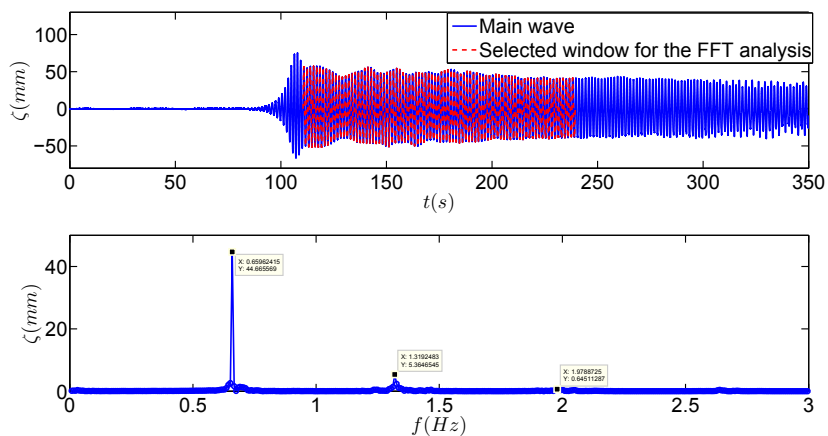


Figure B.9: FFT analysis for the incident wave profile for the case C494.

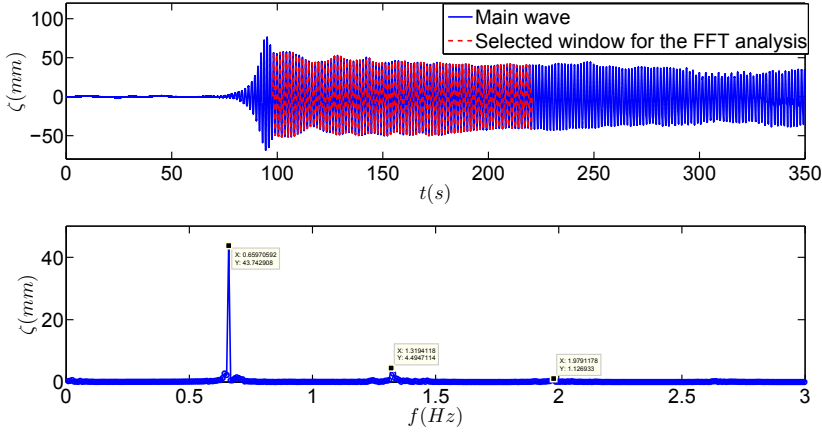


Figure B.10: FFT analysis for the incident wave profile for the case C498.

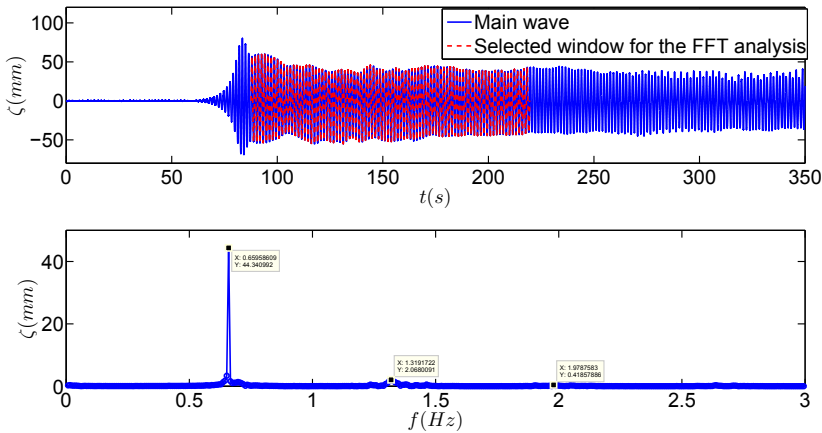


Figure B.11: FFT analysis for the incident wave profile for the case C501.

Since we only used the first harmonic of the waves in the simulations and the first harmonics are the main components for the low steepness waves (the nominal wave steepness here is 0.10), the mean and standard deviation are calculated for them only.

According to the values for the first harmonic of these waves, the mean wave amplitude is $43.83mm$ and the standard deviation is 2.1% of the mean value. The mean frequency for this harmonic is $0.6588Hz$ with a standard deviation as 0.02% of the mean value.

Appendix C

Further experiments and numerical simulations

The comparison of experimental and numerical motions for cases of the fishing vessel without anti-roll tank, was presented in all degrees-of-freedom in chapter 6. For sake of better comparison visibility, here it is provided for heave, roll and pitch motions only, due to their importance.

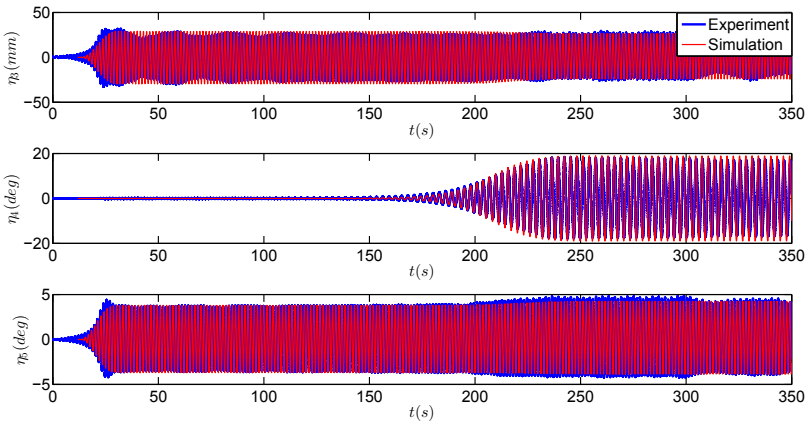


Figure C.1: Comparison of experimental and numerical simulation results for heave, roll and pitch motions for case C457. Frequency ratio $\frac{\omega_{n4}}{\omega_e} = 0.50$, $k\zeta_a = 0.10$ and $Fn = 0$.

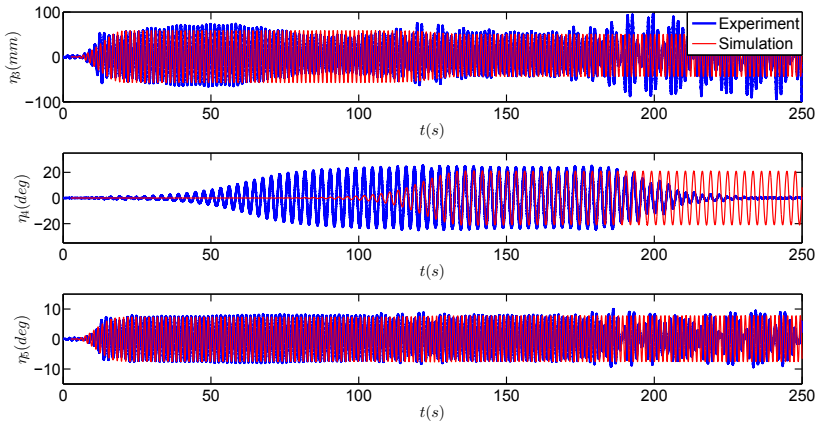


Figure C.2: Comparison of experimental and numerical simulation results for heave, roll and pitch motions for case C483. Frequency ratio $\frac{\omega_{n4}}{\omega_e} = 0.48$, $k\zeta_a = 0.25$ and $Fn = 0$.

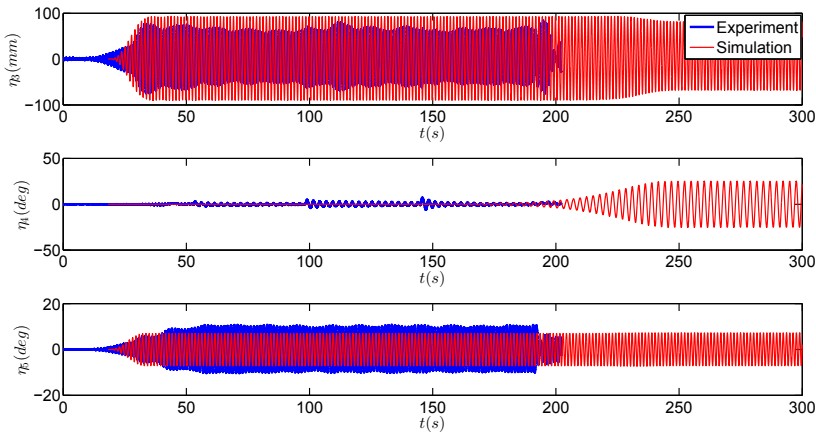


Figure C.3: Comparison of experimental and numerical simulation results for heave, roll and pitch motions for case C537. Frequency ratio $\frac{\omega_{n4}}{\omega_e} = 0.45$, $k\zeta_a = 0.15$ and $Fn = 0.09$.

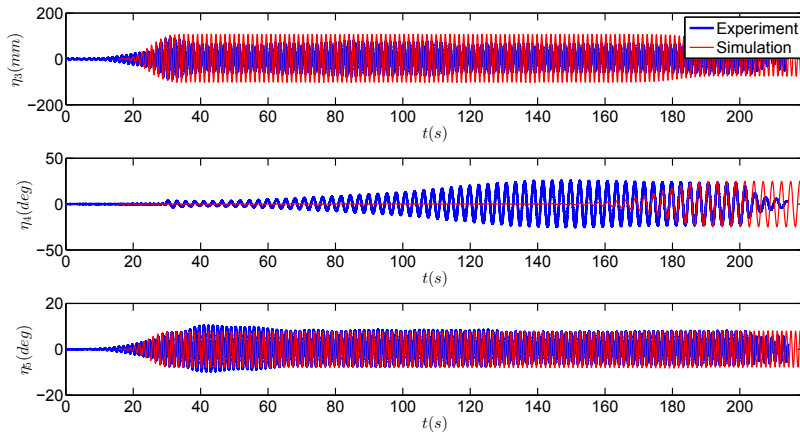


Figure C.4: Comparison of experimental and numerical simulation results for heave, roll and pitch motions for case C536. Frequency ratio $\frac{\omega_{n4}}{\omega_e} = 0.46$, $k\zeta_a = 0.15$ and $Fn = 0.09$.

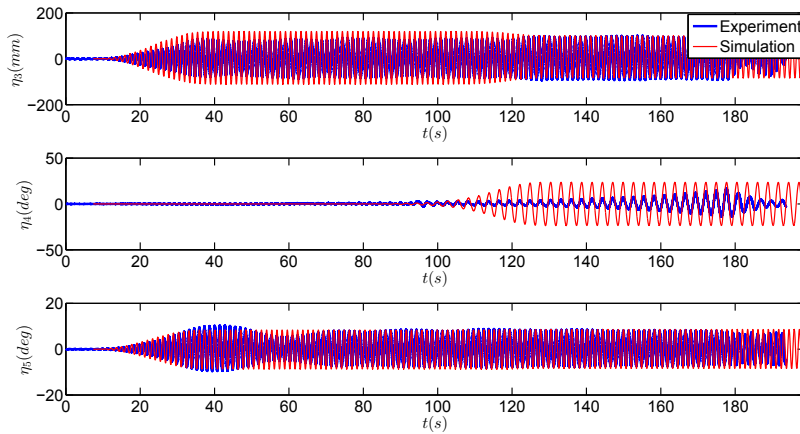


Figure C.5: Comparison of experimental and numerical simulation results for heave, roll and pitch motions for case C522. Frequency ratio $\frac{\omega_{n4}}{\omega_e} = 0.47$, $k\zeta_a = 0.15$ and $Fn = 0.09$.

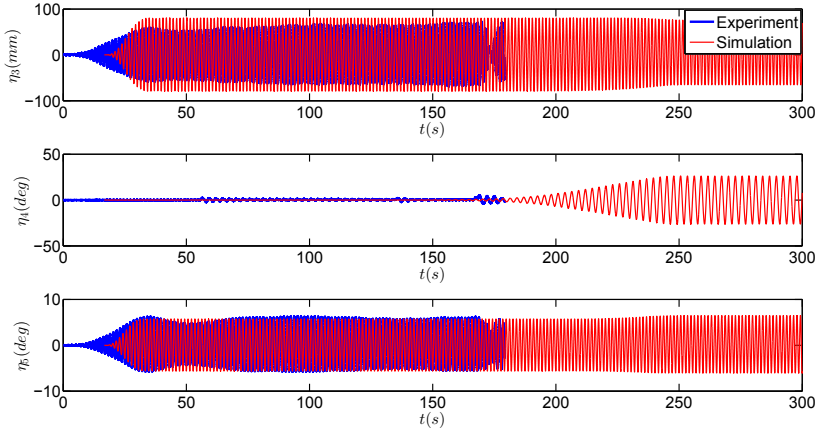


Figure C.6: Comparison of experimental and numerical simulation results for heave, roll and pitch motions for case C521. Frequency ratio $\frac{\omega_{n4}}{\omega_e} = 0.47$, $k\zeta_a = 0.10$ and $Fn = 0.09$.

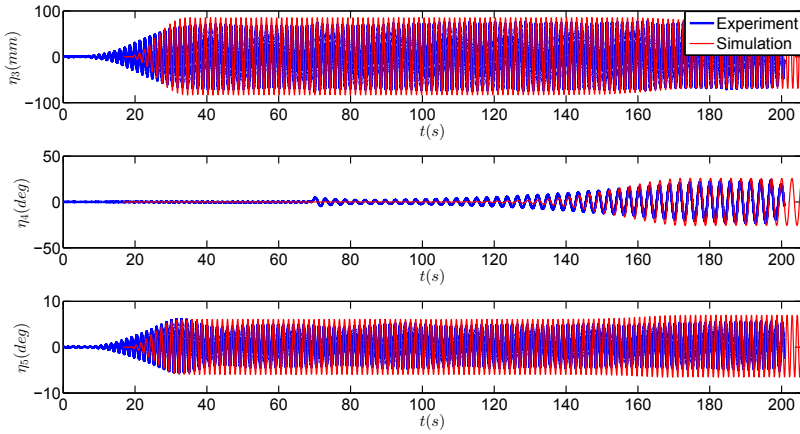


Figure C.7: Comparison of experimental and numerical simulation results for heave, roll and pitch motions for case C538. Frequency ratio $\frac{\omega_{n4}}{\omega_e} = 0.48$, $k\zeta_a = 0.10$ and $Fn = 0.09$.

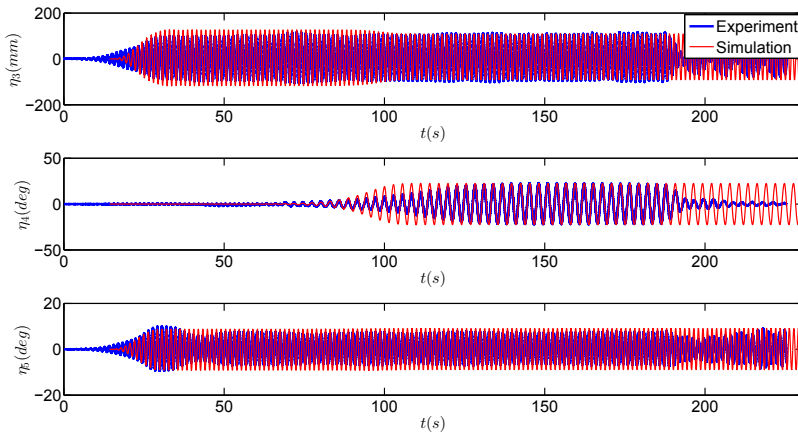


Figure C.8: Comparison of experimental and numerical simulation results for heave, roll and pitch motions for case C533. Frequency ratio $\frac{\omega_{n4}}{\omega_e} = 0.48$, $k\zeta_a = 0.15$ and $Fn = 0.09$.

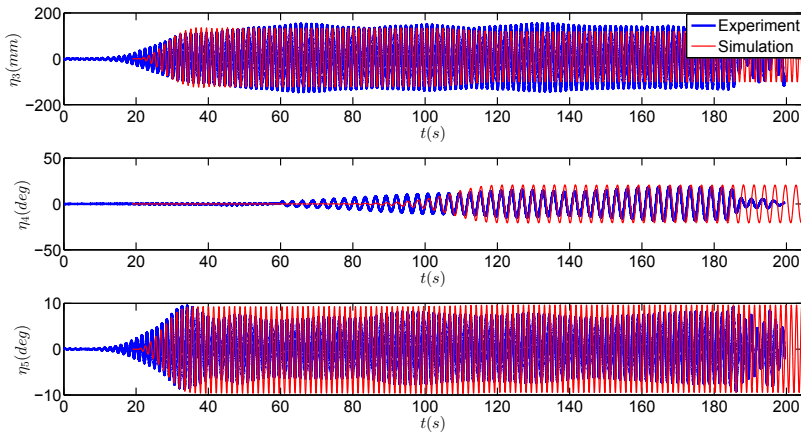


Figure C.9: Comparison of experimental and numerical simulation results for heave, roll and pitch motions for case C534. Frequency ratio $\frac{\omega_{n4}}{\omega_e} = 0.49$, $k\zeta_a = 0.15$ and $Fn = 0.09$.

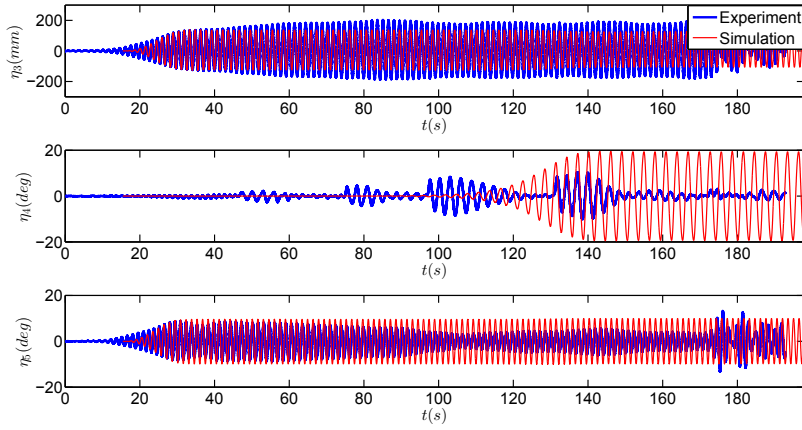


Figure C.10: Comparison of experimental and numerical simulation results for heave, roll and pitch motions for case C535. Frequency ratio $\frac{\omega_{n4}}{\omega_e} = 0.50$, $k\zeta_a = 0.15$ and $Fn = 0.09$.

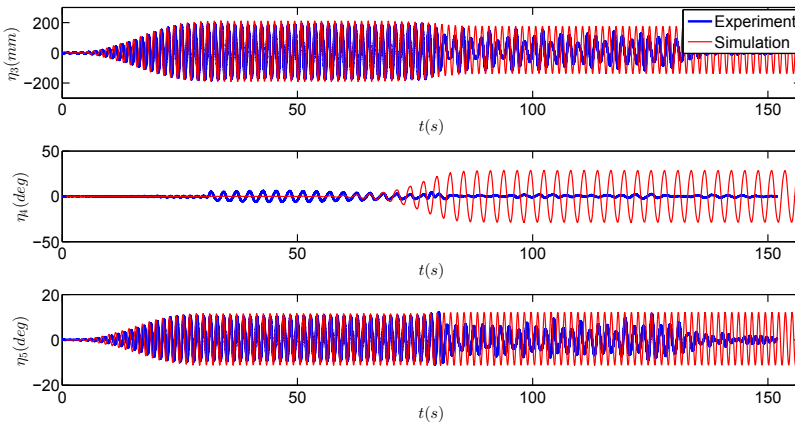


Figure C.11: Comparison of experimental and numerical simulation results for heave, roll and pitch motions for case C545. Frequency ratio $\frac{\omega_{n4}}{\omega_e} = 0.48$, $k\zeta_a = 0.15$ and $Fn = 0.18$.

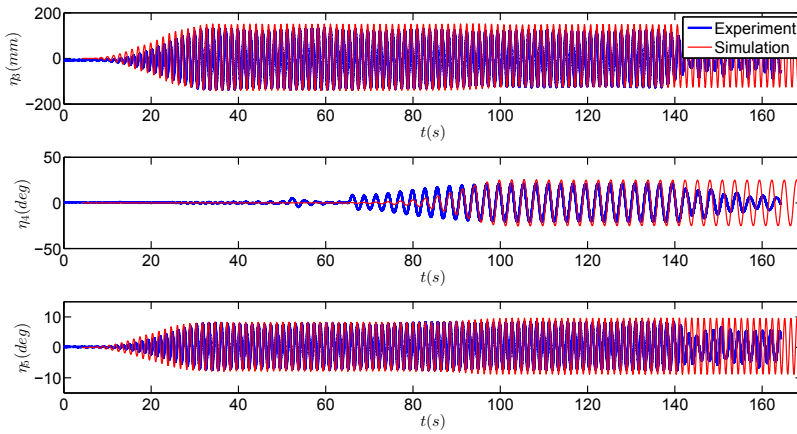


Figure C.12: Comparison of experimental and numerical simulation results for heave, roll and pitch motions for case C548. Frequency ratio $\frac{\omega_{n4}}{\omega_e} = 0.48$, $k\zeta_a = 0.10$ and $Fn = 0.18$.

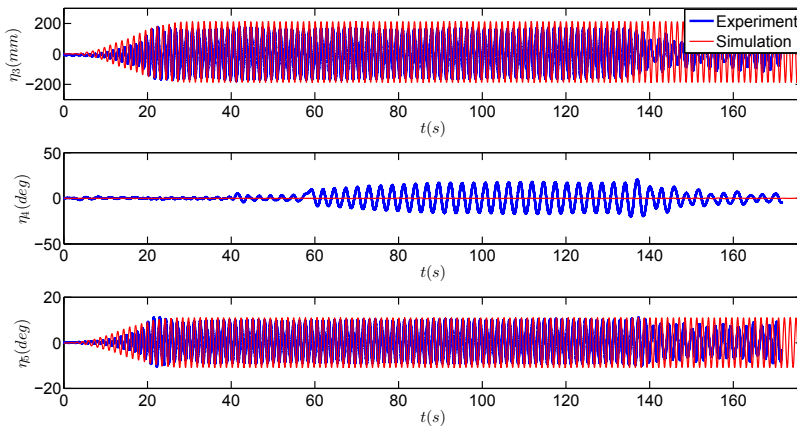


Figure C.13: Comparison of experimental and numerical simulation results for heave, roll and pitch motions for case C549. Frequency ratio $\frac{\omega_{n4}}{\omega_e} = 0.47$, $k\zeta_a = 0.15$ and $Fn = 0.18$.

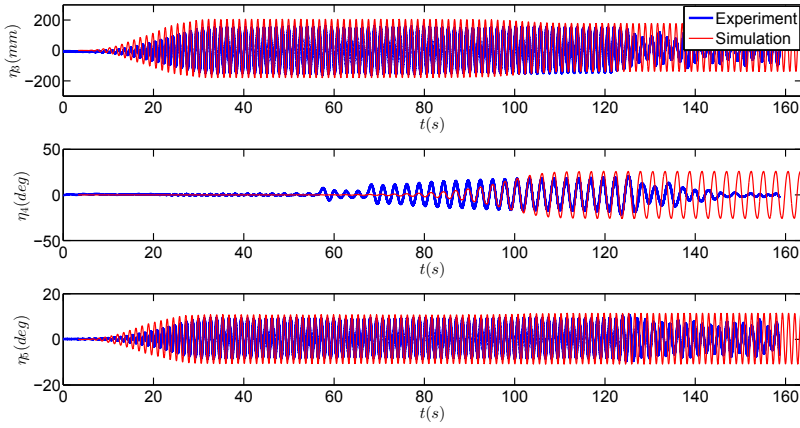


Figure C.14: Comparison of experimental and numerical simulation results for heave, roll and pitch motions for case C550. Frequency ratio $\frac{\omega_{n4}}{\omega_e} = 0.46$, $k\zeta_a = 0.15$ and $Fn = 0.18$.

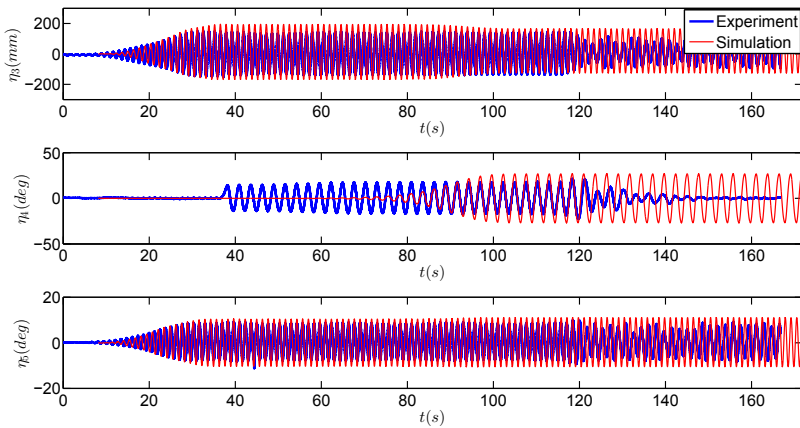


Figure C.15: Comparison of experimental and numerical simulation results for heave, roll and pitch motions for case C551. Frequency ratio $\frac{\omega_{n4}}{\omega_e} = 0.45$, $k\zeta_a = 0.15$ and $Fn = 0.18$.

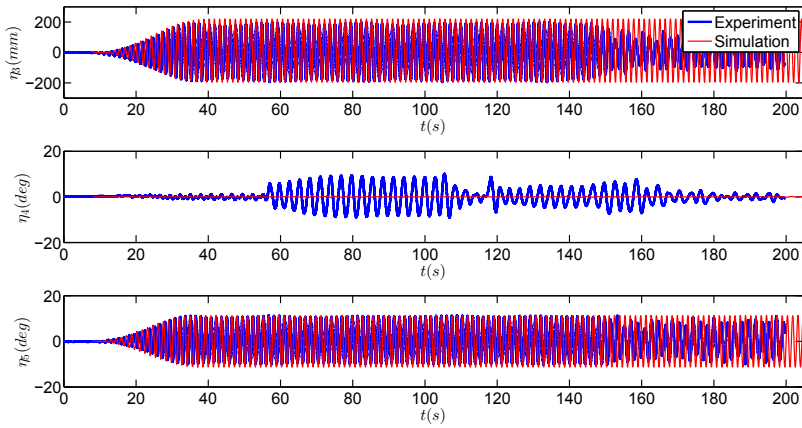


Figure C.16: Comparison of experimental and numerical simulation results for heave, roll and pitch motions for case C552. Frequency ratio $\frac{\omega_{n4}}{\omega_e} = 0.49$, $k\zeta_a = 0.15$ and $Fn = 0.18$.

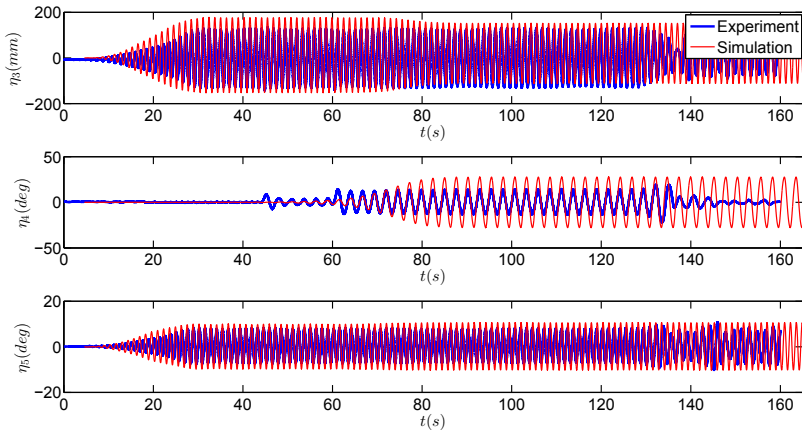


Figure C.17: Comparison of experimental and numerical simulation results for heave, roll and pitch motions for case C553. Frequency ratio $\frac{\omega_{n4}}{\omega_e} = 0.50$, $k\zeta_a = 0.15$ and $Fn = 0.18$.

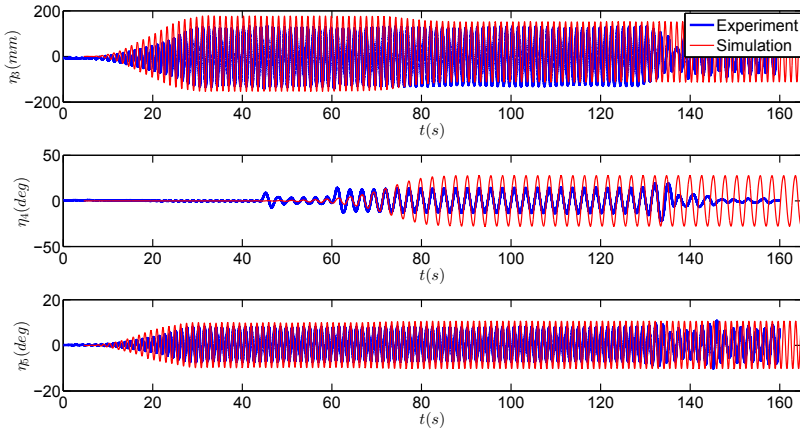


Figure C.18: Comparison of experimental and numerical simulation results for heave, roll and pitch motions for case C554. Frequency ratio $\frac{\omega_{n4}}{\omega_e} = 0.44$, $k\zeta_a = 0.15$ and $Fn = 0.18$.

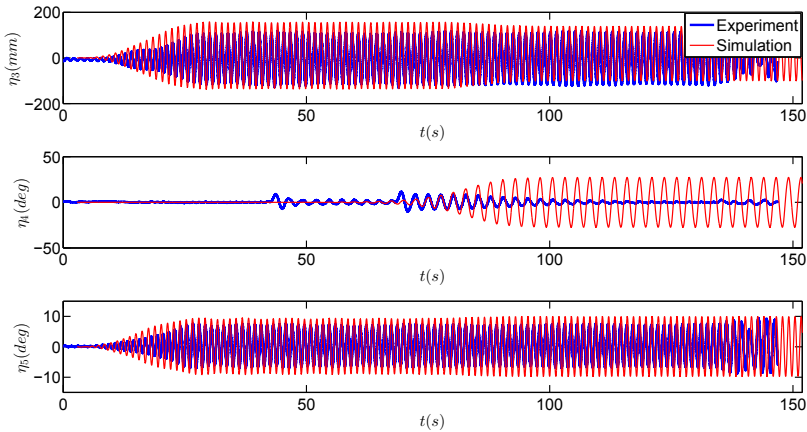


Figure C.19: Comparison of experimental and numerical simulation results for heave, roll and pitch motions for case C555. Frequency ratio $\frac{\omega_{n4}}{\omega_e} = 0.43$, $k\zeta_a = 0.15$ and $Fn = 0.18$.

**Previous PhD theses published at the Department of Marine Technology
(earlier: Faculty of Marine Technology)
NORWEGIAN UNIVERSITY OF SCIENCE AND TECHNOLOGY**

Report No.	Author	Title
	Kavlie, Dag	Optimization of Plane Elastic Grillages, 1967
	Hansen, Hans R.	Man-Machine Communication and Data-Storage Methods in Ship Structural Design, 1971
	Gisvold, Kaare M.	A Method for non-linear mixed -integer programming and its Application to Design Problems, 1971
	Lund, Sverre	Tanker Frame Optimalization by means of SUMT-Transformation and Behaviour Models, 1971
	Vinje, Tor	On Vibration of Spherical Shells Interacting with Fluid, 1972
	Lorentz, Jan D.	Tank Arrangement for Crude Oil Carriers in Accordance with the new Anti-Pollution Regulations, 1975
	Carlsen, Carl A.	Computer-Aided Design of Tanker Structures, 1975
	Larsen, Carl M.	Static and Dynamic Analysis of Offshore Pipelines during Installation, 1976
UR-79-01	Brigt Hatlestad, MK	The finite element method used in a fatigue evaluation of fixed offshore platforms. (Dr.Ing. Thesis)
UR-79-02	Erik Pettersen, MK	Analysis and design of cellular structures. (Dr.Ing. Thesis)
UR-79-03	Sverre Valsgård, MK	Finite difference and finite element methods applied to nonlinear analysis of plated structures. (Dr.Ing. Thesis)
UR-79-04	Nils T. Nordsve, MK	Finite element collapse analysis of structural members considering imperfections and stresses due to fabrication. (Dr.Ing. Thesis)
UR-79-05	Ivar J. Fylling, MK	Analysis of towline forces in ocean towing systems. (Dr.Ing. Thesis)
UR-80-06	Nils Sandsmark, MM	Analysis of Stationary and Transient Heat Conduction by the Use of the Finite Element Method. (Dr.Ing. Thesis)
UR-80-09	Sverre Haver, MK	Analysis of uncertainties related to the stochastic modeling of ocean waves. (Dr.Ing. Thesis)
UR-81-15	Odland, Jonas	On the Strength of welded Ring stiffened cylindrical Shells primarily subjected to axial Compression
UR-82-17	Engesvik, Knut	Analysis of Uncertainties in the fatigue Capacity of

Welded Joints

UR-82-18	Rye, Henrik	Ocean wave groups
UR-83-30	Eide, Oddvar Inge	On Cumulative Fatigue Damage in Steel Welded Joints
UR-83-33	Mo, Olav	Stochastic Time Domain Analysis of Slender Offshore Structures
UR-83-34	Amdahl, Jørgen	Energy absorption in Ship-platform impacts
UR-84-37	Mørch, Morten	Motions and mooring forces of semi submersibles as determined by full-scale measurements and theoretical analysis
UR-84-38	Soares, C. Guedes	Probabilistic models for load effects in ship structures
UR-84-39	Aarsnes, Jan V.	Current forces on ships
UR-84-40	Czujko, Jerzy	Collapse Analysis of Plates subjected to Biaxial Compression and Lateral Load
UR-85-46	Alf G. Engseth, MK	Finite element collapse analysis of tubular steel offshore structures. (Dr.Ing. Thesis)
UR-86-47	Dengody Sheshappa, MP	A Computer Design Model for Optimizing Fishing Vessel Designs Based on Techno-Economic Analysis. (Dr.Ing. Thesis)
UR-86-48	Vidar Aanesland, MH	A Theoretical and Numerical Study of Ship Wave Resistance. (Dr.Ing. Thesis)
UR-86-49	Heinz-Joachim Wessel, MK	Fracture Mechanics Analysis of Crack Growth in Plate Girders. (Dr.Ing. Thesis)
UR-86-50	Jon Taby, MK	Ultimate and Post-ultimate Strength of Dented Tubular Members. (Dr.Ing. Thesis)
UR-86-51	Walter Lian, MH	A Numerical Study of Two-Dimensional Separated Flow Past Bluff Bodies at Moderate KC-Numbers. (Dr.Ing. Thesis)
UR-86-52	Bjørn Sortland, MH	Force Measurements in Oscillating Flow on Ship Sections and Circular Cylinders in a U-Tube Water Tank. (Dr.Ing. Thesis)
UR-86-53	Kurt Strand, MM	A System Dynamic Approach to One-dimensional Fluid Flow. (Dr.Ing. Thesis)
UR-86-54	Arne Edvin Løken, MH	Three Dimensional Second Order Hydrodynamic Effects on Ocean Structures in Waves. (Dr.Ing. Thesis)
UR-86-55	Sigurd Falch, MH	A Numerical Study of Slamming of Two-Dimensional Bodies. (Dr.Ing. Thesis)
UR-87-56	Arne Braathen, MH	Application of a Vortex Tracking Method to the Prediction of Roll Damping of a Two-Dimension Floating Body. (Dr.Ing. Thesis)

UR-87-57	Bernt Leira, MK	Gaussian Vector Processes for Reliability Analysis involving Wave-Induced Load Effects. (Dr.Ing. Thesis)
UR-87-58	Magnus Småvik, MM	Thermal Load and Process Characteristics in a Two-Stroke Diesel Engine with Thermal Barriers (in Norwegian). (Dr.Ing. Thesis)
MTA-88-59	Bernt Arild Bremdal, MP	An Investigation of Marine Installation Processes – A Knowledge - Based Planning Approach. (Dr.Ing. Thesis)
MTA-88-60	Xu Jun, MK	Non-linear Dynamic Analysis of Space-framed Offshore Structures. (Dr.Ing. Thesis)
MTA-89-61	Gang Miao, MH	Hydrodynamic Forces and Dynamic Responses of Circular Cylinders in Wave Zones. (Dr.Ing. Thesis)
MTA-89-62	Martin Greenhow, MH	Linear and Non-Linear Studies of Waves and Floating Bodies. Part I and Part II. (Dr.Techn. Thesis)
MTA-89-63	Chang Li, MH	Force Coefficients of Spheres and Cubes in Oscillatory Flow with and without Current. (Dr.Ing. Thesis)
MTA-89-64	Hu Ying, MP	A Study of Marketing and Design in Development of Marine Transport Systems. (Dr.Ing. Thesis)
MTA-89-65	Arild Jæger, MH	Seakeeping, Dynamic Stability and Performance of a Wedge Shaped Planing Hull. (Dr.Ing. Thesis)
MTA-89-66	Chan Siu Hung, MM	The dynamic characteristics of tilting-pad bearings
MTA-89-67	Kim Wikstrøm, MP	Analysis av projekteringen for ett offshore projekt. (Licenciat-avhandling)
MTA-89-68	Jiao Guoyang, MK	Reliability Analysis of Crack Growth under Random Loading, considering Model Updating. (Dr.Ing. Thesis)
MTA-89-69	Arnt Olufsen, MK	Uncertainty and Reliability Analysis of Fixed Offshore Structures. (Dr.Ing. Thesis)
MTA-89-70	Wu Yu-Lin, MR	System Reliability Analyses of Offshore Structures using improved Truss and Beam Models. (Dr.Ing. Thesis)
MTA-90-71	Jan Roger Hoff, MH	Three-dimensional Green function of a vessel with forward speed in waves. (Dr.Ing. Thesis)
MTA-90-72	Rong Zhao, MH	Slow-Drift Motions of a Moored Two-Dimensional Body in Irregular Waves. (Dr.Ing. Thesis)
MTA-90-73	Atle Minsaas, MP	Economical Risk Analysis. (Dr.Ing. Thesis)
MTA-90-74	Knut-Aril Farnes, MK	Long-term Statistics of Response in Non-linear Marine Structures. (Dr.Ing. Thesis)
MTA-90-75	Torbjørn Sotberg, MK	Application of Reliability Methods for Safety Assessment of Submarine Pipelines. (Dr.Ing. Thesis)

		Thesis)
MTA-90-76	Zeuthen, Steffen, MP	SEAMAID. A computational model of the design process in a constraint-based logic programming environment. An example from the offshore domain. (Dr.Ing. Thesis)
MTA-91-77	Haagensen, Sven, MM	Fuel Dependant Cyclic Variability in a Spark Ignition Engine - An Optical Approach. (Dr.Ing. Thesis)
MTA-91-78	Løland, Geir, MH	Current forces on and flow through fish farms. (Dr.Ing. Thesis)
MTA-91-79	Hoen, Christopher, MK	System Identification of Structures Excited by Stochastic Load Processes. (Dr.Ing. Thesis)
MTA-91-80	Haugen, Stein, MK	Probabilistic Evaluation of Frequency of Collision between Ships and Offshore Platforms. (Dr.Ing. Thesis)
MTA-91-81	Sødahl, Nils, MK	Methods for Design and Analysis of Flexible Risers. (Dr.Ing. Thesis)
MTA-91-82	Ormberg, Harald, MK	Non-linear Response Analysis of Floating Fish Farm Systems. (Dr.Ing. Thesis)
MTA-91-83	Marley, Mark J., MK	Time Variant Reliability under Fatigue Degradation. (Dr.Ing. Thesis)
MTA-91-84	Krokstad, Jørgen R., MH	Second-order Loads in Multidirectional Seas. (Dr.Ing. Thesis)
MTA-91-85	Molteberg, Gunnar A., MM	The Application of System Identification Techniques to Performance Monitoring of Four Stroke Turbocharged Diesel Engines. (Dr.Ing. Thesis)
MTA-92-86	Mørch, Hans Jørgen Bjelke, MH	Aspects of Hydrofoil Design: with Emphasis on Hydrofoil Interaction in Calm Water. (Dr.Ing. Thesis)
MTA-92-87	Chan Siu Hung, MM	Nonlinear Analysis of Rotordynamic Instabilities in Highspeed Turbomachinery. (Dr.Ing. Thesis)
MTA-92-88	Bessason, Bjarni, MK	Assessment of Earthquake Loading and Response of Seismically Isolated Bridges. (Dr.Ing. Thesis)
MTA-92-89	Langli, Geir, MP	Improving Operational Safety through exploitation of Design Knowledge - an investigation of offshore platform safety. (Dr.Ing. Thesis)
MTA-92-90	Sævik, Svein, MK	On Stresses and Fatigue in Flexible Pipes. (Dr.Ing. Thesis)
MTA-92-91	Ask, Tor Ø., MM	Ignition and Flame Growth in Lean Gas-Air Mixtures. An Experimental Study with a Schlieren System. (Dr.Ing. Thesis)
MTA-86-92	Hessen, Gunnar, MK	Fracture Mechanics Analysis of Stiffened Tubular Members. (Dr.Ing. Thesis)

MTA-93-93	Steinebach, Christian, MM	Knowledge Based Systems for Diagnosis of Rotating Machinery. (Dr.Ing. Thesis)
MTA-93-94	Dalane, Jan Inge, MK	System Reliability in Design and Maintenance of Fixed Offshore Structures. (Dr.Ing. Thesis)
MTA-93-95	Steen, Sverre, MH	Cobblestone Effect on SES. (Dr.Ing. Thesis)
MTA-93-96	Karunakaran, Daniel, MK	Nonlinear Dynamic Response and Reliability Analysis of Drag-dominated Offshore Platforms. (Dr.Ing. Thesis)
MTA-93-97	Hagen, Arnulf, MP	The Framework of a Design Process Language. (Dr.Ing. Thesis)
MTA-93-98	Nordrik, Rune, MM	Investigation of Spark Ignition and Autoignition in Methane and Air Using Computational Fluid Dynamics and Chemical Reaction Kinetics. A Numerical Study of Ignition Processes in Internal Combustion Engines. (Dr.Ing. Thesis)
MTA-94-99	Passano, Elizabeth, MK	Efficient Analysis of Nonlinear Slender Marine Structures. (Dr.Ing. Thesis)
MTA-94-100	Kvålsvold, Jan, MH	Hydroelastic Modelling of Wetdeck Slamming on Multihull Vessels. (Dr.Ing. Thesis)
MTA-94-102	Bech, Sidsel M., MK	Experimental and Numerical Determination of Stiffness and Strength of GRP/PVC Sandwich Structures. (Dr.Ing. Thesis)
MTA-95-103	Paulsen, Hallvard, MM	A Study of Transient Jet and Spray using a Schlieren Method and Digital Image Processing. (Dr.Ing. Thesis)
MTA-95-104	Hovde, Geir Olav, MK	Fatigue and Overload Reliability of Offshore Structural Systems, Considering the Effect of Inspection and Repair. (Dr.Ing. Thesis)
MTA-95-105	Wang, Xiaozhi, MK	Reliability Analysis of Production Ships with Emphasis on Load Combination and Ultimate Strength. (Dr.Ing. Thesis)
MTA-95-106	Ulstein, Tore, MH	Nonlinear Effects of a Flexible Stern Seal Bag on Cobblestone Oscillations of an SES. (Dr.Ing. Thesis)
MTA-95-107	Solaas, Frøydis, MH	Analytical and Numerical Studies of Sloshing in Tanks. (Dr.Ing. Thesis)
MTA-95-108	Hellan, Øyvind, MK	Nonlinear Pushover and Cyclic Analyses in Ultimate Limit State Design and Reassessment of Tubular Steel Offshore Structures. (Dr.Ing. Thesis)
MTA-95-109	Hermundstad, Ole A., MK	Theoretical and Experimental Hydroelastic Analysis of High Speed Vessels. (Dr.Ing. Thesis)
MTA-96-110	Bratland, Anne K., MH	Wave-Current Interaction Effects on Large-Volume Bodies in Water of Finite Depth. (Dr.Ing. Thesis)
MTA-96-111	Herfjord, Kjell, MH	A Study of Two-dimensional Separated Flow by a Combination of the Finite Element Method and

		Navier-Stokes Equations. (Dr.Ing. Thesis)
MTA-96-112	Æsøy, Vilmar, MM	Hot Surface Assisted Compression Ignition in a Direct Injection Natural Gas Engine. (Dr.Ing. Thesis)
MTA-96-113	Eknes, Monika L., MK	Escalation Scenarios Initiated by Gas Explosions on Offshore Installations. (Dr.Ing. Thesis)
MTA-96-114	Erikstad, Stein O., MP	A Decision Support Model for Preliminary Ship Design. (Dr.Ing. Thesis)
MTA-96-115	Pedersen, Egil, MH	A Nautical Study of Towed Marine Seismic Streamer Cable Configurations. (Dr.Ing. Thesis)
MTA-97-116	Moksnes, Paul O., MM	Modelling Two-Phase Thermo-Fluid Systems Using Bond Graphs. (Dr.Ing. Thesis)
MTA-97-117	Halse, Karl H., MK	On Vortex Shedding and Prediction of Vortex-Induced Vibrations of Circular Cylinders. (Dr.Ing. Thesis)
MTA-97-118	Igland, Ragnar T., MK	Reliability Analysis of Pipelines during Laying, considering Ultimate Strength under Combined Loads. (Dr.Ing. Thesis)
MTA-97-119	Pedersen, Hans-P., MP	Levendefiskteknologi for fiskefartøy. (Dr.Ing. Thesis)
MTA-98-120	Vikestad, Kyrre, MK	Multi-Frequency Response of a Cylinder Subjected to Vortex Shedding and Support Motions. (Dr.Ing. Thesis)
MTA-98-121	Azadi, Mohammad R. E., MK	Analysis of Static and Dynamic Pile-Soil-Jacket Behaviour. (Dr.Ing. Thesis)
MTA-98-122	Ulltang, Terje, MP	A Communication Model for Product Information. (Dr.Ing. Thesis)
MTA-98-123	Torbergsen, Erik, MM	Impeller/Diffuser Interaction Forces in Centrifugal Pumps. (Dr.Ing. Thesis)
MTA-98-124	Hansen, Edmond, MH	A Discrete Element Model to Study Marginal Ice Zone Dynamics and the Behaviour of Vessels Moored in Broken Ice. (Dr.Ing. Thesis)
MTA-98-125	Videiro, Paulo M., MK	Reliability Based Design of Marine Structures. (Dr.Ing. Thesis)
MTA-99-126	Mainçon, Philippe, MK	Fatigue Reliability of Long Welds Application to Titanium Risers. (Dr.Ing. Thesis)
MTA-99-127	Haugen, Elin M., MH	Hydroelastic Analysis of Slamming on Stiffened Plates with Application to Catamaran Wetdecks. (Dr.Ing. Thesis)
MTA-99-128	Langhelle, Nina K., MK	Experimental Validation and Calibration of Nonlinear Finite Element Models for Use in Design of Aluminium Structures Exposed to Fire. (Dr.Ing. Thesis)
MTA-99-	Berstad, Are J., MK	Calculation of Fatigue Damage in Ship Structures.

129		(Dr.Ing. Thesis)
MTA-99-130	Andersen, Trond M., MM	Short Term Maintenance Planning. (Dr.Ing. Thesis)
MTA-99-131	Tveiten, Bård Wathne, MK	Fatigue Assessment of Welded Aluminium Ship Details. (Dr.Ing. Thesis)
MTA-99-132	Søreide, Fredrik, MP	Applications of underwater technology in deep water archaeology. Principles and practice. (Dr.Ing. Thesis)
MTA-99-133	Tønnessen, Rune, MH	A Finite Element Method Applied to Unsteady Viscous Flow Around 2D Blunt Bodies With Sharp Corners. (Dr.Ing. Thesis)
MTA-99-134	Elvekrok, Dag R., MP	Engineering Integration in Field Development Projects in the Norwegian Oil and Gas Industry. The Supplier Management of Norne. (Dr.Ing. Thesis)
MTA-99-135	Fagerholt, Kjetil, MP	Optimeringsbaserte Metoder for Ruteplanlegging innen skipsfart. (Dr.Ing. Thesis)
MTA-99-136	Bysveen, Marie, MM	Visualization in Two Directions on a Dynamic Combustion Rig for Studies of Fuel Quality. (Dr.Ing. Thesis)
MTA-2000-137	Storteig, Eskild, MM	Dynamic characteristics and leakage performance of liquid annular seals in centrifugal pumps. (Dr.Ing. Thesis)
MTA-2000-138	Sagli, Gro, MK	Model uncertainty and simplified estimates of long term extremes of hull girder loads in ships. (Dr.Ing. Thesis)
MTA-2000-139	Tronstad, Harald, MK	Nonlinear analysis and design of cable net structures like fishing gear based on the finite element method. (Dr.Ing. Thesis)
MTA-2000-140	Kroneberg, André, MP	Innovation in shipping by using scenarios. (Dr.Ing. Thesis)
MTA-2000-141	Haslum, Herbjørn Alf, MH	Simplified methods applied to nonlinear motion of spar platforms. (Dr.Ing. Thesis)
MTA-2001-142	Samdal, Ole Johan, MM	Modelling of Degradation Mechanisms and Stressor Interaction on Static Mechanical Equipment Residual Lifetime. (Dr.Ing. Thesis)
MTA-2001-143	Baarholm, Rolf Jarle, MH	Theoretical and experimental studies of wave impact underneath decks of offshore platforms. (Dr.Ing. Thesis)
MTA-2001-144	Wang, Lihua, MK	Probabilistic Analysis of Nonlinear Wave-induced Loads on Ships. (Dr.Ing. Thesis)
MTA-2001-145	Kristensen, Odd H. Holt, MK	Ultimate Capacity of Aluminium Plates under Multiple Loads, Considering HAZ Properties. (Dr.Ing. Thesis)
MTA-2001-146	Greco, Marilena, MH	A Two-Dimensional Study of Green-Water

			Loading. (Dr.Ing. Thesis)
MTA-2001-147	Heggelund, Svein E., MK		Calculation of Global Design Loads and Load Effects in Large High Speed Catamarans. (Dr.Ing. Thesis)
MTA-2001-148	Babalola, Olusegun T., MK		Fatigue Strength of Titanium Risers – Defect Sensitivity. (Dr.Ing. Thesis)
MTA-2001-149	Mohammed, Abuu K., MK		Nonlinear Shell Finite Elements for Ultimate Strength and Collapse Analysis of Ship Structures. (Dr.Ing. Thesis)
MTA-2002-150	Holmedal, Lars E., MH		Wave-current interactions in the vicinity of the sea bed. (Dr.Ing. Thesis)
MTA-2002-151	Rognebakke, Olav F., MH		Sloshing in rectangular tanks and interaction with ship motions. (Dr.Ing. Thesis)
MTA-2002-152	Lader, Pål Furset, MH		Geometry and Kinematics of Breaking Waves. (Dr.Ing. Thesis)
MTA-2002-153	Yang, Qinzheng, MH		Wash and wave resistance of ships in finite water depth. (Dr.Ing. Thesis)
MTA-2002-154	Melhus, Øyvind, MM		Utilization of VOC in Diesel Engines. Ignition and combustion of VOC released by crude oil tankers. (Dr.Ing. Thesis)
MTA-2002-155	Ronæss, Marit, MH		Wave Induced Motions of Two Ships Advancing on Parallel Course. (Dr.Ing. Thesis)
MTA-2002-156	Økland, Ole D., MK		Numerical and experimental investigation of whipping in twin hull vessels exposed to severe wet deck slamming. (Dr.Ing. Thesis)
MTA-2002-157	Ge, Chunhua, MK		Global Hydroelastic Response of Catamarans due to Wet Deck Slamming. (Dr.Ing. Thesis)
MTA-2002-158	Byklum, Eirik, MK		Nonlinear Shell Finite Elements for Ultimate Strength and Collapse Analysis of Ship Structures. (Dr.Ing. Thesis)
IMT-2003-1	Chen, Haibo, MK		Probabilistic Evaluation of FPSO-Tanker Collision in Tandem Offloading Operation. (Dr.Ing. Thesis)
IMT-2003-2	Skaugset, Kjetil Bjørn, MK		On the Suppression of Vortex Induced Vibrations of Circular Cylinders by Radial Water Jets. (Dr.Ing. Thesis)
IMT-2003-3	Chezian, Muthu		Three-Dimensional Analysis of Slamming. (Dr.Ing. Thesis)
IMT-2003-4	Buhaug, Øyvind		Deposit Formation on Cylinder Liner Surfaces in Medium Speed Engines. (Dr.Ing. Thesis)
IMT-2003-5	Tregde, Vidar		Aspects of Ship Design: Optimization of Aft Hull with Inverse Geometry Design. (Dr.Ing. Thesis)
IMT-	Wist, Hanne Therese		Statistical Properties of Successive Ocean Wave

2003-6		Parameters. (Dr.Ing. Thesis)
IMT-2004-7	Ransau, Samuel	Numerical Methods for Flows with Evolving Interfaces. (Dr.Ing. Thesis)
IMT-2004-8	Soma, Torkel	Blue-Chip or Sub-Standard. A data interrogation approach of identity safety characteristics of shipping organization. (Dr.Ing. Thesis)
IMT-2004-9	Ersdal, Svein	An experimental study of hydrodynamic forces on cylinders and cables in near axial flow. (Dr.Ing. Thesis)
IMT-2005-10	Brodtkorb, Per Andreas	The Probability of Occurrence of Dangerous Wave Situations at Sea. (Dr.Ing. Thesis)
IMT-2005-11	Yttervik, Rune	Ocean current variability in relation to offshore engineering. (Dr.Ing. Thesis)
IMT-2005-12	Fredheim, Arne	Current Forces on Net-Structures. (Dr.Ing. Thesis)
IMT-2005-13	Heggernes, Kjetil	Flow around marine structures. (Dr.Ing. Thesis)
IMT-2005-14	Fouques, Sebastien	Lagrangian Modelling of Ocean Surface Waves and Synthetic Aperture Radar Wave Measurements. (Dr.Ing. Thesis)
IMT-2006-15	Holm, Håvard	Numerical calculation of viscous free surface flow around marine structures. (Dr.Ing. Thesis)
IMT-2006-16	Bjørheim, Lars G.	Failure Assessment of Long Through Thickness Fatigue Cracks in Ship Hulls. (Dr.Ing. Thesis)
IMT-2006-17	Hansson, Lisbeth	Safety Management for Prevention of Occupational Accidents. (Dr.Ing. Thesis)
IMT-2006-18	Zhu, Xinying	Application of the CIP Method to Strongly Nonlinear Wave-Body Interaction Problems. (Dr.Ing. Thesis)
IMT-2006-19	Reite, Karl Johan	Modelling and Control of Trawl Systems. (Dr.Ing. Thesis)
IMT-2006-20	Smogeli, Øyvind Notland	Control of Marine Propellers. From Normal to Extreme Conditions. (Dr.Ing. Thesis)
IMT-2007-21	Storhaug, Gaute	Experimental Investigation of Wave Induced Vibrations and Their Effect on the Fatigue Loading of Ships. (Dr.Ing. Thesis)
IMT-2007-22	Sun, Hui	A Boundary Element Method Applied to Strongly Nonlinear Wave-Body Interaction Problems. (PhD Thesis, CeSOS)
IMT-2007-23	Rustad, Anne Marthine	Modelling and Control of Top Tensioned Risers. (PhD Thesis, CeSOS)
IMT-2007-24	Johansen, Vegar	Modelling flexible slender system for real-time simulations and control applications
IMT-2007-25	Wroldsen, Anders Sunde	Modelling and control of tensegrity structures.

(PhD Thesis, CeSOS)

IMT-2007-26	Aronsen, Kristoffer Høye	An experimental investigation of in-line and combined inline and cross flow vortex induced vibrations. (Dr. avhandling, IMT)
IMT-2007-27	Gao, Zhen	Stochastic Response Analysis of Mooring Systems with Emphasis on Frequency-domain Analysis of Fatigue due to Wide-band Response Processes (PhD Thesis, CeSOS)
IMT-2007-28	Thorstensen, Tom Anders	Lifetime Profit Modelling of Ageing Systems Utilizing Information about Technical Condition. (Dr.ing. thesis, IMT)
IMT-2008-29	Refsnes, Jon Erling Gorset	Nonlinear Model-Based Control of Slender Body AUVs (PhD Thesis, IMT)
IMT-2008-30	Berntsen, Per Ivar B.	Structural Reliability Based Position Mooring. (PhD-Thesis, IMT)
IMT-2008-31	Ye, Naiquan	Fatigue Assessment of Aluminium Welded Box-stiffener Joints in Ships (Dr.ing. thesis, IMT)
IMT-2008-32	Radan, Damir	Integrated Control of Marine Electrical Power Systems. (PhD-Thesis, IMT)
IMT-2008-33	Thomassen, Paul	Methods for Dynamic Response Analysis and Fatigue Life Estimation of Floating Fish Cages. (Dr.ing. thesis, IMT)
IMT-2008-34	Pákozdi, Csaba	A Smoothed Particle Hydrodynamics Study of Two-dimensional Nonlinear Sloshing in Rectangular Tanks. (Dr.ing.thesis, IMT/ CeSOS)
IMT-2007-35	Grytøyr, Guttorm	A Higher-Order Boundary Element Method and Applications to Marine Hydrodynamics. (Dr.ing.thesis, IMT)
IMT-2008-36	Drummen, Ingo	Experimental and Numerical Investigation of Nonlinear Wave-Induced Load Effects in Containerships considering Hydroelasticity. (PhD thesis, CeSOS)
IMT-2008-37	Skejic, Renato	Maneuvering and Seakeeping of a Singel Ship and of Two Ships in Interaction. (PhD-Thesis, CeSOS)
IMT-2008-38	Harlem, Alf	An Age-Based Replacement Model for Repairable Systems with Attention to High-Speed Marine Diesel Engines. (PhD-Thesis, IMT)
IMT-2008-39	Alsos, Hagbart S.	Ship Grounding. Analysis of Ductile Fracture, Bottom Damage and Hull Girder Response. (PhD-thesis, IMT)
IMT-2008-40	Graczyk, Mateusz	Experimental Investigation of Sloshing Loading and Load Effects in Membrane LNG Tanks Subjected to Random Excitation. (PhD-thesis, CeSOS)
IMT-2008-41	Taghipour, Reza	Efficient Prediction of Dynamic Response for Flexible amd Multi-body Marine Structures. (PhD-

		thesis, CeSOS)
IMT-2008-42	Ruth, Eivind	Propulsion control and thrust allocation on marine vessels. (PhD thesis, CeSOS)
IMT-2008-43	Nystad, Bent Helge	Technical Condition Indexes and Remaining Useful Life of Aggregated Systems. PhD thesis, IMT
IMT-2008-44	Soni, Prashant Kumar	Hydrodynamic Coefficients for Vortex Induced Vibrations of Flexible Beams, PhD thesis, CeSOS
IMT-2009-45	Amlashi, Hadi K.K.	Ultimate Strength and Reliability-based Design of Ship Hulls with Emphasis on Combined Global and Local Loads. PhD Thesis, IMT
IMT-2009-46	Pedersen, Tom Arne	Bond Graph Modelling of Marine Power Systems. PhD Thesis, IMT
IMT-2009-47	Kristiansen, Trygve	Two-Dimensional Numerical and Experimental Studies of Piston-Mode Resonance. PhD-Thesis, CeSOS
IMT-2009-48	Ong, Muk Chen	Applications of a Standard High Reynolds Number Model and a Stochastic Scour Prediction Model for Marine Structures. PhD-thesis, IMT
IMT-2009-49	Hong, Lin	Simplified Analysis and Design of Ships subjected to Collision and Grounding. PhD-thesis, IMT
IMT-2009-50	Koushan, Kamran	Vortex Induced Vibrations of Free Span Pipelines, PhD thesis, IMT
IMT-2009-51	Korsvik, Jarl Eirik	Heuristic Methods for Ship Routing and Scheduling. PhD-thesis, IMT
IMT-2009-52	Lee, Jihoon	Experimental Investigation and Numerical in Analyzing the Ocean Current Displacement of Longlines. Ph.d.-Thesis, IMT.
IMT-2009-53	Vestbøstad, Tone Gran	A Numerical Study of Wave-in-Deck Impact using a Two-Dimensional Constrained Interpolation Profile Method, Ph.d.thesis, CeSOS.
IMT-2009-54	Bruun, Kristine	Bond Graph Modelling of Fuel Cells for Marine Power Plants. Ph.d.-thesis, IMT
IMT 2009-55	Holstad, Anders	Numerical Investigation of Turbulence in a Sekwed Three-Dimensional Channel Flow, Ph.d.-thesis, IMT.
IMT 2009-56	Ayala-Uruga, Efen	Reliability-Based Assessment of Deteriorating Ship-shaped Offshore Structures, Ph.d.-thesis, IMT
IMT 2009-57	Kong, Xiangjun	A Numerical Study of a Damaged Ship in Beam Sea Waves. Ph.d.-thesis, IMT/CeSOS.
IMT 2010-58	Kristiansen, David	Wave Induced Effects on Floaters of Aquaculture Plants, Ph.d.-thesis, CeSOS.

IMT 2010-59	Ludvigsen, Martin	An ROV-Toolbox for Optical and Acoustic Scientific Seabed Investigation. Ph.d.-thesis IMT.
IMT 2010-60	Hals, Jørgen	Modelling and Phase Control of Wave-Energy Converters. Ph.d.thesis, CeSOS.
IMT 2010- 61	Shu, Zhi	Uncertainty Assessment of Wave Loads and Ultimate Strength of Tankers and Bulk Carriers in a Reliability Framework. Ph.d. Thesis, IMT/ CeSOS
IMT 2010-62	Shao, Yanlin	Numerical Potential-Flow Studies on Weakly-Nonlinear Wave-Body Interactions with/without Small Forward Speed, Ph.d.thesis,CeSOS.
IMT 2010-63	Califano, Andrea	Dynamic Loads on Marine Propellers due to Intermittent Ventilation. Ph.d.thesis, IMT.
IMT 2010-64	El Khoury, George	Numerical Simulations of Massively Separated Turbulent Flows, Ph.d.-thesis, IMT
IMT 2010-65	Seim, Knut Sponheim	Mixing Process in Dense Overflows with Emphasis on the Faroe Bank Channel Overflow. Ph.d.thesis, IMT
IMT 2010-66	Jia, Huirong	Structural Analysis of Intact and Damaged Ships in a Collision Risk Analysis Perspective. Ph.d.thesis CeSoS.
IMT 2010-67	Jiao, Linlin	Wave-Induced Effects on a Pontoon-type Very Large Floating Structures (VLFS). Ph.D.-thesis, CeSOS.
IMT 2010-68	Abrahamsen, Bjørn Christian	Sloshing Induced Tank Roof with Entrapped Air Pocket. Ph.d.thesis, CeSOS.
IMT 2011-69	Karimirad, Madjid	Stochastic Dynamic Response Analysis of Spar-Type Wind Turbines with Catenary or Taut Mooring Systems. Ph.d.-thesis, CeSOS.
IMT - 2011-70	Erlend Meland	Condition Monitoring of Safety Critical Valves. Ph.d.-thesis, IMT.
IMT – 2011-71	Yang, Limin	Stochastic Dynamic System Analysis of Wave Energy Converter with Hydraulic Power Take-Off, with Particular Reference to Wear Damage Analysis, Ph.d. Thesis, CeSOS.
IMT – 2011-72	Visscher, Jan	Application of Particle Image Velocimetry on Turbulent Marine Flows, Ph.d.Thesis, IMT.
IMT – 2011-73	Su, Biao	Numerical Predictions of Global and Local Ice Loads on Ships. Ph.d.Thesis, CeSOS.
IMT – 2011-74	Liu, Zhenhui	Analytical and Numerical Analysis of Iceberg Collision with Ship Structures. Ph.d.Thesis, IMT.
IMT – 2011-75	Aarsæther, Karl Gunnar	Modeling and Analysis of Ship Traffic by Observation and Numerical Simulation. Ph.d.Thesis, IMT.

Imt – 2011-76	Wu, Jie	Hydrodynamic Force Identification from Stochastic Vortex Induced Vibration Experiments with Slender Beams. Ph.d.Thesis, IMT.
Imt – 2011-77	Amini, Hamid	Azimuth Propulsors in Off-design Conditions. Ph.d.Thesis, IMT.
IMT – 2011-78	Nguyen, Tan-Hoi	Toward a System of Real-Time Prediction and Monitoring of Bottom Damage Conditions During Ship Grounding. Ph.d.thesis, IMT.
IMT- 2011-79	Tavakoli, Mohammad T.	Assessment of Oil Spill in Ship Collision and Grounding, Ph.d.thesis, IMT.
IMT- 2011-80	Guo, Bingjie	Numerical and Experimental Investigation of Added Resistance in Waves. Ph.d.Thesis, IMT.
IMT- 2011-81	Chen, Qiaofeng	Ultimate Strength of Aluminium Panels, considering HAZ Effects, IMT
IMT- 2012-82	Kota, Ravikiran S.	Wave Loads on Decks of Offshore Structures in Random Seas, CeSOS.
IMT- 2012-83	Sten, Ronny	Dynamic Simulation of Deep Water Drilling Risers with Heave Compensating System, IMT.
IMT- 2012-84	Berle, Øyvind	Risk and resilience in global maritime supply chains, IMT.
IMT- 2012-85	Fang, Shaoji	Fault Tolerant Position Mooring Control Based on Structural Reliability, CeSOS.
IMT- 2012-86	You, Jikun	Numerical studies on wave forces and moored ship motions in intermediate and shallow water, CeSOS.
IMT- 2012-87	Xiang ,Xu	Maneuvering of two interacting ships in waves, CeSOS
IMT- 2012-88	Dong, Wenbin	Time-domain fatigue response and reliability analysis of offshore wind turbines with emphasis on welded tubular joints and gear components, CeSOS
IMT- 2012-89	Zhu, Suji	Investigation of Wave-Induced Nonlinear Load Effects in Open Ships considering Hull Girder Vibrations in Bending and Torsion, CeSOS
IMT- 2012-90	Zhou, Li	Numerical and Experimental Investigation of Station-keeping in Level Ice, CeSOS
IMT- 2012-91	Ushakov, Sergey	Particulate matter emission characteristics from diesel engines operating on conventional and alternative marine fuels, IMT
IMT- 2013-1	Yin, Decao	Experimental and Numerical Analysis of Combined In-line and Cross-flow Vortex Induced Vibrations, CeSOS

IMT-2013-2	Kurniawan, Adi	Modelling and geometry optimisation of wave energy converters, CeSOS
IMT-2013-3	Al Ryati, Nabil	Technical condition indexes doe auxiliary marine diesel engines, IMT
IMT-2013-4	Firoozkoohi, Reza	Experimental, numerical and analytical investigation of the effect of screens on sloshing, CeSOS
IMT-2013-5	Ommani, Babak	Potential-Flow Predictions of a Semi-Displacement Vessel Including Applications to Calm Water Broaching, CeSOS
IMT-2013-6	Xing, Yihan	Modelling and analysis of the gearbox in a floating spar-type wind turbine, CeSOS
IMT-7-2013	Balland, Océane	Optimization models for reducing air emissions from ships, IMT
IMT-8-2013	Yang, Dan	Transitional wake flow behind an inclined flat plate----Computation and analysis, IMT
IMT-9-2013	Abdillah, Suyuthi	Prediction of Extreme Loads and Fatigue Damage for a Ship Hull due to Ice Action, IMT
IMT-10-2013	Ramirez, Pedro Agustin Pérez	Ageing management and life extension of technical systems- Concepts and methods applied to oil and gas facilities, IMT
IMT-11-2013	Chuang, Zhenju	Experimental and Numerical Investigation of Speed Loss due to Seakeeping and Maneuvering. IMT
IMT-12-2013	Etemaddar, Mahmoud	Load and Response Analysis of Wind Turbines under Atmospheric Icing and Controller System Faults with Emphasis on Spar Type Floating Wind Turbines, IMT
IMT-13-2013	Lindstad, Haakon	Strategies and measures for reducing maritime CO2 emissons, IMT
IMT-14-2013	Haris, Sabril	Damage interaction analysis of ship collisions, IMT
IMT-15-2013	Shainee, Mohamed	Conceptual Design, Numerical and Experimental Investigation of a SPM Cage Concept for Offshore Mariculture, IMT
IMT-16-2013	Gansel, Lars	Flow past porous cylinders and effects of biofouling and fish behavior on the flow in and around Atlantic salmon net cages, IMT
IMT-17-2013	Gaspar, Henrique	Handling Aspects of Complexity in Conceptual Ship Design, IMT
IMT-18-2013	Thys, Maxime	Theoretical and Experimental Investigation of a Free Running Fishing Vessel at Small Frequency of Encounter, CeSOS
IMT-19-2013	Aglen, Ida	VIV in Free Spanning Pipelines, CeSOS

IMT-1-2014	Song, An	Theoretical and experimental studies of wave diffraction and radiation loads on a horizontally submerged perforated plate, CeSOS
IMT-2-2014	Rogne, Øyvind Ygre	Numerical and Experimental Investigation of a Hinged 5-body Wave Energy Converter, CeSOS
IMT-3-2014	Dai, Lijuan	Safe and efficient operation and maintenance of offshore wind farms ,IMT
IMT-4-2014	Bachynski, Erin Elizabeth	Design and Dynamic Analysis of Tension Leg Platform Wind Turbines, CeSOS
IMT-5-2014	Wang, Jingbo	Water Entry of Freefall Wedged – Wedge motions and Cavity Dynamics, CeSOS
IMT-6-2014	Kim, Ekaterina	Experimental and numerical studies related to the coupled behavior of ice mass and steel structures during accidental collisions, IMT
IMT-7-2014	Tan, Xiang	Numerical investigation of ship's continuous- mode icebreaking in level ice, CeSOS
IMT-8-2014	Muliawan, Made Jaya	Design and Analysis of Combined Floating Wave and Wind Power Facilities, with Emphasis on Extreme Load Effects of the Mooring System, CeSOS
IMT-9-2014	Jiang, Zhiyu	Long-term response analysis of wind turbines with an emphasis on fault and shutdown conditions, IMT
IMT-10-2014	Dukan, Fredrik	ROV Motion Control Systems, IMT
IMT-11-2014	Grimsmo, Nils I.	Dynamic simulations of hydraulic cylinder for heave compensation of deep water drilling risers, IMT
IMT-12-2014	Kvittem, Marit I.	Modelling and response analysis for fatigue design of a semisubmersible wind turbine, CeSOS
IMT-13-2014	Akhtar, Juned	The Effects of Human Fatigue on Risk at Sea, IMT
IMT-14-2014	Syahroni, Nur	Fatigue Assessment of Welded Joints Taking into Account Effects of Residual Stress, IMT
IMT-1-2015	Böckmann, Eirik	Wave Propulsion of ships, IMT
IMT-2-2015	Wang, Kai	Modelling and dynamic analysis of a semi-submersible floating vertical axis wind turbine, CeSOS
IMT-3-2015	Fredriksen, Arnt Gunvald	A numerical and experimental study of a two-dimensional body with moonpool in waves and current, CeSOS
IMT-4-2015	Jose Patricio Gallardo Canabes	Numerical studies of viscous flow around bluff bodies, IMT

IMT-5-2015	Vegard Longva	Formulation and application of finite element techniques for slender marine structures subjected to contact interactions, IMT
IMT-6-2015	Jacobus De Vaal	Aerodynamic modelling of floating wind turbines, CeSOS
IMT-7-2015	Fachri Nasution	Fatigue Performance of Copper Power Conductors, IMT
IMT-8-2015	Oleh I Karpa	Development of bivariate extreme value distributions for applications in marine technology, CeSOS
IMT-9-2015	Daniel de Almeida Fernandes	An output feedback motion control system for ROVs, AMOS
IMT-10-2015	Bo Zhao	Particle Filter for Fault Diagnosis: Application to Dynamic Positioning Vessel and Underwater Robotics, CeSOS
IMT-11-2015	Wenting Zhu	Impact of emission allocation in maritime transportation, IMT
IMT-12-2015	Amir Rasekhi Nejad	Dynamic Analysis and Design of Gearboxes in Offshore Wind Turbines in a Structural Reliability Perspective, CeSOS
IMT-13-2015	Arturo Jesús Ortega Malca	Dynamic Response of Flexibles Risers due to Unsteady Slug Flow, CeSOS
IMT-14-2015	Dagfinn Husjord	Guidance and decision-support system for safe navigation of ships operating in close proximity, IMT
IMT-15-2015	Anirban Bhattacharyya	Ducted Propellers: Behaviour in Waves and Scale Effects, IMT
IMT-16-2015	Qin Zhang	Image Processing for Ice Parameter Identification in Ice Management, IMT
IMT-1-2016	Vincentius Rumawas	Human Factors in Ship Design and Operation: An Experiential Learning, IMT
IMT-2-2016	Martin Storheim	Structural response in ship-platform and ship-ice collisions, IMT
IMT-3-2016	Mia Abrahamsen Prsic	Numerical Simulations of the Flow around single and Tandem Circular Cylinders Close to a Plane Wall, IMT
IMT-4-2016	Tufan Arslan	Large-eddy simulations of cross-flow around ship sections, IMT

IMT-5-2016	Pierre Yves-Henry	Parametrisation of aquatic vegetation in hydraulic and coastal research,IMT
IMT-6-2016	Lin Li	Dynamic Analysis of the Instalation of Monopiles for Offshore Wind Turbines, CeSOS
IMT-7-2016	Øivind Kåre Kjerstad	Dynamic Positioning of Marine Vessels in Ice, IMT
IMT-8-2016	Xiaopeng Wu	Numerical Analysis of Anchor Handling and Fish Trawling Operations in a Safety Perspective, CeSOS
IMT-9-2016	Zhengshun Cheng	Integrated Dynamic Analysis of Floating Vertical Axis Wind Turbines, CeSOS
IMT-10-2016	Ling Wan	Experimental and Numerical Study of a Combined Offshore Wind and Wave Energy Converter Concept
IMT-11-2016	Wei Chai	Stochastic dynamic analysis and reliability evaluation of the roll motion for ships in random seas, CeSOS
IMT-12-2016	Øyvind Selnes Patricksson	Decision support for conceptual ship design with focus on a changing life cycle and future uncertainty, IMT
IMT-13-2016	Mats Jørgen Thorsen	Time domain analysis of vortex-induced vibrations, IMT
IMT-14-2016	Edgar McGuinness	Safety in the Norwegian Fishing Fleet – Analysis and measures for improvement, IMT
IMT-15-2016	Sepideh Jafarzadeh	Energy efficiency and emission abatement in the fishing fleet, IMT
IMT-16-2016	Wilson Ivan Guachamin Acero	Assessment of marine operations for offshore wind turbine installation with emphasis on response-based operational limits, IMT
IMT-17-2016	Mauro Caneloro	Tools and Methods for Autonomous Operations on Seabed and Water Coumn using Underwater Vehicles, IMT
IMT-18-2016	Valentin Chabaud	Real-Time Hybrid Model Testing of Floating Wind Tubines, IMT
IMT-1-2017	Mohammad Saud Afzal	Three-dimensional streaming in a sea bed boundary layer
IMT-2-2017	Peng Li	A Theoretical and Experimental Study of Wave-induced Hydroelastic Response of a Circular Floating Collar
IMT-3-2017	Martin Bergström	A simulation-based design method for arctic maritime transport systems

IMT-4-2017	Bhushan Taskar	The effect of waves on marine propellers and propulsion
IMT-5-2017	Mohsen Bardestani	A two-dimensional numerical and experimental study of a floater with net and sinker tube in waves and current
IMT-6-2017	Fatemeh Hoseini Dadmarzi	Direct Numerical Simulation of turbulent wakes behind different plate configurations
IMT-7-2017	Michel R. Miyazaki	Modeling and control of hybrid marine power plants
IMT-8-2017	Giri Rajasekhar Gunnu	Safety and efficiency enhancement of anchor handling operations with particular emphasis on the stability of anchor handling vessels
IMT-9-2017	Kevin Koosup Yum	Transient Performance and Emissions of a Turbocharged Diesel Engine for Marine Power Plants
IMT-10-2017	Zhaolong Yu	Hydrodynamic and structural aspects of ship collisions
IMT-11-2017	Martin Hassel	Risk Analysis and Modelling of Allisions between Passing Vessels and Offshore Installations
IMT-12-2017	Astrid H. Brodtkorb	Hybrid Control of Marine Vessels – Dynamic Positioning in Varying Conditions
IMT-13-2017	Kjersti Bruserud	Simultaneous stochastic model of waves and current for prediction of structural design loads
IMT-14-2017	Finn-Idar Grøtta Giske	Long-Term Extreme Response Analysis of Marine Structures Using Inverse Reliability Methods
IMT-15-2017	Stian Skjong	Modeling and Simulation of Maritime Systems and Operations for Virtual Prototyping using co-Simulations
IMT-1-2018	Yingguang Chu	Virtual Prototyping for Marine Crane Design and Operations
IMT-2-2018	Sergey Gavrilin	Validation of ship manoeuvring simulation models
IMT-3-2018	Jeevith Hegde	Tools and methods to manage risk in autonomous subsea inspection, maintenance and repair operations
IMT-4-2018	Ida M. Strand	Sea Loads on Closed Flexible Fish Cages
IMT-5-2018	Erlend Kvinge Jørgensen	Navigation and Control of Underwater Robotic Vehicles

IMT-6-2018	Bård Stovner	Aided Inertial Navigation of Underwater Vehicles
IMT-7-2018	Erlend Liavåg Grotle	Thermodynamic Response Enhanced by Sloshing in Marine LNG Fuel Tanks
IMT-8-2018	Børge Rokseth	Safety and Verification of Advanced Maritime Vessels
IMT-9-2018	Jan Vidar Ulveseter	Advances in Semi-Empirical Time Domain Modelling of Vortex-Induced Vibrations
IMT-10-2018	Chenyu Luan	Design and analysis for a steel braceless semi-submersible hull for supporting a 5-MW horizontal axis wind turbine
IMT-11-2018	Carl Fredrik Rehn	Ship Design under Uncertainty
IMT-12-2018	Øyvind Ødegård	Towards Autonomous Operations and Systems in Marine Archaeology
IMT-13-2018	Stein Melvær Nornes	Guidance and Control of Marine Robotics for Ocean Mapping and Monitoring
IMT-14-2018	Petter Norgren	Autonomous Underwater Vehicles in Arctic Marine Operations: Arctic marine research and ice monitoring
IMT-15-2018	Minjoo Choi	Modular Adaptable Ship Design for Handling Uncertainty in the Future Operating Context
MT-16-2018	Ole Alexander Eidsvik	Dynamics of Remotely Operated Underwater Vehicle Systems
IMT-17-2018	Mahdi Ghane	Fault Diagnosis of Floating Wind Turbine Drivetrain- Methodologies and Applications
IMT-18-2018	Christoph Alexander Thieme	Risk Analysis and Modelling of Autonomous Marine Systems
IMT-19-2018	Yugao Shen	Operational limits for floating-collar fish farms in waves and current, without and with well-boat presence
IMT-20-2018	Tianjiao Dai	Investigations of Shear Interaction and Stresses in Flexible Pipes and Umbilicals
IMT-21-2018	Sigurd Solheim Pettersen	Resilience by Latent Capabilities in Marine Systems
IMT-22-2018	Thomas Sauder	Fidelity of Cyber-physical Empirical Methods. Application to the Active Truncation of Slender Marine Structures
IMT-23-2018	Jan-Tore Horn	Statistical and Modelling Uncertainties in the Design of Offshore Wind Turbines

IMT-24-2018	Anna Swider	Data Mining Methods for the Analysis of Power Systems of Vessels
IMT-1-2019	Zhao He	Hydrodynamic study of a moored fish farming cage with fish influence
IMT-2-2019	Isar Ghamari	Numerical and Experimental Study on the Ship Parametric Roll Resonance and the Effect of Anti-Roll Tank